DOE/NASA/0342-1
NASA CR-174783

Methods for Heat Analysis and Temperature Field Analysis of the Insulated Diesel

Phase I Progress Report

Thomas Morel, Paul N. Blumberg,
Edward F. Fort, and Rifat Keribar
Integral Technologies Incorporated

August 1984

Prepared for
NATIONAL AERONAUTICS AND SPACE ADMINISTRATION
Lewis Research Center
Under Grant DEN 3-342

for
U.S. DEPARTMENT OF ENERGY
Conservation and Renewable Energy
Office of Vehicle and Engine R&D

DISCLAIMER

Printed in the United States of America

Available from
National Technical Information Service
U.S. Department of Commerce
5285 Port Royal Road
Springfield, VA 22161

NTIS price codes[1]
Printed copy: A12
Microfiche copy: A01

[1]Codes are used for pricing all publications. The code is determined by the number of pages in the publication. Information pertaining to the pricing codes can be found in the current issues of the following publications, which are generally available in most libraries: *Energy Research Abstracts (ERA); Government Reports Announcements* and Index (*GRA* and I); *Scientific and Technical Abstract Reports (STAR);* and publication, NTIS-PR-360 available from NTIS at the above address.

DISPLAY 11/2/1

85N16699*# ISSUE 7 PAGE 1056 CATEGORY 85 RPT#: NASA-CR-174783
DOE/NASA/0342-1 NAS 1.26:174783 CNT#: DEN3-342 DE-AI01-80CS-50194
84/08/00 274 PAGES UNCLASSIFIED DOCUMENT

UTTL: Methods for heat transfer and temperature field analysis of the insulated

AUTH: A/MOREL, T.; B/BLUMBERG, P. N.; C/FORT, E. F.; D/KERIBAR, R.
CORP: Integral Technologies, Inc., Westmont, Ill. AVAIL.NTIS SAP: HC A12/MF A01
MAJS: /*CONVECTIVE HEAT TRANSFER/*DIESEL ENGINES/*HEAT RADIATORS/*RADIATIVE HEAT TRANSFER
MINS: / ENERGY CONVERSION EFFICIENCY/ ENGINE DESIGN/ FUEL CONSUMPTION/ TEMPERATURE DISTRIBUTION/ THERMAL ANALYSIS/ THERMODYNAMIC CYCLES
ABA: R.S.F.
ABS: Work done during phase 1 of a three-year program aimed at developing a comprehensive heat transfer and thermal analysis methodology oriented specifically to the design requirements of insulated diesel engines is reported. The technology developed in this program makes possible a quantitative analysis of the low heat rejection concept. The program is comprehensive in that it addresses all the heat transfer issues that are critical to the successful development of the low heat rejection diesel engine: (1) in-cylinder convective and radiative heat transfer; (2) cyclic transient heat transfer in thin solid layers at component surfaces

ENTER: P

DISPLAY 11/2/1

adjacent to the combustion chamber; and (3) steady-state heat conduction in the overall engine structure. The Integral Technologies, Inc. (ITI) program is comprised of a set of integrated analytical and experimental tasks. A detailed review of the ITI program approach is provided, including the technical issues which underlie it and a summay of the methods that were developed.

DOE/NASA/0342-1
NASA CR-174783

Methods for Heat Analysis and Temperature Field Analysis of the Insulated Diesel

Phase I Progress Report

Thomas Morel, Paul N. Blumberg,
Edward F. Fort, and Rifat Keribar
Integral Technolgies Incorporated
Westmont, Illinois 60559

August 1984

Prepared for
NATIONAL AERONAUTICS AND SPACE ADMINISTRATION
Lewis Research Center
Cleveland, Ohio 44135
Under Grant DEN 3-342

for
U.S. DEPARTMENT OF ENERGY
Conservations and Renewable Energy
Office of Vehicle and Engine R&D
Under Interagency Agreement DE-AI01-80CS50194

TABLE OF CONTENTS

SUMMARY

This report describes the work carried out during Phase I of a three-year, three-phase program sponsored by DOE and administered by NASA. Phase I consists of a number of integrated analytical and experimental tasks. These tasks form elements of a broad program whose objective is to develop a comprehensive analytical methodology for studies of combustion chamber heat transfer and temperature distribution in the related structure of an insulated diesel engine. The work carried out to date concentrated on the parallel development of certain heat transfer and thermal models: specifically convection and radiation heat transfer models, a one-dimensional transient heat conduction model, and a multi-dimensional steady-state heat conduction model. During the same period, work in progress at Purdue University concentrated on the development of experimental methods and instrumentation needed to acquire accurate engine test data for model calibration and validation.

The development of a new convective heat transfer model is reported in Chapter I. The convective coefficients are based on the gas velocities predicted by a three-region bowl-in-piston flow model. The flow model solves equations describing radial and axial velocities, angular momentum (swirl), as well as turbulence, and tracks them during the entire engine cycle, including intake, compression, combustion, expansion and exhaust. From these are calculated the effective convective gas velocities adjacent to six "elementary" surfaces which form the combustion chamber. Each of the surfaces thus has its own convective heat transfer coefficient which is based on the effective velocities. As a result, the present model provides a high degree of spatial and temporal heat flux resolution important for addressing insulated engine design issues.

The other component of gas-wall heat transfer is heat radiation discussed in Chapter II. The radiation model is built around a two-zone combustion model which provides the needed radiation temperatures and a description of the radiating soot-laden zone. The heat flux absorbed by the surrounding surfaces will be described by a zonal geometrical model which will account for appropriate view factors between the burning zone

and the individual elementary surfaces, as well as for radiation and reflection of adjoining surfaces.

The conduction through the structure of the heat transferred from the gas, and the heat deposited by piston and ring friction on the liner, is handled by a transient cyclic analysis (Chapter III) and by a steady-state heat conduction model (Chapter IV). The transient analysis is based on the solution of the one-dimensional heat conduction equation, solved for a number of surfaces of interest. The transient code is numerically highly efficient, which permits its incorporation into the overall thermodynamic cycle code. It provides the description of the wall temperature dynamics such as wall temperature swing and penetration depth of the transient temperature waves. The steady-state heat conduction model, solved together with the cycle calculation, provides a realistic approximation to the thermal profile in the surrounding structure, described by over 150 elements. This permits studies of the effects of insulating layers placed at selected locations in the combustion chamber, including effects of their properties and layer thicknesses as well.

The program plan calls for continued model development, followed by validation with test data from conventionally cooled baseline engine experiments, and by full integration of all models, to be carried out in Phase II. To get an early reading on the progress of the program, the plan provided for integration of all completed model elements at the end of Phase I, and for sample parametric studies of insulation strategies to be carried out at that time (Chapter V). The objectives of these early calculations were to verify the correct functioning of the models, obtain feedback on additional needed refinements and capabilities to be carried out during Phase II, and to gain some preliminary insights into engine performance and thermal environment effects of different insulated design strategies. It is in this light that the results presented here should be viewed; although preliminary, they demonstrate some of the capabilities that the methodology will have when it is complete.

The experimental work in Phase I included installation of a Cummins single cylinder research engine at Purdue University (Chapter VI). The development of experimental techniques needed for accurate engine data acquisition is described in Chapter VII. It includes the design, fabrication and testing of a novel optical proximeter which will be used for accurate determination and phasing of crank angle data. A fast response thermocouple was built to record in-cylinder surface temperatures from which one can deduce transient heat fluxes. Heat radiation will be measured using an infrared radiation detector, shielded by a window, which will be used to deduce radiation temperatures and heat flux through spectral resolution of the detector signal.

ACKNOWLEDGEMENTS

The work reported herein has benefited from the contributions of many individuals and organizations.

The authors wish to thank Mr. James Wood, Project Manager at NASA-Lewis, for his constant interest and support, and for his valuable suggestions during the course of the program. Mr. Harry Davison of NASA-Lewis has also provided significant support of the program through his technical and administrative interest in its progress.

ITI wishes to acknowledge the highly supportive role of Messrs. Albert Chesnes and Edward Gregory of DOE staff in Washington, DC, contributing to the early integration of the ITI work into the overall Heavy Duty Transport and Ceramic Technology programs. The Purdue University subcontract effort under Professor Colin Ferguson has laid a firm foundation for a successful engine experimental program to be carried out in Phases II and III of the contract. Finally, Cummins Engine Company has proven to be a very active voluntary industrial participant in this program giving generously of their time and material resources. Dr. Alan Lyn and Messrs. Charles White and Robert Hoffmeister were instrumental in organizing the participation of the Cummins Engine Company in the program. Dr. S. M. Shahed and Messrs. Kevin Hoag and Mostafa Kamel have been very constructive in their technical liaison role, providing data for model development and application, and consultation with respect to the single cylinder engine Cummins has donated to Purdue University for this work.

INTRODUCTION

A world-wide technological thrust is currently in progress to develop insulated, low heat rejection diesel engines which exhibit higher thermal efficiency and improved system reliability, power density and package size. Both industrial and government funded programs of significant magnitude are in place to develop the high temperature materials, lubricants and technical know-how required to achieve this potential.

Integral Technologies Incorporated (ITI) is carrying out a three year program, funded by the U.S. Department of Energy and administered by NASA-Lewis Research Center, aimed at developing a comprehensive heat transfer and thermal analysis methodology oriented specifically to the design requirements of insulated diesel engines. The technology developed in this program will make possible a quantitative analysis of the low heat rejection concept, including the determination of the degree of heat transfer reduction and performance improvement that may be realistically achieved, the identification of design strategies that may be adopted toward that end, and a detailed characterization of the thermal environment in which new materials, lubricants and lubricant concepts will have to exist.

The program is comprehensive in that it addresses all of the heat transfer issues that are critical to the successful development of the low heat rejection diesel engine, i.e.:

1) in-cylinder convective and radiative heat transfer;
2) cyclic transient heat transfer in thin solid layers at component surfaces adjacent to the combustion chamber;
3) steady-state heat conduction in the overall engine structure;
4) "slow" transients in the engine structure resulting from warmup or changes in speed and load.

Key heat transfer data for development and validation of the metholodogy are being acquired at Purdue University under subcontract. In order

that practical considerations are adequately taken into account in the development of the analytical methods, the program is structured around a commercial, state-of-the-art, heavy-duty diesel engine. Early in the program, NASA approved ITI's request to involve a major diesel engine manufacturer in the program on a voluntary, non-funded basis. As a result, the Cummins Engine Company and ITI have reached an agreement along these lines and Cummins' extensive design and testing experience in this field is available to the program.

The ITI program is comprised of a set of integrated analytical and experimental tasks. This Phase I report provides a detailed review of the ITI program approach, including the technical issues which underlie it, a summary of the methods that have been developed and the results which have been obtained in the first year of the contract effort.

TECHNICAL ISSUES UNDERLYING ITI PROGRAM

A controlled amount of heat transfer is incorporated by design in current metal engines to assure adequate cooling of internal surfaces even at the highest thermal loadings, i.e. at the highest fuel flow rates occurring at the rated speed and load. The result is that a substantial amount of fuel energy is carried away from the combustion chamber, reducing the in-cylinder cycle efficiency and the energy availability of the exhaust gases. For typical Class 8 highway truck diesel engines the heat transfer from the combustion chamber gases ranges from over 10 to 30 percent of the fuel energy depending on the operating conditions. For smaller truck engines with swirl combustion systems and for automotive diesels the percent heat loss is higher.

In order to reduce the rate of in-cylinder heat transfer substantially, it is necessary to increase the temperature of in-cylinder surfaces from current values near 500°K to well over 1000°K. Since the current levels of heat transfer are near the lowest achievable with practical metal components, efforts are concentrated on the design of components using

high temperature materials which would require less engine cooling. For a number of reasons, cost being prominent among them, ceramics appear to be the most likely candidates to satisfy the requirements set by practical considerations. However, their use as engine structural materials introduces a multitude of materials-oriented, engine design considerations. Some of the more prominent of these are:

1. material strength, toughness and stability at elevated temperatures;
2. thermal conductivity of high temperature, high strength, durable materials;
3. fatigue due to high cyclical thermal loading;
4. thermal expansion matching for ceramic and metallic materials;
5. lubricant stability and performance at high temperatures;
6. friction and wear characteristics with new structural materials and lubricants, which should be at least comparable to current technology engines.

As a result, substantial programs to evaluate insulated engine materials and designs and exhaust energy recovery methods (e.g., power turbine, organic Rankine cycle) are currently in progress, supported by both the industry and by the government. To be most effective, these efforts should be grounded in a comprehensive system analysis, which combines thermodynamic and heat transfer considerations and is designed to fully assess the implications of the concept as well as its feasibility and benefits in practical terms. The need for such an analysis becomes apparent once one considers some basic facts about the engine heat transfer process:

1. Combustion gas temperatures (spatially averaged) may be expected to reach values of up to 1800-2000°K at the highest thermal loading, which corresponds to a cycle-averaged temperature of 1300-1400°K. Therefore, in order to eliminate or substantially reduce the convective heat transfer, the average wall temperature must be allowed to rise up to or near these levels.

2. Materials available for combustion chamber application appear to be limited to about 1400°K, which is close to the value estimated above for the desired average wall temperature. However, the materials limitations are accentuated by the fact that the wall temperature is non-uniform spatially as well as temporally.

3. Some of the heat transfer is due to heat radiation, which is cited in the literature to be on the order of 20-30% of the total heat rejected. This radiation emanates from the hottest portions of the flame (2500-3000°K) which are well above any envisioned wall temperatures. Consequently, it is likely that in insulated engines with low convective heat transfer, a much higher percentage of the heat transfer will be through the radiation mechanism.

4. There is a complex interaction between the piston, piston rings, lubricants and the cylinder liner surface which determines the amount of energy (approximately five percent of the fuel energy) which is dissipated into heat at the interfaces and the direction of the resulting heat flow. At these interfaces issues of adequate lubricant life must be balanced against heat rejection paths created by lubricant cooling.

Therefore, due to fundamental physical phenomena (i.e., radiation, piston ring friction and limitations posed by currently envisioned materials, some engine heat transfer to coolant will have to be permitted. Additional limitations on maximum permissible temperatures may also be imposed by the lubricant properties. Beyond these, there are numerous other considerations, such as the magnitude of wall temperature swings and their impact on thermal stress fatigue, temperature limitations deriving from the large expansions to which the hot components will be subjected, and special cooling that may have to be provided for injectors and exhaust valves.

OUTLINE OF THE ITI PROGRAM

It is apparent that the task of development of the low heat rejection engine is a multifaceted one, and it requires a synergistic approach combining a number of engineering disciplines and technologies. Prominent among these are: heat transfer, thermodynamics, engine design and development, high temperature structural materials, and high temperature lubrication. All of these issues are coupled and need to be assessed and ultimately solved together. They are linked together by what might be termed the "engine environment," i.e., gas temperatures and pressures, wall surface temperatures, transient and steady state thermal profiles within the walls, etc. This environment has impact on engine heat transfer and thermodynamic efficiency and at the same time is a key input into the selection of materials and high temperature lubricants. The constraints that derive from the ranges of applicability of practical and forthcoming materials and lubricants must serve to keep specific designs for reduced heat rejection engines within realistic bounds. For cost effective development of this technology one must be able to assess the merits of different approaches in achieving significant reductions in heat rejection without compromising engine durability.

In view of all the technical issues discussed previously, the ITI program is structured around the development of an integrated methodology which can address the special design considerations inherent in the insulated engine concept. The general objectives of the program are:

1. Development of a systematic methodology for quantitative assessment of heat transfer and thermal processes in insulated engines which can serve as a tool for concept optimization;

2. Validation of the methodology with experimental data;

3. Application of the resulting methods to a comprehensive analysis of insulated engine design and operation, including evaluation of temperature fields in structure materials and temperature of lubricated surfaces.

To achieve these objectives, a number of closely related program elements or task areas have been defined. These are:

1) development of convection and radiation heat transfer submodels,
2) analysis of conductive heat transfer during fast and slow engine transients,
3) analysis of steady state conduction heat transfer,
4) thermodynamic cycle analysis,
5) baseline cooled engine experiments and calibration of heat transfer models,
6) insulated engine experiments and code validation,
7) comprehensive analysis of the insulated engine concept and of materials implications.

These elements are described in more detail below.

Heat Transfer Models. Because they lack the basic physics of the convective process, the engine heat transfer correlations available in the literature are not applicable to detailed studies of heat transfer such as those needed in insulated engine analysis. New correlations are being developed in the ITI program for convective heat transfer, which include the effects of actual gas velocity, turbulence and zoned combustion. At the same time a sophisticated model is being developed for heat radiation, which will include features such as the use of flame temperature instead of average chamber temperature, extinction coefficients based on soot concentration, and geometrical mean-beam length model accounting for geometrical details of the combustion chamber and of the burned zone. Both of these correlations will predict heat transfer in a spatially resolved fashion as well as time resolved.

Transient Conduction. The heat flux to the wall is highly transient with concentrated bursts of high heat flux followed by relatively long periods of low heat flux rates. This pattern produces temperature transients in thin layers adjacent to the combustion wall surfaces. This dynamic heat conduction through the chamber walls is being analyzed

by a transient one-dimensional heat conduction code which includes the effects of finite wall heat capacity. The model can handle layered or laminated walls, and this is an important capability, permitting studies of unconventional materials. Of interest are the surface temperature dynamics (time-varying wall temperature can reduce heat transfer) as well as thermal stress and fatigue produced by the temperature waves in the thin layer near the surface.

Steady State Conduction. The heat flux from the gases to the surfaces of the combustion chamber passes through the thin transient layer into the structure below. There the temperature field is steady-state (at fixed engine speed and load). It may be solved for by a variety of techniques, e.g., by finite-element methods. Such a solution provides information about the temperature distribution produced in the structure by the engine combustion process. The calculated details of surface temperatures in the piston, along the head and in valves and along the liner set boundary conditions for the one-dimensional transient heat transfer calculations and feed back into the gas-wall heat transfer calculations. In this manner, the whole heat transfer/thermal problem is closed, and may be solved by appropriate analytical techniques.

Thermodynamic Analysis. The entire heat transfer problem is driven by the engine air flow and combustion phenomena. Thus, the central element around which the methodology must operate is a reliable, detailed model of the engine operation. This model has to provide time resolved information about combustion chamber pressure, temperature and thermodynamic properties (separately for burned and unburned bases), flow velocities and mass flow through valves, intake angular momentum flux, details of the injection process, as well the instantaneous piston location and chamber geometry. The heat transfer calculations in turn feed back into the thermodynamic analysis and they have an effect on the instantaneous energy balance which ultimately determines the piston work done and exhaust temperatures. The engine model used in this work is described in the Appendix. In addition to the capability to describe the in-cylinder processes, it also treats the engine as a system, including the

turbocharger, aftercooler and power turbine. This allows prediction of the effects of insulation on the ultimate performance objective -- i.e., the overall system thermal efficiency.

Baseline Engine Experiments. Experiments will be carried out on the Cummins single cylinder engine based on the 14 liter NH series, representing a typical state-of-the-art (non-insulated) DI diesel engine. The engine will be run over a wide range of speeds and loads to provide an essential data base for subsequent analyses. This includes measurements of combustion chamber pressure and also the development and application of a technique for measurements of radiative heat transfer. The acquired data will be used to test and calibrate the new correlations for convection and radiation heat transfer developed in this program, using the thermodynamic cycle analysis in the p-t or reverse mode. In order to obtain the highest quality experimental data, state-of-the-art techniques and instrumentation for accurate pressure-time data acquisition are being developed. This includes accurate calibration of pressure transducers and the development of a precise method of crank angle indication based on an optical proximeter approach. A multiple-color method will be applied to obtain accurate measurement of heat radiation in the engine environment, supported by an in-depth analytical study of heat radiation from sooting flames.

Insulated Engine Experiments. The baseline engine will be converted to an insulated engine by implementation of substitute materials. The main objective of these experiments will be to generate a reliable data base for testing and validation of the heat transfer and thermal methodology developed in this program. Accordingly, in choosing the locations and methods of insulation, use will be made of the methodology to produce meaningful changes in heat rejection, but at the same time every effort will be made to insure that the insulation applied does not interfere with the ability to acquire accurate data. The experience of Cummins Engine Company, available to the program, is expected to be a very valuable resource during this portion of the work. The baseline data obtained in the initial set of experiments (see above) will provide a

reference for before-and-after comparisons. In preparation for the experimental evaluation, instrumentation for temperature, heat flux and pressure measurements will be developed. These have to be suitable for high temperature operation, and in addition, techniques for their correct implantation into the ceramic components have to be found. The acquired data on temperatures, heat fluxes and engine performance will feed back into the thermodynamic cycle analysis and will be used to validate the design methods and concepts developed in the course of this project. Thus, a solid foundation for the refinement of the heat rejection strategies and for amplifying the design insights obtained in the analytical part of this program will be established.

Heat Rejection Analysis. Using the complete methodology, i.e., the thermodynamic cycle code, heat transfer submodels, one-dimensional heat conduction model for the near surface layers, the multi-dimensional heat conduction model for the surrounding structure and engine system model including turbocharger and a power turbine, studies of heat rejection and engine performance will be made. The studies will include baseline cooled engine, superinsulated limiting case, and will span a whole range of intermediate insulating strategies. The analysis matrix will include several prescribed design strategies which will be analyzed by comparison to a conventional metallic engine. The designs will include spray coatings, monolithic ceramics and novel concept materials as information becomes available. The engine conditions will include rated speed/load, peak torque, rated speed/quarter load and idle. The addition of the turbocharger and power turbine to the model will provide a more meaningful assessment of efficiency gains and also of materials requirements for these components.

One of the key outputs of the calculations will be the definition of the operating dynamic thermal environment of an insulated engine, knowledge of which is an essential input not only for selection and application of high temperature structural materials and lubricants but is also critically important in guiding the extensive research and development efforts that are underway in these fields. In this context different

strategies of heat rejection with different degrees of insulation will be investigated, weighing the growing severity of problems arising from increasing degree of insulation against the well-known benefits of increased thermodynamic efficiency, greater available energy in the exhaust and reduced or eliminated cooling system.

I. CONVECTIVE HEAT TRANSFER MODEL

Introduction

The heat transfer process in internal combustion engines has always played an important role in engine design. One aspect of heat transfer is the loss of energy from the combustion chamber gases which reduces the amount of piston work, and a parallel consideration relates to durability of engine components exposed to high combustion temperatures. In modern engine design the amount of cooling applied should be optimized with respect to the balance between these two considerations, i.e., every effort should be made to keep engine cooling at the minimum level compatible with the materials temperature limits. To achieve the proper cooling, and to predict the effect of heat transfer on engine performance, one needs to have the analytical capability to estimate heat transfer rates. That has been recognized for a long time, and the earliest heat transfer correlations date well back even before comprehensive thermodynamic cycle simulations became practical engineering tools. The need for such correlations has been growing steadily because of an increasing number of areas requiring heat transfer analysis as an input. These include, among others, heat transfer distribution and thermal stresses in the engine structure, emissions modeling, liner lubricant temperatures, etc. More recently, the importance of engine heat transfer has further increased due to interest in insulated diesels lined with ceramic materials, which promise higher thermodynamic efficiency and smaller cooling systems.

The problem of optimum engine cooling requires the solution of the coupled problem of heat transfer from gases to walls and of heat conduction through the structure. The heat conduction portion of such a calculation can be carried out fairly routinely, and to acceptable accuracy, using finite element models (FEM).

By contrast, gas-to-wall heat transfer modeling is still in a developmental state. This presents a major stumbling block, since the gas-to-

wall heat transfer correlations are needed to provide the necessary boundary conditions for the FEM codes. The calculated temperature field in the structure depends very critically on these boundary conditions, which must be well grounded in physics, if they are to provide an accurate description of the heat flux rates and of their spatial and temporal variation within the combustion chamber.

The model for in-cylinder heat transfer described below advances the state-of-the-art in that it gives a more accurate and more detailed description of the heat flux distribution in the combustion chamber. When used in a thermodynamic cycle model, it gives a more accurate description of the effects of heat transfer on engine performance. Its use in conjunction with FEM codes improves the ability to address the issues of maximum material temperatures, temperatures of lubricated surfaces in sliding contact and of cooling load carried by engine coolant and by oil.

Previous Convective Heat Transfer Models

The standard approach to modeling of convective heat transfer is to assume that the heat flux may be described by an expression

$$q(t) = h_g(t)\,[T_g(t) - T_w(A)] \qquad (1\text{-}1)$$

where h_g is heat transfer coefficient, T_g is gas temperature responsible for convective heat transfer, T_w is wall temperature and A is local surface area. This is essentially a quasi-steady approximation, which postulates that the heat flows in the direction of instantaneous differential between T_g and T_w. This assumption has been questioned from time to time on account of observed phase shift between the heat flux and the measured temperature differential, but this shift, if real, is not large enough to have a significant effect on the overall parameters that arise in engines. Because of that the use of equation (1-1) is practically universal.

The main differences between the various approaches stem from the definitions of h_g employed. Surveying the history of these approaches one finds that they can be divided into three "generations," starting with simple dimensional models, to more fundamentally based dimensionless models, to models that attempt to describe in some detail the fluid motions that drive the convective heat transfer.

Early Dimensional Models. These were the first models which date back over 60 years. The first, apparently, was the model of Nusselt (1923) who carried out experiments in a spherical combustion bomb, and based on these he extrapolated a relation for internal combustion engines in the form

$$h_g = a\ \sqrt[3]{p^2T}\ (b_1+b_2V_p) \qquad (1\text{-}2)$$

where V_p is the mean piston speed, p and T are combustion chamber pressure and temperature, and a, b_1 and b_2 are constants to be fitted to experimental data. This model was used for many years, although it was based on data from a quiescent bomb not representative of actual engines. Another problem was that the model was not dimensionless and that presented scaling problems. Several subsequent investigators attempted to improve the correlation by changing the model constants, but none of these provided any real improvement.

Another popular model was that due to Eichelberg (1939), who proposed

$$h_g = a(V_p)^{1/3}\ (pT)^{1/2} \qquad (1\text{-}3)$$

The choice of this particular form of the correlation appears to have been quite arbitrary, and the constant a was determined by comparison to engine data. As with the Nusselt's model, the main drawback is again the lack of physics and the difficulty in scaling due to the dimensional form of the expression.

Second "Generation" Dimensionless Models. The first correlation guided by dimensional analysis appears to have been that of Elser (1955) who proposed

$$Nu = h_g B/k_g \sim Re^{1/2} P^{1/2} \qquad (1\text{-}4)$$

where the proportionality factor includes a controversial "entropy increase" term, and

$$Re \equiv \rho V_p B/\mu \quad \text{and} \quad P \equiv C_p \mu/k_g$$

Reexamination of all data available at the time, led Annand (1963) to propose that the proper dimensionless form is

$$Nu = a\ Re^b \qquad (1\text{-}5)$$

which follows the lines of the well known Reynolds analogy between heat and momentum transfer in fully developed turbulent boundary layers. The value of the exponent b was chosen to be 0.7, and for this value of b the corresponding value of a was found to be between 0.35 and 0.80 depending on the "intensity of the charge motion." The Reynolds number was again based on the mean piston speed.

A similar expression with exponent of 0.7 was also proposed by Sitkei (1962), and others have proposed somewhat different values, e.g., Alcock (1962) who favored b=0.75.

The widely used Woschni (1967) correlation follows this line of approach by proposing

$$Nu = h_g B/k_g = a\ (\rho BU/\mu)^{0.8} \qquad (1\text{-}6)$$

where the characteristic velocity U is defined as

$$U = c_1 V_p + \text{"additional gas velocity"} \qquad (1\text{-}7)$$

The second term in equation (1-7) is calculated from the instantaneous difference between firing and motoring pressures, and is an attempt to step beyond the constant characteristic velocity in the Reynolds analogy. It may be noted that for motoring engines the second term in equation (1-7) is zero and Woschni's model reverts to the general form proposed by Annand.

Third "Generation" Flow-Based Models. The previous class of models represented the effects of fluid motions only tangentially through the use of V_p. This reflects the expected trend that magnitude of gas velocities will tend to increase with increasing engine speed. However, the actual crank angle by crank angle variation of gas velocities is not represented, nor are the changes from engine to engine. These are serious shortcomings, which make the models insensitive to several engine design details that are well known to enhance heat transfer, such as port and valve size and shape, and piston crown geometry.

This deficiency was recognized by some, among whom Knight (1964) was apparently the first to propose that the mean piston velocity be replaced by a more meaningful measure of the characteristic velocity. He proposed the use of a gas velocity calculated from the mean kinetic energy of the combustion chamber gas as

$$V_{gas} = \sqrt{E/2m} \qquad (1\text{-}8)$$

The mean kinetic energy E is calculated from

$$(mE)^{\cdot} = \Sigma \dot{m}_{in} V_{in}^2/2 + \text{squish kinetic energy} - \dot{m}_{out} E \qquad (1\text{-}9)$$

where subscript in represents valve inflows and injection. The calculated V_{gas} was attenuated by an ad hoc friction factor based on pipe flow data. As defined, the gas flow velocity in effect lumps together some elements of the mean (bulk) velocity with turbulence, and this represents a definite step forward in convective heat transfer modeling.

Among the objections one may raise to the model is that it does not take into account the chamber geometry. Also, the effects of wall friction should have been included in equation (1-9), rather than applied to the resultant velocity, and the equation should have a term that would represent the decay of turbulence by dissipation. All of the terms in the equations are based on geometrical (displacement) relations, and exclude important effects of pressure differentials across the valves. And yet another objection is that the effects of air swirl are not included.

A different approach was taken by Dent and Suliaman (1977) who used in the Reynolds number definition a characteristic velocity based on swirl alone, with

$$Re = \rho \omega r^2/\mu$$

where the swirl angular velocity ω is presumably to be obtained by solving an equation for conservation of angular momentum. The heat transfer coefficient is then obtained from

$$Nu = h_g B/k_g = a\ B/r\ (\rho \omega r^2/\mu)^{0.8} \qquad (1\text{-}10)$$

and it varies with radius along the piston and head, and is constant along the liner. It excludes the effects of intake flow and squish, important in many typical engine configurations.

The role of turbulence in heat transfer was explicitly considered by Borgnakke, et. al. (1980), who proposed the solution of global two equation k and ε turbulence model for the combustion chamber in conjunction with a two-zone combustion model. Subsequent development of this model (Davis and Borgnakke, 1982) led to the use of Reynolds analogy in the form

$$Nu = h_g \ell/k_g = a\ Re^b = a\ (\rho k^{\frac{1}{2}} \ell/\mu)^{0.7} \qquad (1\text{-}11)$$

where the effective velocity is taken to be the square root of turbulent kinetic energy k, and ℓ is the length scale of turbulence defined as $\ell \equiv k^{1.5}/\varepsilon$. The two turbulence equations are solved for each of two zones, burned and unburned, separately, and so the heat transfer coefficients of the two zones have different values which are uniform spatially over each of the two zones. An important omission is the neglect of the mean flow effects on heat transfer. As will be shown later, the mean flow is always important, and in the case of high swirl it is the dominant driving force behind heat transfer.

A recent model of Poulos and Heywood (1983) considers convective heat transfer to be driven by both the mean-motion and turbulence. They solve two equations, one for conservation of mean kinetic energy, K, and one for turbulent kinetic energy, k, in the form

$$(mK)^{\cdot} = \dot{m}_i V_i^2/2 - mP - K\dot{m}_e \qquad (1\text{-}12)$$

$$(mk)^{\cdot} = m(P-\varepsilon) - k\dot{m}_e \qquad (1\text{-}13)$$

where P is the production of turbulence. The dissipation rate ε is modeled as

$$\varepsilon = (2k/3)^{1.5}/\ell = (2k/3)^{1.5}\,\pi B^2/4V$$

i.e., the turbulence length scale ℓ is equal to the average distance between the piston and the head. The production term is modeled as

$$P = a\,(K/\ell)\,k^{1/2}$$

Once K and k have been calculated, the heat transfer coefficient is obtained from

$$h_g \ell/k_g = a\,Re^{0.8}\,P^{0.33} = a\,(\rho V_{gas}\ell/\mu)^{0.8}\,P^{0.33}$$

where the gas velocity is related to K, k, and the instantaneous piston speed as

$$V_{gas} = [2K + 2k + (V_p(t)/2)^2]^{1/2}$$

The calculated heat transfer coefficient is spatially uniform.

The model does not include the effects of swirl and squish, critically important in many engines. Also, the mean kinetic energy equation (equation 1-12) is in error, containing the term (-mP) instead of an appropriate stress gradient term. In addition, the approximation to the production term P in the turbulence kinetic energy equation they use is only approximate, and it excludes the effect of compression on turbulence, as well as effects of swirl and squish. Nevertheless, the Poulos and Heywood model is the most comprehensive model to date.

Summary. The development of convective heat transfer correlations has progressed over the years very significantly. However, even the most advanced ones suffer from a number of shortcomings, the more important ones among them being that:

-- Models do not describe all key fluid motions responsible for convective heat transfer. As a result they are not extrapolable and their predictions for a given engine vary by a factor of 3 or more from each other, especially those of the first two groups.

-- Spatial resolution is non-existent or inadequate.

Present Convective Heat Transfer Model

In view of the need for accuracy and detail in the analysis of heat transfer in insulated diesels, a new model for convective heat transfer has been developed which removes many of the deficiencies of past models and provides a tool for addressing significant engine design issues.

The starting point for the model is the instantaneous heat flux equation written in terms of the heat transfer coefficient h_g

$$q(t,A) = h_g(t,A)\,[T_g(t,A) - T_w(t,A)] \qquad (15)$$

This equation has a form similar to those used by previous investigators, but there are important differences:

1. h_g is spatially varying,
2. T_g is spatially varying during combustion, depending on the extent and location of the burned zone,
3. T_w is time dependent as well as spatially varying to allow a more detailed description of wall temperatures and the inclusion of the effects of surface temperature swings.

The convective heat transfer is assumed to be driven by fluid motions and the coefficient of the convective heat transfer is assumed to be related to the strength of the fluid motions through the Colburn analogy

$$h_g = \tfrac{1}{2}\, C_f\, \rho\, U_{eff}\, C_p\, P^{-2/3} \qquad (16)$$

for compressible flows, where U_{eff} is an effective velocity outside a boundary layer at a particular surface location, ρ is average boundary layer desity and C_f is a skin friction coefficient. Inspection of equation (16) shows that the model essentially predicts that the heat transfer coefficient is mainly driven by the product $\rho\, U_{eff}$ with a

weaker modulation by $C_f\ C_p\ P^{-2/3}$ (all less strongly varying under engine conditions than $\rho\ U_{eff}$).

In the model the effective velocity is defined as

$$U_{eff} = (U_x^2 + U_y^2 + 2k)^{1/2} \tag{1-17}$$

where U_x and U_y are the two velocity components parallel to the surface in question and just outside of the boundary layer, and k is the kinetic energy of turbulence. This means that the model has to have the means of calculating all three mean velocity components and k. Further, equation (1-16) requires the knowledge of skin friction coefficient C_f, which is proposed to be modeled by a correlation obtained in flat plate boundary layers and fully developed pipe flow, i.e.,

$$C_f = a\ (\rho U_{eff}\delta/\mu)^{-1/4} \tag{1-18}$$

where the constant a has a value of 0.046 in flat plate boundary layers and 0.067 for fully developed pipe flow. At present we use the mean of these two values.

The above equations require values of C_p, P and μ, and these can be calculated from gas properties provided one knows the gas temperature and composition. Also, we need to define the values of T_g and ρ during the combustion period. For all of this one needs to build a zonal model defining the extent and location of the burned zone, which will be discussed below following the description of the flow model.

Flow Model

The in-cylinder mean flow depends strongly on the chamber geometry. When calculated using detailed multidimensional Navier-Stokes models, the requisite information about the chamber geometry is communicated through the boundary conditions. However, the solution of Navier-Stokes equations within a cycle simulation is prohibitive in terms of the

computer resources required. An alternative approach to calculation of the mean flow is to use to the maximum degree possible available empirical information and physical intuition allowing an approximate description of the flow field. Although such a simplified approach cannot provide the detail that could be, in principle, obtained from a Navier-Stokes solution, it can in some instances provide enough information to achieve most of what is needed--and at a minute fraction of the effort.

A case at hand is a typical diesel engine geometry, which is, except for the valves, axisymmetric. A very good case can be made in this instance, that a relatively simple regional model can be constructed from which one could calculate, with a reasonable degree of confidence, the overall levels of the mean motion. Thus, in the present model, the combustion chamber is divided into three flow regions defined as the squish area above the piston crown, cup volume and the region above the cup lip. This is shown schematically in Figure (1-1) which defines the three regions, including a provision for a squish lip (reentrant bowl) geometry.

In each of the three flow regions one has to solve for:

- o radial velocity
- o axial velocity
- o swirl
- o turbulence intensity
- o turbulence length scale

Radial and Axial Velocities. The first two velocity components, axial and radial, are calculated, to the degree possible, simply from mass conservation and from piston kinematics. For the axial velocity component this means the piston motion relative to the liner, and for the radial component it is the squish and reverse squish velocity along the piston crown where the flow is one-dimensional and the approximation is appropriate. Other radial and axial velocity components such as inflow into a cup or valve flow are essentially three-dimensional, and cannot

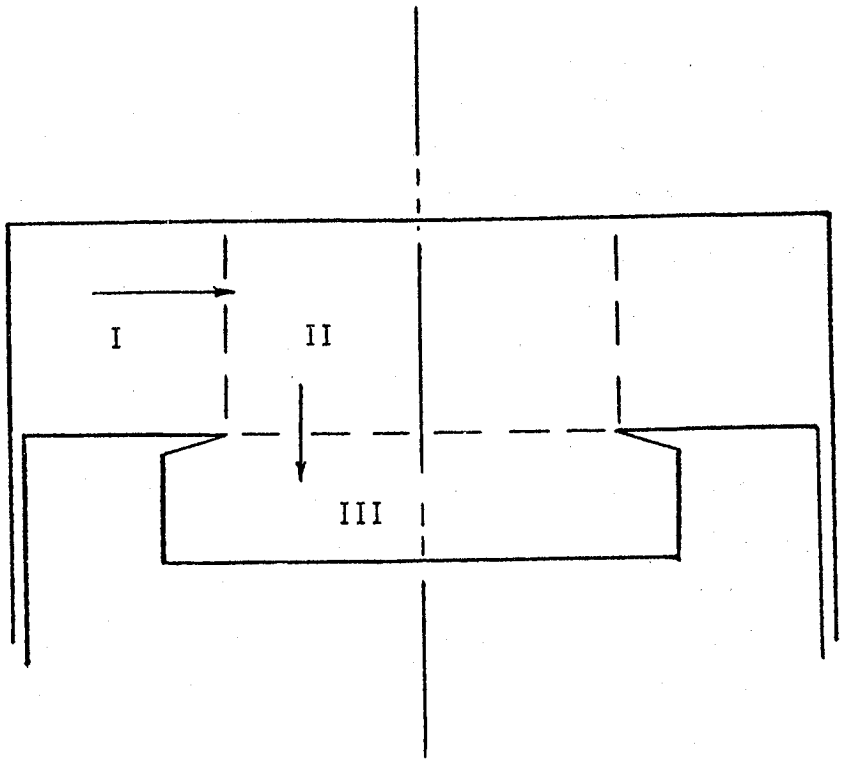

Figure 1-1. Flow regions appropriate for typical diesel engine geometries. Arrows indicate flow direction during compression stroke.

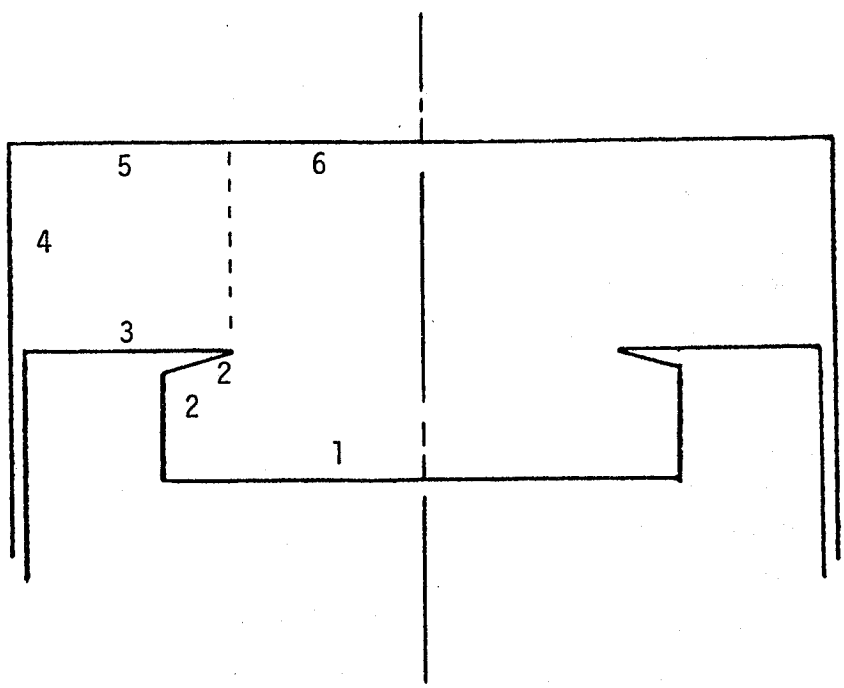

Figure 1-2. Six elementary combustion chamber surfaces.

be obtained without a detailed solution of Navier-Stokes equations. Those elements of the flow field are lumped in the present model into turbulence.

Swirl Equation. The swirl component is obtained from the solution of a differential equation for angular momentum in each of the three flow regions. The assumption is made that, in each region separately, the flow spins with a constant angular velocity (solid body rotation). The governing equation for each region is

$$(I_j\omega_j)^{\cdot} = \Sigma\dot{m}_{ij}\omega_{ij}\tilde{r}_{ij}^2 + \Sigma\rho U_{dif}(\omega_i-\omega_j)\int r^2 dA \qquad (1\text{-}19)$$

$$+ \dot{m}_{intake}\, M_{intake}^{*} - \dot{m}_{exhaust}\omega_j\tilde{r}_j^{\,2*} - \tfrac{1}{2}\rho\int C_f r^3\omega_j dA$$

where

$$\tilde{r}_j^{\,2} = I_j/m_j$$

$$M_{intake} = C_T v_{is}\, B/2$$

$$U_{dif} = k^{\frac{1}{2}}\ell_m/L$$

and where subscript j refers to the region at hand, subscript i refers to the adjoining regions, subscript ij refers to situations where the subscript is either i or j depending on the flow direction across the region boundary and v_{is} is the isentropic velocity of the valve seat. Tensorial summation rules do not apply to this notation. The terms on the right hand side represent convection from region to region, diffusion from one region to another by the action of turbulence (this term may also be viewed as inter-regional friction), intake flux of angular momentum, exhaust flux out and wall friction, respectively. It should be noted that by intake we mean inflow through either intake or exhaust

---

*Regions 1 and 2 only

valve, and a similar convention is used for the exhaust term. The intake swirl coefficient, C_T, is defined for both valves along the lines described in Uzkan, Borgnakke and Morel (1983). The diffusion velocity may be argued on physical grounds to be proportional to the turbulence velocity scale, i.e., $k^{1/2}$. It represents a bodily exchange of fluid between two adjoining regions due to turbulent motions. Since the extent of the mixing between the two regions also depends on the turbulence length scale, the effective diffusion velocity was assumed to be proportional to the ratio of the turbulent length scale to a characteristic zone dimension. This characteristic dimension is taken to be $L = 0.1B$ for diffusion between regions 1 and 2, and $L = 0.1$ (h_{cup} + clearance) for diffusion between regions 2 and 3. Also, the values of k and ℓ_m (mixing length) used in the definition of U_{dif} are evaluated in region 1 for 1-2 diffusion and in region 3 for 2-3 diffusion. This particular choice was made for swirl as well as for the turbulence equations on the basis of experimentation with the model and it was found to produce plausible rates of diffusion between the regions. The skin friction coefficient is obtained from equation (1-18).

The swirl model includes the effects of squish which forces gas from region 1 into region 2, where the swirl is amplified. The swirl is set up during the induction period after which the angular momentum is gradually dissipated by the action of viscous friction on the surrounding walls.

Turbulence Equations. Turbulence is modeled by the k-ε turbulence model. This model is usually described in terms of two partial differential equations. For the purposes of the present approach, which considers three adjoining volumes rather than a multitude of computational nodes, the equations were rewritten. Integrating the equations over each of the flow regions, one obtains a set of six coupled ordinary differential equations which have to be integrated simultaneously in time. Both k and ε are assumed to be uniform over each flow region.

The governing equations include the following terms:

- o generation of turbulence;
- o viscous decay by turbulent dissipation rate;
- o convection from zone to zone;
- o length scale limitation by action of boundary layers;

where the generation terms include effects of:

- o mean strain field including compression;
- o kinetic energy of squish motion, intake flow and injection;
- o swirl gradients at region interfaces;

and they are written in a form similar to the swirl equation

$$(m_j k_j)^{\cdot} = \Sigma \dot{m}_{ij} k_{ij} + \Sigma \rho U_{diff} (k_i - k_j) A + m_j S_k \qquad (1\text{-}20)$$

$$+ \dot{m}_{int}\, k^{*}_{int} - \dot{m}_{exh}\, k^{*}_{j} + \dot{m}_{inj} k^{**}_{inj} + \dot{m}_{sq}\, k_{sq}{}^{**}$$

$$(m_j \varepsilon_j)^{\cdot} = \Sigma \dot{m}_{ij} \varepsilon_{ij} + \Sigma \rho U_{diff} (\varepsilon_i - \varepsilon_j) A + m_j S_\varepsilon \qquad (1\text{-}21)$$

$$+ \dot{m}_{int}\, \varepsilon^{*}_{int} - \dot{m}_{exh}\, \varepsilon^{*}_{j} + \dot{m}_{inj} \varepsilon^{**}_{inj} + \dot{m}_{sq}\, \varepsilon_{sq}{}^{**} + k_j^2 / L_j^2$$

The inflow source terms have the following definitions:

$$k_{int} = \tfrac{1}{2} v_{is}^2 \qquad \varepsilon_{int} = \tfrac{1}{2} k_{int}^{3/2} / B$$

$$k_{inj} = \tfrac{1}{2} v_{inj}^2 \qquad \varepsilon_{inj} = \tfrac{1}{2} k_{inj}^{3/2} / B$$

$$k_{sq} = \tfrac{1}{2} U_{12}^2 \qquad \varepsilon_{sq} = \tfrac{1}{2} k_{sq}^{3/2} / B$$

where $v_{inj} = 2(P_{inj} - Pc)/\rho_{fuel}$, and U_{12} is the radial velocity at the boundary between regions 1 and 2. The source terms S_k and S_ε include a

---

* Regions 1 and 2 only
** Regions 2 and 3 only

number of terms representing turbulence generation by the mean strains and also its dissipation:

$$S_k = \mu_t/\rho\ (P_1+P_2)k^2/\varepsilon + P_3 k + P^k_{ang} - \varepsilon \qquad (1\text{-}22)$$

$$S_\varepsilon = \mu_t/\rho\ (C_1 P_1 + C_1' P_2)k + C_1'' P_3 \varepsilon + P^\varepsilon_{ang} - \varepsilon^2/k \qquad (1\text{-}23)$$

where

$$P_1 = 2S_{mn}S_{mn} \qquad P_2 = -\tfrac{2}{3} S^2_{nn} \qquad P_3 = -\tfrac{2}{3} S_{nn}$$

and in these last three definitions the tensorial summation rules are meant to apply. It may be noted that P_1, P_2 and P_3 taken together also describe the generation by compression. The tensor S_{mn} represents the velocity strain field in which, under the current approximations to the mean velocity components, only the diagonal terms are non-zero and, therefore,

$$P_1 = 2\int[\partial v_z/\partial z)^2 + (\partial v_r/\partial r)^2 + (v_r/r)^2]\ \mathrm{dvol/vol}$$

where v_z is the axial and v_r the radial velocity component, respectively. The values of the coefficients C_1' and C_1'' are calculated as a function of the strain field parameters as described in Morel and Mansour (1982).

The additional generation terms P_{ang} represent turbulence generation at the interfaces between two adjoining regions in the form

$$P^k_{ang} = \Sigma \int \mu_t[(\omega_i-\omega_j)r/2\ell_m]^2 \ell_m dA\ /\ m_j$$

$$P^\varepsilon_{ang} = C_1\ P^k_{ang}\ \varepsilon/k$$

where μ_t is the turbulent viscosity and ℓ_m is the mixing length defined as

$$\mu_t = C_\mu \rho k^2/\varepsilon \qquad \ell_m = C_\mu^{3/4} k^{3/2}/\varepsilon$$

The last term in the dissipation rate equation (1-21) is an ad hoc representation of the boundary layer effects on the bulk dissipation rate. This term becomes important whenever the dissipation length scale $L_\varepsilon = k^{3/2}/\varepsilon$ becomes comparable to the smallest dimension of the given zone and its effect is to increase the dissipation rate, thus limiting the growth of the mixing length. The value of L_j is set at twice the minimum geometrical dimension of the region. When one uses the full Navier-Stokes equations with a fine grid mesh, this term is not needed as its function is automatically supplied by the diffusion of the dissipation rate from the boundary layers into the interior of the flow region.

Elementary Chamber Surfaces. The three flow regions are bounded by a total of six surfaces shown in Figure (1-2). The model calculates for each of these a number of variables needed for calculation of individual heat transfer coefficients.

These include the three velocity components, which are area-averaged over each surface. Adding to these the turbulent kinetic energy, one obtains through equation (1-17) the effective velocities.

The boundary layer thickness needed in equation (1-18) cannot be easily calculated in the present context. Instead, it is proposed to relate it to the geometrical dimensions of the combustion chamber. At present the boundary layer thicknesses pertaining to the six elementary surfaces are approximated as

$$\delta_1 = 0.05\ (h_{cup} + s(d'/d_{cup})^2)$$

$$\delta_2 = 0.05\ d_{cup}$$

$$\delta_3 = \delta_5 = 0.05\ s$$

$$\delta_4 = 0.05\ B$$

$$\delta_6 = 0.05\ (s + h_{cup}(d'/d_{cup})^2)$$

where the geometrical variables are defined in Figure (1-2). This approximation is expected to be adequate as the boundary layer thickness is used only in equation (1-18), i.e., raised to a small power.

Finally, the skin friction coefficients and heat transfer coefficients are obtained by using the above variables together with transport properties and density evaluated at the "film" temperature

$$T_f = 0.5\ (T_{conv} + T_{wall})$$

from equations (1-18) and (1-16).

Two Zone Combustion Model

During the combustion period a physically intuitive, quasi-dimensional burned zone model defining the location of the burned gases is superimposed on the three flow regions. The thermodynamic cycle code supplies the mass of the burned gases and their temperature and composition at every time step. From this information one can calculate the fraction of the total volume occupied by the burned gases. Then, requiring that the burned zone is located in some particular form or location, one can calculate on a purely geometrical basis the burned zone shape and dimensions. The present formulation prescribes the burned zone to be axisymmetric and to be located centrally. Another constraint is that the distances from the burned zone to cup bottom and to the head are equal. The last geometrical constraint on the zone shape is the requirement that the distances from the burned zone to cylinder liner and to cup side wall are such that the aspect ratio of the burned zones in the clearance volume (regions 1 plus 2) and in the cup equal the aspect ratio of the whole clearance volume and whole cup, respectively. With these constraints the problem is fully defined, and

the burned zone dimensions can be calculated at every time step (Figure 1-3).

The intersections of the burned zone with the flow regions define the ratios of burned volume and mass in each region, and these are used to calculate the proper values of a number of parameters needed for calculation of the heat transfer coefficients from equations (1-15) and (1-16) and for the solution of the flow model equations. These include gas transport properties, density and temperature. The last of these, the gas temperature "seen" by the surfaces in a given flow region and responsible for the convective heat transfer is calculated as

$$T_{conv} = T_u \left(1 - (m_b/m_u)^2\right) + T_b \left(m_b/m_u\right)^2 \qquad (1\text{-}24)$$

We favor this particular form of dependence rather than the normally used mass-weighted average which gives equal weight to the burned and unburned gases. The form we use is meant to represent the actual situation where combustion chamber surfaces are preferentially in contact with gas elements from the cooler unburned zone, especially early in the combustion process when the burned zone is small and is located in the central portion of the charge.

In addition to the above uses, the zonal model also provides for representation of the following phenomena:

- o flow velocities generated by combustion (expansion in one region driving the gases into another region);
- o different gas temperatures seen by surfaces in the three regions;
- o effect of burned zone location on radiation heat transfer.

Test of Skin Friction Submodel

One of the key empirical inputs to the present model is the skin friction correlation. The model accepts the general functional relationship

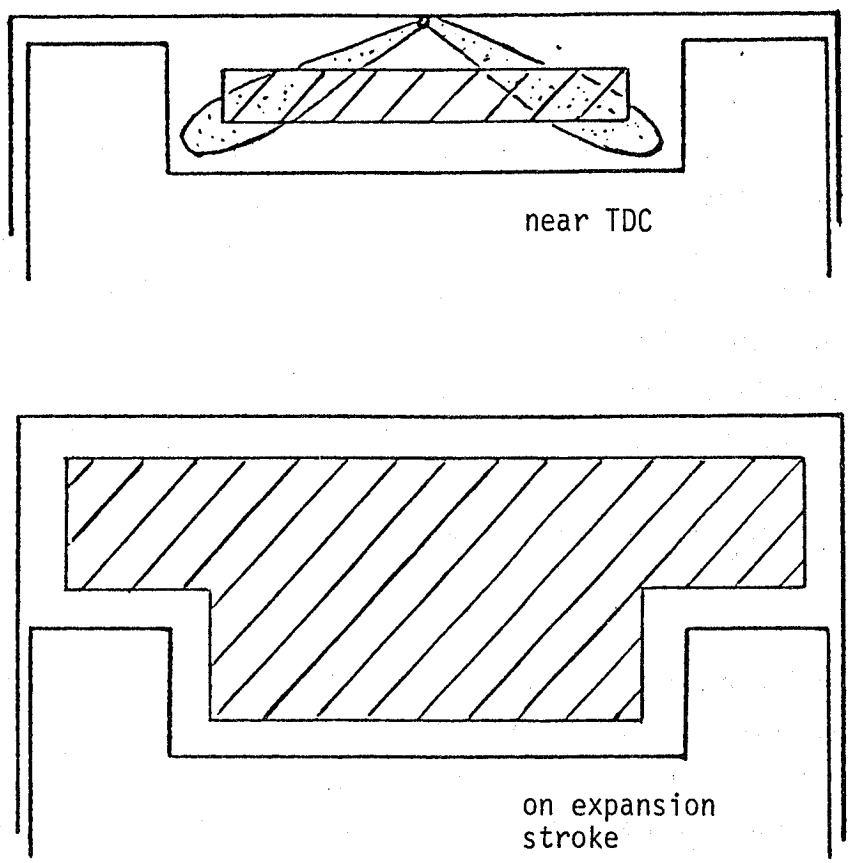

Shaded areas identify burned mixture zones

Figure 1-3: Gas zones, burned and unburned, superposed on the flow regions.

deduced experimentally for flat-plate boundary layers and pipe flows, equation (1-18). Furthermore, the current version uses even the specific correlation constants derived for those flows, taking them to be the average between the flat-plate and pipe data.

The skin friction correlation is an important part of the model. It enters into the calculation of swirl decay, and it is an important element of the heat transfer correlation itself (equation 1-16). It is thus important to verify that this correlation is applicable.

One good test case suitable for this purpose is provided by a detailed data set obtained at Sandia National Laboratories by P. Witze, described in a paper by Johnston, et. al. (1979). This data was obtained in a specially designed research engine with pancake combustion chamber geometry and compression ratio of 5.4. The engine was motored at 460 RPM, and a laser-Doppler system was used to measure the tangential velocity profiles as a function of crank angle (Figure 1-4). Due to the tangential intake valve used, the swirl levels produced were extremely high, with swirl ratio of 18.25 at 160° BTDC (equivalent to 200° in Figure 1-4). Due to the high initial swirl value, the percentage swirl decay over a 220° crank angle range over which the data extend is very high, making it ideally suitable for model testing. The swirl profile set up by the intake valve was not linear (i.e., solid body) but had a maximum at around $r/R = 0.7$. The profile shape was almost independent of crank angle, i.e., the rate of swirl decrease was roughly the same at all radial positions. To represent the profile in our model, which assumes solid-body rotation (linear from centerline to the wall), we chose a linear profile which had the maximum value (at the wall) close to the maximum tangential velocity of the experimental profile (at $r/R = 0.7$). This provided about equal initial angular momentum for the calculation and for the experiment.

During the 220° period over which the measurements were taken, the piston went through 140° of the compression stroke, passed through TDC and then went through 60° of the expansion stroke. This movement varied

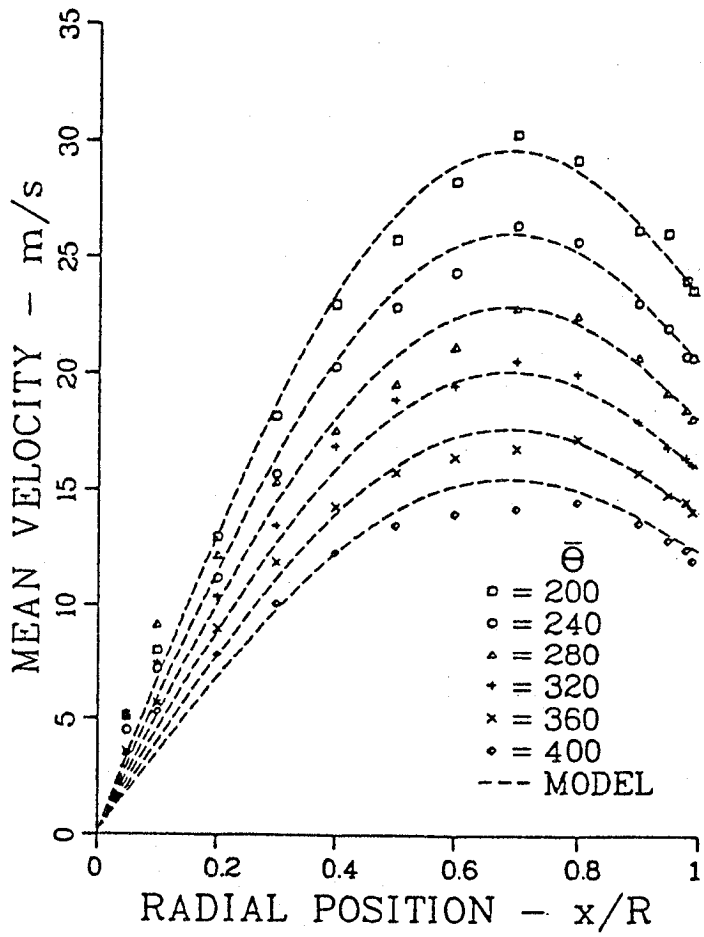

Figure 1-4: Swirl profiles vs. crank angle in a high swirl engine (From SAE Paper 790092)

the aspect ratio of the combustion chamber, changing the proportion of liner contact area to head and piston areas, as well as the overall surface to volume ratio; all of these changes have an effect of the rate of swirl decay. The decay itself is very substantial, reducing by more than half the swirl magnitude. The results of the calculations are shown in Figure (1-5), superposed on experimental data for the point of maximum swirl (at r/R = 0.7). Although these two are not exactly comparable as the model can approximate the actual profiles only imperfectly, the excellent agreement of the two curves is very encouraging. The predicted trends are certainly right, providing an indication that the skin friction formula based on boundary layer data is applicable in the engine context.

The fact that very good agreement was obtained for skin friction, using unmodified empirical data from the literature, has an important positive implication for the heat transfer calculations. Since the skin friction coefficient plays a key role in the heat transfer coefficient, increased confidence in the procedures used to calculate the friction coefficient is therefore very valuable. Furthermore, for engines employing swirl, the dominant component of the effective velocity during most of the cycle is the swirl velocity. The magnitude of the swirl velocity is influenced by the rate at which swirl is dissipated once the intake valve closes, and so it is highly significant that the model correctly represents the swirl decay.

Convective Heat Transfer Model Predictions

The model produces a wide range of information about a number of parameters, all resolved as a function of crank angle. These are illustrated here in terms of eight standard plots:

1. Convective velocities at boundaries between the flow regions defined in Figure (1-1);
2. Swirl ratios for the three individual flow regions (assuming solid body rotation in each) defined as swirl angular velocity/engine angular velocity;

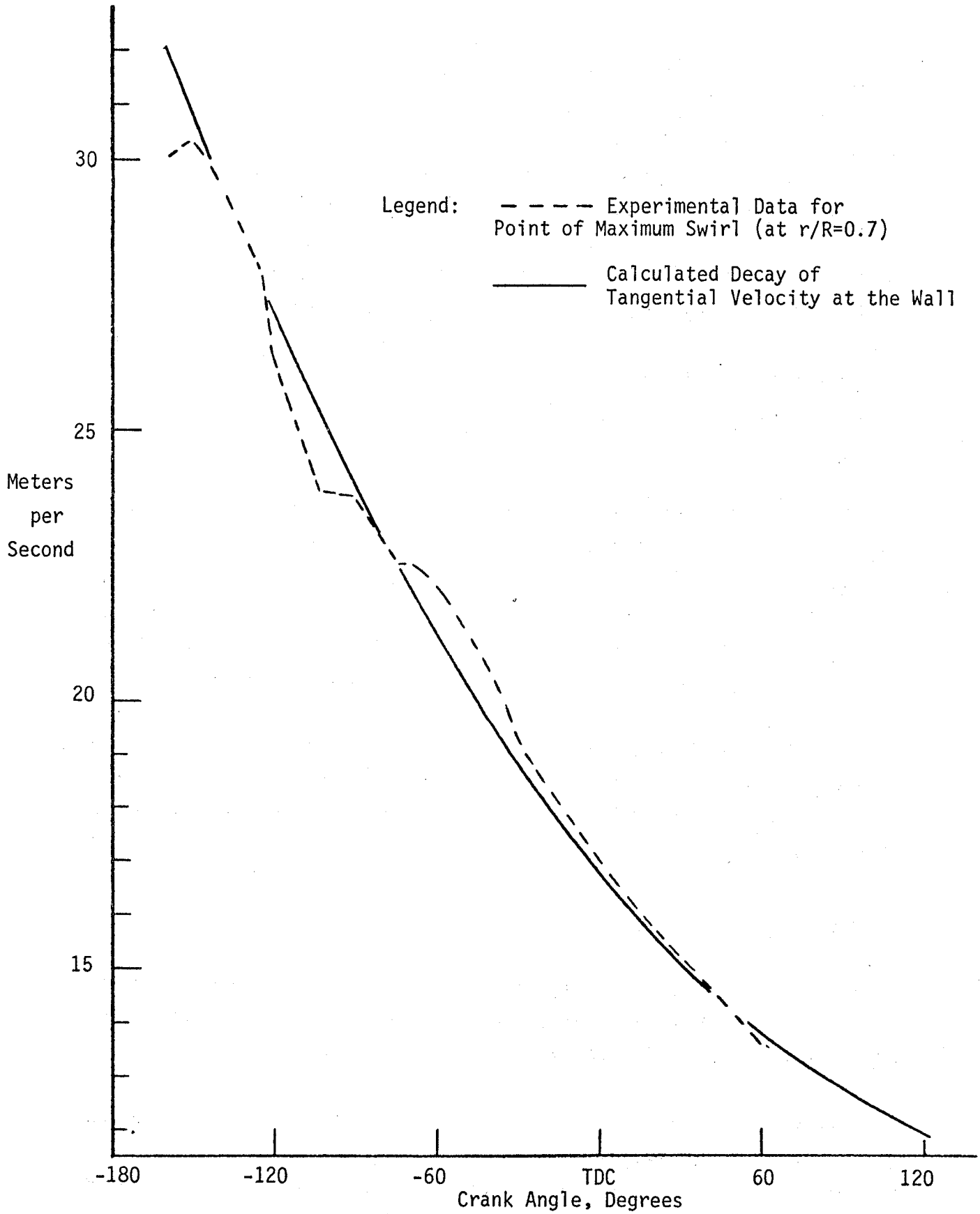

Figure 1-5. Comparison of calculated and experimental swirl decay. (Data from SAE Paper 790022).

3. Turbulence intensities for three flow regions defined as $\sqrt{k}/V_p$;
4. Turbulence length scales for three flow regions defined as mixing length/bore;
5. Effective velocities for three different elementary combustion chamber surfaces, where we have chosen to present the piston cup bottom surface, top piston land surface and the liner surface;
6. Skin friction coefficients on the same surfaces;
7. Heat transfer coefficient area-averaged over all six elementary combustion chamber surfaces;
8. Local heat transfer coefficients on the same three surfaces as items 5 and 6, presented in relation to the area averaged coefficient. In effect, this plot shows the departures from the mean, i.e., the degree of spatial non-uniformity.

In the following set of graphs, Figures (1-6) - (1-13), results are presented for one particular engine configuration and operating condition; this test case will be referred to in the text as the baseline test case. The engine modeled is a turbocharged DI diesel with displacement of 2ℓ/cylinder, operating at 1800 RPM at 220 psi IMEP. The combustion chamber has a compression ratio of 14.8 and it includes a piston cup with cup diameter/bore ratio of 0.67, containing 88 percent of the chamber volume at TDC. This piston cup will be referred to later in the text as cup 1.

The first figure in this set refers to the radial and axial velocities. The radial velocities are assumed to peak at the boundary between regions 1 and 2, decaying from there towards the liner and towards the centerline, where they take on zero values. The axial velocity is a linear function of the piston velocity, increasing from zero at the head to the piston velocity at the piston face, augmented by a component due to inflow into the cup. This latter component is assumed to peak at the boundary between regions 2 and 3, decaying to zero at the head and at the piston. The two inter-regional velocities used to scale the radial and axial velocities are shown in Figure (1-6), where the positive directions of both velocities are taken to be as indicated by the sketch

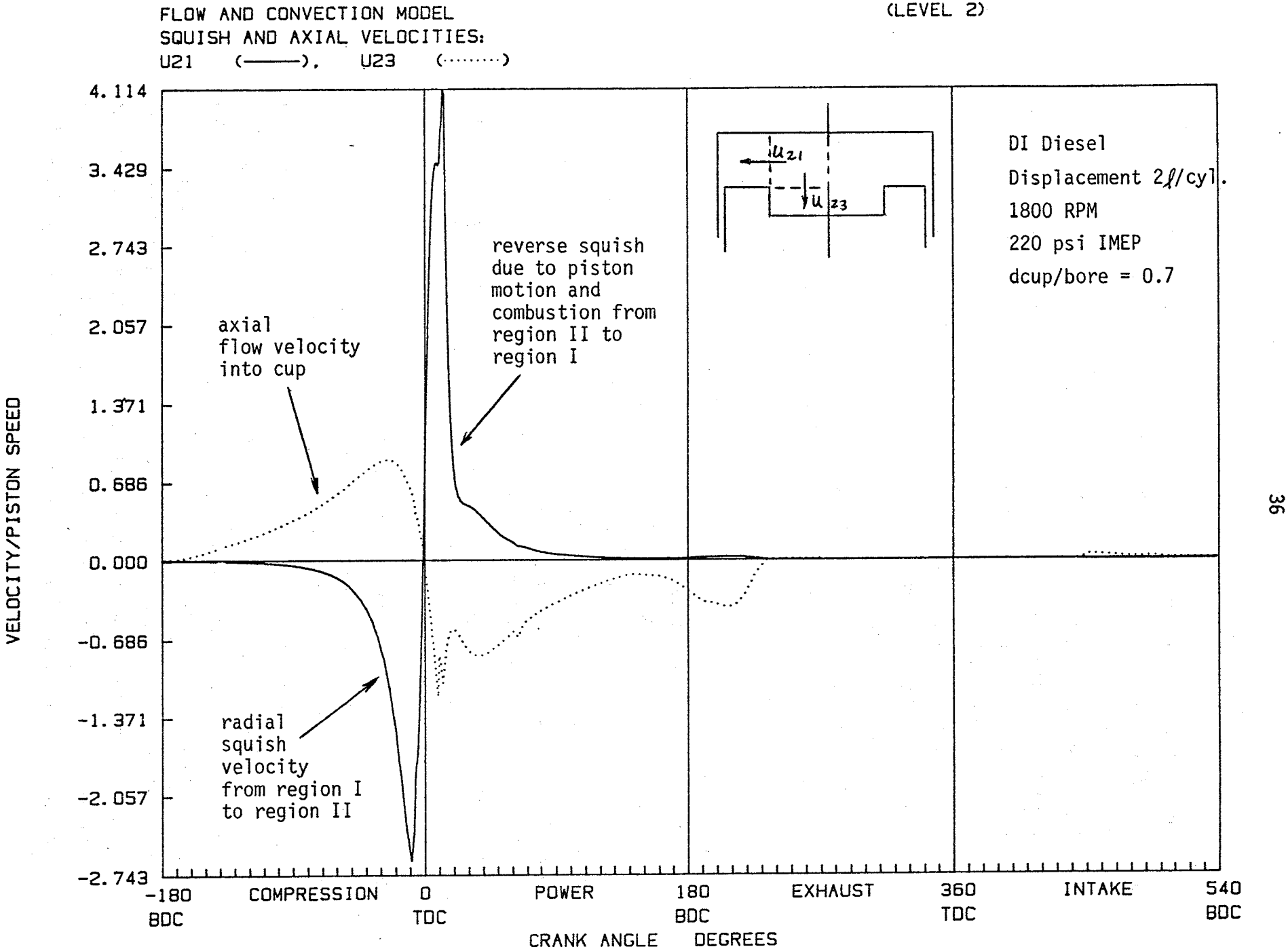

Figure 1-6. Inter-regional velocities predicted by the flow model for the baseline case

Figure (1-6) points out some of the physical phenomena behind the features seen in the curves, including squish during compression, and reverse squish and combustion generated flow on the power stroke.

The swirl development in Figure (1-7) shows levels characteristic of a medium-swirl combustion system. Prominent in the figure are the effects of intake, which generates the swirl, and swirl amplification during compression which is due to reduced moment of inertia of the fluid forced from the outer region into the cup. The present model allows the decoupling of the swirl levels in the three regions. As a result, the fluid that remains near TDC above the piston crown is seen to lose angular momentum rapidly due to wall friction, while the other two flow regions go through a period of very high swirl levels. The total angular momentum for all three regions is of course less than at the preceding BDC due to skin friction effects. Interestingly, the region directly above the cup always shows a higher swirl peak than the cup itself, and this may be shown to be consistent with the angular momentum flux and wall friction terms in the governing equations. During the intake period, regions 1 and 2, which receive the intake flow directly, spin up rapidly, with the cup lagging behind. Under the influence of interregional transfer of momentum, all three regions tend rapidly towards the same swirl level as piston descends to BDC.

The turbulence intensity has a prominent peak near TDC of the compression stroke due to the kinetic energy of injection and of the squish motion leaving the region 1 (Figure 1-8). In the squish zone (region 1) the turbulence is first reduced by increased viscous dissipation (small clearance) and then increased during reversed squish. Turbulence generation due to compression is responsible for the knee visible in the curves during the compression stroke. Without this generation mechanism, the turbulence would have continued its rapid decay seen in the during the intake period and beginning of compression. During the rest of the cycle the turbulent kinetic energy is about equal in all three regions. An exception is the intake period when the cup contents, somewhat isolated from the intake flow, have a lower turbulence level.

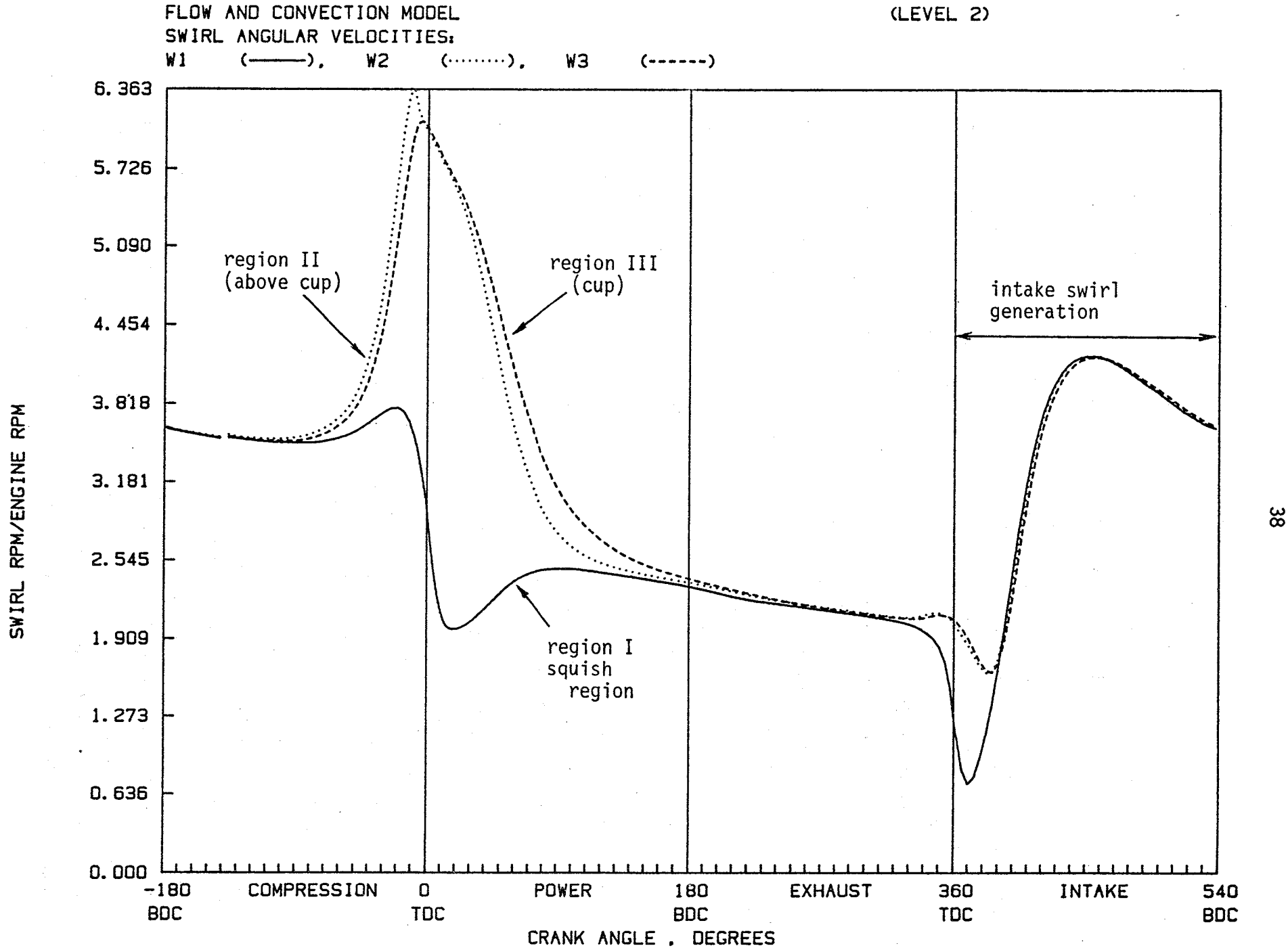

Figure 1-7. Swirl angular velocities in the three flow regions

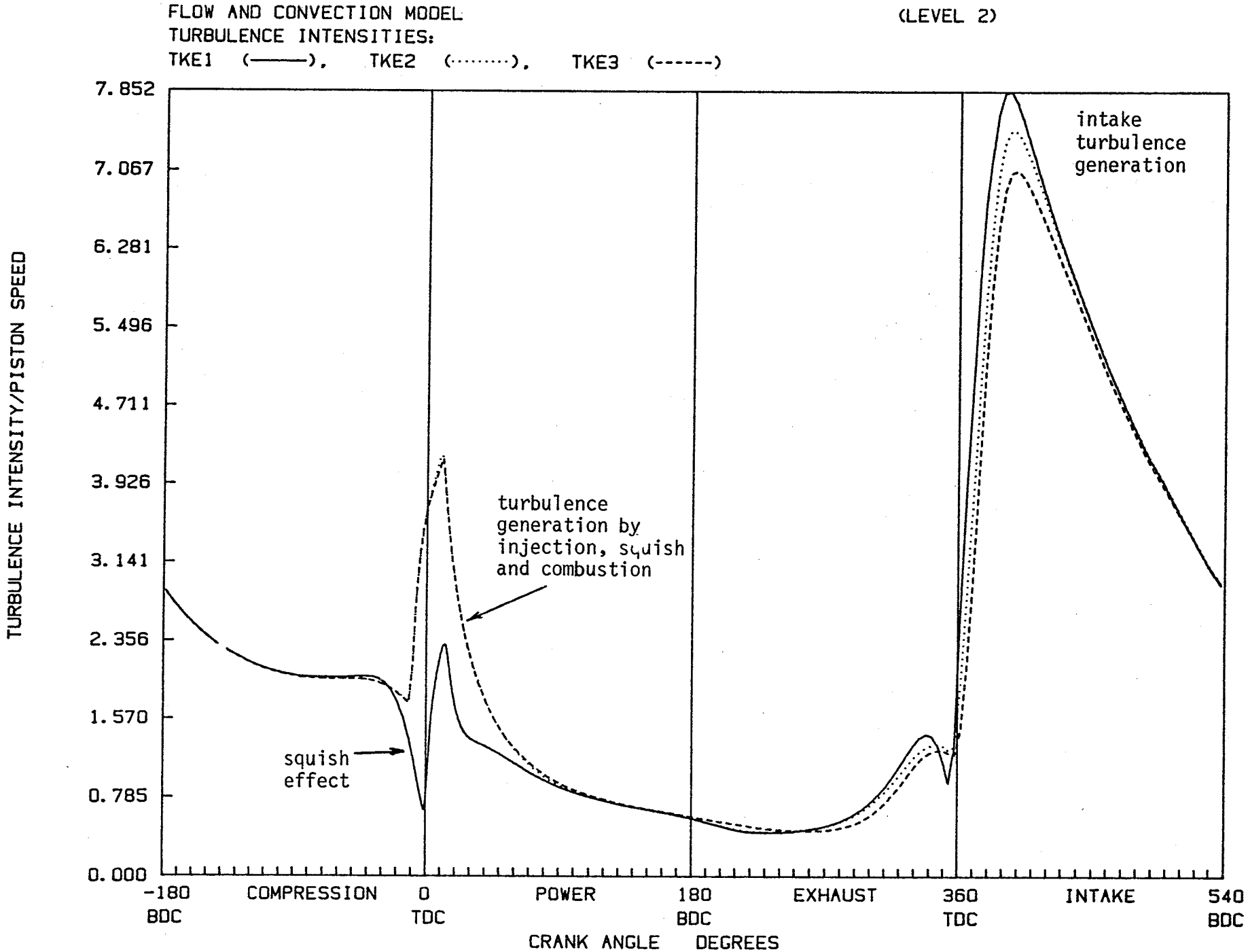

Figure 1-8. Turbulence intensity in the three flow regions

Turbulence length scale, shown as the ratio of mixing length to cylinder bore, follows to a large degree the instantaneous distance between the piston and the head, although some differences are seen during the exhaust stroke (Figure 1-9). The differences between the regions are small in this example with a fairly shallow cup, except near TDC when the length scale in region 1 becomes very small.

The effective convective velocities are calculated as the area-averaged values of mean velocity and turbulence from equation (1-17). These are shown in Figure (1-10) for three of the six elementary surfaces, i.e., bottom of the cup, piston crown and liner. The effective velocities on these surfaces are seen to vary over the range from 2 to 9.5 times the mean piston velocity. This large variation shows one of the main reasons why previous heat transfer correlations which use mean piston speed as the characteristic flow velocity, are inadequate in dealing with issues requiring the knowledge of spatially and temporally resolved heat transfer rates. The skin friction coefficient also varies from surface to surface, as well as a function of crank angle as shown in Figure (1-11). The observed variation is caused by changes in the Reynolds number, i.e., by changes in flow velocity, boundary layer thickness and density.

Based on equation (1-16) and the values of C_f, U_{eff}, etc., heat transfer coefficients can be calculated for all combustion chamber surfaces. They are summarized by a single curve in Figure (1-12) as the area-averaged value. Only in this form the present formulation can be compared to the Annand correlation prediction for the same test case, where the constant of the Annand's correlation was adjusted so that the overall cycle-integrated engine heat transfer would be the same as that predicted by the present model. The value used for the multiplicative constant was a = 0.435. The differences between the two models are substantial, as would be expected since the curve due to Annand varies essentially as a function of gas density, with some smaller dependence on temperature. The present curve adds to that the dependence on the fluid motions. The heat transfer coefficient obtained from the flow model is substantially

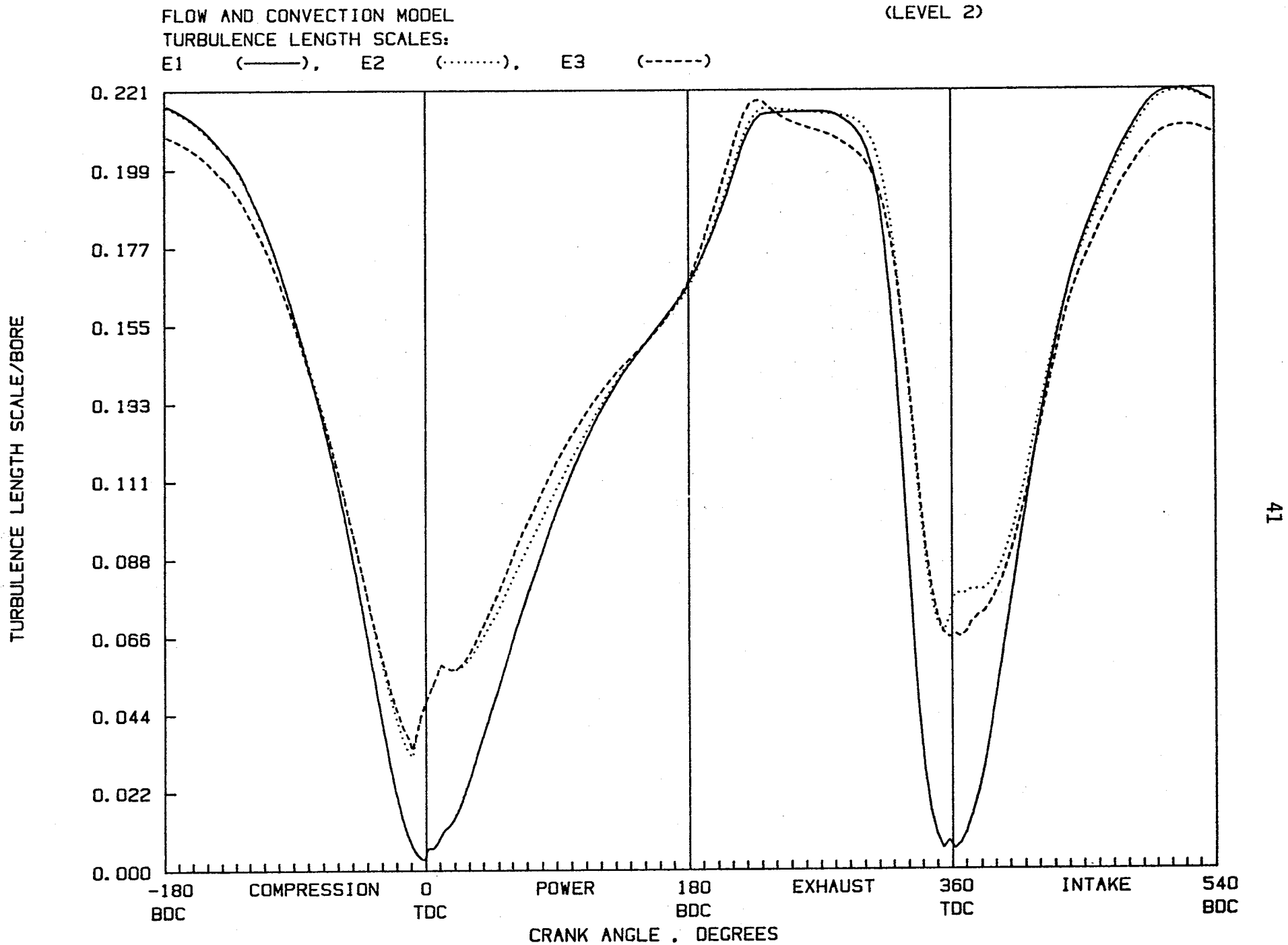

Figure 1-9. Turbulence length scale in the three flow regions

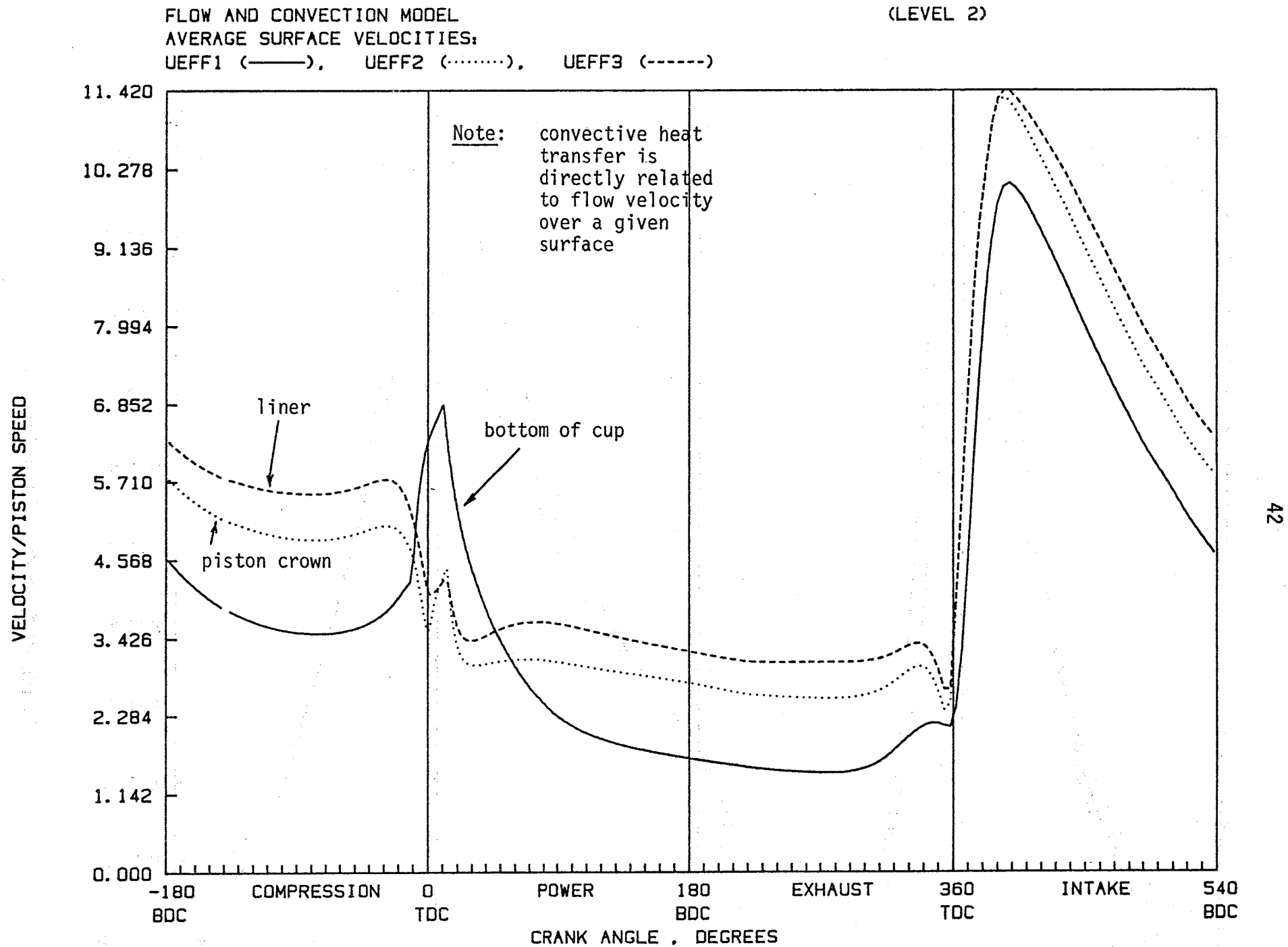

Figure 1-10. Area-averaged convective velocities adjacent to three combustion chamber surfaces

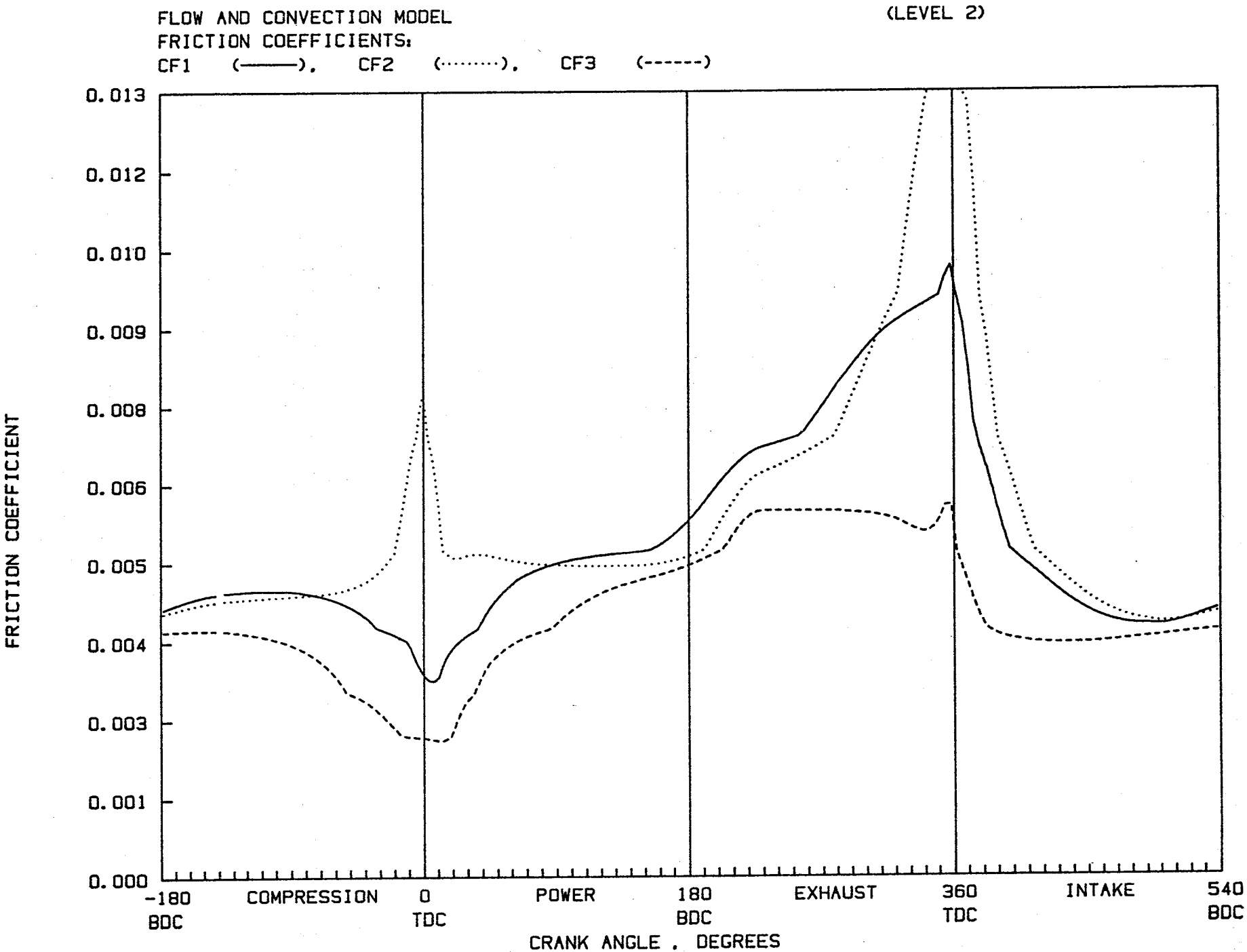

Figure 1-11. Area-averaged skin friction coefficients on three combustion chamber surfaces

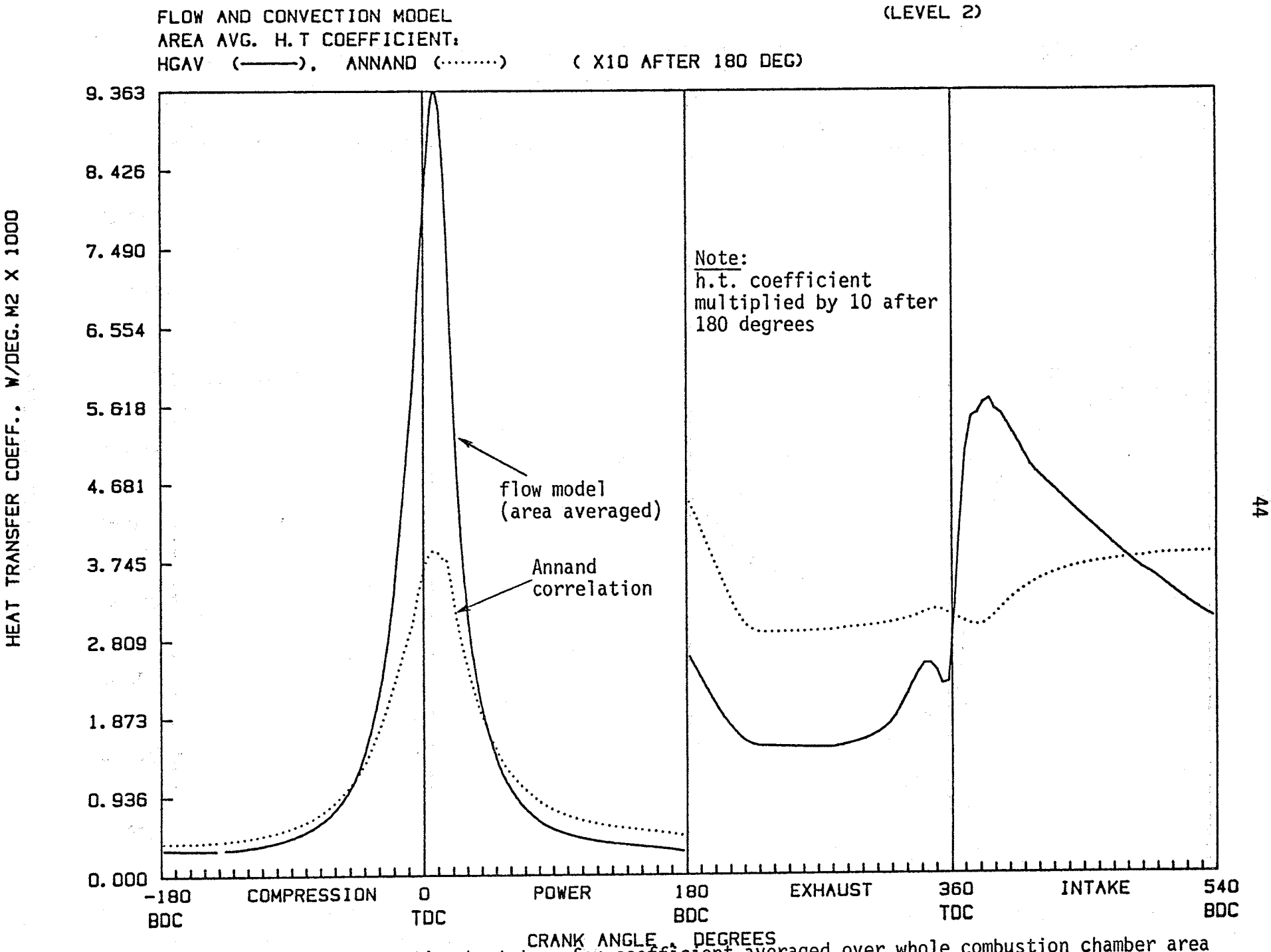

Figure 1-12. Convective heat transfer coefficient averaged over whole combustion chamber area

more peaked at TDC, its maximum value being 2.4 times larger; this difference is offset by lower values away from TDC, as it has to since the two heat transfer rates integrate to the same values. Other important differences occur in the gas exchange period. During the exhaust stroke, when the gas temperature is relatively high, the flow model predicts lower values of h, while during the intake period when the gases are relatively cool, the rapid fluid motions produced by the incoming flow generate substantially higher heat transfer coefficients. This difference is quite important in the context of insulated engines, where heat transfer during the intake period has an important negative effect on volumetric efficiency, requiring increased turbocharger boost to maintain high engine power density.

The comparison of area averaged coefficients reveals only the differences in the temporal sense, but there are other differences. While the Annand curve is the same for all combustion chamber surfaces, the present model gives six different values that often differ very substantially, revealing the spatial non-uniformity of the convective heat transfer. This is illustrated in Figure (1-13), showing the departures from the average values for the three particular surfaces. The variations in time and space are seen to be substantial, differing up to 57 percent from the mean, and even a larger percentage from one to another.

Effects of Piston Geometry on Flow and Heat Transfer Coefficients. One of the attributes of the model is that it is sensitive to details of geometry. To test this capability, the model was exercised by simulating a wide range of engine geometrical configurations and operating conditions. From these, the following four configurations were selected for presentation in this report:

1. Pancake combustion chamber,
2. Cup 1 -- d_{cup}/bore = 0.67, h_{cup}/d_{cup} = 0.25, (already discussed in the previous section),

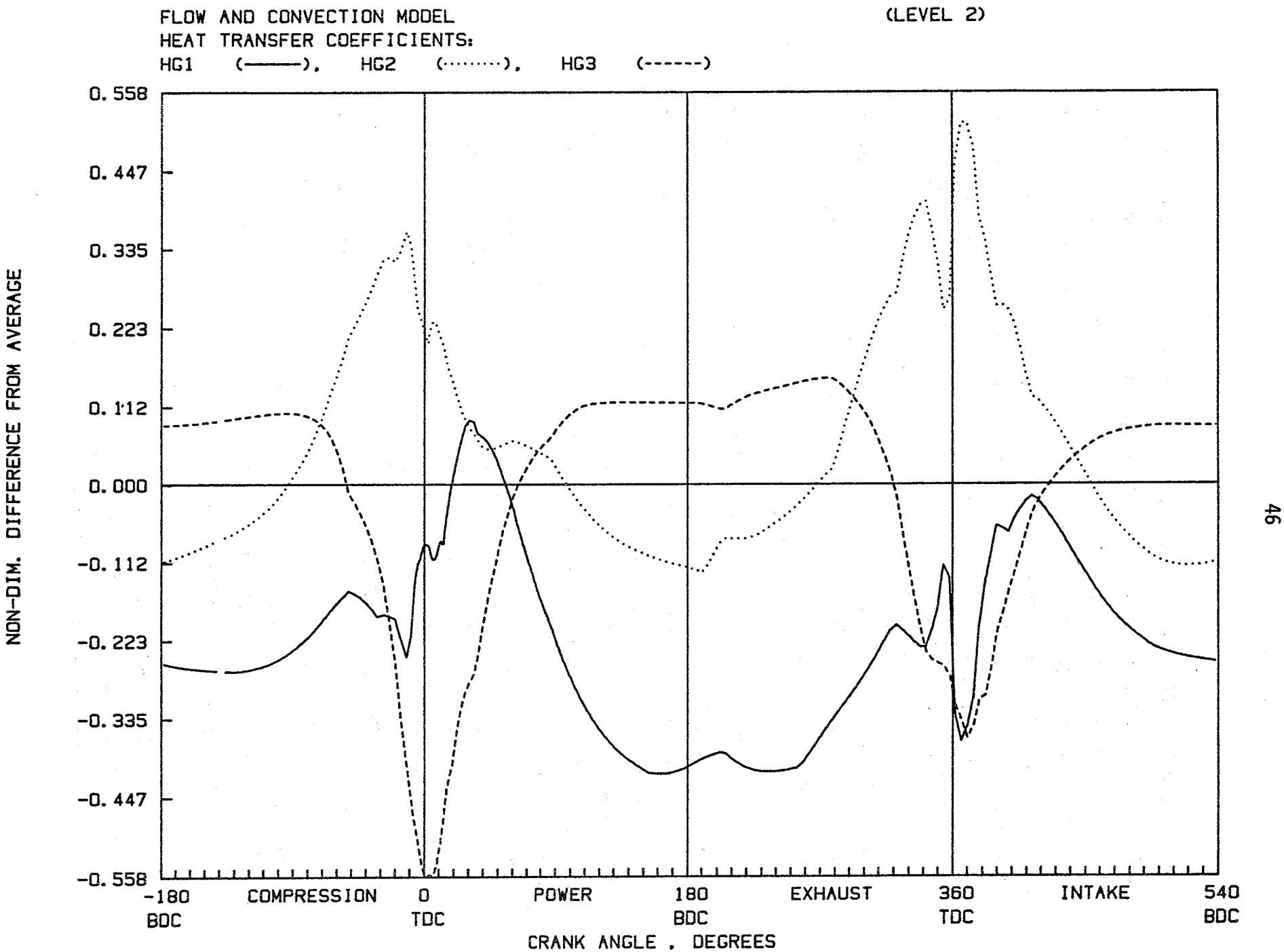

Figure 1-13. Variation of heat transfer coefficients on three surfaces (departure from mean).

3. Cup 2 -- d_{cup}/bore = 0.46, h_{cup}/d_{cup} = 0.76,
4. Cup 3 -- d_{cup}/bore = 0.67, h_{cup}/d_{cup} = 0.25
   with a lip, d_{lip}/bore = 0.46,

All of the cases were run with the same simulated heavy duty diesel engine already referred to in the previous section. All of the cases had about the same swirl level at BDC, swirl ratio S=3.6, where S is defined as the ratio of air angular velocity to engine angular velocity. Taking cup 1 as the reference, one can discuss the effects of geometry as predicted by the model.

Starting with the axial and radial velocities, one observes that these are small for the pancake geometry, consisting only of the relatively small piston motion, and of the radial velocity produced by expansion of the burning zone (Figure 1-14). In the other two cases with cup in the piston, the features of the radial and axial flow were similar to cup 1, Figure (1-6), except that the magnitudes are about twice as large due to the larger squish.

Swirl evolution in the pancake geometry (Figure 1-15) is relatively uneventful (note that for pancake geometry regions 2 and 3 collapse and that only a simple curve, broken line, refers to both). One of the main features of interest is the rapid decrease of swirl near TDC, which is due to large surface to volume ratio and associated friction, and due to the expansion of the central burning zone which moves the mass outward and thus increases the air moment of inertia. The subsequent speed up of the inner zone is due to reverse expansion in the latter stages of combustion. The smaller cup 2 enhances peak swirl over cup 1 (Figure 1-16), as would be expected. The re-entrant geometry produces a more complex swirl development (Figure 1-17). The swirl in the cup has about the same magnitude as for cup 1 which has the same diameter. The swirl above the lip has a pronounced double-peaked shape. Another effect of the lip is that the swirl levels in the three regions are more decoupled due to the restricted communication.

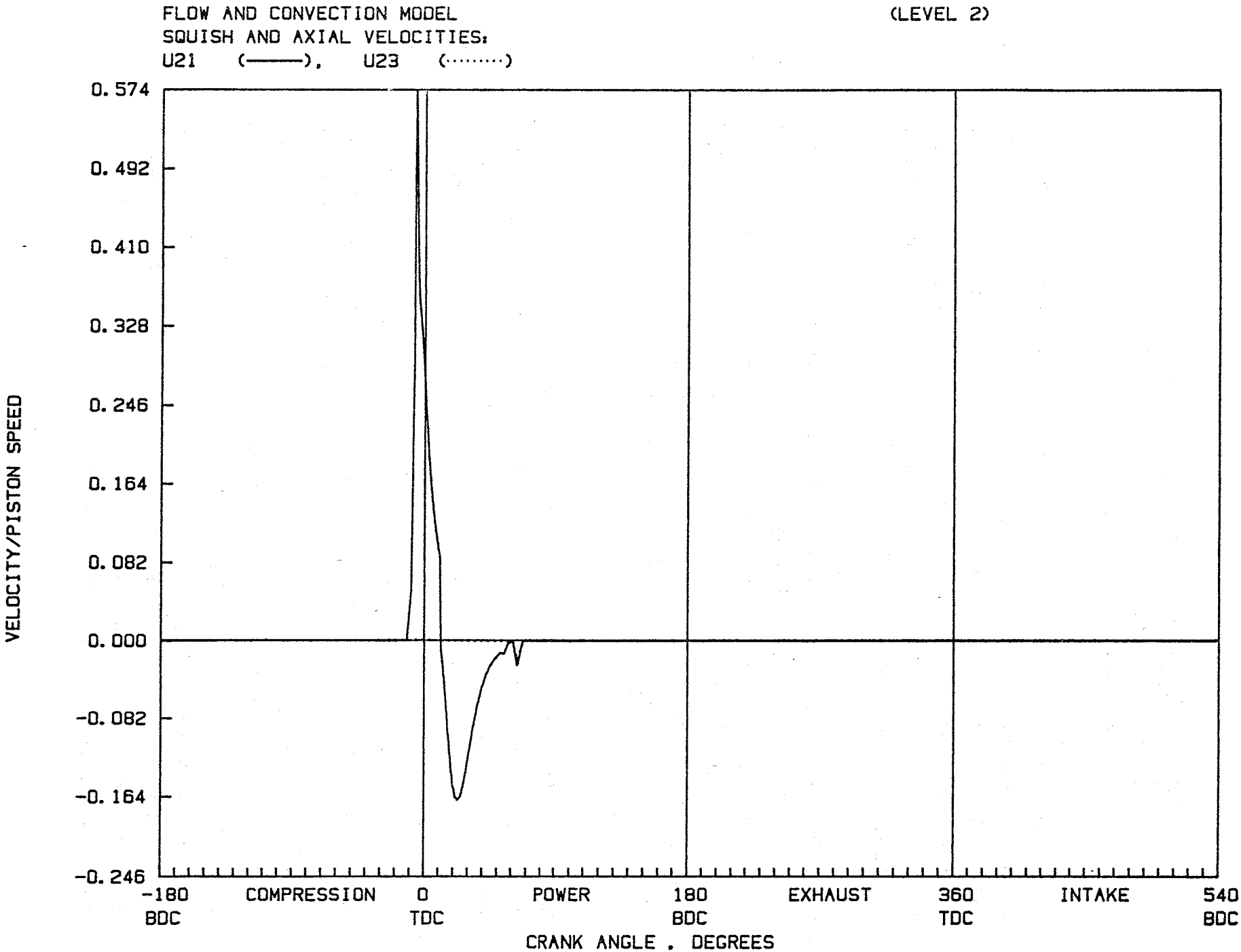

Figure 1-14. Inter-regional velocities for pancake geometry, high swirl case.

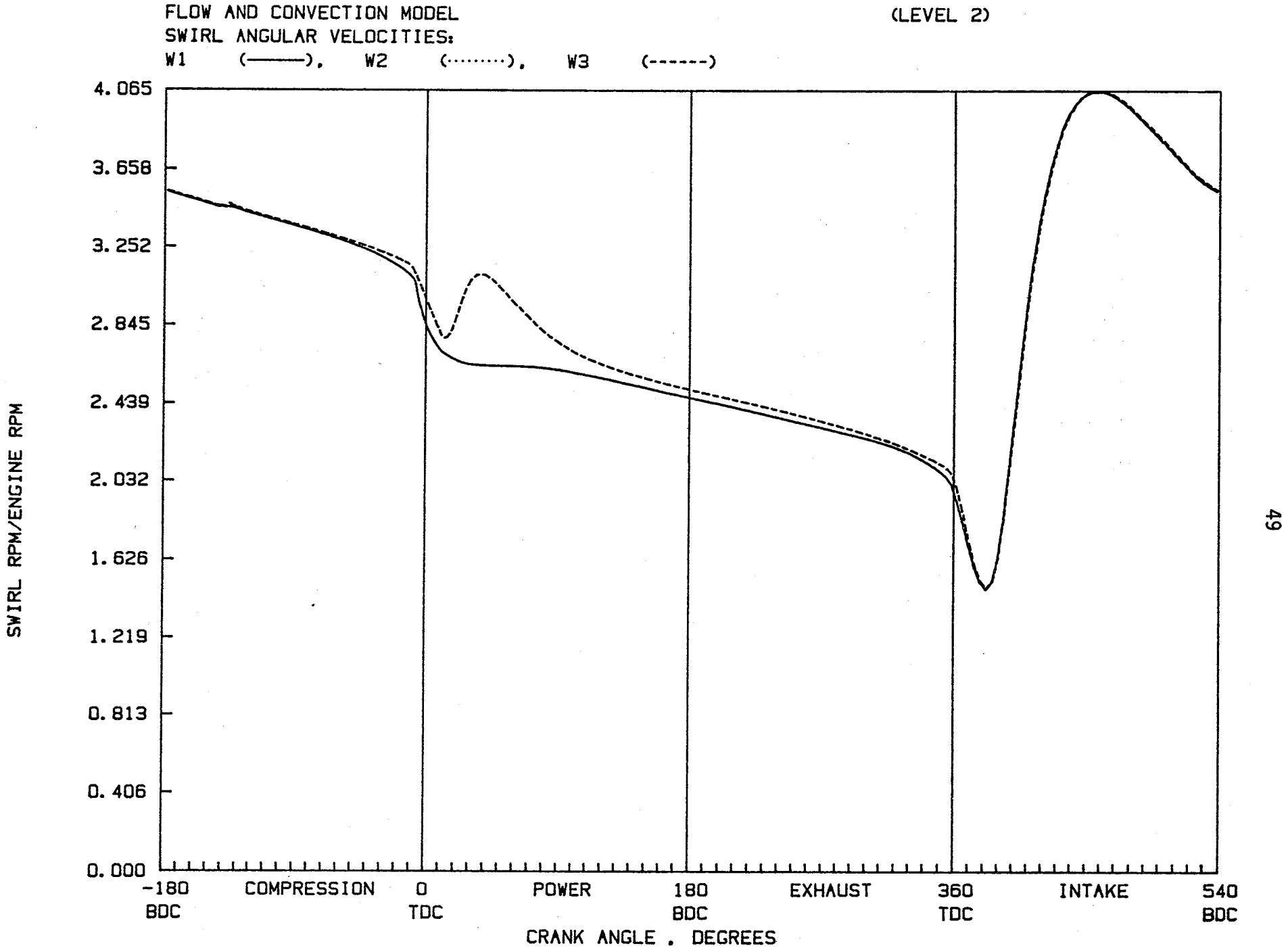

Figure 1-15. Swirl variation for pancake geometry, high swirl case.

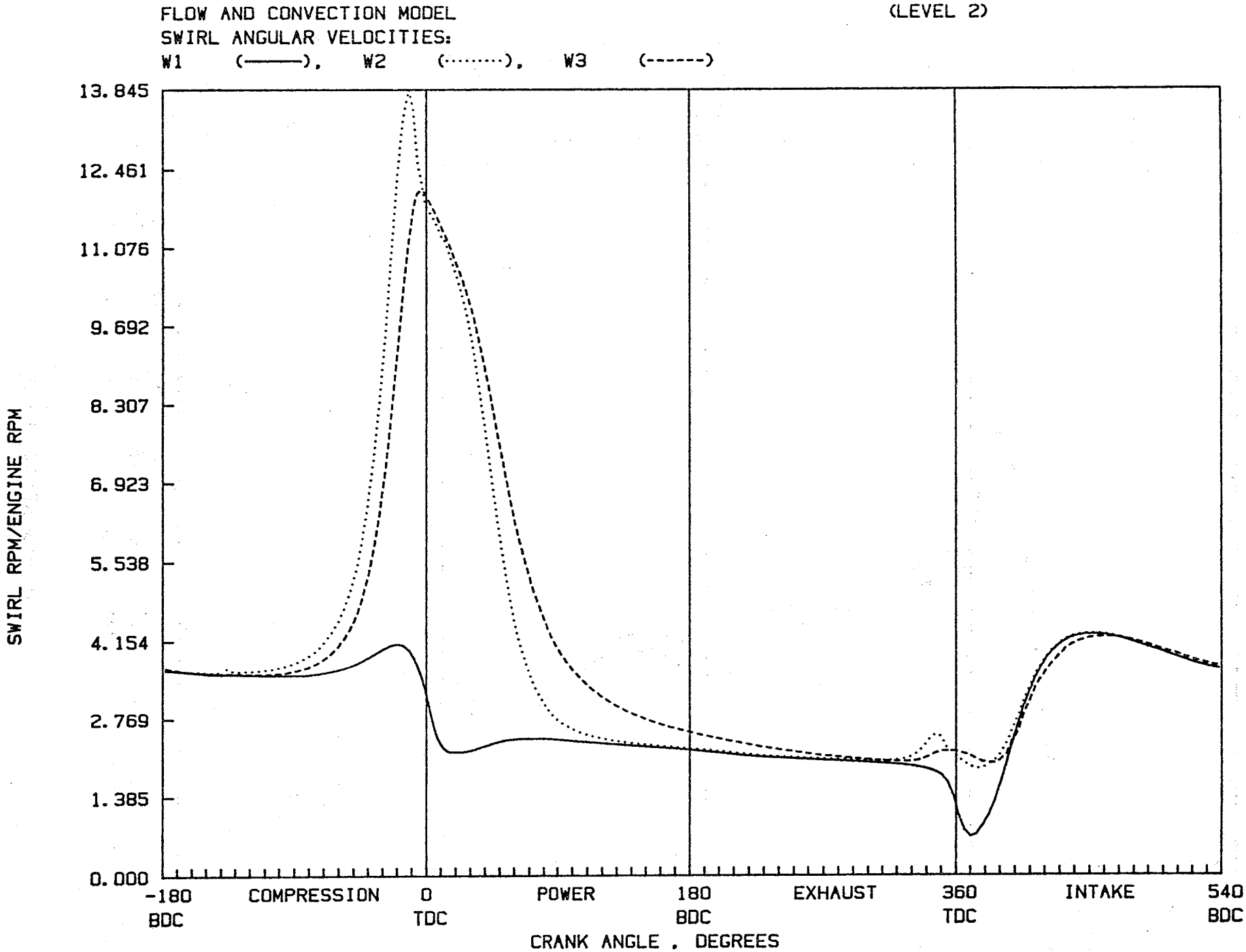

Figure 1-16. Swirl variation for Cup 2, high swirl case.

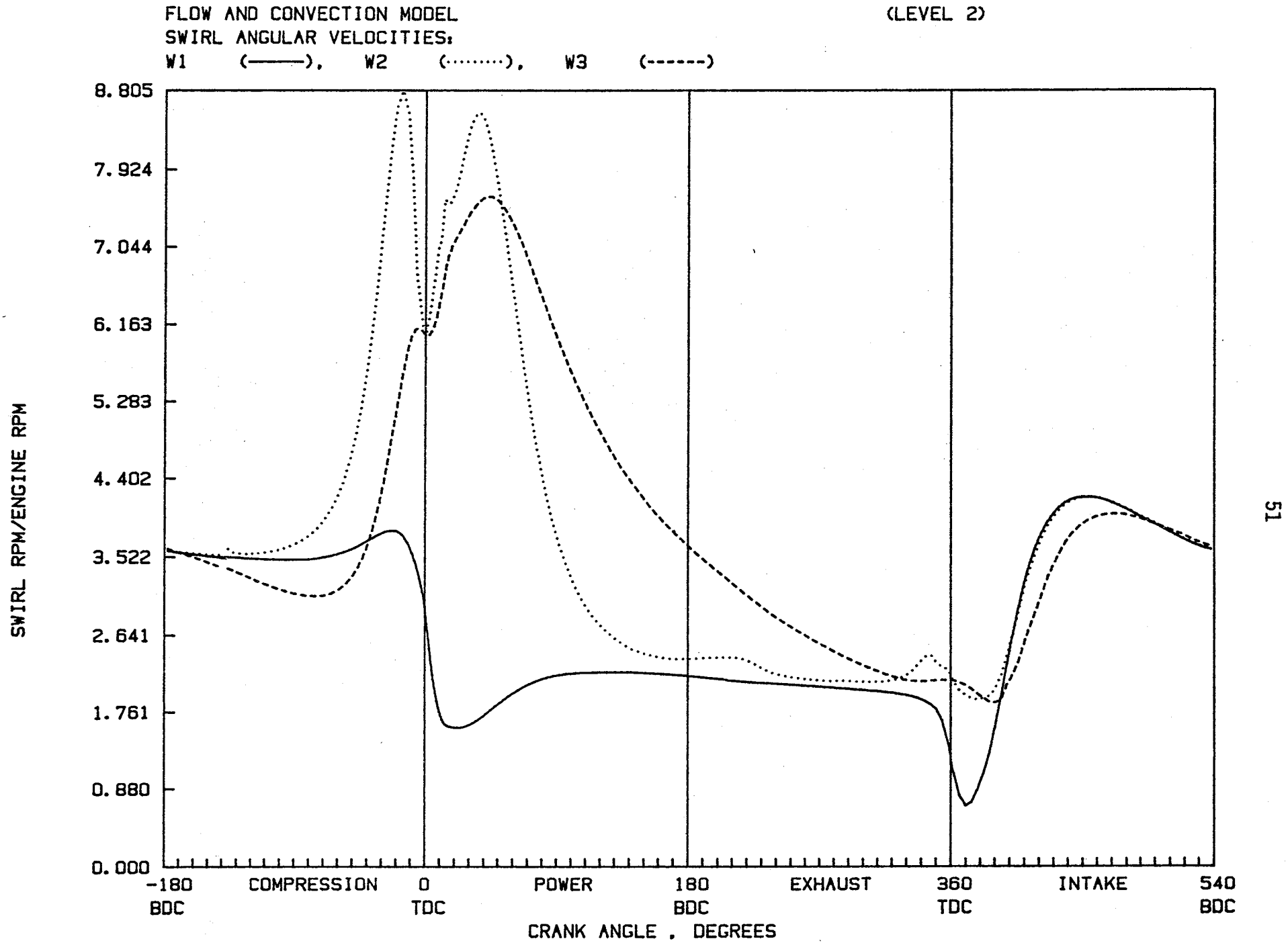

Figure 1-17. Swirl variation, Cup 3, high swirl case.

Turbulence intensity shows similar features for all geometries, the main differences being an increase in intensity near TDC with increasing squish (Figure 1-18). Another trend is that going from the pancake geometry to cup 3 there is a progressive growth of differences between intensities in the three regions during the intake stroke, the highest intensity being above the piston crown and the lowest in the cup. The profiles of turbulence length scale are similar for all cases. The differences between the scales in the different regions increase with decreasing cup diameter. For the pancake geometry they are almost identical, except at TDC of compression stroke, while there are substantial differences for the small cup (Figure 1-19).

The resulting heat transfer coefficients depend strongly on the level of fluid motions, with a peak area-averaged value of 7830 $W/m^2{}^oCA$ for the pancake geometry (Figure 1-20), to 11541 $W/m^2{}^oCA$ for cup 2 (Figure 1-21). They are compared with Annand's global correlation whose constant was fixed at the value 0.435 that gave the same overall (spatially and temporally integrated) heat flux from the combustion chamber as cup 1; the global curve is identical for all piston geometries, as it cannot account for variation in in-cylinder velocities.

In summary, the presented results show the predictions of the in-cylinder flow velocities produced with various geometries and different intake swirl levels. They show the variation in effective flow velocities as a function of crank angle and from surface to surface. The determination of this variation is the key contribution of this convective heat transfer model, as it is the effective velocity which determines the heat transfer coefficient. It permits us to step beyond the existing state of the art models (Annand, Woschni, etc.) which do not take into account the flow velocities and which predict spatially uniform heat transfer coefficients. In practice, these models have to be calibrated for each engine design to give an approximately correct level of spatially and cycle-averaged heat transfer for a given engine that arises due to its particular geometry, and flow characteristics. Due to its expanded physical basis, it is expected that the present model will

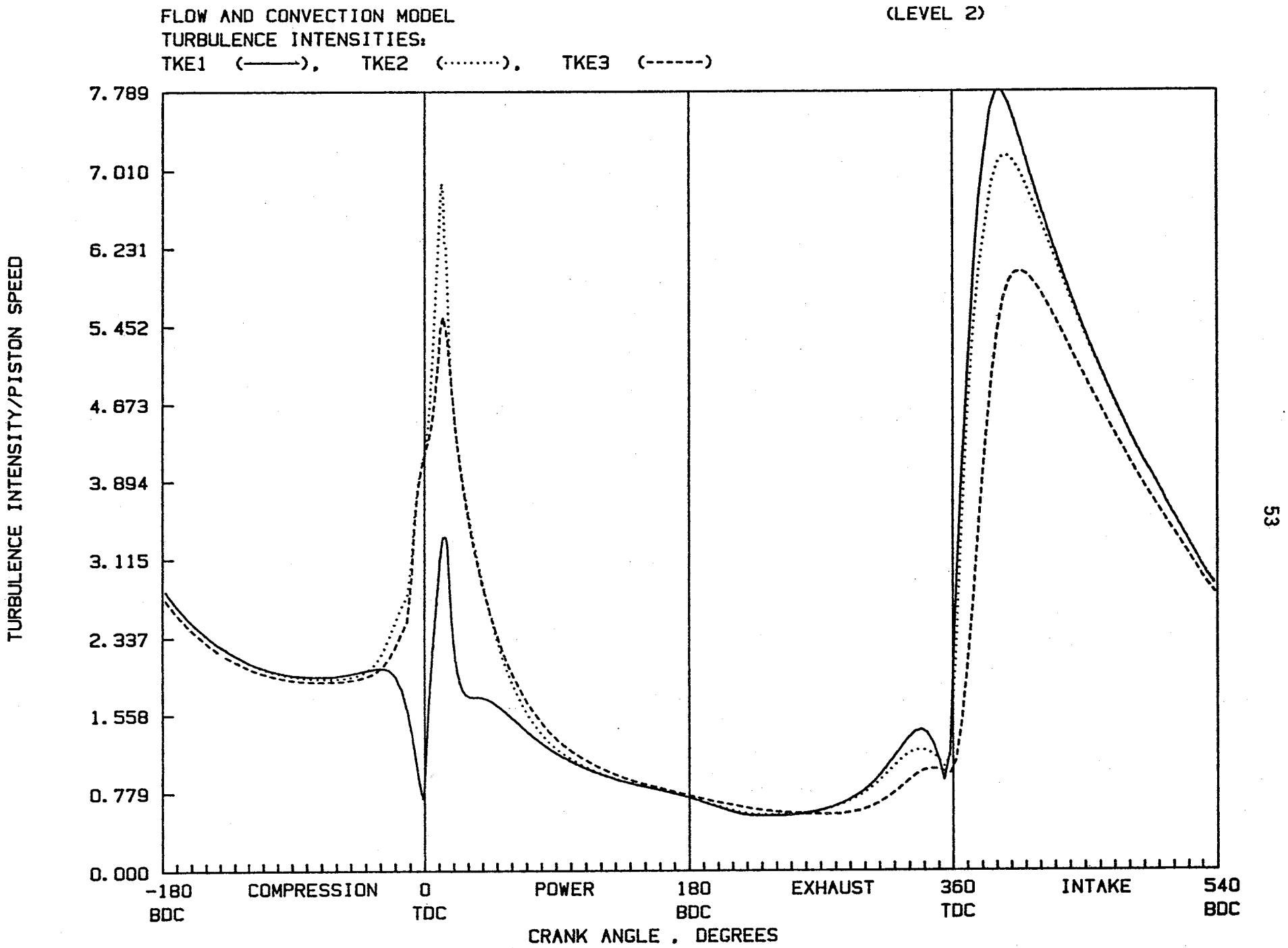

Figure 1-18. Turbulence intensity, Cup 2, high swirl case.

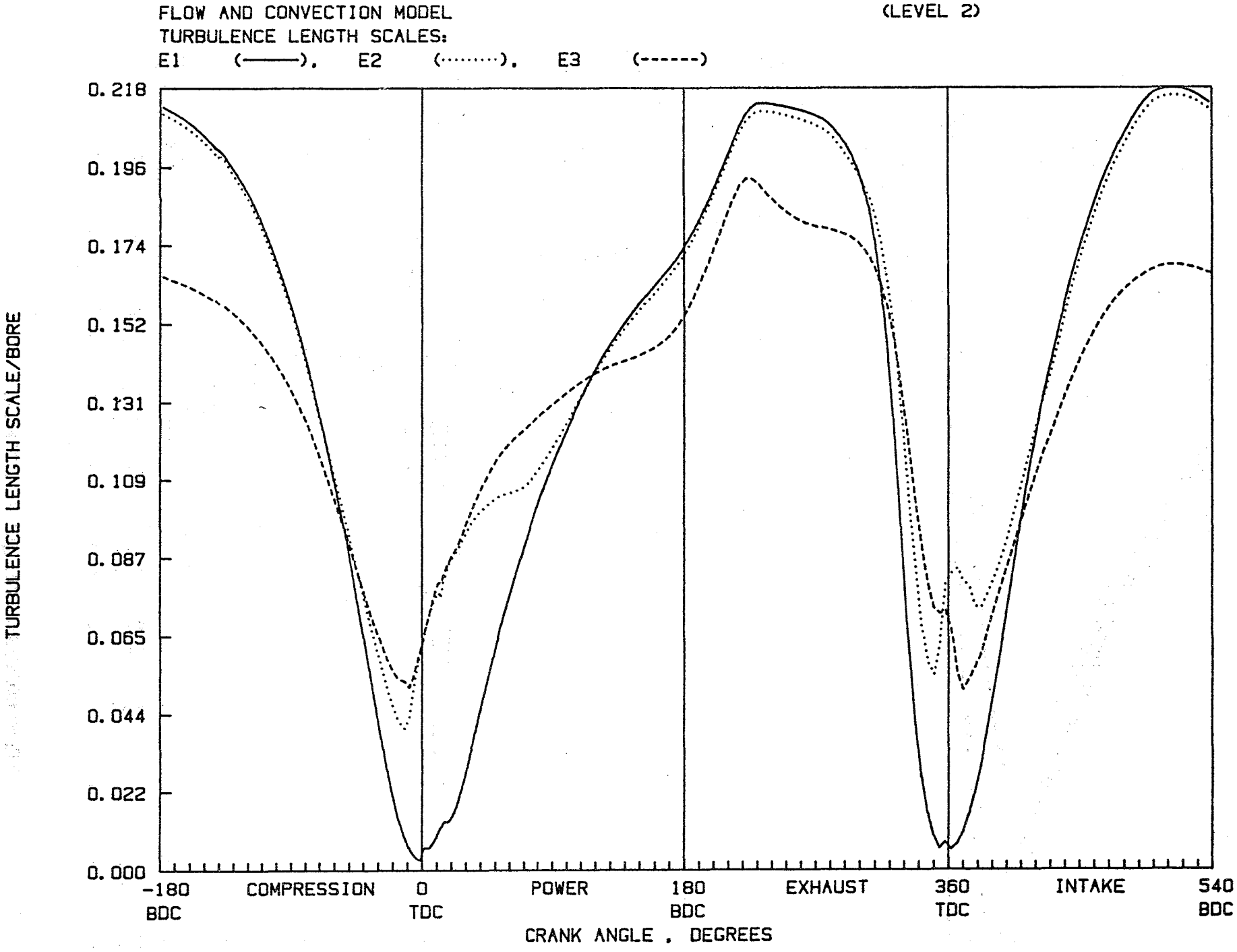

Figure 1-19. Turbulence length scale, Cup 2, high swirl case.

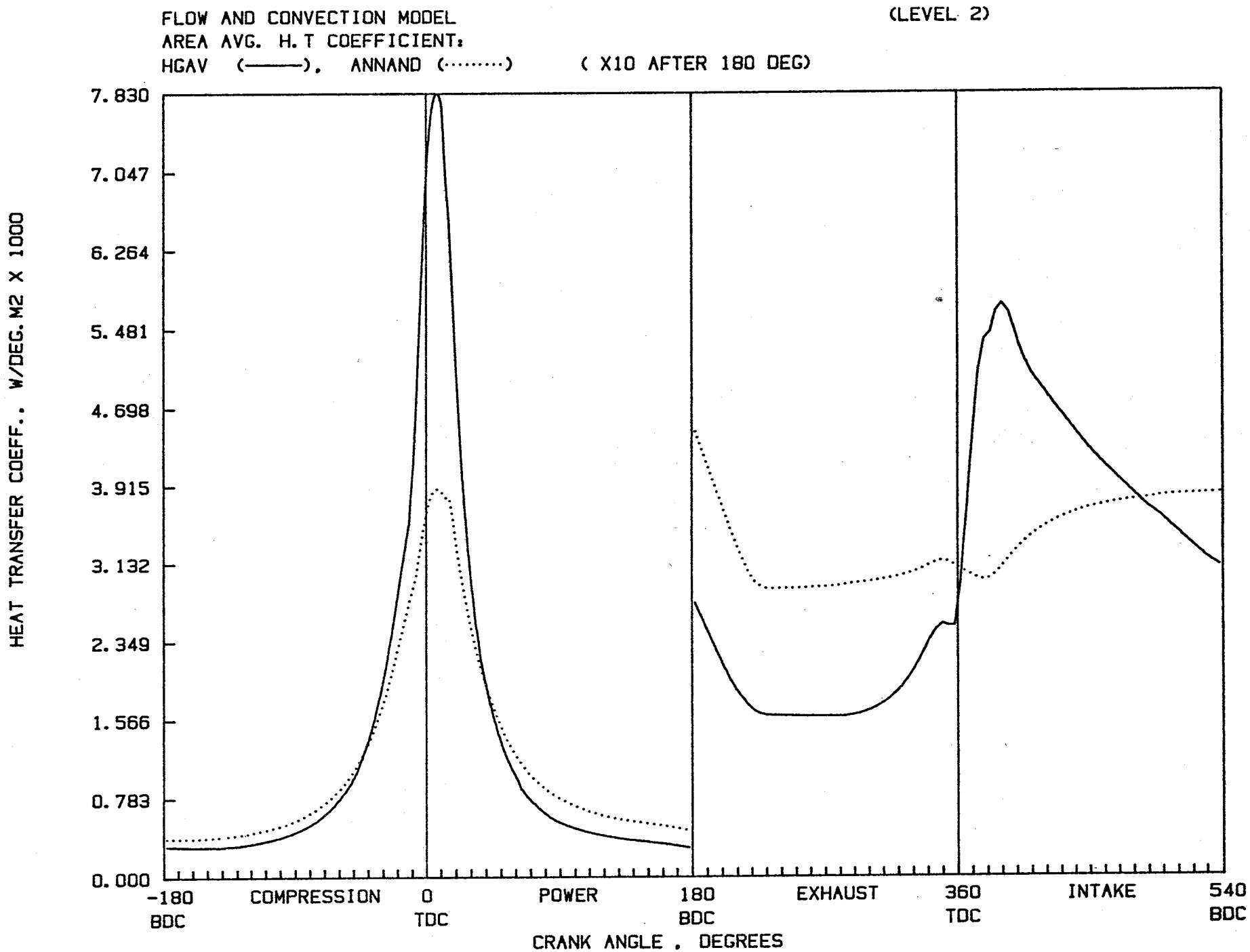

Figure 1-20. Area-averaged heat transfer coefficient, pancake geometry, high swirl.

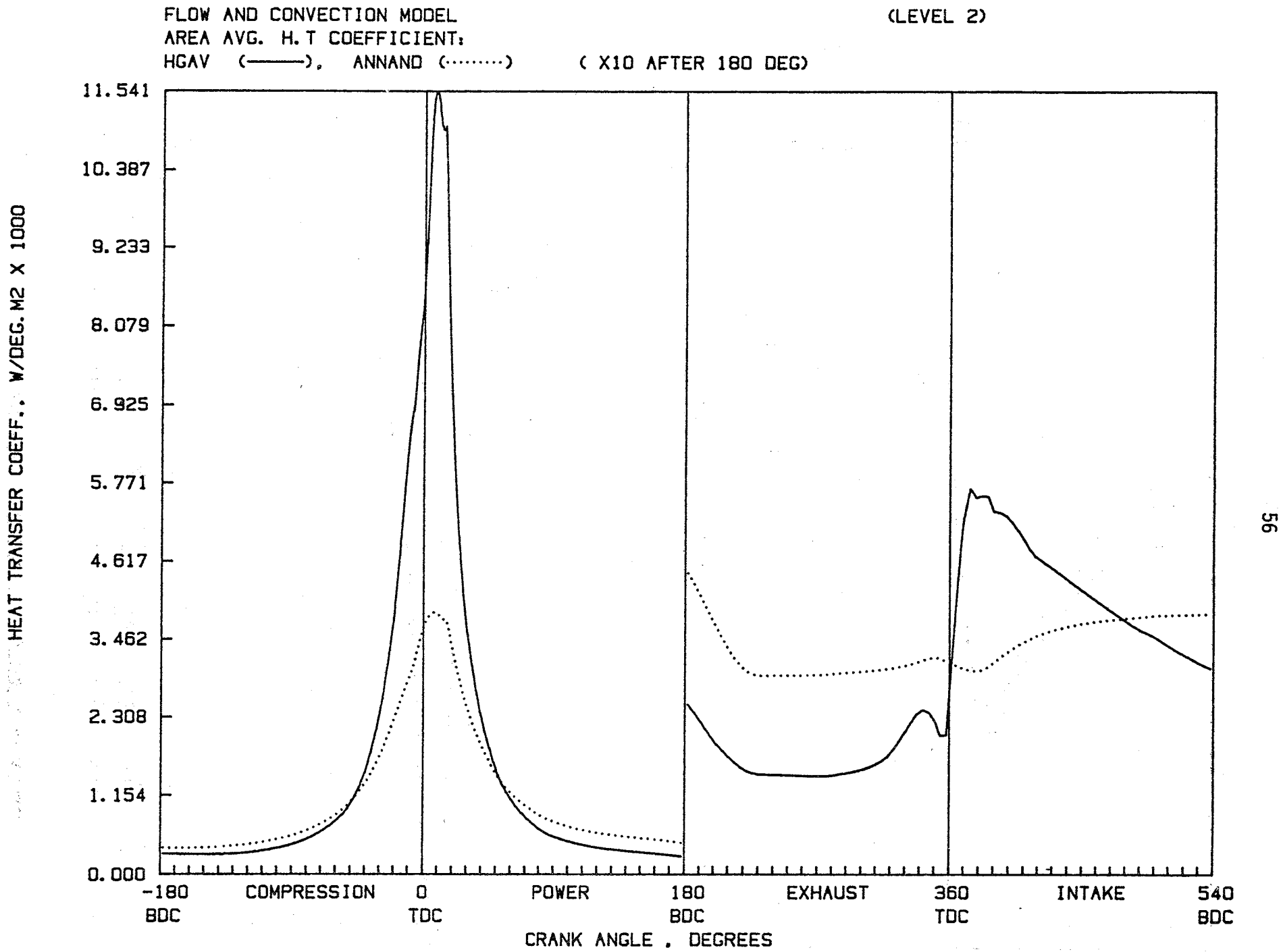

Figure 1-21. Area-averaged heat transfer coefficient, Cup 2, high swirl.

require much smaller adjustments to account for engine-to-engine differences than the previous models.

Predictions of Detailed Heat Flux Distribution

The calculation of a detailed heat flux distribution requires the knowledge of wall temperatures. To get these one has to couple the cycle model to a heat conduction model representing the surrounding structure. This is handled by a coupling subroutine, permitting arbitrary discretization of the structure and of the combustion chamber surface in a finite element or a similar heat conduction model. The coupling subroutine calculates the intersections of the conduction model surfaces with the six elementary surfaces and linearly averages the elementary heat transfer coefficients and convective temperatures needed as boundary conditions for the individual surfaces of the heat conduction model.

The particular heat conduction model employed here uses a heat resistance network approach described in the Appendix. This model represents the in-cylinder surface by eleven individual surface elements, seen in Figure (1-22), which shows the schematics of the network representation of the engine structure.

Baseline Case. The calculated heat transfer coefficients feed into heat flux calculations, together with the solution of the energy equation which provides other needed quantities such as gas temperature for the burned and unburned zones and cylinder pressure. The gas temperatures and pressure are shown in Figures (1-23) and (1-24) for the baseline case, which is the same turbocharged diesel engine discussed earlier, with piston cup 1. It should be noted that the gas temperature used to calculate the heat transfer during the combustion period lies between the unburned-zone temperature T_u and the mass-averaged temperature T_c, tending towards the latter at the end of the combustion period. The exact variation of the convective heat transfer temperature with crank angle is different for all three flow regions, depending on the burned/unburned mass split in each through equation (1-24).

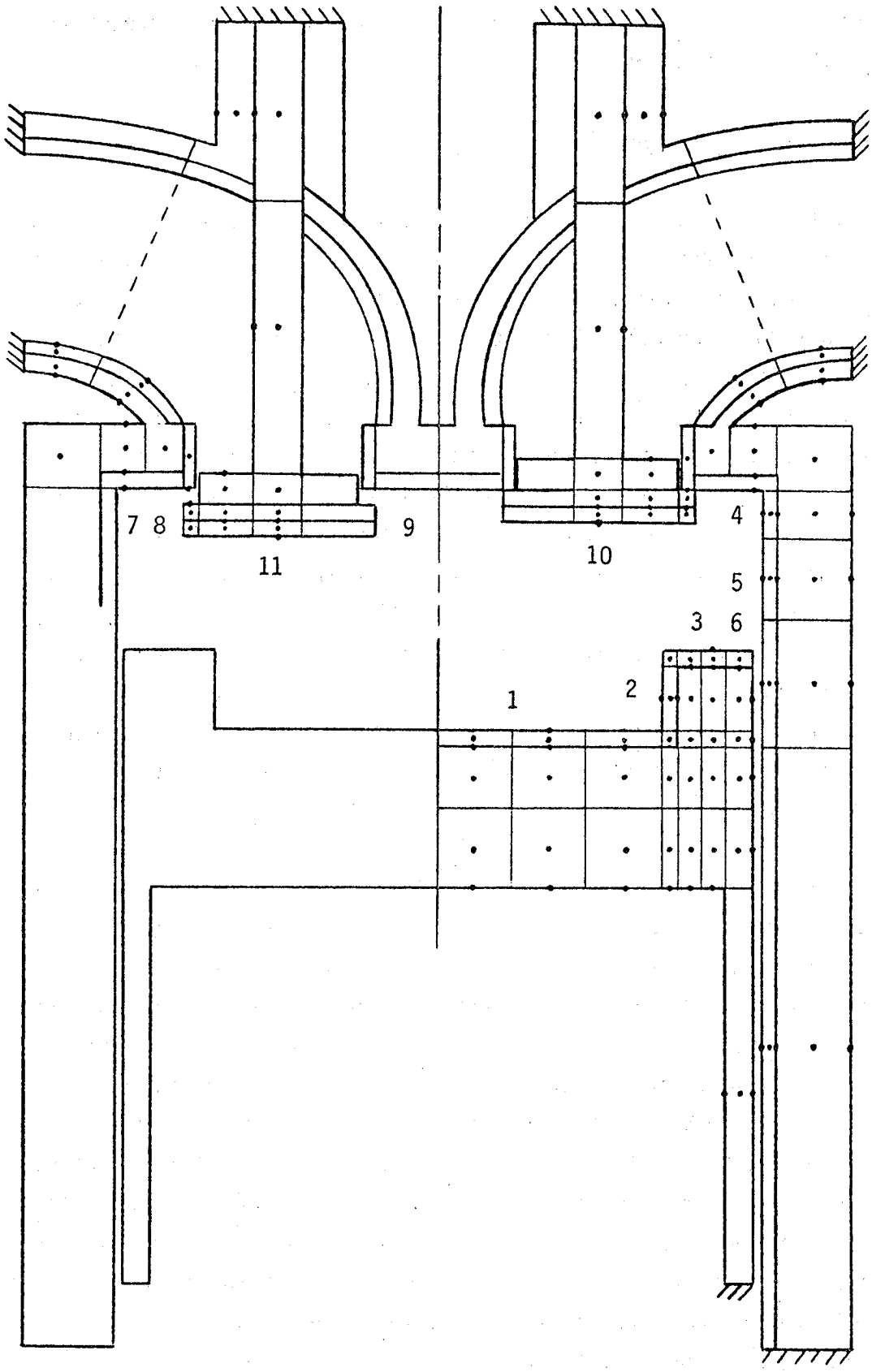

Figure 1-22. Schematic of heat conduction network elements for a cup-in-piston geometry. Numbers identify eleven in-cylinder surface areas.

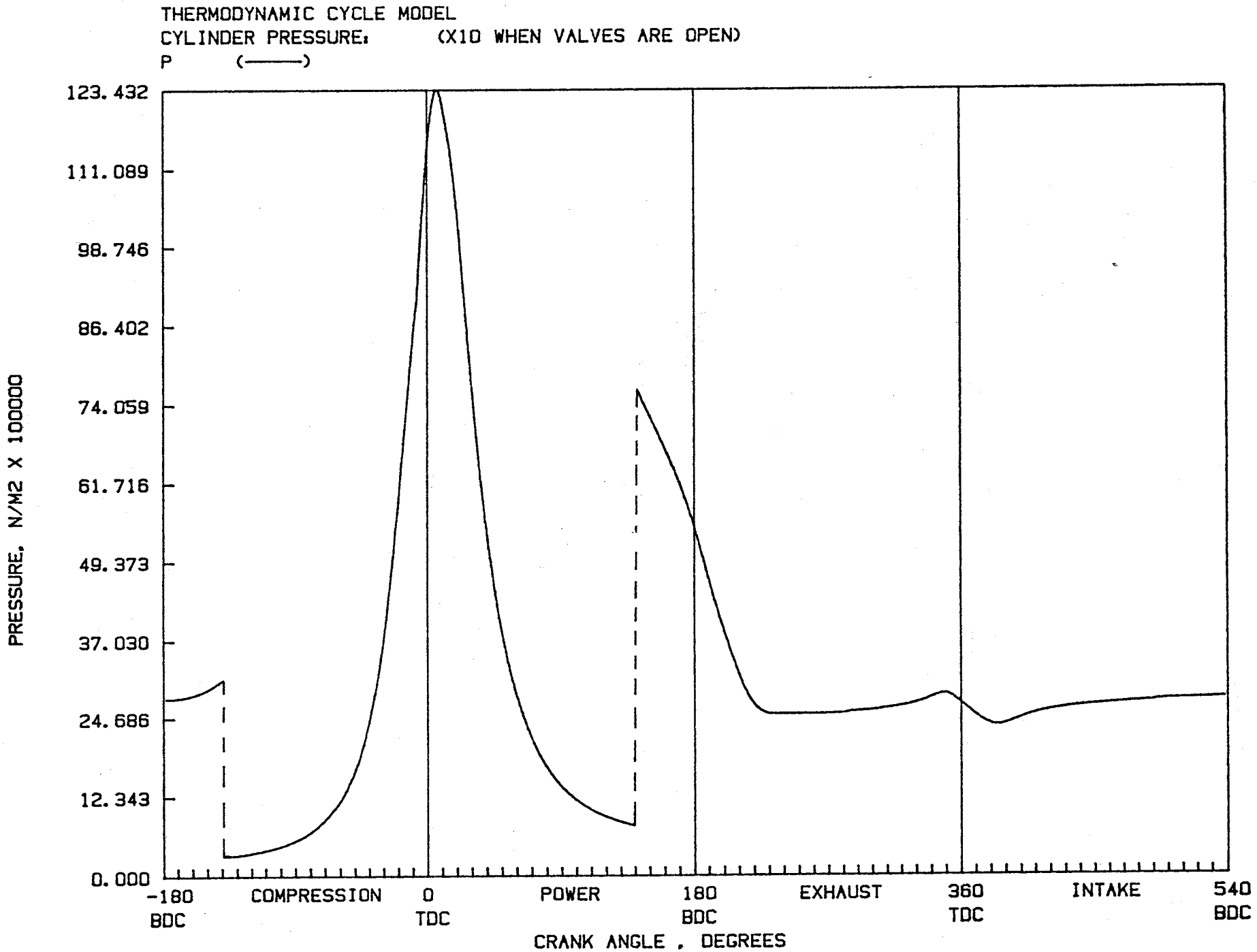

Figure 1-23. Cylinder gas pressure, Cup 1, high swirl.

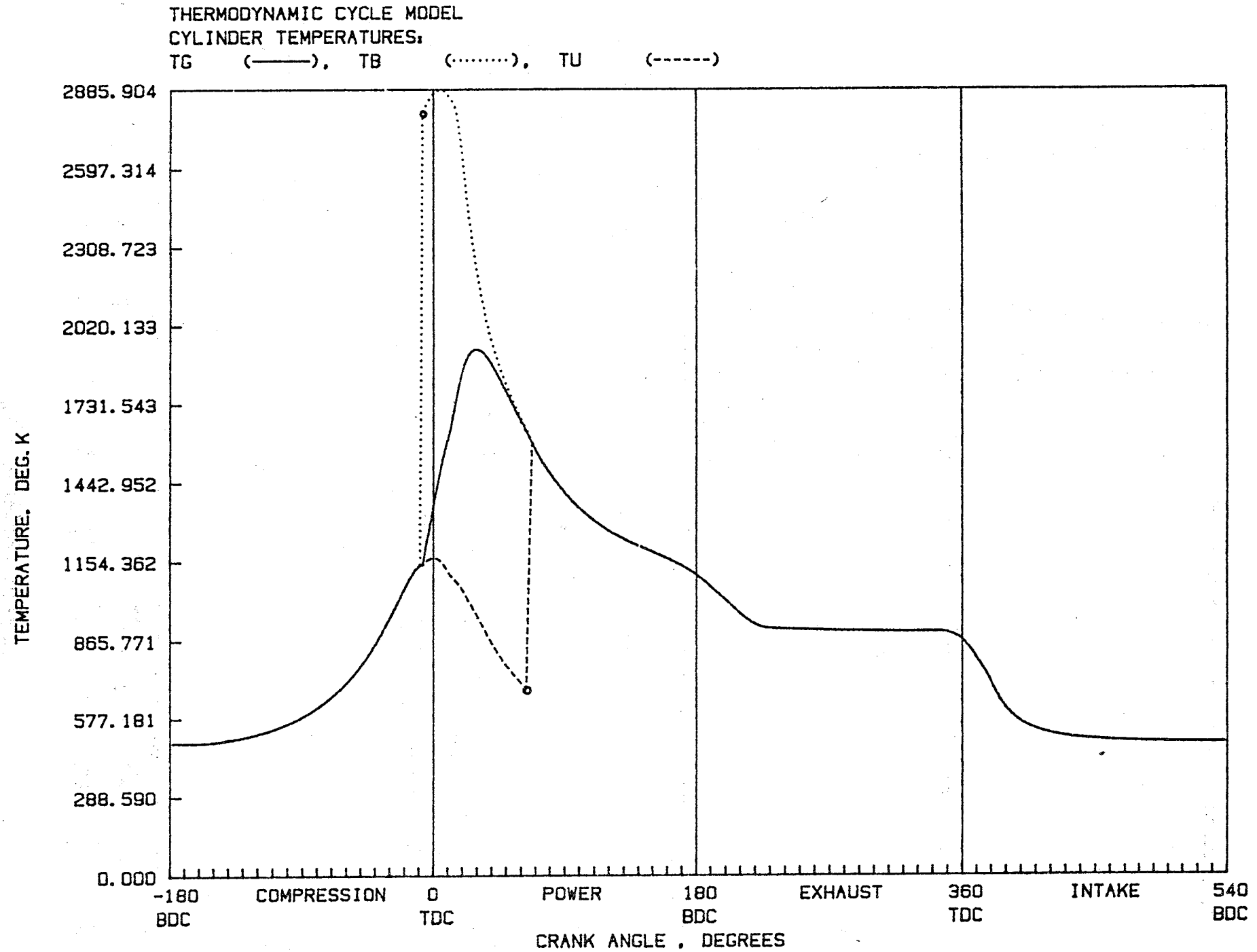

Figure 1-24. Cylinder gas temperatures, Cup 1, high swirl.

The area-averaged total heat transfer rate is shown in Figure (1-25). It should be noted that the radiation heat transfer was suppressed in these calculations, in order to focus the attention on the convective heat transfer. The heat transfer rate is highly peaked with a maximum rate of about 169 KW, while the average over 720 crank angle degrees is only 19.5 kW.

The breakdown of the total heat transfer rate between the piston, liner and head is shown in Figure (1-26). The most notable feature is the relation of the liner heat transfer to the other two surfaces: due to piston shielding, it goes through a minimum at TDC where the other two peak, and it dominates during the latter part of power stroke and during the exhaust period. During the intake, the direction of heat transfer into the liner is opposite to the direction into the other two surfaces. A further breakdown of the heat transfer into individual piston surfaces (Figure 1-27) reveals subtle differences between them. These differences are amplified with smaller diameter cups. In the case of the liner, the differences are much more substantial, as may be seen in Figure (1-28), showing the heat transfer distribution between the three elements that form the liner wall -- surface 4 covers one-sixth of the maximum exposed liner area (stroke and clearance), surface 5 covers one-third and surface 6 covers the bottom half of the area. The rates of convective heat transfer for surfaces 5 and 6 are zero when these are fully masked by the piston. It should be noted that when the piston shields the surface and convection is reduced or eliminated, the conductive element of heat transfer, i.e., between the piston and the liner, comes into play. That portion of the heat transfer is handled by the conduction model.

Another detail of the in-cylinder heat transfer is shown in Figure (1-29), relating to valve heat transfer. Although the intake and exhaust valves are of the same size, the heat transfer to the intake valve is larger, and this is due to its lower temperature. The instantaneous heat transfer rates in intake and exhaust ports are depicted in Figure (1-30). It shows a large peak in heat transfer rates to the

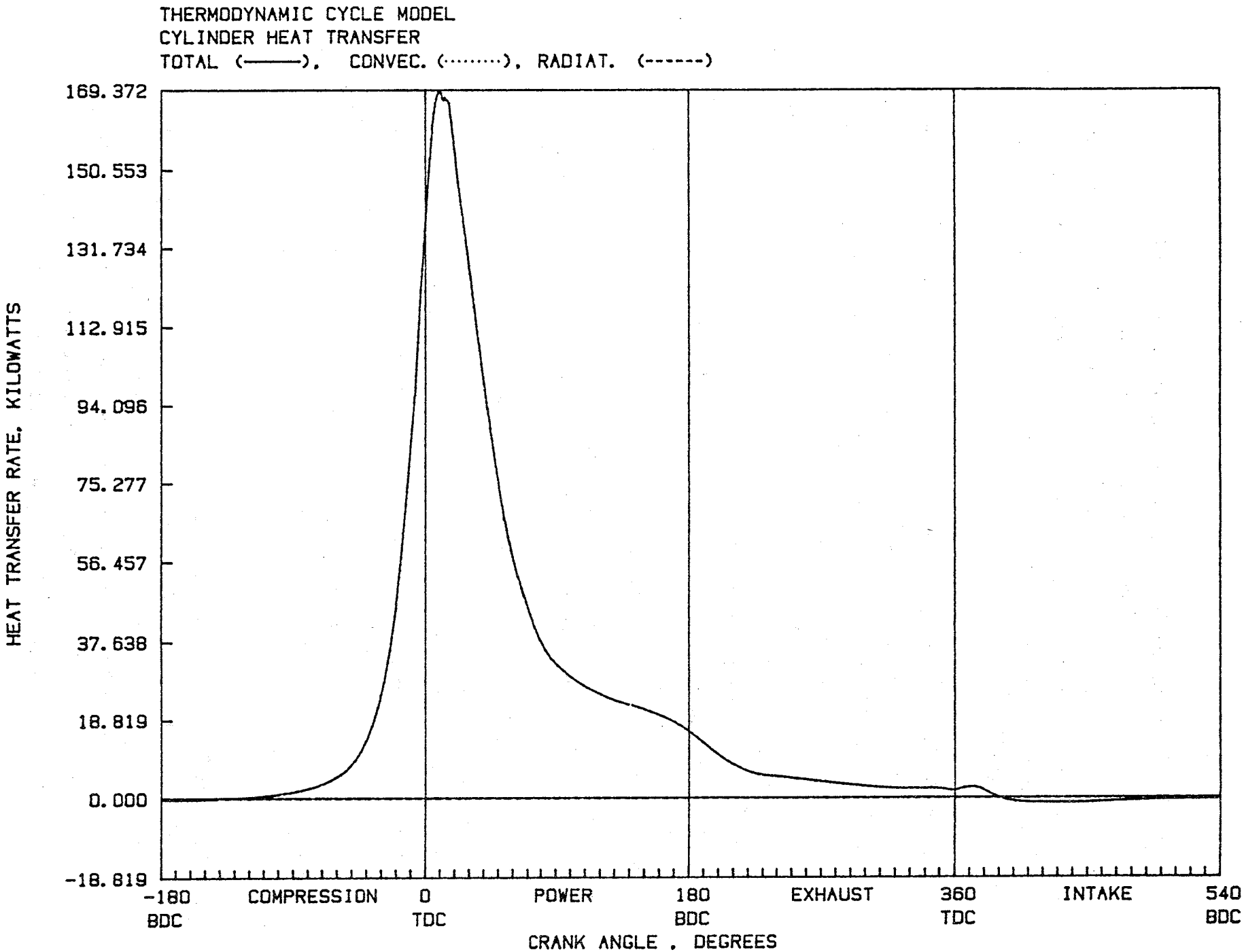

Figure 1-25. Area-integrated heat transfer rate, Cup 1, high swirl.

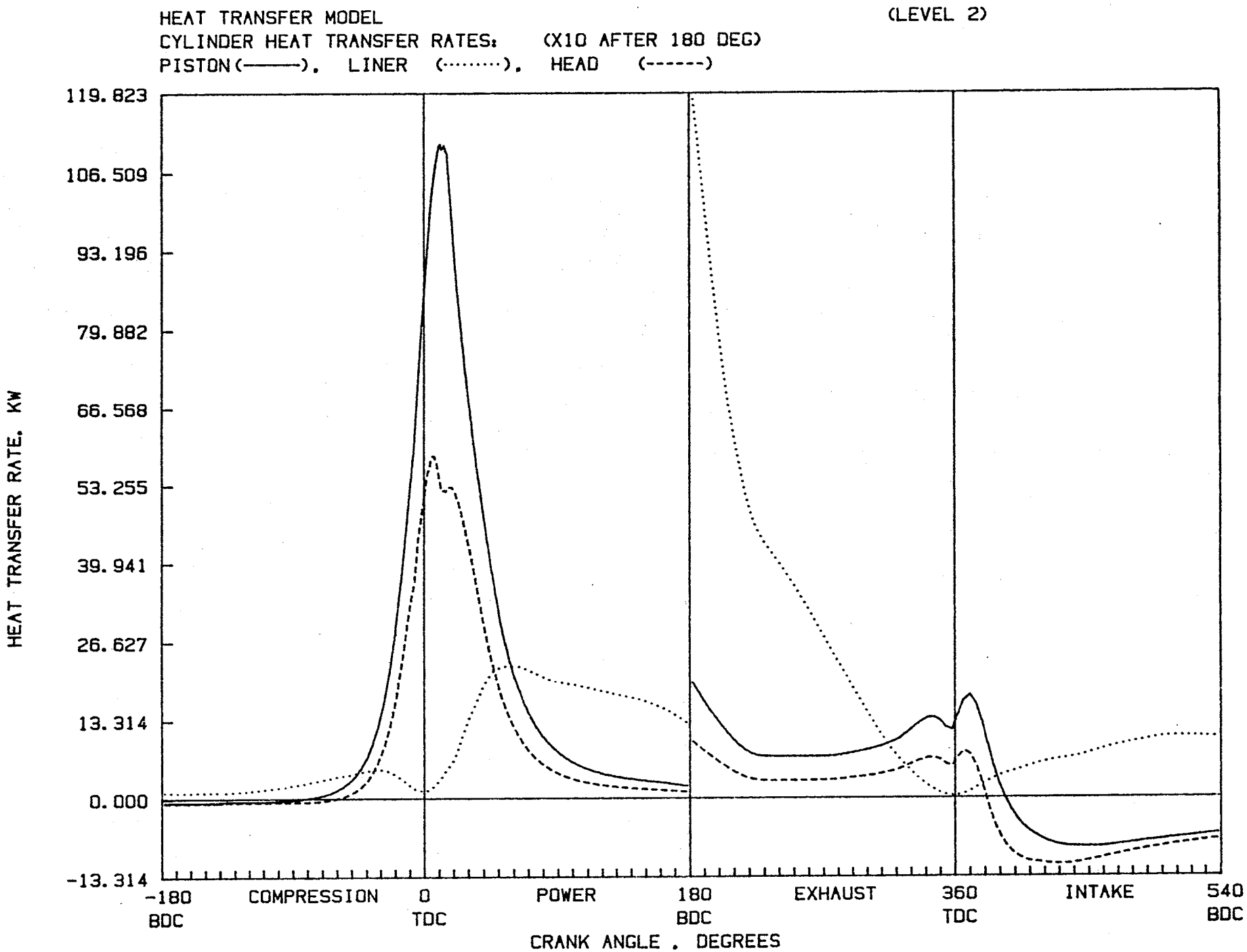

Figure 1-26. Breakdown of heat transfer rates: piston, liner, head, Cup 1, high swirl.

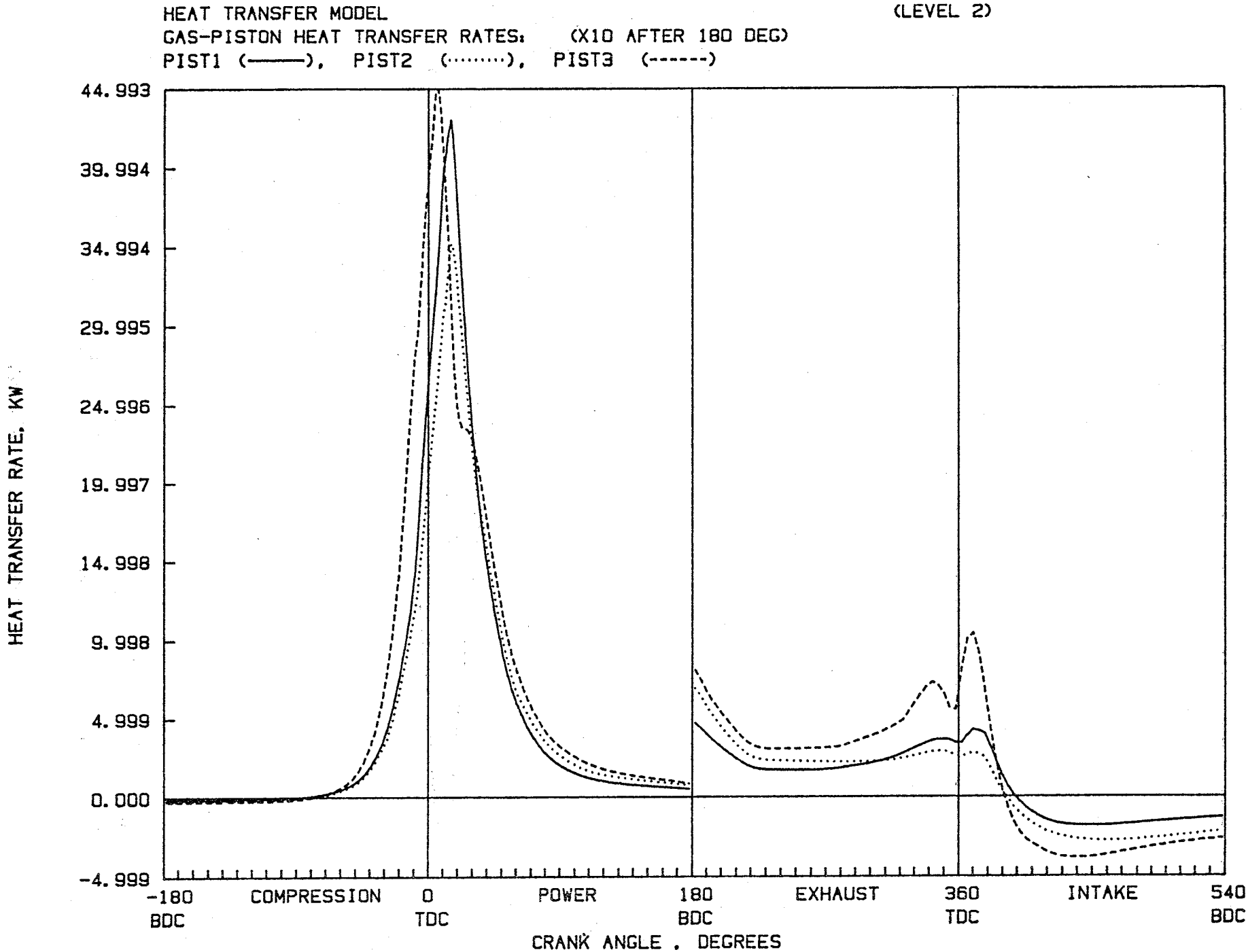

Figure 1-27. Heat transfer rate into the three piston surfaces, Cup 1, high swirl.

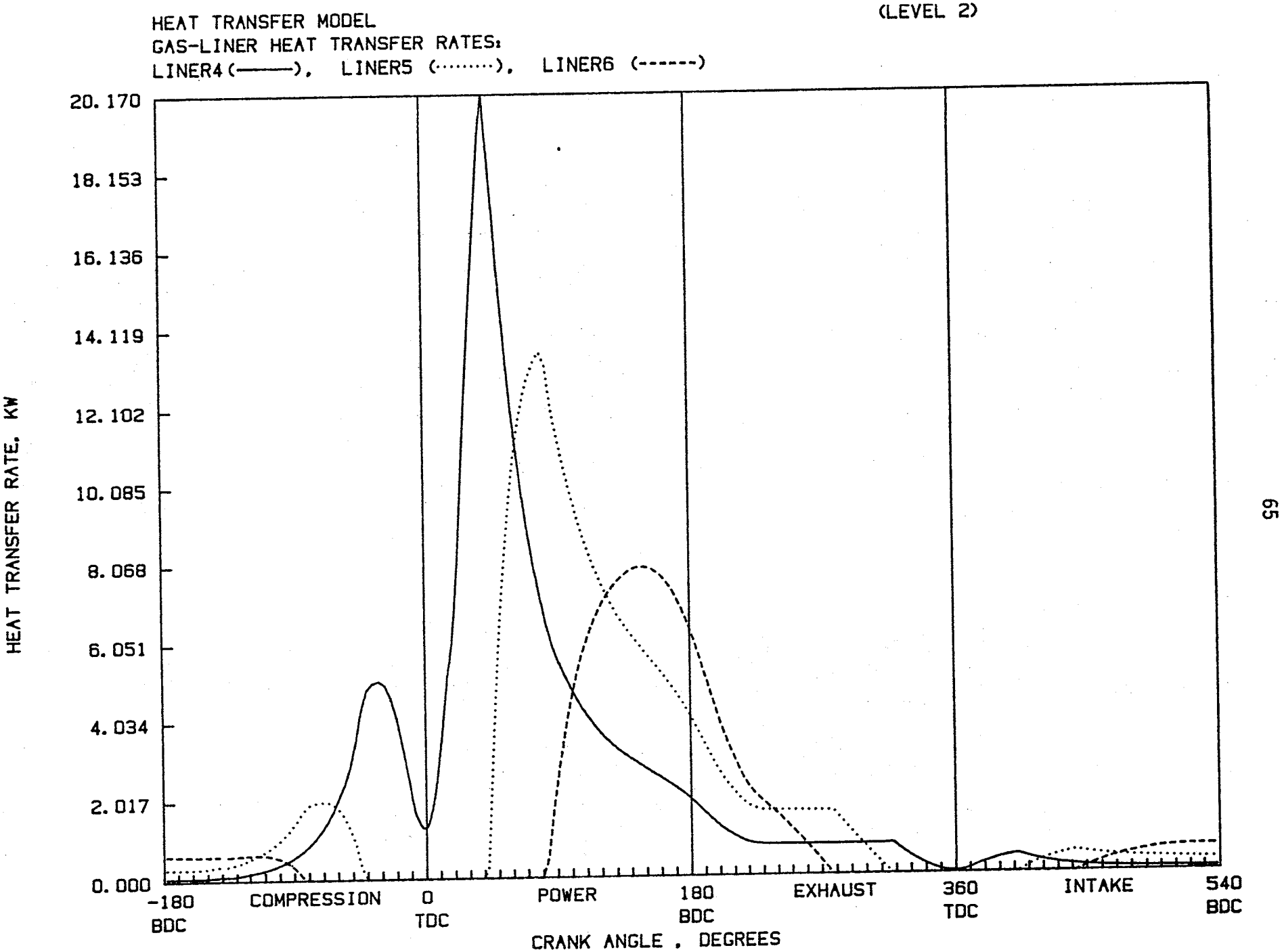

Figure 1-28. Heat transfer rates into the three liner elements, Cup 1, high swirl.

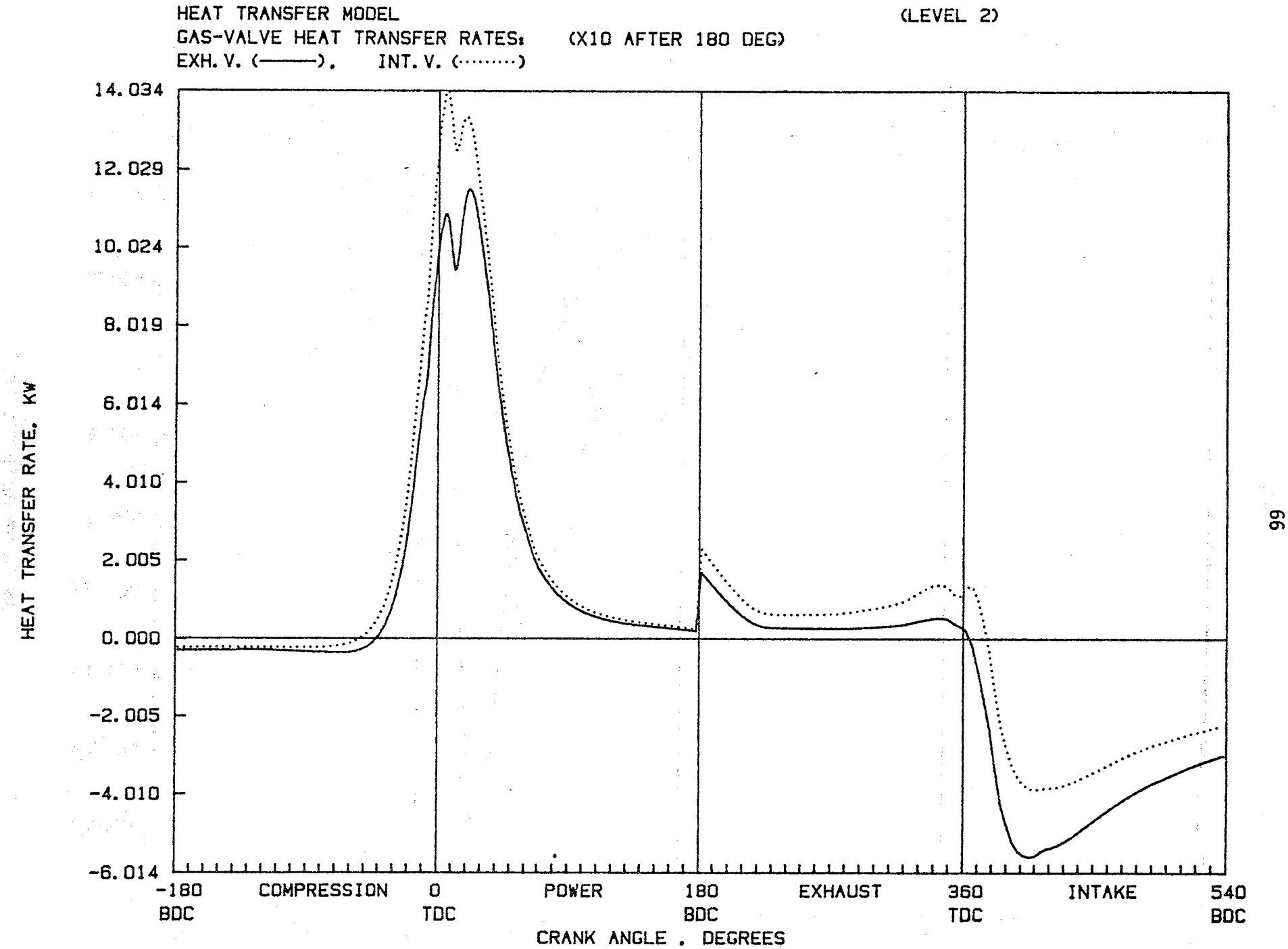

Figure 1-29. Heat transfer from combustion chamber into valves, Cup 1, high swirl.

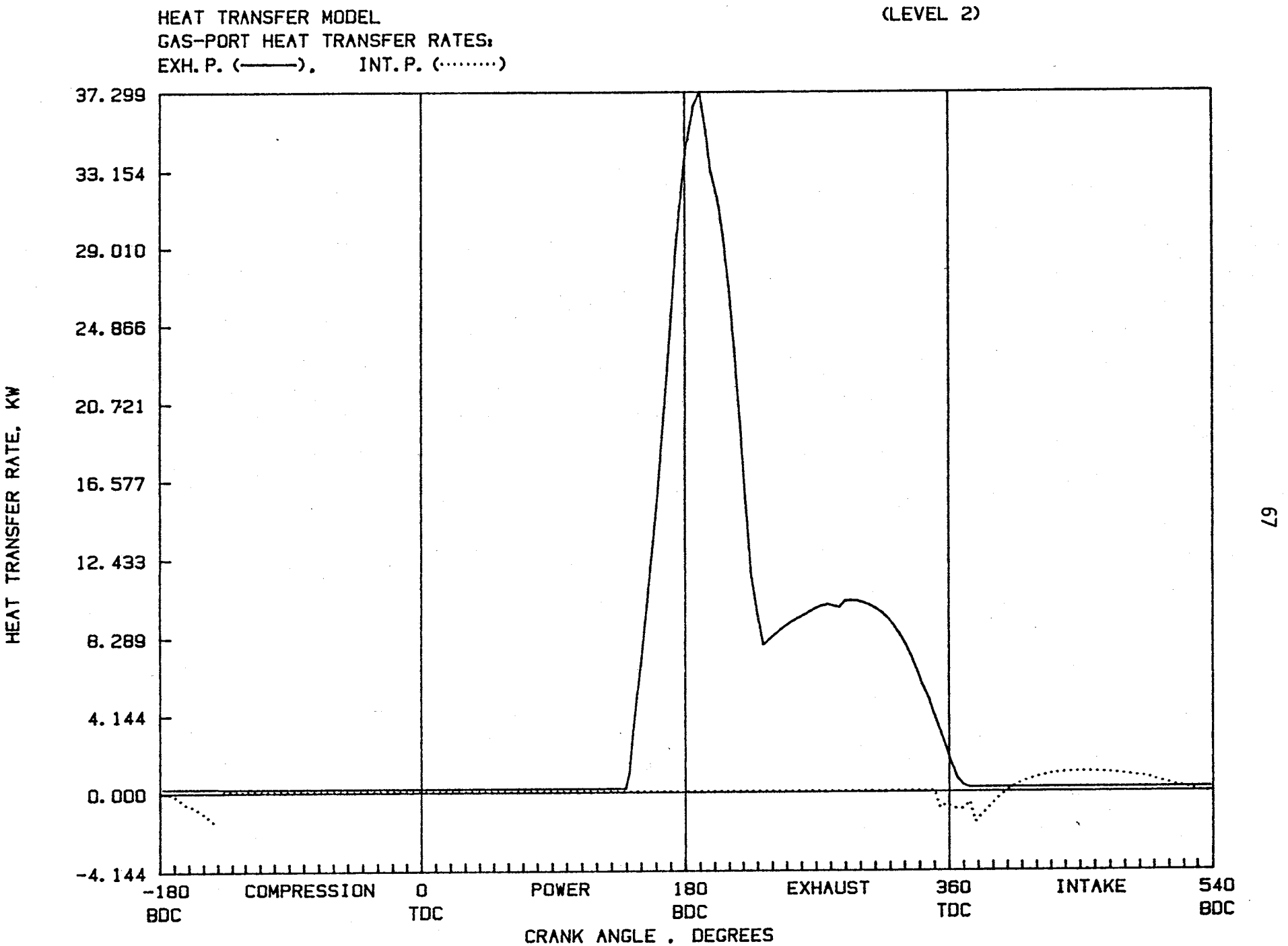

Figure 1-30. Heat transfer rates into the two ports, Cup 1, high swirl.

exhaust port during the initial blowdown after the valve opening, followed by a second smaller peak during the latter part of the exhaust stroke. In the intake port there is a smaller peak of heat transfer during the intake event from the intake air which is assumed to exit the compressor with a temperature of 460°K, i.e., warmer than the port walls.

Effect of Piston Geometry and Swirl on Heat Flux Distribution. Among the different cases examined, there were also runs made with twenty times lower inlet swirl coefficient, carried out to assess the importance of swirl. These cases had a very low swirl level of S=0.2 at BDC, simulating small unavoidable level of swirl set up in quiescent combustion chambers. Two such cases, with pancake and cup 1 piston geometries, are included here for comparison with the high swirl cases already discussed.

Piston geometry was found to have a large effect on the predicted cycle-averaged heat transfer rates at both the high and low swirl levels, but not on the peak rates. At high swirl the peak rates were found to vary from 145kW for the pancake geometry to 230 kW for cups 2 and 3, while the cycle-averaged rates varied from 17.6 kW to 22.1 kW for cup 3. With the lower swirl level the peak heat transfer rates were about the same as with the high swirl, but cycle-averaged rates were only 12.2kW for the pancake and 14.0kW for the cup 1.

The breakdown between the three major areas -- piston, liner and head was quite different from case to case, depending strongly on both the geometry and the swirl level. The effects of geometry for the high swirl case may be observed by comparing the pancake geometry, Figure (1-31), and the cup 2, Figure (1-32). It may be seen that the proportion of heat transfer that goes into the piston is greatly increased by the presence of the cup. The effects of increased swirl level are mainly effective in raising the liner heat transfer during the power stroke and exhaust periods, as may be seen by comparing Figures (1-33) and (1-26).

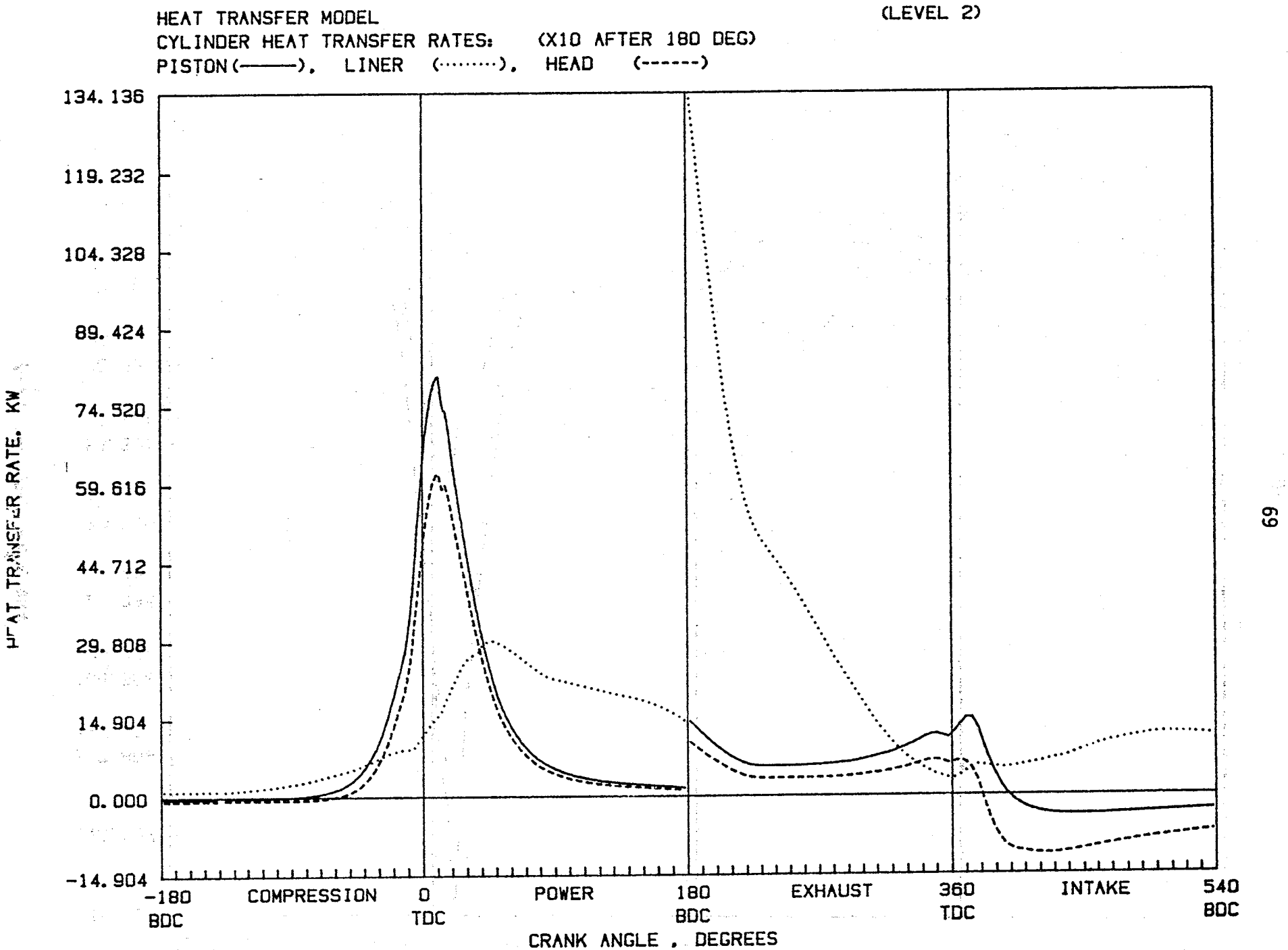

Figure 1-31. Breakdown of heat transfer rates: piston, liner, head; pancake, high swirl.

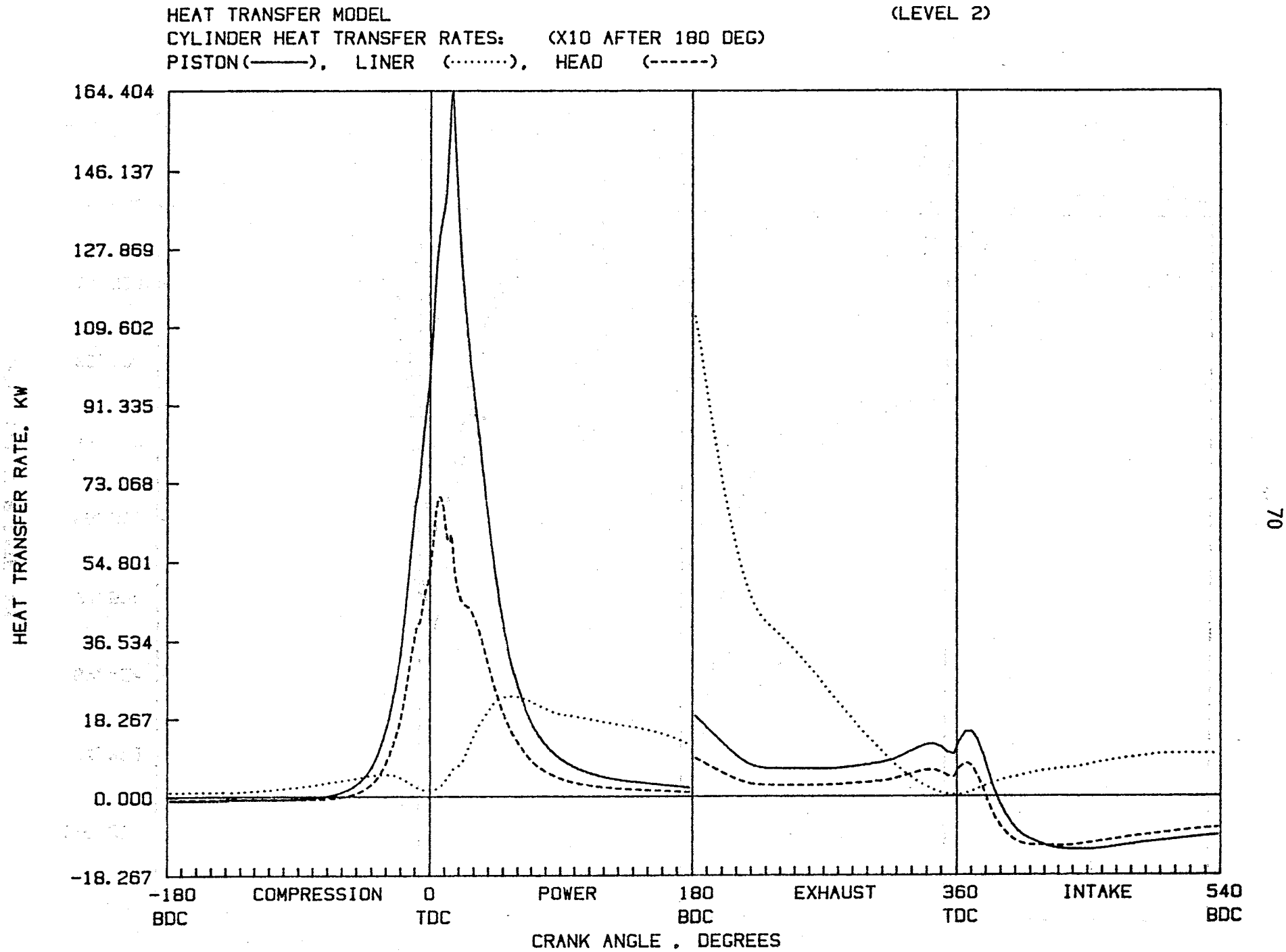

Figure 1-32. Breakdown of heat transfer rates: piston, liner, head, Cup 2, high swirl.

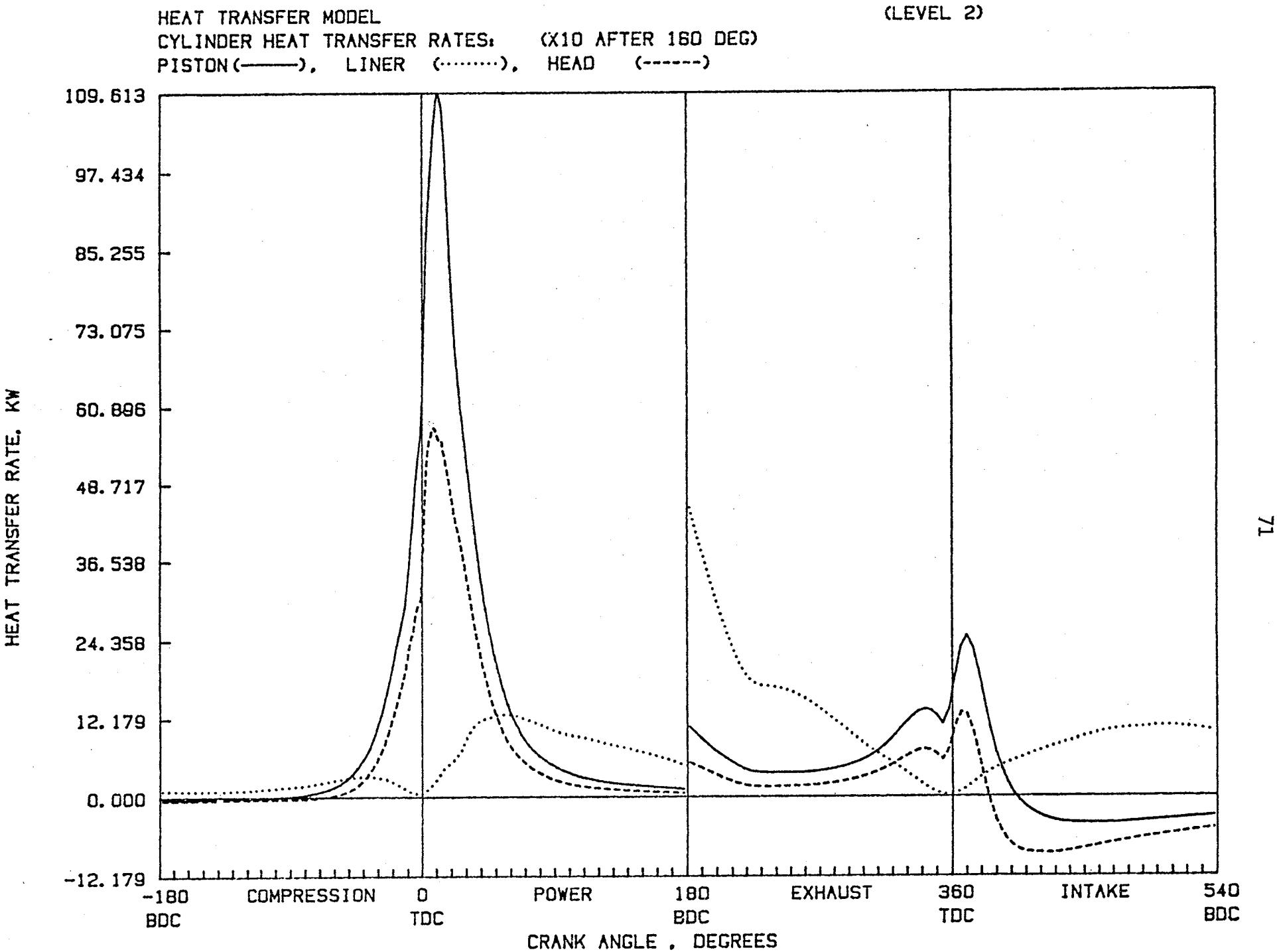

Figure 1-33. Breakdown of heat transfer rates: piston, liner, head, Cup 1, low swirl.

The cycle-integrated heat transfer rates into the eleven individual in-cylinder surfaces, and the resulting wall temperatures produced on those surfaces, are summarized in Table 1-1. The variations in heat transfer rates reflect the differences in heat transfer coefficients, wall temperatures and areas of the individual surfaces.

The results in Table 1-1 reveal the differences in predicted heat transfer as a function of swirl level and chamber geometry. For a pancake geometry with a low swirl, the convective heat transfer amounts to 11.5% of fuel energy. Quadrupling the swirl level produced a heat transfer rate of 16.63% of fuel energy. Keeping the same swirl level and introducing a piston cup (at the same compression ratio) led to a further increase in heat transfer rate mainly due to an increase in heat transfer into the piston. The broad cup 1 increased the heat transfer rate by an amount equal to 1.7 percent of fuel energy, cup 2 increased it by 3.9 percent, and the broad cup 3 with a re-entrant lip increased it by 4.2 percent of the fuel energy. Simultaneously, the piston surface temperatures rose substantially in accord with the increased heat transfer rates, with the area-averaged wall temperature ranging from 487°K for the low swirl pancake geometry, to 568°K for high swirl cup 3.

The percentage of heat transfer for the three major combustion chamber areas -- piston, liner and head -- is given in the last three lines of Table 1-1. There is a wide variation in the split and it shows that increasing the swirl level in a pancake geometry tends to increase mainly the heat transfer rate to the liner. The introduction of the cup leads to an increase in the percentage of heat transfer that goes to the cup, while reducing the liner share. The share of the head plus valves is relatively constant, being near 25 percent of the total.

In order to explore the increased spatial resolution that the new convective heat transfer model provides, compared with the prior state of the art, a sample run was also performed with the Annand correlation replacing the convective heat transfer model. The multiplier constant of the Annand model was adjusted to 0.435 to match the heat transfer

Table 1-1

Comparison of heat transfer rates and wall temperatures for individual surfaces

		Pancake low swirl	Pancake high swirl	Cup #1 low swirl	Cup #1 high swirl	Cup #2 high swirl	Cup #3 high swirl	Annand Correlation
Heat transfer (% fuel energy)		11.52	17.28	13.21	18.34	20.58	20.82	18.34
	(KW)	12.20	18.30	14.0	19.50	21.80	22.10	19.50
Piston	1 HTR (W)	2900	3100	2470	2850	1490	3350	
	T (°K)	539	575	539	578	596	627	
	2 HTR	-	-	1920	2590	4910	4270	
	T	-	-	555	607	640	678	
	3 HTR	1980	3110	2620	3470	4740	4070	
	T	517	562	560	613	650	679	
Liner	4 HTR	1880	3330	1380	2290	2340	2170	
	T	445	487	438	467	470	467	
	5 HTR	1230	2630	1120	2110	2050	1960	
	T	420	440	427	443	448	448	
	6 HTR	641	1570	632	1340	1270	1240	
	T	405	415	411	421	425	426	
Head	7 HTR	632	981	834	1130	1180	1120	
	T	511	567	531	577	585	578	
	8 HTR	721	918	771	969	1030	990	
	T	563	607	573	614	625	619	
	9 HTR	656	716	599	694	737	867	
	T	594	618	584	614	625	653	
Ex. Valve	10 HTR	668	852	700	882	904	898	
	T	802	837	807	831	836	835	
Int. Valve	11 HTR	925	1120	970	1150	1180	1170	
	T	682	742	695	749	761	760	
Area Avg. Wall Temp		487	517	504	536	553	568	
Piston		40%	34%	50%	46%	51%	53%	39%
Liner		31%	41%	28%	29%	26%	24%	39%
Head		29%	25%	22%	25%	23%	23%	22%

level obtained for the cup 1 (recommended values vary from 0.35 to 0.80). Since the Annand model is not sensitive to swirl level nor to the cup geometry, it gives the same results for all of the cases in Table 1-1 (except for small differences due to piston surface area). Using the geometry for cup 1, it was found that the Annand's model predicts the split between the three surfaces given in the last column of Table 1-1. This prediction of area and cycle averaged heat transfer rates matches none of the flow test six cases presented in Table 1-1.

References

Alcock, J. F., "Heat Tranfer in Diesel Engines," Proceedings 1961-62 Int. Heat Transfer Conf., ASME, University of Colorado, Boulder, Colorado, P. 174, 1962.

Annand, W. D., "Heat Transfer in the Cylinders of Reciprocating Internal Combustion Engines," Proc. Instn. Mech. Engnrs., 1963, Vol. 177, No. 36, p. 973.

Borgnakke, C., Arpaci, V. S. and Tabaczynski, R. J., "A Model for Instantaneous Heat Transfer and Turbulence in a Spark Ignition Engine," SAE Paper 800287, 1980.

Davis, G. C. and Borgnakke, C., "The Effect of In-Cylinder Flow Processes (Swirl, Squish and Turbulence) on Engine Efficiency - Model Predictions," SAE Paper 820045, 1982.

Dent, J. C. and Suliaman, S. L., "Convective and Radiative Heat Transfer in a High Swirl Direct Injection Diesel Engine," SAE Paper No. 770407, 1977.

Eichelberg, G., "Some New Investigations on Old Combustion-Engine Problems," Engineering, Vol. 148, p. 547, 1939.

Elser, K., "Der Instationaere Waermeuebergang in Diesel-Motoren," Mitt. Inst. Thermodyn. Zurich, No. 15, 1954.

Johnston, S. C., Robinson, C. W., Rorke, W. S., Smith, J. R. and Witze, P. O., "Application of Laser Diagnostics to an Injected Engine," SAE Paper 790092, 1979.

Knight, B. E., "The Problem of Predicting Heat Transfer in Diesel Engines," Proc. Instn. Mech. Engrs., 1964-65, Vol. 179, Pt. 3C, p. 99.

Morel, T. and Mansour, N. N., "Modeling of Turbulence in Internal Combustion Engines," SAE Paper 820040, 1982.

Nusselt, W., "Der Waermeuebergang in der Verbrennungskraftmaschine," Z. Ver. Dtsch. Ing, Vol. 67, p. 692, 1923.

Poulos, S. G. and Heywood, J. B., "The Effect of Chamber Geometry on Spark-Ignition Engine Combustion," SAE Paper 830334, 1983.

Sitkei, G., "Beitrag zur Theorie des Waermeueberganges im Motor," Konstruktion, Vol. 15, p. 67, 1962.

Uzkan, T., Borgnakke, C. and Morel, T., "Characterization of Flow Produced by a High-Swirl Inlet Port," SAE Paper 830266, 1983.

Woschni, G., "A Universally Applicable Equation for the Instantaneous Heat Transfer Coefficient in the Internal Combustion Engine," SAE Transactions, Vol. 76, p. 3065, 1967.

II. RADIATION HEAT TRANSFER MODEL

In order to carry out heat transfer calculations for highly insulated diesels it is necessary to model heat radiation correctly. Radiation heat transfer in internal combustion engines is mainly produced by soot particles which are present during the combustion process and by carbon dioxide and water molecules. Radiation is also emitted by many of the intermediate chemical species formed during combustion, but their concentration levels are small and so their effect is less important. Unlike soot, whose radiation is broad band, radiation from gaseous species is concentrated in narrow spectral bands, and its total magnitude is substantially smaller than that produced by soot.

In spark ignition engines, where the combustion is relatively soot free, the radiation heat transfer is always small compared to the convection heat transfer. By contrast, in diesel engines the radiation heat transfer during the combustion process can be of the same order of magnitude as the convection heat transfer. The relative magnitude of these two components for the overall cycle is a point argued about in the literature, which tends to place the radiation magnitude between 10 and 50 percent of the convection heat transfer magnitude. The uncertainty about this stems mainly from the fact that the split between radiation and convection heat transfer is highly dependent upon the engine design and operating characteristics. However, it seems to be well established that in state of the art metallic engines the heat transfer from gases to wall is dominated by convection, and radiation adds a smaller contribution. Thus it has been considered acceptable until now to treat radiation heat transfer in a rudimentary fashion or to lump it together with convection.

That approach becomes untenable in insulated diesels. By applying insulating materials to diesel engines, one may expect to reduce the convective heat transfer more than the radiation heat transfer, making the latter the dominant source of gas-to-wall heat transfer. Thus, whereas the heat radiation has been a relatively minor element in studies of conventional diesel engines, its role in insulated engines is

much more pronounced, and must be studied and quantified. Because of this, a part of the overall effort in the development of the heat transfer methodology is directed at developing a new radiation heat transfer submodel.

The model will calculate the heat radiation during the combustion period, and will treat the combustion gases as divided into two volumes, burned and unburned. The gas properties, temperature, density, composition, etc., will be considered uniform in each volume, and they will be calculated using a two-zone combustion model. The most appropriate method for handling of this type of problem is the zonal method. In this chapter we review the key concepts in heat radiation modeling and introduce two methods of solution -- mean beam length method (discussed here only because it helps to clarify some concepts used in radiation) and the zonal method. The final section deals with an investigation of the effects of radiation scattering by fuel droplets.

A. Governing Equations

The starting point for studies of radiation heat transfer is the equation describing the intensity of radiation at any point along a path through a participating medium, where the intensity is defined as the radiant energy leaving a surface per unit area normal to the pencil of rays, per solid angle and per unit time (Figure 2-1). This equation can be written as

$$d(i_\lambda(s'))/ds' = -a_\lambda i_\lambda(s') + a_\lambda i_{\lambda b}(s') - \sigma_\lambda i_\lambda(s') + \sigma_\lambda \int_{4\pi} i_\lambda(s',\omega_i)\Phi(\lambda,\omega,\omega_i)d\omega_i/4\pi \qquad (2\text{-}1)$$

where s' is the coordinate along the path, ω is solid angle measured from the direction s', a_λ and σ_λ are absorption and scattering coefficients, respectively, and Φ is a phase function. Subscript λ is used to indicate dependence on wavelength of radiation, and subscript b refers to blackbody radiation. The first term in the right represents energy loss by absorption, the second term represents energy gain by emission,

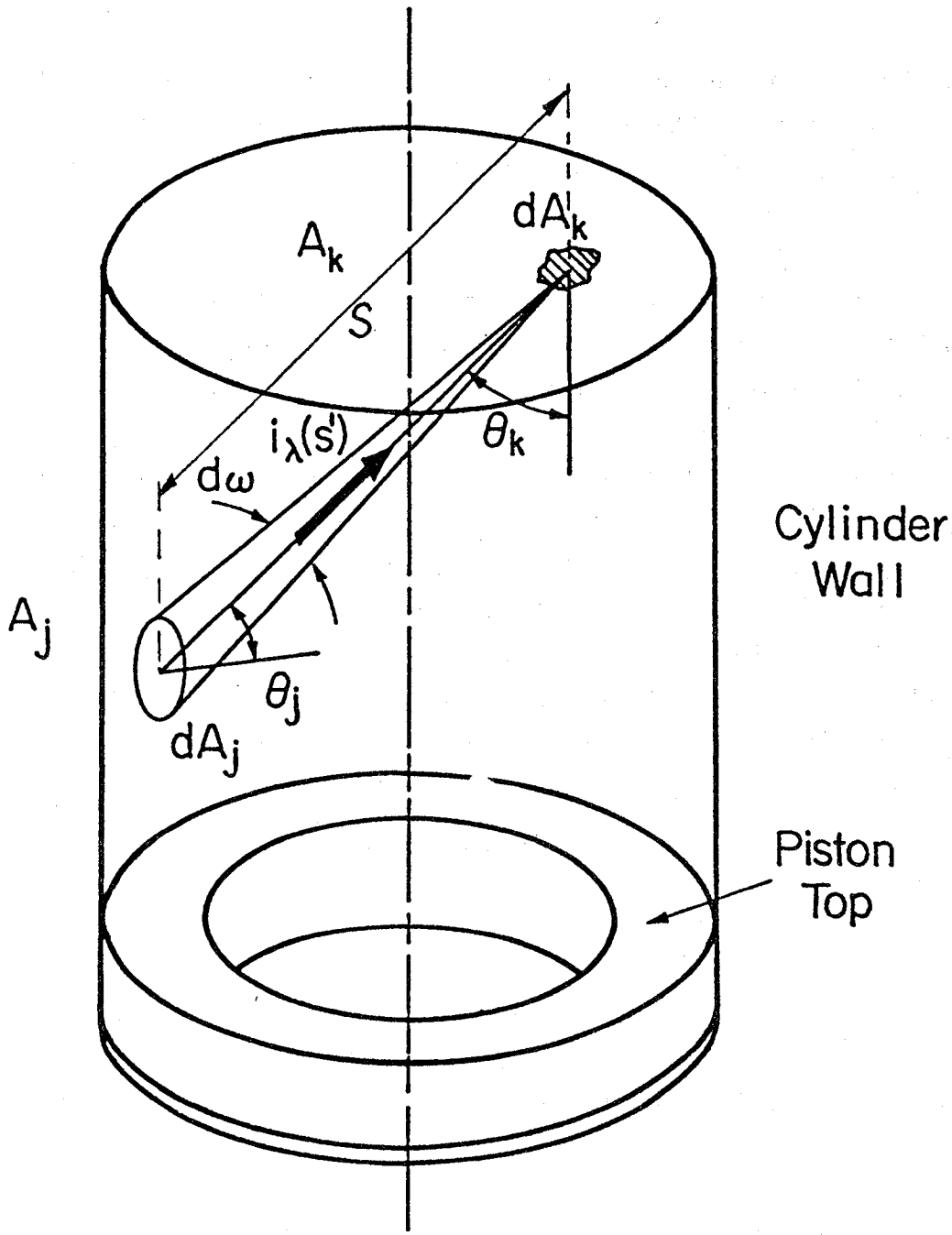

Figure 2-1. Schematic of radiation heat transfer process

and the third and fourth term represent energy loss and gain, respectively, by scattering. Radiation heat transfer by emission and absorption alone will be considered first; the effect of scattering will be considered later in the context of scattering by fuel droplets present in the combustion gases.

Thus, for emission and absorption only, the equation of radiation heat transfer is given by

$$d(i_\lambda(s'))/ds' = -a_\lambda i_\lambda(s') + a_\lambda i_{\lambda b}(s') \qquad (2\text{-}2)$$

To calculate the radiation heat transfer in an enclosure filled with radiating soot laden gases, including radiation between surfaces, requires the solution of equation (2-2). That is a computationally formidable task because of the multidimensional spatial dependence compounded by a spectral dependence. To reduce the computational load, one can resort to approximate solutions. In a typical approach, using assumptions (or approximations) of spatial or spectral homogeneity of various parameters, the governing equations can be reduced to simpler global expressions for averaged variables. One of the key approximations made in engineering heat radiation calculations is that the gas temperature and composition are uniform over the finite physical space, and so is the gas absorption coefficient.

A common approach to engineering calculation of gas radiation (Siegel and Howell, 1981, p. 439) is to treat it by analogy to radiative interchange between surfaces without intervening media, by introducing the concept of absorptance, emittance and transmittance of a gas volume. The first two are analogous to the emissivity and absorptivity of opaque bodies, and they are defined only for volumes of gases of uniform temperature and composition. These quantities depend not only on the temperature and composition, but also on volume size and shape.

The spectral absorptance of a volume is defined as the fraction of the energy within a solid angle $d\omega$ that is absorbed by the gas while traversing along the distance s:

$$\alpha_\lambda(s) = 1 - \exp(-a_\lambda s) \qquad (2\text{-}3)$$

The spectral transmittance is a quantity complementary to the absorptance. It is the fraction of the incident energy that passes through the gas volume.

$$\tau_\lambda(s) = 1 - \alpha_\lambda(s) \qquad (2\text{-}4)$$

Finally, the emittance of the gas volume is the ratio of the energy emitted in the direction s' by the conical volume of the solid angle $d\omega$ to the energy emitted into that direction by a blackbody at the same temperature.

$$\varepsilon_\lambda(s) = 1 - \exp(-a_\lambda s) \qquad (2\text{-}5)$$

The spectral emittance has the same value as the spectral absorptance. However, the total emittance, integrated over the whole spectrum, does not equal the total absorptance. The exception is the case of gray gas in which $a_\lambda = a$, i.e., the absorption coefficient is independent of wavelength.

The absorption coefficient a_λ in equation (2-2) is a function of wavelength of radiation. Its values can be predicted for gases using so-called narrow band models which describe the spectral distribution of radiation from individual molecules (similar to the kinetic theory of motion for gases). These models are discussed e.g. by Ludwig et. al. (1973) and Tien and Lee (1982). These models are exceedingly detailed and require enormous amounts of computing time. Much of the physics these models describe may be captured by wide-band models, which predict the individual peaks in the spectrum, but not the fine quantum mechanical details superposed on these peaks. Their relationship to the narrow band models is not unlike that of the continuum Navier-Stokes equations to the Liouville equation of kinetic theory. Wide band models are reviewed by Tiwari (1976), Edwards and Mennard (1964), Edwards and Balakrishan (1973) and Tien and Lee (1982).

In a wide band model one deals with each band separately. A total band absorptance is defined with respect to the blackbody intensity evaluated at the band central wavelength, i.e., as an integral of spectral absorptance over the whole band width of a single band:

$$\alpha_\mu(s) = \int[1 - \exp(-a_\lambda(\lambda)s]d\lambda \qquad (2\text{-}6)$$

where μ is a band index. The total gas radiation over the whole spectrum is then evaluated by summation over all the bands. Expressed in terms of total gas emittance for a volume of gas of uniform temperature and composition one can write

$$\varepsilon_g \sigma T_g^4 = \Sigma E_{\lambda b,\mu} \alpha_\mu(s) \qquad (2\text{-}7)$$

where the total emittance ε_g is defined as the ratio of the energy emitted by the gas volume in direction s', to the energy emitted into that direction by a blackbody at the same temperature. The total absorptance of the gas depends on the spectral distribution of the incident radiation emitted by a solid wall with temperature T_w, the total gas absorptance may be approximated by

$$\alpha_g = \varepsilon_g \, (T_g/T_w)^n \qquad (2\text{-}8)$$

where n is constant and equals 0.45 for H_2O and 0.65 for CO_2 (Edwards and Nelson, 1962).

The previous discussion has concerned a single gas component. However, in a mixture, overlapping of spectral lines and bands generally occurs. Therefore, a correction is required to find the gas emittance and absorptance. For a mixture of two constituent gases the emittance is given by

$$\varepsilon_g = \varepsilon_1 + \varepsilon_2 - \Delta\varepsilon \qquad (2\text{-}9)$$

where the last term on the right is defined as the overlap correction

$$\Delta\varepsilon = \int_0^\infty E_{\lambda b}(1-\exp(-a_{\lambda 1}s))(1-\exp(-a_{\lambda 2}s))d\lambda/\sigma T_g^4 \qquad (2\text{-}10)$$

The overlap correction for the gas absorptance, $\Delta\alpha$, can be found in a way similar as for the emittance.

The specific wide band approximation to gas radiation used here, is based on the model proposed by Edwards and Balakrishnan (1973).

Radiation from soot depends on its spatial distribution, particle sizes and their refractive indices. For the small sizes encountered in diesel combustion an approximation known as the Rayleigh limit applies. This approximation simplifies the computation considerably over the far field solutions to the Maxwell equations as obtained by Mie; these are discussed by van de Hulst (1957) and Dalzell and Sarofim (1969). From the Mie theory (van de Hulst, 1957), the absorption coefficient can be written

$$a_{\lambda s} = \frac{36\pi f_v}{\lambda} \frac{nk}{(n^2-k^2+2)^2 + (2nk)^2} = \frac{f_v}{\lambda} g(n,k) \qquad (2\text{-}11)$$

where f_v is the volume fraction of soot in the gas and n and k are the refraction and absorption index, respectively, both of which are functions of the particular fuel properties and of λ. Based on experimental data Hottel (1954, p. 100) shows that the spectral distribution of $a_{\lambda s}$ is broad band with a shape

$$a_{\lambda s} \sim f_v/\lambda^m \qquad (2\text{-}12)$$

where m is close to unity in the infrared region and approaching 1.4 in the visible range. This suggests that the function g(n,k) in equation (2-11) is approximately independent of the wavelength.

For a volume with uniform temperature and composition, one can calculate spectral emittance of soot for a layer of thickness L from

$$\varepsilon_{\lambda s} = 1 - \exp(-a_{\lambda s} L) \tag{2-13}$$

Assuming that g(n,k) is indeed independent of wavelength, and substituting equation (2-11) into (2-12), and integrating over the entire wavelength space, the total soot emittance can be expressed as (Yuen and Tien, 1977)

$$\varepsilon_s = 1 + 15/\pi^4 \, \Psi^{(3)}(1 + f_v g T/C_2 L) \tag{2-14}$$

where $\Psi^{(3)}$ is the pentagamma function, x is path length, and C_2 is a constant in Planck's spectral energy distribution.

Close approximations to the above equation are expressions

$$\varepsilon_s = 1 - \exp\,(-3.6\, f_v g T/C_2 L) \tag{2-15}$$

and

$$\varepsilon_s = 1 - 1/(1+f_v g T/C_2 L)^4 \tag{2-16}$$

Experimental data (Gray and Mueller, 1974, p. 69) show that the function g has values that depend on the fuel hydrogen-to-carbon ratio. For oil flames

$$g \approx 6.3 \tag{2-17}$$

For further discussion of soot models see e.g. Sarofim and Hottel (1978), Dalzell and Sarofim (1969), Yuen and Tien (1977), and Tien and Lee (1982).

When the soot is present in a radiating gas, the total emittance of the mixture can be treated in the same way as for a mixture of gases. The same type of overlap correction is required as discussed in the context of a mixture of gases, although since gas radiation is quite small under diesel engine conditions, this correction is of minor importance.

B. Mean Beam Length Model

This is the simplest model for representation of radiation heat transfer within an enclosure filled with radiating gas and it was used in this study only as a stepping stone to the zonal model. The main assumption is that the gas has uniform temperature and composition throughout the enclosure, although it can be non-gray (a_λ can be a function of wavelength). Walls are assumed to be diffuse (reflectance independent of direction) with uniform temperature. Scattering in the gas is considered negligible. Emission and reflection from the boundaries are neglected (walls are assumed to be cool relative to the gas).

Digressing for the moment from the mean beam length model, one can develop useful relationships relevant to the problem. If the gas has a uniform temperature T_g and a uniform spectral absorption coefficient, equation (2-2) can be integrated to produce the radiation intensity incident on surface k

$$i_{\lambda,j-k} = i_{\lambda o,j-k}\,\tau_\lambda(s) + i_{\lambda b,g}(T_g)\alpha_\lambda(s) \qquad (2\text{-}18)$$

where we define transmittance $\tau_\lambda(s) = \exp(-a_\lambda s)$ and absorptance $\alpha_\lambda(s) = 1 - \exp(-a_\lambda s)$, $i_{\lambda o,j-k}$ is a spectral intensity leaving dA_j, s is the total distance along direction s', and subscript j-k refers to the interchange between surfaces j and k. This physical situation is shown schematically in Figure (2-1).

The incoming energy on surface k can be written in a differential form as

$$dQ_{\lambda,j-k} = i_{\lambda,j-k} dA_k \cos\theta_k d\omega_k d\lambda \qquad (2\text{-}19)$$

where the solid angle is $d\omega_k = dA_j \cos\theta_j / s^2$. For a diffuse wall (surface reflectance is independent of direction) $dq_{\lambda o,j} = \pi i_{\lambda o,j} d\lambda$ and $E_{\lambda b,g} = \pi i_{\lambda b,g}$. Substituting these relations into equation (2-4) and integrating over the emitting and receiving surfaces, we obtain

$$dQ_{\lambda,j-k} = \int_{A_k} \int_{A_j} [\tau_\lambda(s) dq_{\lambda o,j} + \alpha_\lambda(s) E_{\lambda b,g}(T_g) d\lambda] \cos\theta_k \cos\theta_j / \pi s^2 \, dA_j dA_k \tag{2-20}$$

Since the wall temperature is uniform, the emissive power $dq_{\lambda o,j}$ is also uniform; similarly since T_g is uniform, so is $E_{\lambda b,g}$. Thus, these two quantities can be pulled out of the integral in equation (2-20) and one can define a geometric-mean transmittance and absorptance, respectively:

$$\bar{\tau}_{\lambda,j-k} = \frac{1}{F_{j-k} A_j} \int_{A_k} \int_{A_j} \tau_\lambda(s) \cos\theta_k \cos\theta_j / \pi s^2 \, dA_j dA_k \tag{2-21a}$$

$$\bar{\alpha}_{\lambda,j-k} = \frac{1}{F_{j-k} A_j} \int_{A_k} \int_{A_j} \alpha_\lambda(s) \cos\theta_k \cos\theta_j / \pi s^2 \, dA_j dA_k \tag{2-21b}$$

where F_{j-k} is the viewing factor between surfaces j and k, defined as

$$F_{j-k} = \frac{1}{A_j} \int_{A_k} \int_{A_j} \cos\theta_k \cos\theta_j / \pi s^2 dA_j dA_k \tag{2-22}$$

Then equation (2-20) may be written as

$$dQ_{\lambda,j-k} = A_j F_{j-k} (\bar{\tau}_{\lambda,j-k} dq_{\lambda o,j} + \bar{\alpha}_{\lambda,j-k} E_{\lambda b,g}(T_g) d\lambda) \tag{2-23}$$

It should be noted that the transmittance and absorptance are complementary, i.e.,

$$\bar{\tau}_{\lambda,j-k} = 1 - \bar{\alpha}_{\lambda,j-k}$$

The mean beam length model is used to determine the energy radiated from a uniform gas volume to all or part of the volume boundaries, and as already mentioned, the emission and reflection from the walls are neglected. Under these conditions equation (2-23) reduces to

$$dQ_{\lambda,j-k} = A_j F_{j-k} \bar{\alpha}_{\lambda,j-k} E_{\lambda b,g}(T_g) d\lambda \tag{2-24}$$

The geometric-mean absorptance can be expressed as

$$\bar{\alpha}_{\lambda,j-k} = 1 - \exp(-a_\lambda L_{m,j-k}) \tag{2-25}$$

This expression defines L_m as a characteristic length referred to as mean beam length (Hottel and Sarofim, 1967). Substituting (2-25) into (2-24) and integrating over the wavelength one obtains

$$Q_{j-k} = A_j F_{j-k} \int_o^\infty (1-\exp(-a_\lambda L_{m,j-k}))E_{\lambda b,g}\, d\lambda \tag{2-26}$$

If all mean-beam lengths are taken to be equal and related to the volume size and surface area (Siegel and Howell, 1981, p. 617)

$$L_{m,j-k} = L_m \sim 0.9\ (4V/A) \tag{2-27}$$

the radiant heat transfer can be summed over all surfaces, using the relation $\Sigma\Sigma A_j F_{j-k} = \Sigma A_j = A$ to yield

$$Q = A \int_o^\infty [1-\exp(-a_\lambda L_m)]E_{\lambda b,g}\, d\lambda \tag{2-28}$$

Substituting appropriate models for a_λ, the total heat transfer to the walls can be calculated.

The model was applied to calculation of radiation in a turbocharged Cummins NH series engine geometry operating at rated conditions (2100 rpm, overall equivalence ratio Φ=0.5). The radiation model was coupled to a simple thermodynamic cycle simulation. This code has a single-zone combustion model (i.e., uniform gas temperature and composition). The soot volume fraction, used in equation (2-15), was estimated by the following expression

$$f_v = (B_1 m_f + B_2 \dot{m}_{fi}/\omega)/\rho_s V \tag{2-29}$$

where m_f = total mass of fuel in cylinder, m_{fi} = mass burning rate, ω = engine frequency, ρ_s = soot density, and V = cylinder volume. Choosing $B_1 = 10^{-3}$ resulted in $f_v = 7.4 \times 10^{-6}$ at top dead center and $f_v = 4.2 \times 10^{-8}$ at the end of expansion. These numbers are the same order of magnitude found in combustion and exhaust sampling experiments reported in the literature (Sarofim and Hottel, 1978; Sato et al., 1969).

Results obtained are shown in Figure (2-2) for a cooled engine with low wall temperatures. For comparison purposes only, the figure includes also the convective heat transfer predicted using a correlation due to Woschni (1967). The results show that during the combustion the radiation amounts to about 8 percent of the convection. It should be realized, that the simple cycle code used here had a single zone combustion model, which gave much too low radiation temperatures. If the correct radiation temperatures were used, the predicted heat radiation rates would have been several times larger.

Although the mean-beam length method does not include wall heat emission, a simple approximate method exists to include this effect (Siegel and Howell, 1981, p. 626). This approximate method is applicable when the enclosure walls are black. Taking a heat balance on the gas, one observes that the heat flux removed from the gas volume equals the gas emission to the wall, minus the emission from the wall absorbed by the gas, i.e.,

$$Q = A\sigma \left[\varepsilon_g T_g^4 - \alpha_g(T_w) T_w^4\right] \qquad (2\text{-}30)$$

The absorptance α_g depends on T_w, as the wall temperature determines the spectral distribution of the radiation received by the gas.

Incorporating this treatment of wall emission, calculation was made of the area-integrated heat radiation from the gas to the wall for an insulated engine with hot walls. All walls were assumed to be at 1200K and the previous calculation was repeated (Figure 2-3). The heat convection

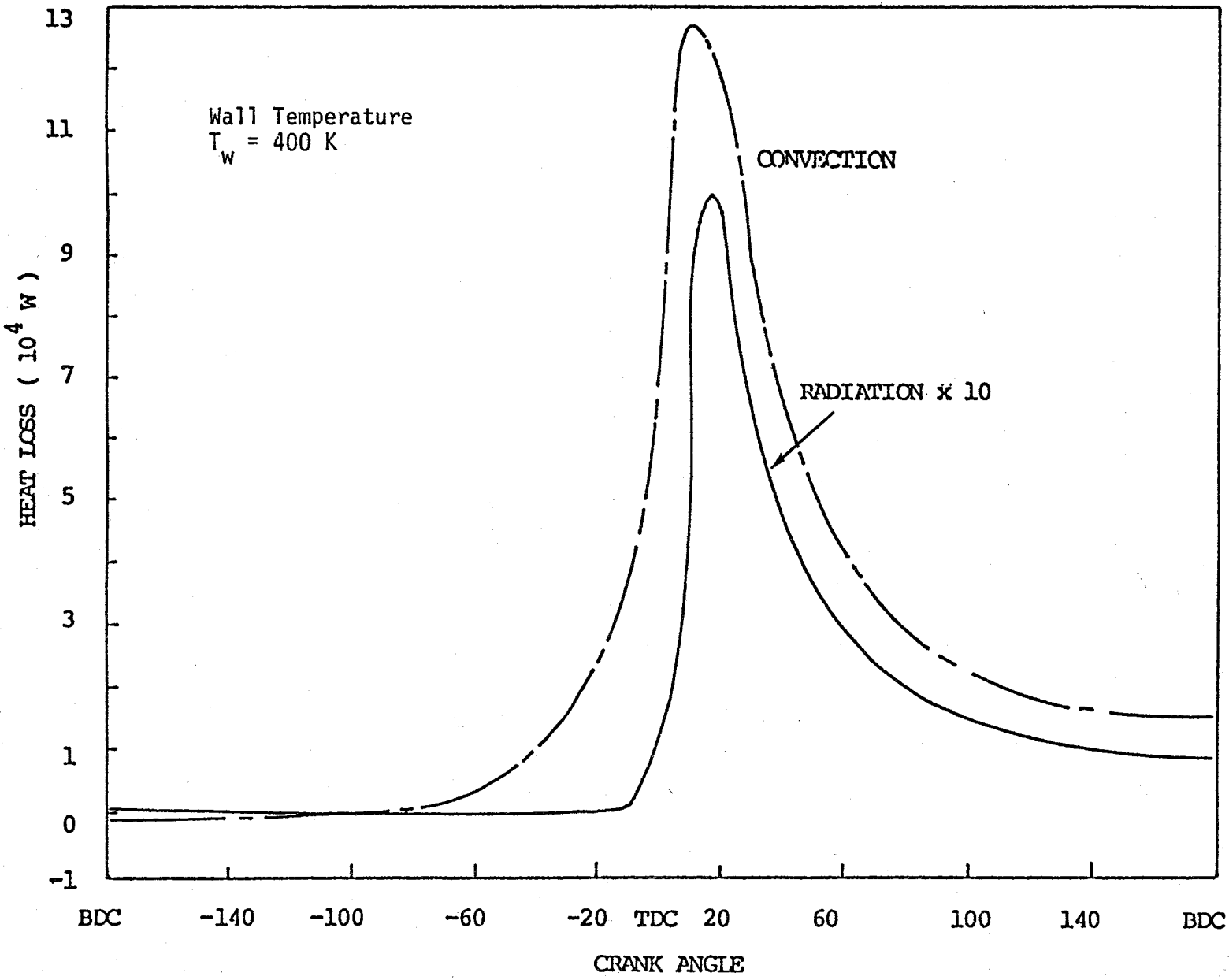

Figure 2-2. Radiation heat transfer calculated using radiation temperatures produced by a single zone combustion model, in comparison with convection, as a function of crank angle. Wall temperature T_w=400^{0}K.

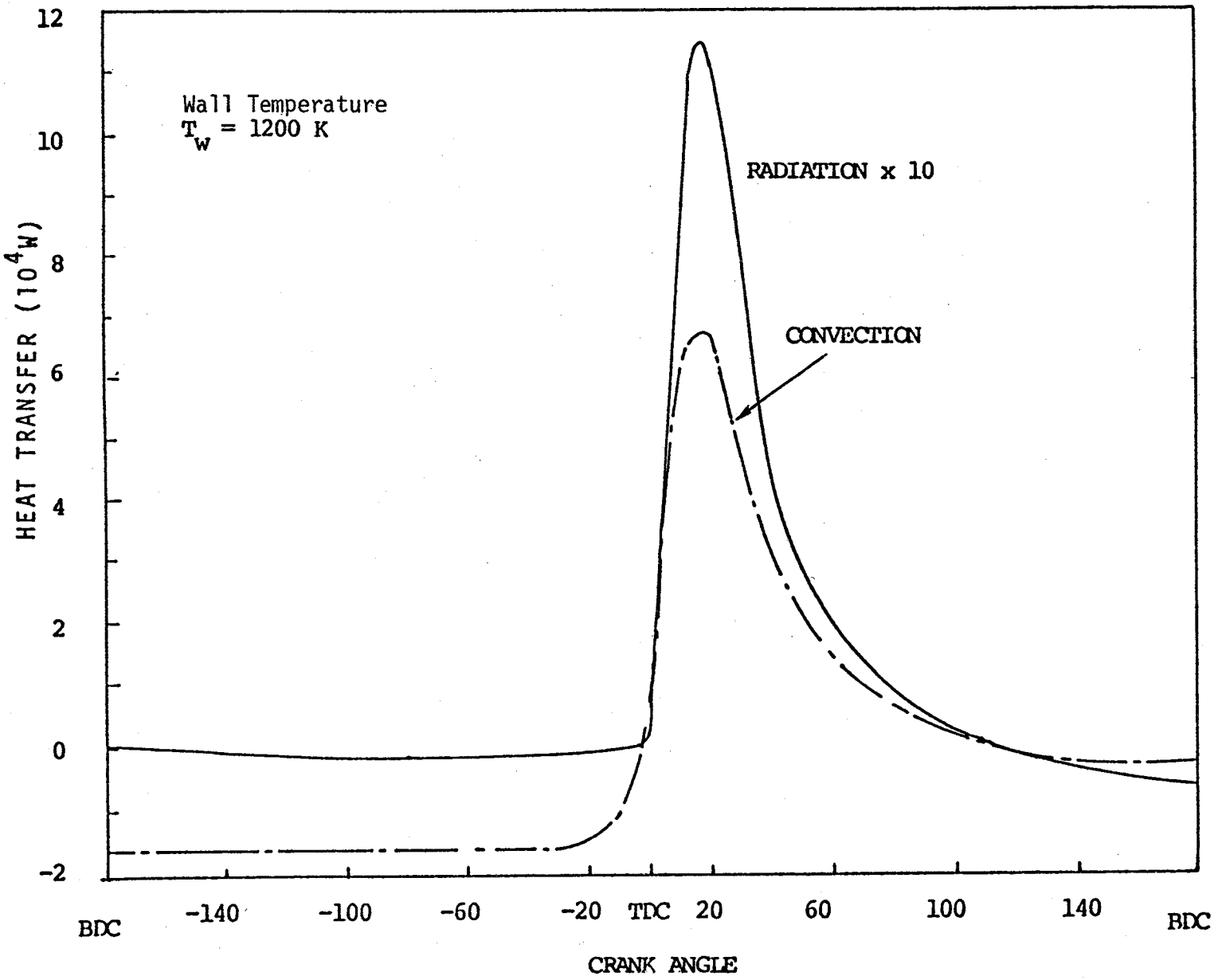

Figure 2-3. Radiation heat transfer in comparison with convection as a function of crank angle.

is seen to be substantially lower than before, as would be expected on account of the high wall temperature. In fact, the convection heat transfer is negative during the compression stroke. The radiation heat transfer is increased, because the relatively small increase in gas temperature easily outweighs the wall emission due to the fourth power dependence on temperature. Here again, the comment may be made that the radiation heat transfer would have been higher if a two-zone or multi-zone combustion model had been employed.

C. Zonal Method

The method that will be ultimately used for the heat radiation calculation is the zonal method. The particular method employed here is an extension of the zonal method developed by Hottel and Cohen (1958). The method consists of subdividing the enclosure, filled with radiating gas of spatially varying temperature and composition, into smaller areas and volumes (zones) that can be considered to be of uniform temperature.

The development of the approximate equations is similar to that used in the previous section, equations (2-18) to (2-23). The major differences are:

1) the gas to wall radiation is treated by integration over elementary gas volumes;
2) the total transmittance and absorptance are lumped into so-called direct exchange areas;
3) gas is assumed to be gray.

The energy arriving to surface A_k from surface A_j is thus written as

$$Q_{j-k} = q_{o,j}\,\overline{s_j s_k} \tag{2-31}$$

where

$$\overline{s_j s_k} \equiv \int_{A_k}\int_{A_j} \exp(-\int a\,ds)\,\cos\theta_j \cos\theta_k / \pi s^2\, dA_j\, dA_k \tag{2-32}$$

is the "surface-surface direct exchange area". The energy arriving to the same surface from a finite gas volume V_n that has uniform gas

temperature and absorption coefficient is written as

$$Q_{n-k} = \sigma T_n^4 \overline{g_n s_k} \tag{2-33}$$

where

$$\overline{g_n s_k} \equiv a \int_{V_n} \int_{A_k} \exp(-\int a ds) \cos\theta_k / \pi s^2 \, dA_k dV_n \tag{2-34}$$

is the "gas-surface direct exchange area."

Summing the contributions to the heat transfer to the surface A_k from J enclosure surfaces and N finite gas volumes

$$Q_k = \sum^{J} q_{o,j} \overline{s_j s_k} + \sum^{N} \sigma T_n^4 \overline{g_n s_k} \tag{2-35}$$

To calculate radiation heat transfer from equation (2-35), equations (2-32) and 2-34) have to be integrated. To this end consider the gas and the walls to be divided axially, radially, and azimuthally into the finite zones as shown by solid lines in Figure (2-4). Each zone can then be discretized into smaller divisions denoted by broken lines in Figure (2-4); as the number of divisions approaches infinity, the divisions become differential in nature. Equations (2-32) and (2-34) may be written in a discretized form (Voelkel, 1983), in which the integrals are replaced by sums over individual divisions of the finite zones. If the wall is black and thermodynamic equilibrium occurs in an enclosure, a summation rule is derived (Noble, 1975):

$$A_k = \sum^{J} \overline{s_j s_k} + \sum^{N} \overline{g_n s_k} \tag{2-36}$$

which is a useful tool to check the accuracy of numerical integration.

First calculations made with the zonal model concerned the effect of a nonuniform wall and gas temperature on the radiation heat transfer. The results are shown in Table 2-1, where F(s) and f(r) represent the temperature distribution at the wall and the gas, respectively, for several different test cases. All cases have the same volume-averaged and surface-averaged temperatures as the baseline case with uniform wall

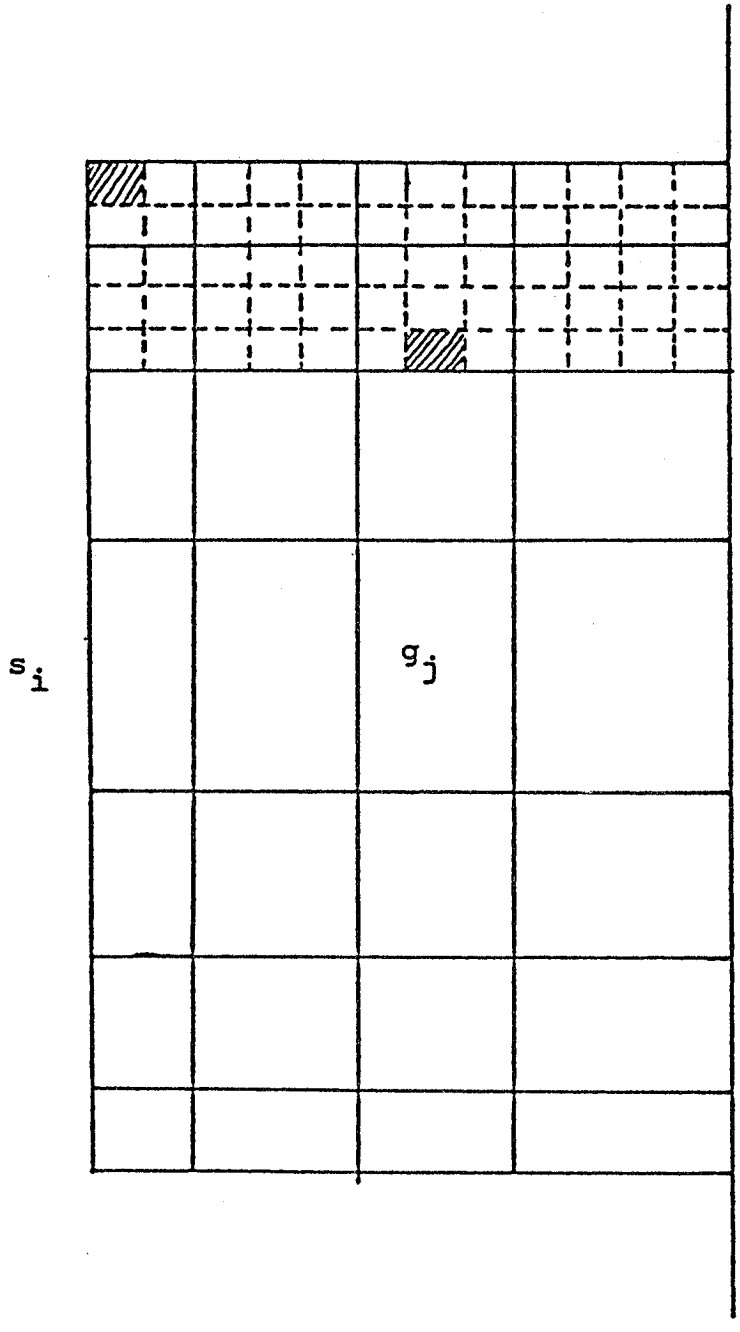

Figure 2-4. Side View of Cylinder Showing Divisions of Gas and Wall Zones

Table 2-1

The effect of nonuniform temperature distribution on radiation heat transfer

Bore=0.14 m, head-to-piston distance=0.14 m, absorption coefficient a=0.75.

	Tg(K)	Tw(K)	Heat Transfer(W)	deviation (%)
A	2000	817	5501	0.0
B	2000	1000,800,700	5491	0.1
C	2000	F(s)	5466	0.7
D	f(r)	817	4469	18.8

F(s): 1165, 1076, 993, 916, 846, 764, 890, 1000, 747, 717, 593, 642, 695, 753, 815.

f(r): 2456, 2150, 1985, 1883, 1693

and gas temperatures. Results obtained are for the same Cummins engine operating conditions as before. The combustion chamber geometry is pancake-shaped fixed at one given crank angle. The effect of a non-uniform wall temperature on the radiative transfer is found to be negligible (the heat losses in cases B and C deviate less than one percent from the baseline case A). However, the effect of a non-uniform gas temperature (case D) on the radiation heat transfer is significant as shown in Table 2-1. The results indicate that proper gas temperatures must be used rather than a mean value.

D. Effect of Scattering By Fuel Droplets

In the above models, the two terms representing the scattering process have been neglected in the equation of transfer (equation 2-1). However, fuel droplets and liquid particulates condensed from heavy molecules during combustion will no doubt scatter radiation to some degree. This in effect increases the path length of photons trying to reach the walls and thereby increases the probability that they will be absorbed by the gas or the soot. To quantify the significance of this effect requires the solution of the full radiative transfer equation. In this section, we will discuss the solution of the complete equation of transfer accounting for scattering in the medium carried out to investigate the effects of scattering due to fuel droplets present in a typical diesel engine environment. The P_3-spherical harmonic approximation (Krook, 1955; Davison, 1957) was used to predict the effect of scattering. In this model, inhomogeneity of the radiative properties of medium as well as of the radiation characteristics of the boundaries are allowed for, and the boundaries are assumed to be diffusely emitting and reflecting. The scattering phase function is represented by the delta-Eddington approximation (Joseph et al., 1976). The mathematical formulation of the method will not be presented here as general discussions are available elsewhere (Davison, 1957; Menguc and Viskanta, 1984a and b). All the results presented were generated using a computer code written originally by Menguc and Viskanta for furnace calculations (1984b).

The simulation was carried out in an axisymmetric pancake geometry meant to approximate a diesel combustion chamber at a fixed crank angle position. The physical situation examined is shown in Figure 2-5. An axisymmetric cylindrical flow field was divided into two zones: a core region containing soot and fuel droplets, and an outer region where the radiation is due to the residual gas. The core is assumed to be at 2200 K and the outer region at 1100 K. The optical depth in the core was chosen to be consistent with values reported in the literature. Droplet concentrations were computed assuming a core equivalence ratio of $\phi = 1.0$, but with only one quarter of the fuel still in liquid form. The data used to calculate the number of the fuel droplets are assumed to be as follows: density of fuel $\rho = 850$ kg/m^3, diameter of the droplets $D = 6 - 25$ μm, number density $N_D = 3.25 \times 10^{12}$ part./m^3 ($D = 6$ μm) and $N_D = 4.49 \times 10^{10}$ part./m^3 ($D = 25$ μm).

Figure (2-6) shows the effect of the single scattering albedo on radiative heat flux at the piston and the cylinder head. (A single scattering albedo model assumes that radiation scattered off an individual droplet travels to the surrounding surfaces without further encounters with the scattering medium). The results in Figure (2-6) are for the radiation heat flux at two of the bounding walls and for three different values of the single scattering albedos. It should be noted that the values of the scattering albedo ω based on fuel droplet diameter $D = 25$ μm and $D = 6$ μm are $\omega = 0.1$ and 0.38, respectively. The case with $\omega = o$ corresponds to no scattering.

The conclusion one can draw is that scattering by fuel droplets reduces the heat transfer to the walls by a small amount. This is due to the more tortuous path the scattered photons have to follow, which increases the probability of absorption in the sooting medium. The droplet scattering radiation model used for this assessment does not include a solution of the energy equation, which would predict a change in the medium temperature due to the heat radiation to the walls. In the scattering case the medium would have a higher temperature than when $\omega=o$, somewhat reducing the calculated differences in the radiation flux

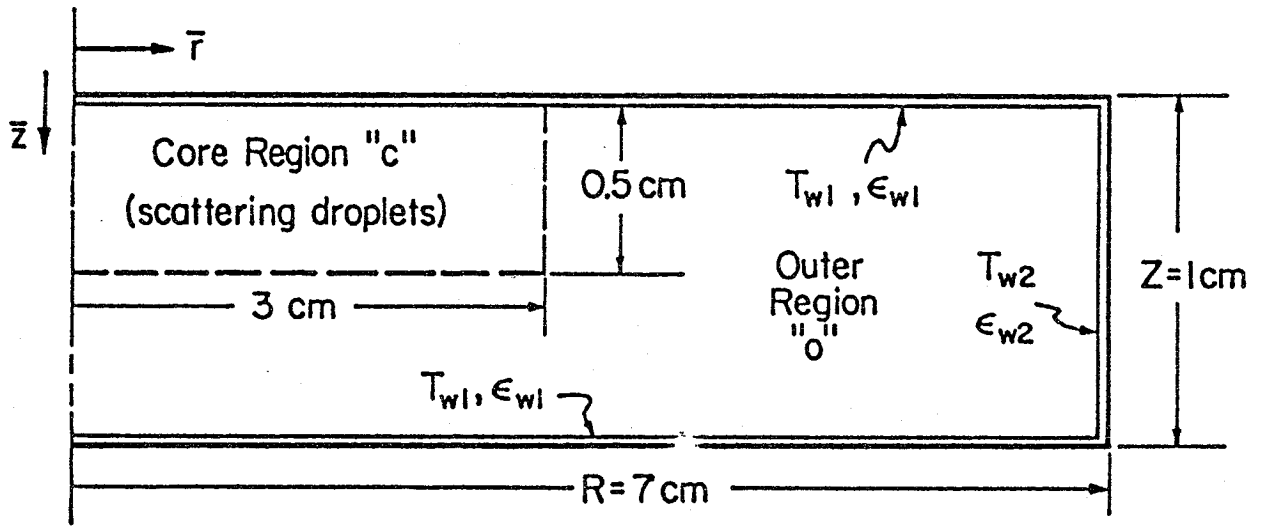

Figure 2-5. Physical model and coordinate system; k_c= 470 m^{-1}, T_c= 2200K, k_o=25 m^{-1}, T_o= 1100K, T_{w1}= 500K, T_{w2}= 450K, ϵ_{w1}= 1.0, ϵ_{w2}=0.8.

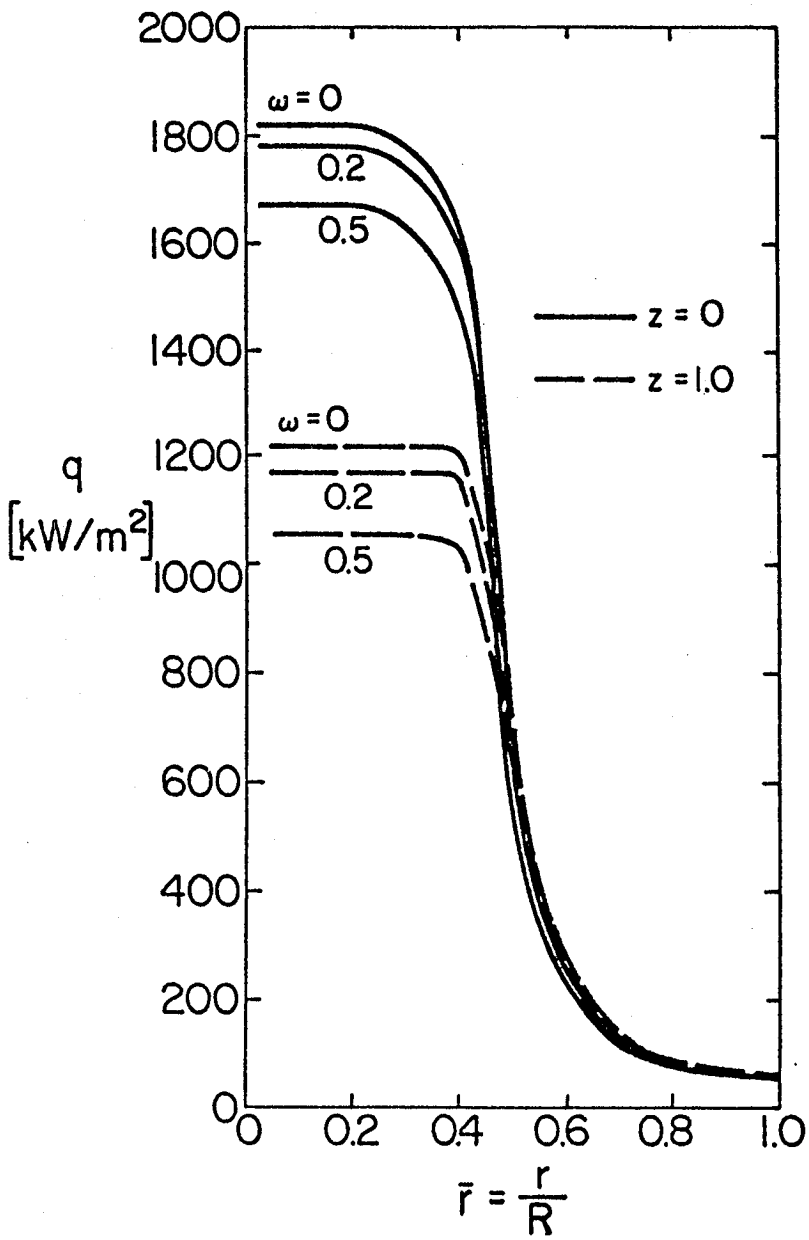

Figure 2-6. Effect of single scattering albedo on piston and end surface radiative flux

impacting the walls caused by the presence of the droplets. Even with this simplification, which amplifies the effect of scattering, the model predicts a decrease of radiation intensity by at most 10% for realistic levels of droplet concentrations. Our conclusion from this study is that the effect of scattering by fuel droplets is negligible, especially in view of other uncertainties in radiation modeling. Having resolved this issue, we are now continuing the modeling work along the originally planned lines.

E. Simple Quasi-Dimensional Radiation Model

While the work is progressing on the zonal model, a simple quasi-dimensional model is being used to represent the heat radiation in the calculations presented in this report. The model is akin to the mean beam length model discussed above. It assumes that only soot-to-wall radiation is important, and neglects gas radiation and wall-to-wall radiation, both of which are known to be much smaller than soot radiation.

The radiation received by a surface k is calculated from a gray model

$$Q_k = A_k \sigma \varepsilon_w \varepsilon_s \, (T_r^4 - T_w^4) \tag{2-37}$$

where ε_w is wall emissivity, T_r is radiation temperature defined below and ε_s is soot emissivity defined by equation (2-15) where we take $g = 6.3$, i.e.

$$\varepsilon_s = 1 - \exp\,(-1575\, f_v T_r L_m)$$

or

$$\varepsilon_s = 1 - \exp[-1575\, (f_m/\rho_s)\rho T_r L_m] \tag{2-38}$$

where f_m is soot mass fraction in the gas, ρ_s is soot density and ρ is gas density.

In order to account for variations of mean beam lengths (and therefore

attenuation of emissivity) from surface to surface, ITI's simple radiation model uses the following approximating expressions for mean beam lengths pertaining to the various surfaces:

$$
\begin{aligned}
L &= s + h_{cup} && \text{for cup base} \\
&= d_{cup} && \text{for cup wall} \\
&= \text{bore} && \text{for liner} \\
&= s + 1/2\ h_{cup} && \text{for head}
\end{aligned}
$$

where s is instantaneous distance of piston crown from head, h_{cup} is cup depth, and d_{cup} is cup diameter.

The radiating soot temperature to be used has always been an issue in engine radiation modeling, because it is difficult to predict. Previous investigations used for example the mean gas temperature (recognized now to be much too low) and adiabatic flame temperature. In the ITI model T_{rad} is calculated from the burned zone temperature according to the following definition:

$$T_{rad} = r_b^2\ T_b + (1-r_b^2) T_{b,max} \qquad (2\text{-}39)$$

where $r_b = (m_b/m_u)^2$, where T_b is burned zone temperature, Tb_{max} is peak of burn zone temperature, m_b is burned mass and m_u is unburned mass. This particular form of the radiation temperature was adopted in order to reflect the fact that the effective soot radiating temperature is dominated by the actively burning flame front, whose temperature is higher than the average of the burned zone (which includes actively burning species as well as burned-out products). Better radiating temperature prediction could probably be obtained from a more detailed burned zone model tracking 3 or more zones during combustion.

The volume soot concentration f_v, needed in equation (2-38) as a function of equivalence ratio and crank angle, was deduced from experimental data. In this work we used the data of Sitkei and Ramanaiah (1972), who

measured radiation in a prechamber diesel engine over a range of engine loads. Based on measured apparent emissivities (resolved as a function of crank angle) whose maxima were on the order of 0.3 to 0.4, they deduced an extinction factor k from the equation

$$\varepsilon = \varepsilon_w (1-\exp(-kp\ell)) \qquad (2\text{-}40)$$

where they used engine pressure in atmospheres and ℓ defined as 3.6 V/A in meters, where V is the cylinder volume and A is cylinder surface area. From this calculation they obtained a plot of k as a function of crank angle and excess air ratio α, which is the inverse of the overall equivalence ratio Φ (Figure 2-7).

Comparing equations (2-38) and (2-40) one finds

$$f_m/\rho_s = 0.63 \times 10^{-8} (p/\rho T_r)\ell/L_m k$$

This expression was used to deduce the peak values of (f_m/ρ_s) from the data of Sitkei and Ramanaiah. Assuming that near the peak the radiation temperature is close to the burned zone temperature, and L_m is about one-half of ℓ one obtains

$$(f_m/\rho_s)_{peak} = 0.37 \times 10^{-5} \; k$$

Using this relation one obtains from Figure 2-7 a correlation for the peak soot concentration as a function of the equivalence ratio (Figure 2-8).

As for the variation of the soot concentration with respect to crank angle, we used experimental evidence for instantaneous soot concentrations as a guide, replacing the shapes deduced by Sitkei and Ramanaiah. The soot concentration is known to begin building up once the combustion starts (especially during the diffusion-controlled portion of combustion), reach a peak somewhere near midpoint of combustion and then gradually decrease due to soot oxidation down to the level found in the exhaust gas. The function chosen to describe this expected behavior is

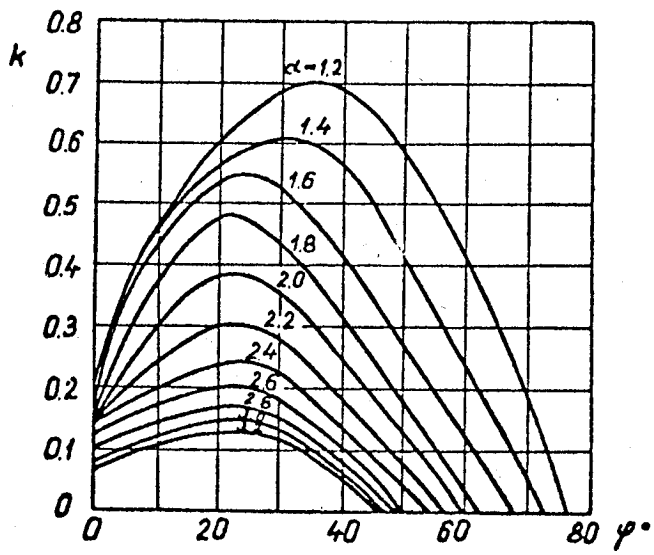

Figure 2-7. Absorption factor versus crank angle at different excess air factors.

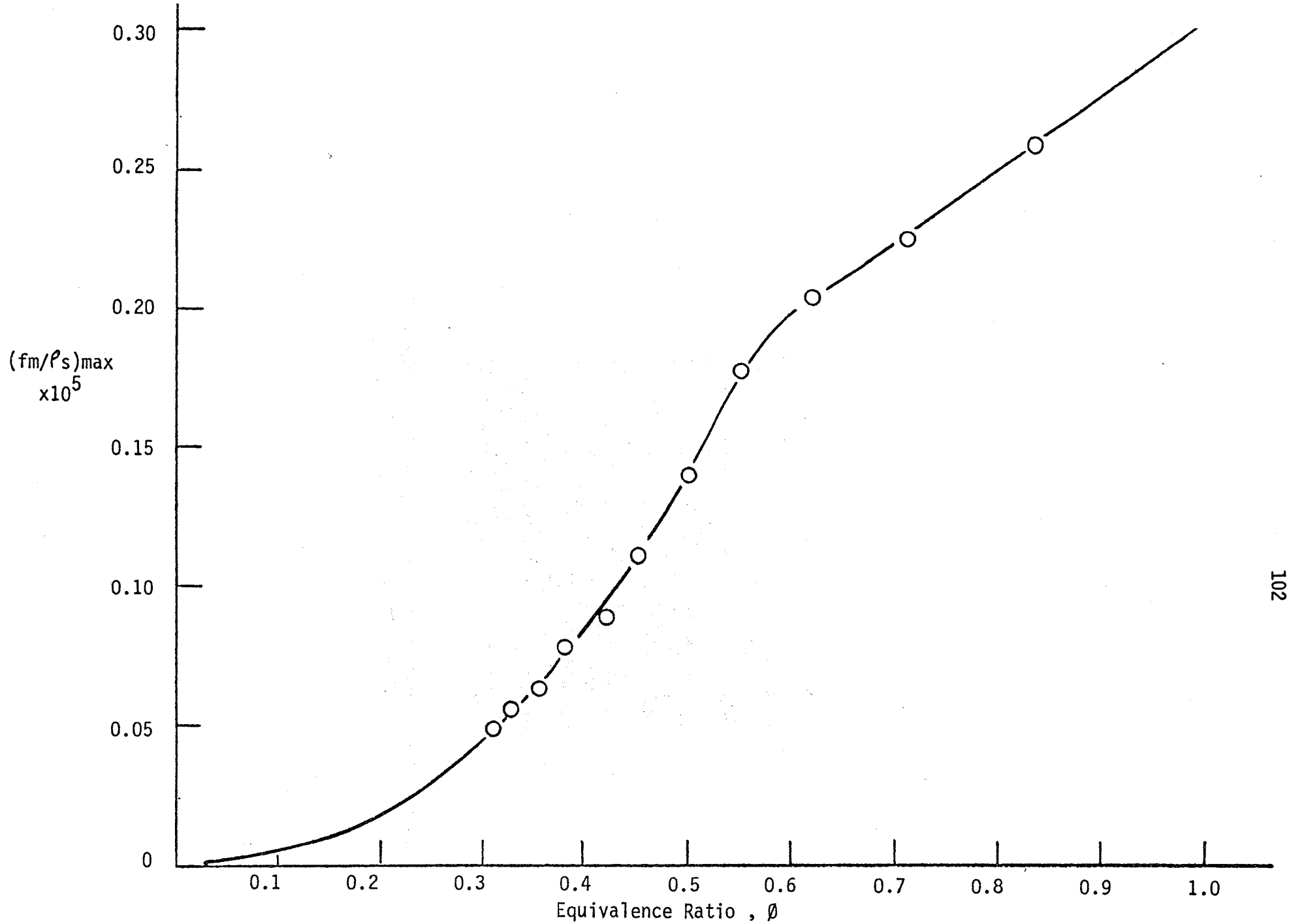

Figure 2-8. Maxima of the soot concentration parameter derived from data of Sitkei and Ramanaiah.

a cubic peaking around the 40 percent point of the combustion period and decreasing to 20 percent of the peak at the end of combustion (Figure 2-9).

This radiation model has built into it several features that go beyond the current models in state-of-the-art cycle simulations. It uses radiation temperature which is much more realistic than the mean gas temperature used by others; it has a simplified mean beam length model representing the geometrical characteristics of the chamber and their effects on the radiation flux to the six elementary cycle model surfaces; and the normalized soot concentration correlation is a synthesis of quantitative results and qualitative observations reported in the literature.

The current form of the extinction coefficient correlation is an interim one. It will be further developed based on an extensive literature survey of soot concentration and heat radiation data currently underway. Eventually, this model will be merged with the more comprehensive zonal radiation model that is currently under development at Purdue University.

References

Chang, S. L. and Rhee, K. T. (1983), "Computation of Radiation Heat Transfer in Diesel Combustion," SAE Paper 831332.

Chapman, M., Friedman, M. C., and Aghan A. (1983), "A Time-Dependent Spatial Model for Radiant Heat Transfer in Diesel Engines," SAE Paper 831725.

Dalzell, W. H. and Sarofim, A. F. (1969), "Optical Constants of Soot and Their Application to Heatflux Calculations," J. Heat Transfer, Vol. 91, no. 1, pp. 100-104.

Davison, B. (1958), Neutron Transport Theory, Clarendon Press, Oxford.

Dunkle, R. V. (1964), "Geometric Mean Beam Lengths for Radiant Heat Transfer Calculations," J. Heat Transfer, Vol. 86, No. 1, pp. 75-80.

Edwards, D. K. and Balakrishnan A. (1973), "Thermal Radiation by Combustion Gases," Int. Heat Mass Transfer, Vol. 16, pp. 25-40.

Edwards, D. K. and Menard, W. A. (1964), "Comparison of Models for Correlation of Total Band Absorption," Appl. Opt., Vol. 3, no. 5, pp. 621-625.

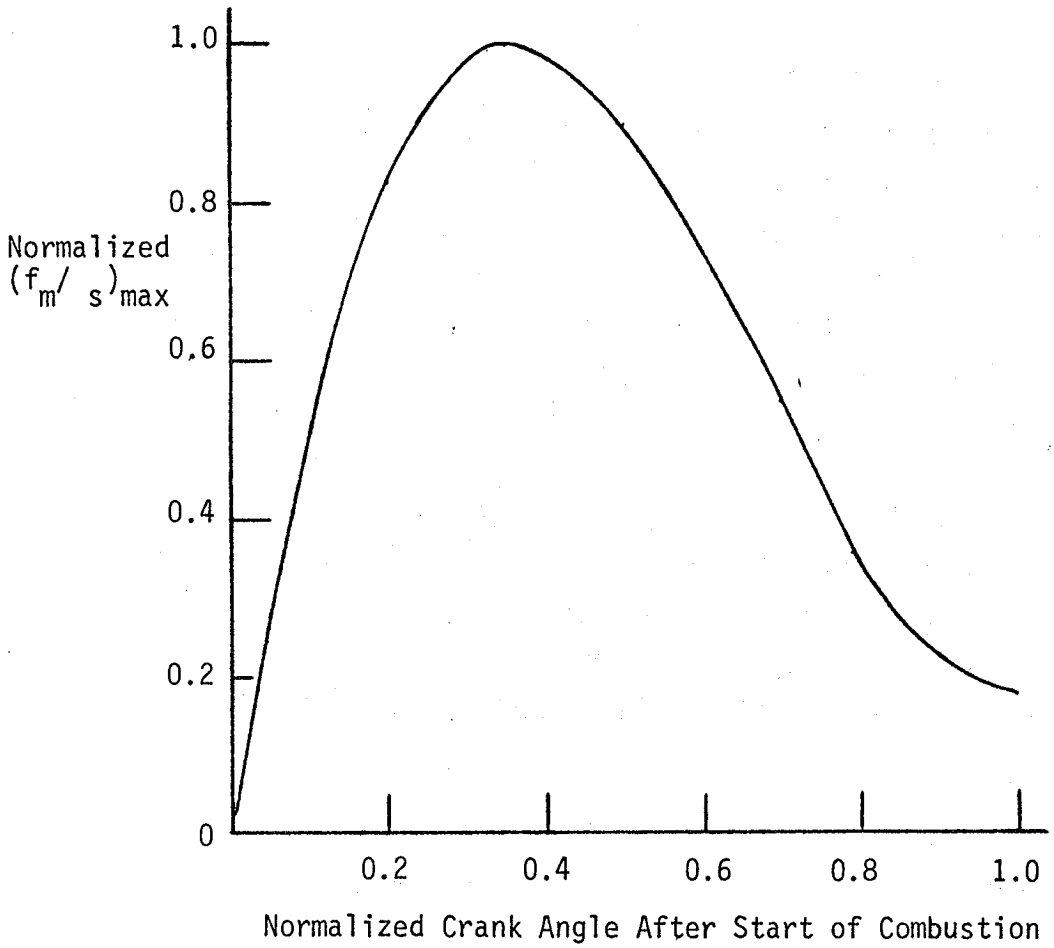

Figure 2-9. Soot concentration parameter normalized with its maximum value, plotted against normalized combustion duration.

Edwards, D. K. and Nelson, K. E. (1962), "Rapid Calculation of Radiant Energy Transfer between Nongray Walls and Isothermal H2O or CO2 Gas," Journal of Heat Transfer, Vol. 84, pp. 273-278.

Einstein, T. H. (1963), "Radiant Heat Transfer to Absorbing Gases Enclosed in a Circular Pipe With Conduction, Gas Flow, and Internal Heat Generation," NASA TR R-156.

Felske, J. D. and Tien, C. L. (1974), "Infrared Radiation from Non-homogeneous Gas Mixtures Having Overlapping Bands," J. Quant. Spectrosc. Radiat. Transfer, Vol. 14, pp. 35-48.

Fiveland, W. A. (1982), "A Discrete Ordinates Method for Predicting Radiative Heat Transfer in Axisymmetric Enclosures," ASME Paper 82-HT-20.

Gray, W. A. and Mueller, R. (1974), "Engineering Calculations in Heat Transfer," Pergaman Press.

Grosshandler, W. L. (1980), "Radiative Heat Transfer in Nonhomogeneous Gases: A Simplified Approach," Int. J. Heat Mass Transfer, Vol. 23, pp. 1447-1459.

Hottel, H. C. (1954), "Radiant-Heat Transmission," in Heat Transmission, Ed. W. M. McAdams, McGraw-Hill, Chapter 4, 1954.

Hottel, H. C. and Cohen, E. S. (1958), "Radiant Heat Exchange in a Gas-filled Enclosure: Allowance for Nonuniformity of Gas Temperature," AICHEJ., Vol. 4, no. 1, pp. 3-14.

Hottel, H. C. and Sarofim, A. F. (1967) Radiative Transfer, McGraw-Hill Book Company, New York.

Joseph, J. H., Wiscombe, W. J., and Weinman, J. A. (1976), "The Delta-Eddington Approximation for Radiative Heat Transfer," Journal of Atmospheric Sciences, Vol. 33, pp. 2452-2559.

Krook, M. (1955), "On the Solution of Equation of Transfer. I," Astrophys. J., Vol. 122, pp. 448-497.

Ludwig, C. B., Malkmus, W., Reardon, J. E., and Thomson, J. A. L. (1973), "Handbook of Infrared Radiation from Combustion Gases," NASA SP-3080.

Menguc, M. P. and Viskanta, R. (1984a), "Radiative Transfer in Three-dimensional Rectangular Enclosures," to be presented in 22nd ASME National Heat Transfer Conference, Niagara Falls, New York.

Menguc, M. P. and Viskanta, R. (1984b), "Radiative Transfer in Axisymmetric, Finite Cylindrical Enclosures," Submitted for ASME Annual Meeting, New Orleans, Louisiana.

Noble, J. J. (1975), "The Zone Method: Explicit Matrix Relations for Total Exchange Areas," Int. J. Heat Mass Transfer Vol. 18 pp. 261-269.

Sarofim, A. F. and Hottel, H. C. (1978), "Radiative Transfer in Combustion Chambers: Influence of Alternative Fuels," Sixth Int. Heat Transfer Conf., Toronto, Vol. 6, pp. 199-217.

Sato, T., Kunitomo, T., Yoshi, S. and Hashimoto, T. (1969), "On the Monochromatic Districution of the Radiation from the Luminous Flame," Bull. Jpn. Soc. Mech. Eng., Vol. 12, pp. 1135-1143.

Siegel, R. and Howell, J. R. (1981), Thermal Radiation Heat Transfer, 2nd Edition, McGraw-Hill Book Company, New York.

Sitkei, G. and Ramanaiah, G. V. "A Rational Approach for Calculation of Heat Transfer in Diesel Engines," SAE Paper 720027, 1972.

Smith, T. F., Kim, T. K., and Shen, Z. (1981), "Evaluation of Direct Exchange Areas for Cylindrical Enclosure," Technical Report E-TFS-81-007, Division of Energy Engineering, The University of Iowa, Iowa City.

Tien, C. L. and Lee, S. C. (1982), "Flame Radiation," Prog. Energy Combustion Science, 1982, Vol. 8, pp. 41-59.

Tiwari, S. N. (1976), "Band Models and Correlations for Infrared Radiation, in Radiative Transfer and Thermal Control," Vol. 49 of Progress in Astronautics and Aeronautics Series, pp. 155-182, AIAA.

Yuen, W. W. and Tien, C. L. (1977), "A Simple Calculation Scheme for the Luminous-Flame Emissivity," Sixteenth Symp. Int. Combustion, The Combustion Institute, pp. 1481-1487.

Van der Hulst, H. C. (1957), Light Scattering by Small Particles, John Wiley & Sons, Inc., New York.

Viskanta, R. (1984), "Radiative Heat Transfer," Fortschrifte der Verfahrenstechnik, Vol. 22, Section A, pp. 51-81.

Voelkel, D. D. (1983), "Model of Thermal Radiation Recuperator for Furnace Waste Heat Recovery," M. S. Thesis, Purdue University, Indiana.

III. ONE-DIMENSIONAL ANALYSIS OF FAST TEMPERATURE TRANSIENTS

Introduction

One of the complex features of engine heat transfer is the existence of temperature swings produced in the structure by the gas-wall heat transfer. As was shown in the previous chapter, the heat flux to the wall is highly transient with concentrated bursts of high heat flux followed by relatively long periods of low heat flux rates (Figure 1-24). This pattern produces temperature transients in thin layers adjacent to the combustion wall surfaces.

The fact that the surface temperature is not constant influences heat transfer rates, as heat transfer depends on the instantaneous difference between the gas and the wall temperatures. Another reason for interest in this problem is that temperature transients have an impact on thermal stresses in the engine structure and they can also contribute to material aging and fatigue. The maximum surface temperature obtained during the temperature swing also has impact on lubrication and wear of piston, ring and liner surfaces, which are in sliding contact.

The transient temperature wave, produced by the time-dependent boundary conditions at the gas-wall interface, propagates into the structure for only a limited distance, before being damped out by thermal inertia. The penetration distance is usually quite small, on the order of 1 mm. The temperature profile thus varies much more rapidly in the direction perpendicular to the surface than in directions parallel to it. Because of that, it is appropriate to describe the problem by a model which considers the temperature wave to be one-dimensional and perpendicular to the surface. This is the approach taken here, as well as that taken by others who considered the problem of wall temperature swings. For example, Bradish, et. al. (1966) solved the one-dimensional heat conduction equation numerically and used it to calculate the effects of wall deposits on heat transfer and wall temperatures. This work was extended by Shamah (1967) who used the numerical solution procedure to make some

predictions of the effects of temperature dynamics on engine performance. Wallace, et. al. (1979) used analytical methods (Fourier decomposition) to address the effects of different structure materials on the temperatures of an idealized surface and on engine performance. For simplicity, they limited their calculations to the fundamental frequency of the heat flux (i.e., once per two revolutions), but since the actual shape of the heat flux is very highly peaked, this must have resulted in a strong underestimation of the actual swing amplitude.

In the present work the problem is solved within the context of the whole engine: the solution of the one-dimensional equation is coupled to a detailed thermodynamic simulation of the engine and a model of the steady-state conduction through the structure. The approach to the one-dimensional model is comprehensive and it includes the following features:

- -- boundary conditions are obtained from realistic gas-wall heat transfer correlations based on advanced convection and radiation heat transfer models;
- -- mean wall temperatures are obtained from a geometrical model identifying specific surfaces;
- -- temperature-dependent material properties are included in the one-dimensional model formulation.

In addition, the code has been applied to a wide range of conditions and properties to produce plots of key parameters which elucidate the main features of the transient heat conduction problem.

Decomposition of Conduction Heat Transfer

Since the structure temperature cannot respond to the rapid cyclical heat flux transients and becomes steady-state a small distance below the surface, it would be quite pointless to try to solve the whole heat conduction as a multidimensional transient problem. Instead, it is expedient to decompose the problem into two parallel, interacting parts

-- one time-dependent and one steady-state. A further advantage of the decomposition is that only the steady-state part needs to be solved as multidimensional, while the transient part may be solved as one-dimensional.

A schematic of such a decomposition is shown in Figure (3-1). Essentially, the steady-state solution is calculated for the whole structure including the transient region, with an "apparent" steady-state temperature on the combustion chamber side. The transient solution is calculated only for the relatively thin transient region. The two solutions are then matched so that the heat fluxes calculated for both solutions are equal.

The heat conduction equation valid throughout the structure may be written as

$$\rho c \partial T/\partial t = \nabla \cdot (k \nabla T) \tag{3-1}$$

and is subject at the gas-wall interface to boundary conditions consisting of convective and radiative heat fluxes to the wall

$$- k \partial T/dn = h_g(T_g - T_w) + q_{rad} \tag{3-2}$$

The essence of the decomposition is to solve transient heat transfer using a one-dimensional version of equation (3-1) and the full boundary conditions (3-2), and separately obtain a steady-state solution for the structure from equation

$$\nabla \cdot (k \nabla T_{ss}) = 0 \tag{3-3}$$

subject to steady-state boundary conditions or the combustion chamber walls producing a steady-state heat flux that equals the time-average of the time unsteady heat flux. The manner in which the two solutions are coupled will be described below.

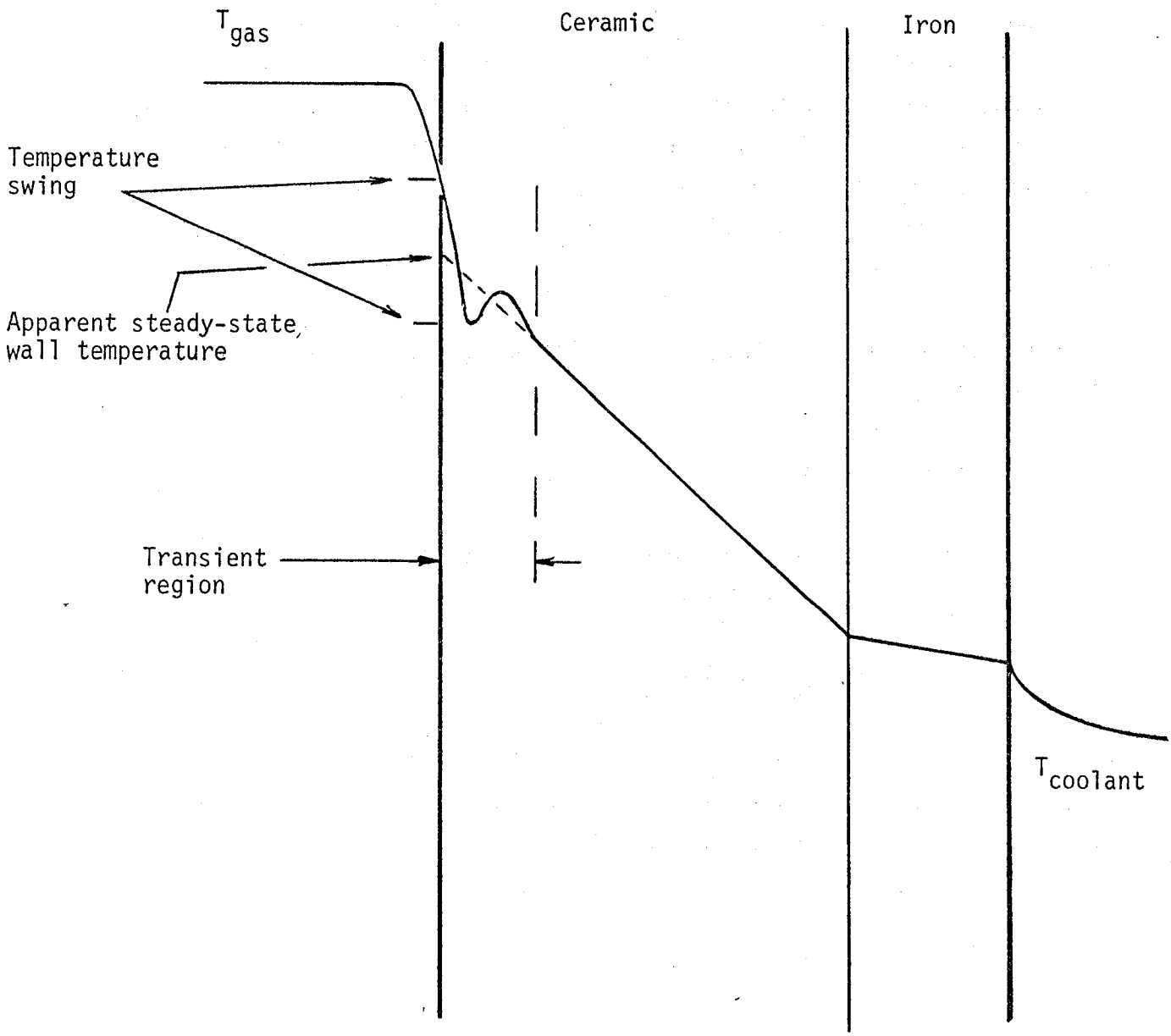

Figure 3-1. Sketch of a typical temperature profile in a combustion chamber wall, showing the transient region, temperature swing and apparent steady state wall temperature.

In order to solve the steady-state portion of the heat conduction, one needs to address the question of the "apparent" wall temperature which is the temperature the steady-state solution will predict for the combustion chamber surface. The steady-state solution solves equation (3-3) which describes accurately the conditions everywhere except in the thin transient layers. There the appropriate equation is the one-dimensional heat conduction equation:

$$\rho c \partial T/\partial t = \partial(k \partial T/\partial x)/\partial x \qquad (3\text{-}4)$$

Let us separate all the dependent variables into time-mean and fluctuating parts and then time-average equation (3-4). This process yields

$$0 = \partial(\bar{k} \partial \bar{T}/\partial x)/\partial x = \partial(\overline{k' \partial T'}/\partial x)/\partial x \qquad (3\text{-}5)$$

where all the barred quantities are time averages defined as

$$\bar{f} = \int_0^1 f \, d\tau$$

where τ is a dimensionless time coordinate $\tau \equiv$ t/period (720 degrees). The left hand side of equation (3-5) is zero because the term $\rho c \, \partial T/\partial t$ integrates to zero for a steady-state engine condition even for temperature dependent material properties. The second term in equation (3-5) is a non-linear contribution due to temperature-dependent conductivity; this term is zero outside the transient region. The importance of this term is that due to it, within the transient region, the time average heat flux does not equal the heat flux calculated based on time-averaged conditions, i.e.,

$$\partial(\overline{k \partial T/\partial x})/\partial x \neq \partial(\bar{k} \partial \bar{T}/\partial x)/\partial x \qquad (3\text{-}6)$$

As a consequence, the time-averaged temperature T is not equal to T_{ss}, the solution of the steady-state equation (3-3). (The exception is the case with the constant material properties where the second term on the

rhs. of equation (3-5) vanishes and $T_{ss} = \overline{T}$.) Thus, in general, the apparent wall temperature, which is the steady-state solution for the combustion chamber surface, does not equal the time-average temperature calculated by the transient solution for the same surface.

The difference between the two can be readily obtained from the transient solution. The apparent surface temperature is that which would exist under the mean heat flux if the surface layer were steady-state. Thus, once can integrate from the inner edge of the transient layer, where the time mean solution of the transient equation equals the steady-state temperature, through the layer to the surface to obtain the apparent temperature as

$$T_a = \overline{T}_p + \overline{q} \int_o^{\delta} dx/\overline{k} \qquad (3\text{-}7)$$

where the values of the temperature at the penetration depth, $\overline{T}_p$, mean heat flux $\overline{q}$ and $\overline{k}(x)$ are obtained from the transient solution. The time-average surface temperature $\overline{T}_w$ is also known from the transient solution, and so one can calculate the shift

$$\Delta T_{wa} = \overline{T}_w - T_a \qquad (3\text{-}8)$$

This shift is due to temperature-dependent heat conductivity only, and vanishes when the conductivity is constant. It may also be noted that this term is not affected by temperature-dependency of ρc as that term drops out of equation (3-5) entirely.

The remaining part of the decomposition problem is the determination of the proper boundary conditions for the steady-state solution, which is the time-averaged heat flux into the wall

$$\bar{q} = \overline{h_g (T_g - T_w)} + \bar{q}_{rad} \qquad (3\text{-}9)$$

$$= \bar{h}_g (T_{eff} - \bar{T}_w - \Delta T_{wh}) + \bar{q}_{rad}$$

where

$$T_{eff} = \overline{h_g T_g} \; / \; \bar{h}_g \qquad (3\text{-}10)$$

and

$$\Delta T_{wh} = \overline{h_g T_w'} \; / \bar{h}_g \qquad (3\text{-}11)$$

i.e., the term ΔT_{wh} involves the correlation between the fluctuating part of the wall temperature and the heat transfer coefficient. It may be viewed as a term that modifies the effective gas temperature T_{eff}. In a typical situation the wall temperature tends to follow the gas temperature and is positively correlated with the gas heat transfer coefficient. The term is thus usually positive and tends to reduce the cycle-averaged heat transfer. The value of this correlation term is again readily obtained from the transient solution.

The final form of the boundary condition for the steady-state solution is

$$k_{ss} \, \partial T_{ss}/\partial n = \bar{h}_g (\bar{T}_{eq} - T_a) + \bar{q}_{rad} \qquad (3\text{-}12)$$

where

$$\bar{T}_{eq} = T_{eff} - \Delta T_{wh} - \Delta T_{wa} \qquad (3\text{-}13)$$

and the coupled problem is solved by iteration. The radiation term contains wall temperature raised to the fourth power, but its influence on the term is very small under typical engine conditions where the radiating sooting flame has a substantially higher temperature than the walls even though these may be insulated. This small feedback is automatically taken into account during the iteration.

Finite Difference Formulation of the Transient Solution

The governing equation (3-4) was solved by a finite-difference procedure, which has the capability to handle arbitrarily spaced discrete nodes. For these we write a finite-difference equation derived using a control volume approach. For a single control element, i, which extends from a mid-point between nodes i-1 and i, to a mid-point between nodes i and i+i we write

$$a_i\Delta T_{i-1} - (a_i+b_i+c_i)\,\Delta T_i + c_i\Delta T_{i+1} = a_i\,(T^\circ_{i-1}-T^\circ_i)+c_i(T^\circ_i-T^\circ_{i+1}) \tag{3-14}$$

where, $\Delta T_i \equiv T_i - T^\circ_i$, superscript $^\circ$ denotes old time value

and,

$$a_i \equiv \frac{k_{i-1}(\bar{T}_{i-1})}{d_{i-1}}$$

$$b_i \equiv \frac{1}{2\,\Delta t}\quad [\,\rho c_{i-1}(\bar{T}_{i-1})\,d_{i-1} + \rho c_i(\bar{T}i)\,d_i]$$

$$c_i \equiv \frac{k_i(\bar{T}_i)}{d_i}$$

$$\bar{T}_i \equiv (T_i + T_{i+1})/2$$

$d_i \equiv$ width of element lying between nodes i-1 and i.

The meaning of these definitions is that the materials properties for a given element are to be evaluated at a temperature which is the arithmethic mean between the temperatures at the two node points between which the element lies. In doing so, it is assumed that each element is made of one material. This means that when dealing with laminated walls, one has to ensure that each boundary between two lamina is also a node point in the calculations. Since the differencing method accepts

arbitrary element sizes, this condition is easy to satisfy in practice. The formulation is consistent, unconditionally stable, and insures continuous heat fluxes across boundaries between elements.

Validation and Grid Optimization

After the finite difference formulation was implemented, the resulting computer code was tested by comparison to a special case of transient heat transfer for which exact solutions to the conduction equation exist. (There is no need, in this instance, for comparison to experiments rather than to the exact solutions because the transient heat conduction equation is a precise representation of the physical process.) The objective of the comparison was to determine:

a) whether the numerical, finite difference discretization of the heat conduction equation was correctly implemented; and

b) the minimum number of grid points that are needed to adequately describe the transient temperature which propagates into the wall.

Due to the periodic nature of the engine operation the most appropriate exact solution was felt to be one with periodic boundary conditions. Therefore, we chose the case of a sinusoidally varying fluid temperature periodically heating and cooling a semiinfinite slab, with a convective boundary condition, depicted schematically in Figure (3-2).

$$\dot{q} = h_g (T_g - T_{wg})$$

where, h_g, the gas heat transfer coefficient, is constant, T_{wg} is the temperature at the wall/gas interface and T_g, the gas temperature, varies according to the relation

$$T_g = \bar{T}_g + \Delta T_g \cos 2\pi f t$$

For constant material properties (temperature independent) the exact solution shows that the surface wall temperature responds with an oscil-

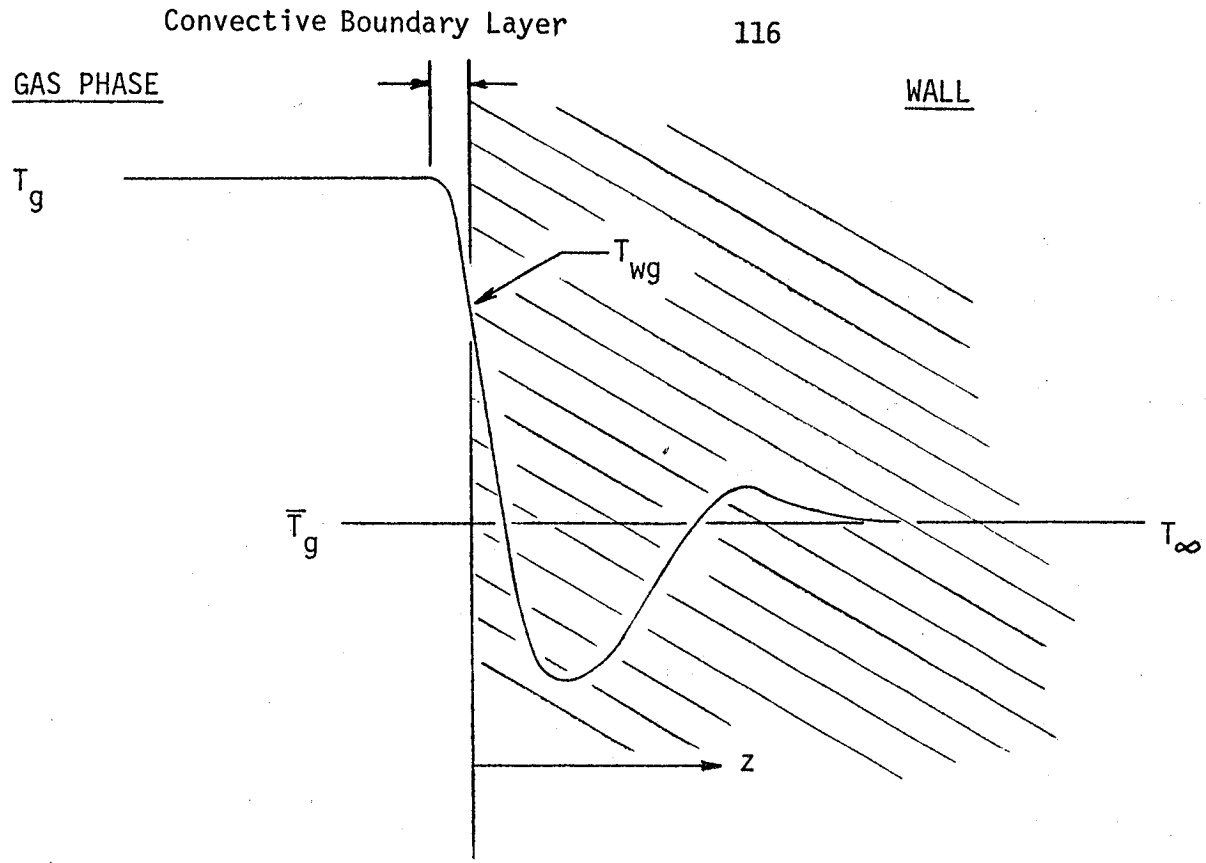

Figure 3-2. Schematic of temperature profile corresponding to the exact solution.

Wall Temp. Swing / Gas Temperature	Penetration Depth / Wall Thickness: 0.022	0.112	0.710
0.013	×	×	×
0.062	×	×	×
0.300	×	○	×
0.950	×	×	×

○ : Data for This Combination Shown in Figures 3-3 and 3-4

Table 3-1. Test case matrix for validating solutions to the 1-D heat conduction model.

lation (swing) whose magnitude is

$$\Delta T_{wg} = \Delta T_g \left(1 + \sqrt{2N^{-1} + N^{-2}}\right)^{-1/2} \qquad (3\text{-}15)$$

where $N = h_g/(2\pi\rho ckf)^{1/2}$ and f is the frequency of oscillations. The penetration distance, defined as the point at which the wall temperature amplitude decays to one percent of the surface temperature wave, is

$$d \simeq 2.5\ (k/\rho cf)^{1/2}. \qquad (3\text{-}16)$$

The surface temperature T_{wg} is not in phase with the gas temperature, but lags behind it by a phase shift

$$\delta = \tan^{-1}\ [1\ /(1+N)]$$

the maximum of which is $\pi/4$ or 90° crankangle degrees.

Since the temperature variation decays to negligible levels beyond the penetration depth, it is not necessary to place many grid points in that region. By the same argument, a semiinfinite wall may be represented by a finite-thickness wall as long as the latter extends beyond the penetration depth. To resolve the important layer near the surface, the numerical model was set up with a variable size grid, with grid spacing tailored to the penetration depth. The first node length was chosen to be 0.01 of the penetration depth and the subsequent ones were placed at progressively larger values, each larger by a fixed factor relative to the previous one. A series of calculations was then made to determine the maximum acceptable value for this factor (the smallest number of grid points) for which accurate results compared to the exact solution are still obtained.

The real variation of cylinder gas temperatures, although periodic, is not sinusoidal. However, any general gas temperature profile may be decomposed into a sine/cosine series, and since the equation is linear, the solution corresponding to the general temperature profile equals the

sum of all the solutions corresponding to the individual terms of the sine/cosine series. Therefore, for the purposes of validation of the 1-D computer code, it is sufficient to verify that the code predictions agree with the exact solution for the fundamental oscillation (720 crank angle degrees) as well as for individual higher frequency harmonics.

Analysis of a typical temperature profile obtained from our cycle simulation and its decomposition into a sine/cosine series showed that the most important are the first 8 harmonics. The coefficients of the harmonics decrease with increasing order to below 7 percent of the fundamental function by the 8th order. Further, the wall temperature waves due to unit gas temperature wave decrease rapidly in amplitude and penetration. Therefore, it is not necessary to test the numerical solution up to very high orders; the eighth harmonic should be sufficient, although in this work we did look at orders up to the twentieth.

To provide a comprehensive validation, a matrix of test cases was chosen spanning a wide range of wall surface temperature swings between 0.01 and 0.95 times the gas temperature amplitude, and penetration depths ranging from 0.22 mm to 7.1 mm in a 10 mm thick wall, for a total of 12 cases. The criteria for accuracy were: a) the maximum difference between the exact and the numerical solution at any node and at any point in time, b) ratio of numerical solution wall surface temperature swing to the exact solution, and c) the difference in numerically computed and exact phase shift. Comparisons were made for harmonics up to the eighth (8 times the fundamental frequency) for all of these test cases, and up to the twentieth harmonic for the specific case denoted in Table (3-1).

Over the range of this test matrix the numerical solution was found to give a uniform degree of agreement with the exact solution, independent of any particular combination of physical parameters producing the quoted swings and penetration depths. The level of agreement depended only on the number of grid points employed, i.e., on the factor used to increase the successive grid spacings. For a factor of 1.27, which

required 20 grid points, the accuracy of the numerical solution was excellent -- better than one percent accuracy in temperature, and negligible differences in predicted temperature swings and phase shifts. A very good accuracy was obtained for a factor of 1.38, with 15 grid points. The largest error in the predicted surface temperature swing was one percent and the error in phase shift was at most 0.7° and usually much less. This may be seen in Figures (3-3) and (3-4), which show comparisons of the exact and numerical solutions obtained with 15 points for the case denoted in Table I. For the fundamental frequency, the penetration distance is 0.112 of the wall thickness, surface temperature swing is 0.299 times the gas temperature swing and the phase shift is 65.6°. The eighth harmonic has a much smaller penetration depth (0.040), wall temperature swing (0.125) and phase shift (10°) than the fundamental. For the twentieth harmonic the penetration depth was only 0.025 of the wall thickness, with a swing ratio of 0.082 and phase shift of 4.2°. The maximum error in temperature was two percent of the surface swing (i.e., 0.175 percent of gas temperature swing). This confirmed that the numerical method resolves even the 20th harmonic with a good accuracy. The accuracy obtained for this case is typical of all the others, and the agreement is seen to be excellent. As a result of this study we concluded that an adequate level of detail is obtained by using 15 grid points to describe the wall temperature profile, of which 11 were placed within the transient region.

The program was also tested for application to thin coatings by resolving a case with a temperature penetration depth of only 0.1 mm, placing the first grid point at 0.001 mm. The agreement with the exact solution was as good as with the other cases, verifying that the program has the capability to analyze temperature dynamics in thin coatings and surface deposits.

Based on these results, the program was given the capability to automatically choose the grid (i.e., element) size for the optimum accuracy by placing the most of the node points in the rapidly changing transient region near the surface, while putting only a small number of points in

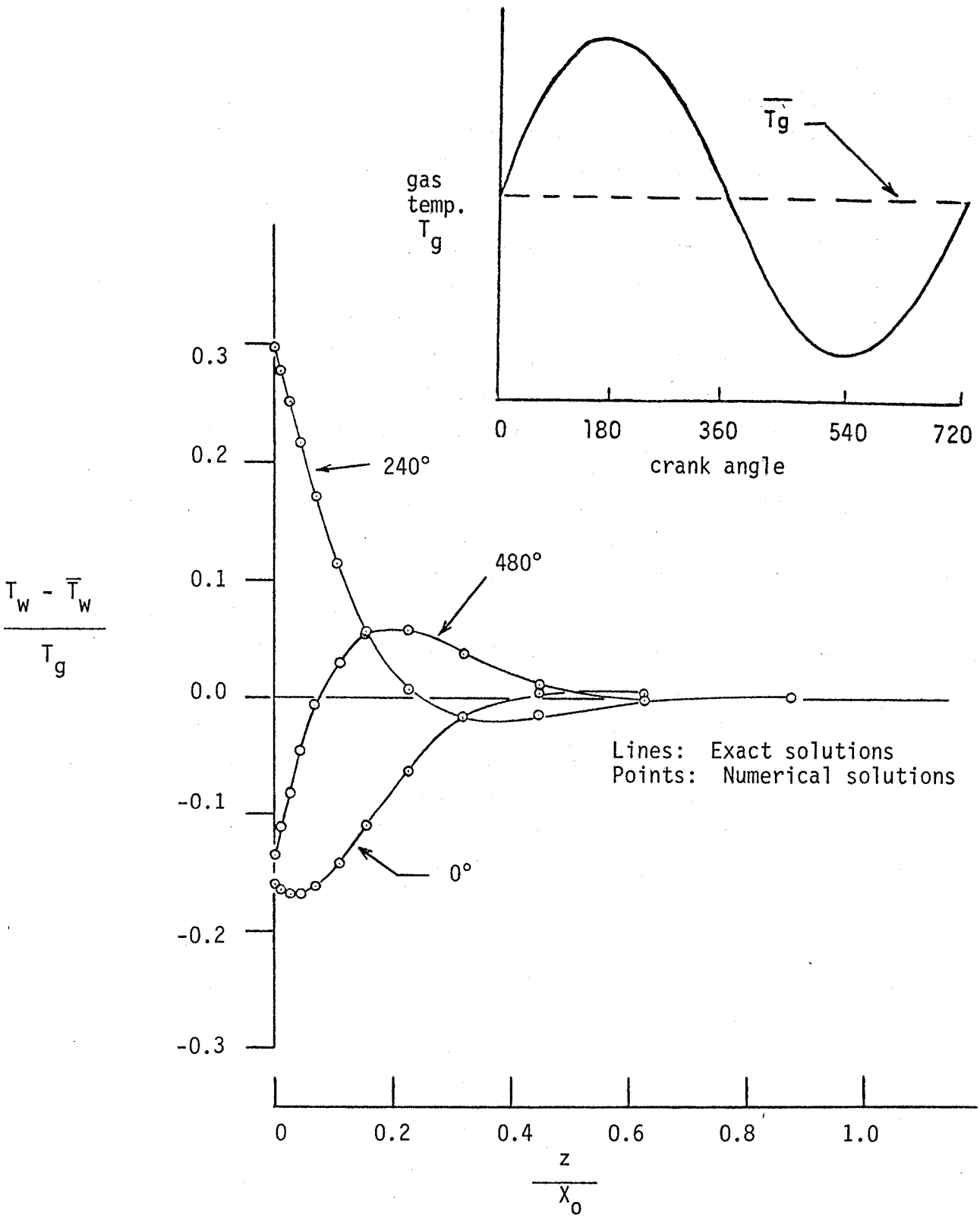

Figure 3-3. Comparison of numerical and exact solutions for the fundamental frequency (Period of 720^o). The angle 0^o corresponds to the instant where T_g equals $\overline{T}_g$ and is going up. L is the wall thickness and X_o is the wavelength of the fundamental temperature waves.

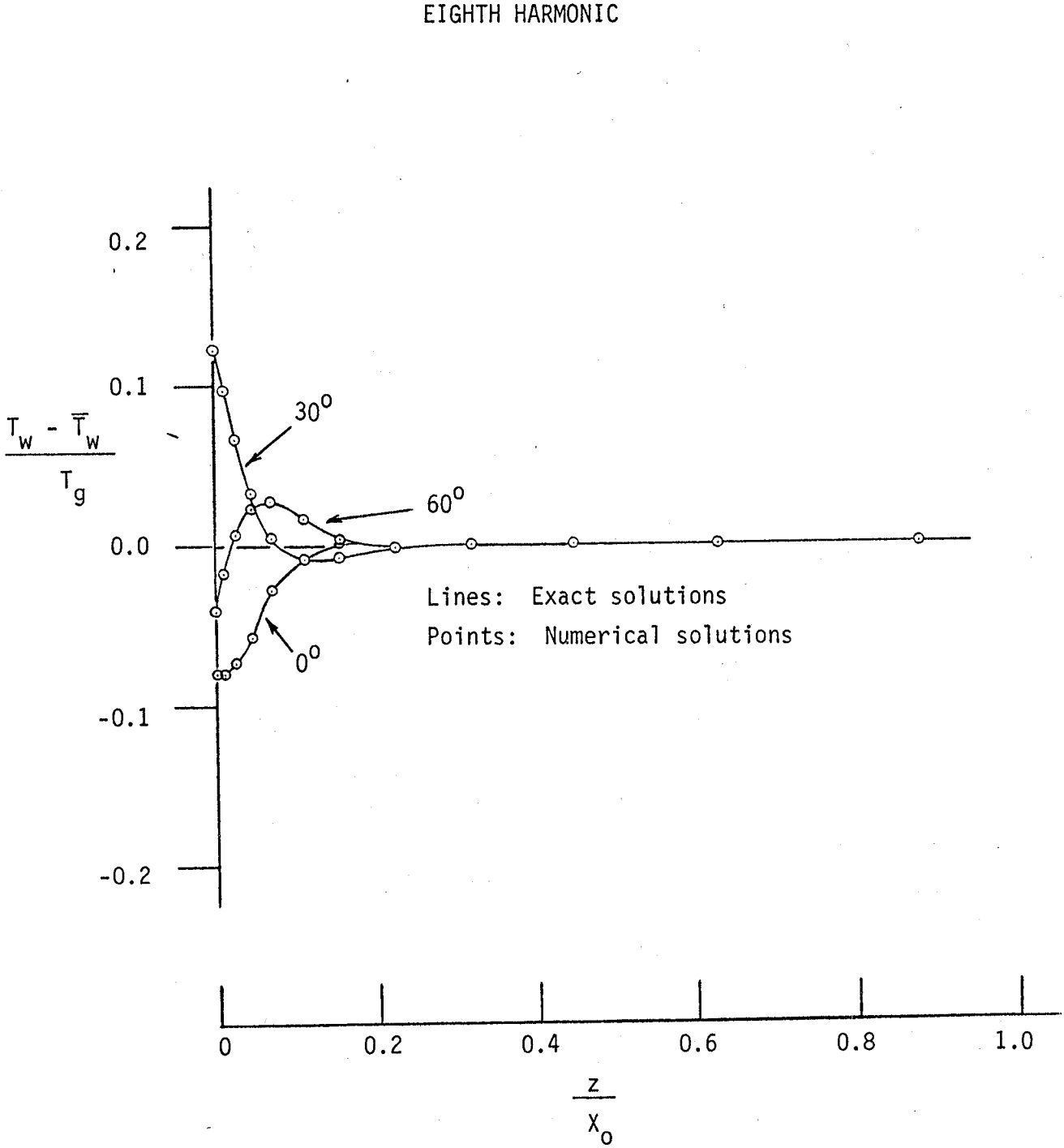

Figure 3-4. Comparison of numerical and exact solutions for the eighth harmonic (Gas temperature oscillating with the same amplitude as in Figure 3-3 but with eight time higher frequency). It is plotted against the same dimensionless depth as in Figure 3-3 (z/X_o).

the region beyond the "penetration depth" (calculated from equation 3-16) where, for a periodic gas temperature, the temperature profile is invariant in time once a steady-state is reached.

Effect of Temperature-Dependent Material Properties

As already discussed in an earlier section, temperature-dependence of material properties has an effect on the transient heat transfer, and we have seen that it may be shown that one effect of the variable conductivity is to make the apparent and time-average surface temperatures differ from each other. Separately from this effect, both k and ρc influence the temperature dynamics and surface swings. These effects are typically ignored in studies dealing with engine insulated materials. Since they have the potential of becoming significant when the temperature swings are large, as is the case in well-insulated engines, they were investigated as a part of this study.

Available literature shows that the variation of both ρc and k can be quite substantial over the anticipated range of temperatures between 300° and 1400°K. For example, the data collected by Goldsmith, et. al. (1961) for silicon carbide show an increase in specific heat, c, by a factor of over two in this temperature range, and an order of magnitude decrease in thermal conductivity, k, over the same temperature range. The effect of temperature-dependent properties is to make the governing partial differential equation non-linear, and the result of the non-linearity is hard to predict. To evaluate these effects, a series of test runs was made with a hypothetical ceramic material whose conductivity varied by a factor of four over the range 300° to 1400°K (Figure 3-5). Using a finite wall 10 mm thick with adiabatic conditions on the far surface, we have applied to the near surface a sinusoidal gas temperature ranging from 300°K to 1800°K, and a constant heat transfer coefficient, h_g. Allowing a sufficient number of cycles to reach a steady-state condition, leads to the result shown in Figure (3-6). In it, the time average heat flux into and through the wall is zero. However, the time averaged temperature profile (which would be constant

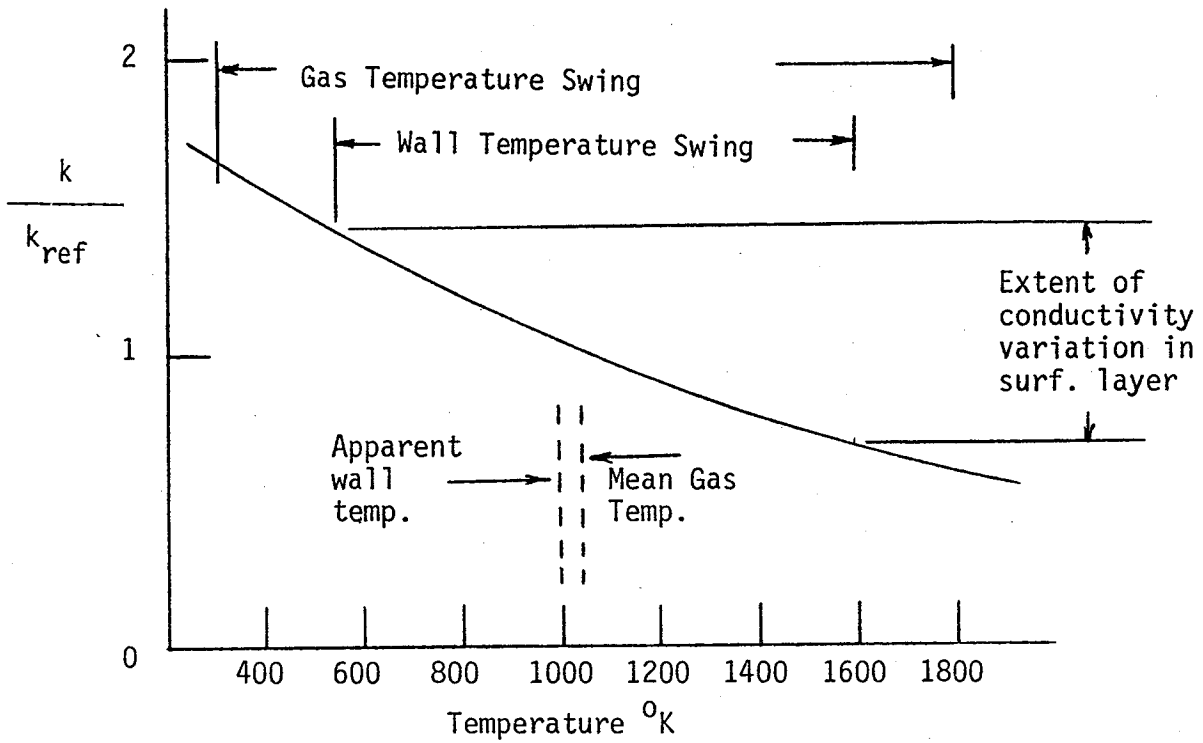

Figure 3-5. Assumed temperature dependence of heat conductivity, used to generate results presented in Figure 3-6.

if k were temperature independent) showed a sharp gradient at the periodically heated surface. The envelopes of the maximum and minimum wall temperatures serve to indicate, together with Figure (3-5), the range of conductivity values arising during each cycle at any given depth. It should be stressed again that the presence of a finite gradient in the time-mean temperature does not indicate a non-zero time-averaged heat flux: as a consequence of the non-linearity introduced by the variable k, the time-averaged heat flux does not equal the product of the time-averaged temperature gradient and time-averaged k.

Figure (3-6) also clearly demonstrates that if k is temperature dependent, the time-averaged wall surface temperature does not equal the surface temperature that would be obtained by extrapolation from the steady-state region to the surface. Interestingly, the amplitude of the surface temperature swing was almost identical to one that would obtain with a constant conductivity, but it was skewed upward. This skew was additive to the already noted difference between the time-averaged surface temperature and the "apparent" surface temperature, to produce a combined total shift of 12 percent of the maximum wall temperature. This effect has to be taken into account in materials evaluation, as it accentuates the peak temperatures occuring in the material.

The effect of variable heat capacity was investigated using another hypothetical material, in which ρc was prescribed to increase with temperature by a factor of four over the range 300° to 1000°K. The swing amplitude was almost identical to that obtained with constant properties, but it was again skewed, this time downward, by an amount which was about 60 percent of that produced by the variable k in Figure (3-6). In agreement with the derivations concerning the effects of variable properties discussed earlier below equation (3-8), the apparent wall temperature was found to equal the mean surface temperature. Since the observed effects of variable ρc were not too large, even though the variation in ρc with temperature in this hypothetical material probably was on the high side of what one would expect in realistic materials, it appears that temperature dependence of ρc will be a less important

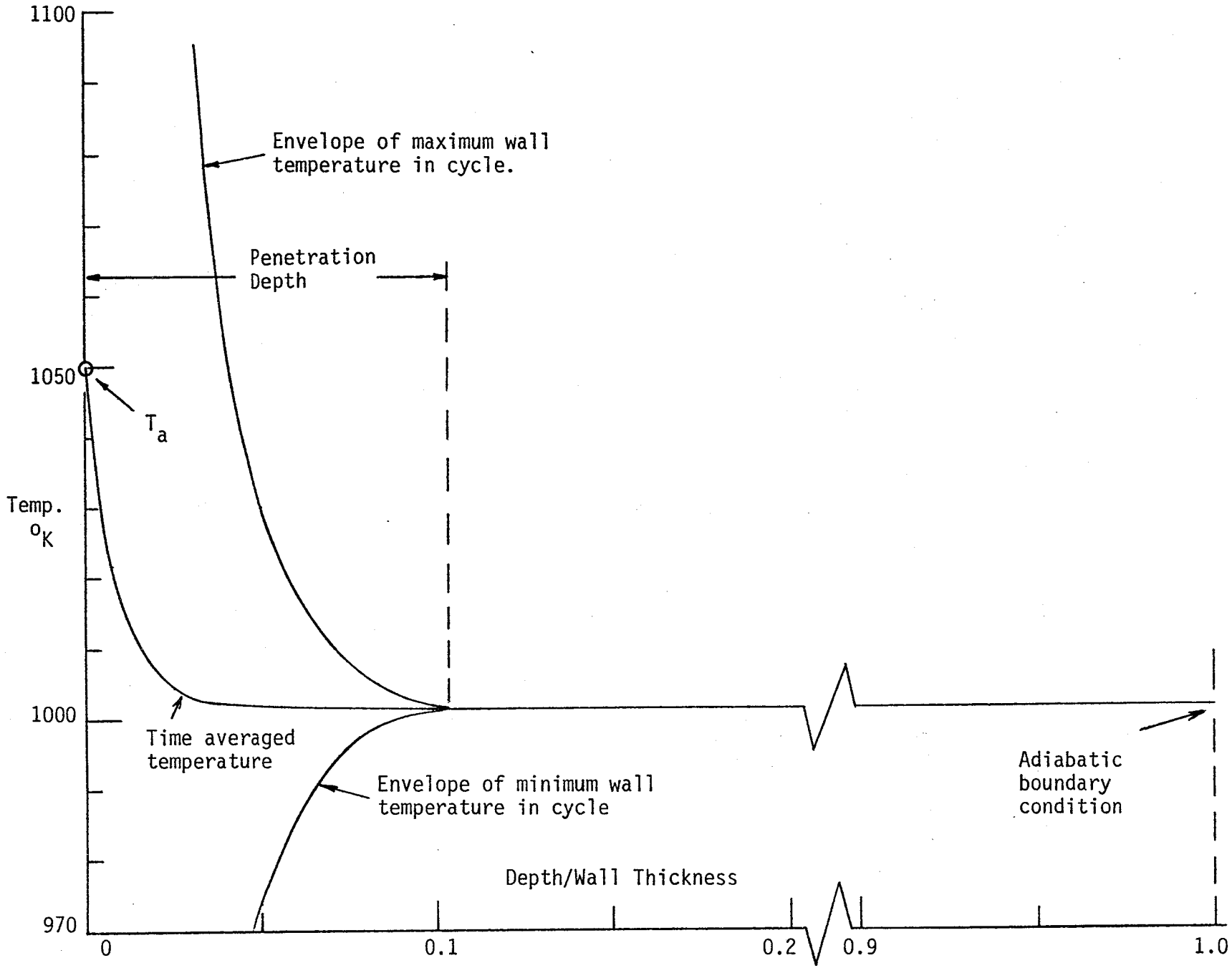

Figure 3-6. Wall temperature in a ceramic material under simulated engine conditions. The non-linear variation of the time-averaged temperature in the transient layer is due to temperature dependence of the wall conductivity (see Figure 3-5).

factor in materials selection than the temperature dependence of heat conductivity.

Lumped Parameter Analysis

An important consideration in the construction of the overall methodology is the computer running time of the complete package. Because of this, close attention is given to each code element and especially to those that are computationally intensive. The one-dimensional model falls into that category because it has to be solved separately for each of the eleven individual areas which represent the total combustion chamber surface in the cycle model. Since each such solution is demanding on computer time, it was determined at an early point in the program to investigate the practicality of evaluating the swing magnitude from an approximate expression based on a lumped parameter analysis -- in effect a swing correlation. One objective of this effort was to generate a very efficient method of implementing the swing effects into the thermodynamic cycle calculations. Another benefit of a lumped parameter analysis is a much improved understanding of swing trends correlated with global parameters which could be of use in materials development, evaluation and selection.

Analyzing the physics of the problem, represented mathematically in the 1-D heat conduction equation and its boundary conditions, one observes that the swing magnitude depends on material heat conductivity, heat capacity and density, on gas temperature and heat transfer coefficient, and on engine speed. To the extent that these quantities are significant they must appear in the swing correlation. In order to derive a suitable form of such a correlation, one can use as a guide exact solutions of the heat conduction equation with periodic boundary conditions. Two such solutions are of particular relevance; one for convective boundary conditions with sinusoidally varying gas temperature and a constant heat transfer coefficient, and one for a sinusoidally varying surface heat flux. The real engine situation differs from the first case in that the heat transfer coefficient varies quite strongly with

crank angle, roughly in phase with the gas temperature. Furthermore, it differs from both cases in that the time variation, although periodic, is not sinusoidal. Both of these differences had to be considered in the development of the correlation.

In accounting for the first difference, the problem was approached by expansion of the instantaneous heat flux into steady-state and fluctuating parts, i.e., by writing

$$q = h_g (T_g - T_w) = (\bar{h}_g + h'_g)(\bar{T}_g + T'_g - \bar{T}_w - T'_w) \qquad (3\text{-}17)$$

where we lump convection and radiation into an "enhanced" convection, by augmenting the instantaneous gas temperatures by an amount equal to

$$\Delta T_{gr} = q_{rad}/h_g$$

Subtracting from equation (3-17) the time-averaged heat flux q, one obtains the fluctuating heat flux into the wall

$$q' = \overline{h_g}\,(T'_g - T'_w) + h'_g\,(\bar{T}_g - \bar{T}_w) +$$

$$(h'_g\,T'_g - \overline{h'_g\,T'_g}) - (h'_g\,T'_w - \overline{h'_g\,T'_w}) \qquad (3\text{-}18)$$

which produces a temperature wave in the solid wall, whose amplitude is proportional to the heat flux amplitude. The fluctuating heat flux is seen to consist of two terms oscillating with the fundamental periodicity (the first two terms on rhs) and of two higher harmonic terms which will be neglected below to make the swing correlation tractable. The first term is that due to fluctuating gas and wall temperatures and the second due to a fluctuating heat transfer coefficient. If the Tg and hg variations were sinusoidal and T'_w were small compared to the ampli-

tude of T_g, then by analogy to the exact solution, equation (15), the response to the first two terms would be sinusoidal with amplitude at the surface

$$DT_w = DT_g/hw_1 + Dh_g(\bar{T}_g - \bar{T}_w)/\bar{h}_g/hw_o \qquad (3\text{-}19)$$

where DT_g, DT_w and Dh_g are the amplitudes of the three variables, which for simplicity are all assumed to be in phase. The variable hw_o is defined as

$$hw_o = (2\pi\rho ckf)^{\frac{1}{2}}/\bar{h}_g \qquad (3\text{-}20)$$

and hw_1 as

$$hw_1 = (1 + \sqrt{2}\, hw_o + hw_o{}^2)^{\frac{1}{2}} \qquad (3\text{-}21)$$

where f is the oscillation frequency (per 720° CA) and ρ, c and k are material properties.

As it is, the profiles of T_g and h_g are not sinusoidal and this requires the definition of characteristic values for Dh_g, DT_g, h_g and T_g which would reduce the actual profiles to equivalent sinusoidal cases for which equation (3-19) applies. A number of possible formulations for the characteristic values were tested over a wide range of material properties and h_g, T_g variations. After some experimentation it was found that using rms values of h_g and T_g to represent Dh_g and DT_g is appropriate, and it was also found necessary to replace hw_o by hw_1 in the second term of equation (19). When tested over a broad set of conditions, the swing correlation (equation 19) was found to predict all trends very faithfully, despite the neglect of higher order terms, and to give absolute values with an error not exceeding 20 percent and usually better than this.

The swing correlation is quite useful for making quick estimates of expected temperature swings and also for understanding of the physical parameters involved in the temperature dynamics. Although it is limited to studies of constant-property materials, it is still applicable to a wide range of general questions that do not even consider this aspect of the problem. A more serious problem arises from the need to apply the model, within an engine simulation, to liner surfaces. These surfaces do not have the constant contact with combustion gases assumed in the development of the correlation, and so the correlation cannot be properly used for them.

Example of Temperature Swing Prediction

The one-dimensional model can be used to predict wall temperature dynamics under realistic engine conditions. The following example was carried out using analytical data generated by the cycle simulation program. The simulation described the Cummins NTC-350 engine operating at its maximum torque, i.e. at 1300 rpm, full load. One particular surface was studied, the bottom of the cup, lined by a plasma-sprayed coating of zirconia 1.5 mm thick (0.060"). The properties of the zirconia coating were $k = 0.6$ W/mK and $\rho c = 1.1$ J/m^{3}K, taken from Cawley (1984).

The boundary conditions on the gas side were supplied by the cycle simulation, as schematically shown in Fig. (3-7). The coating was assumed to be supported by a metal substructure, limited by material properties to temperatures up to 575°K. Therefore, in the calculation the boundary condition on the metal side was set to 575°K. The applied gas temperature and heat transfer coefficient are shown in Figs. (3-8) and (3-9), and these specifically pertain to the cup bottom; other surfaces of the combustion chamber have their own, different, T_g and h_g profiles. The radiation heat flux into the surface is shown in Fig. (3-10).

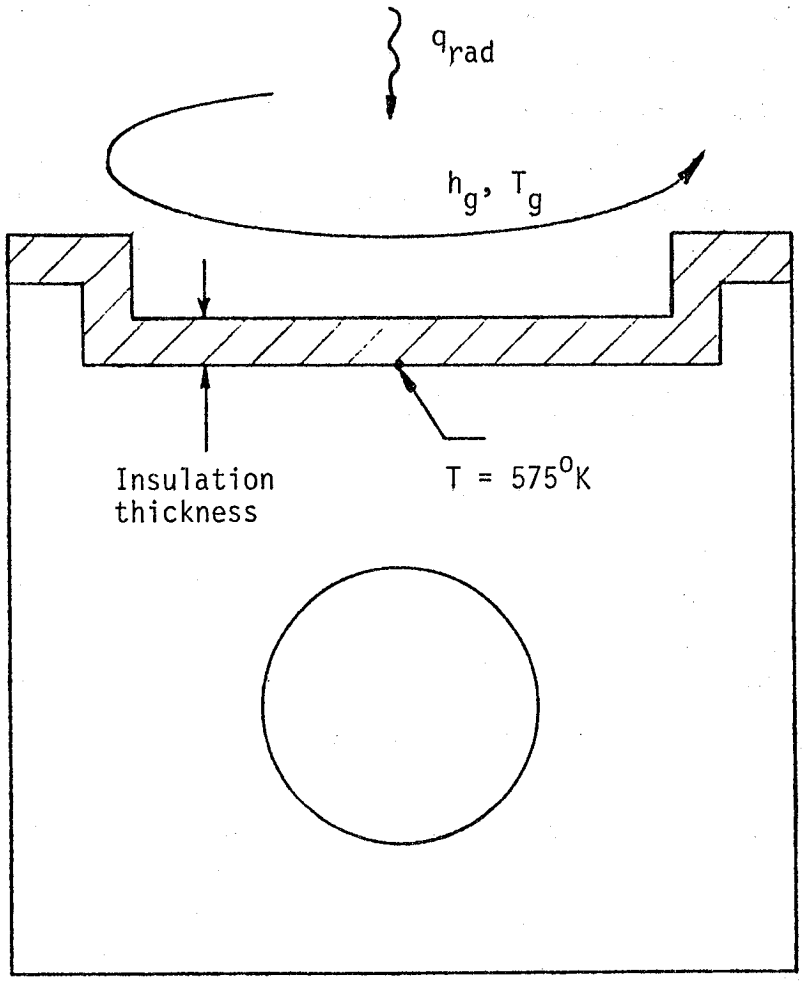

Figure 3-7. Schematic of boundary conditions applied in the parametric study of effect of material properties on wall temperature swings and heat flux in the bottom of the cup.

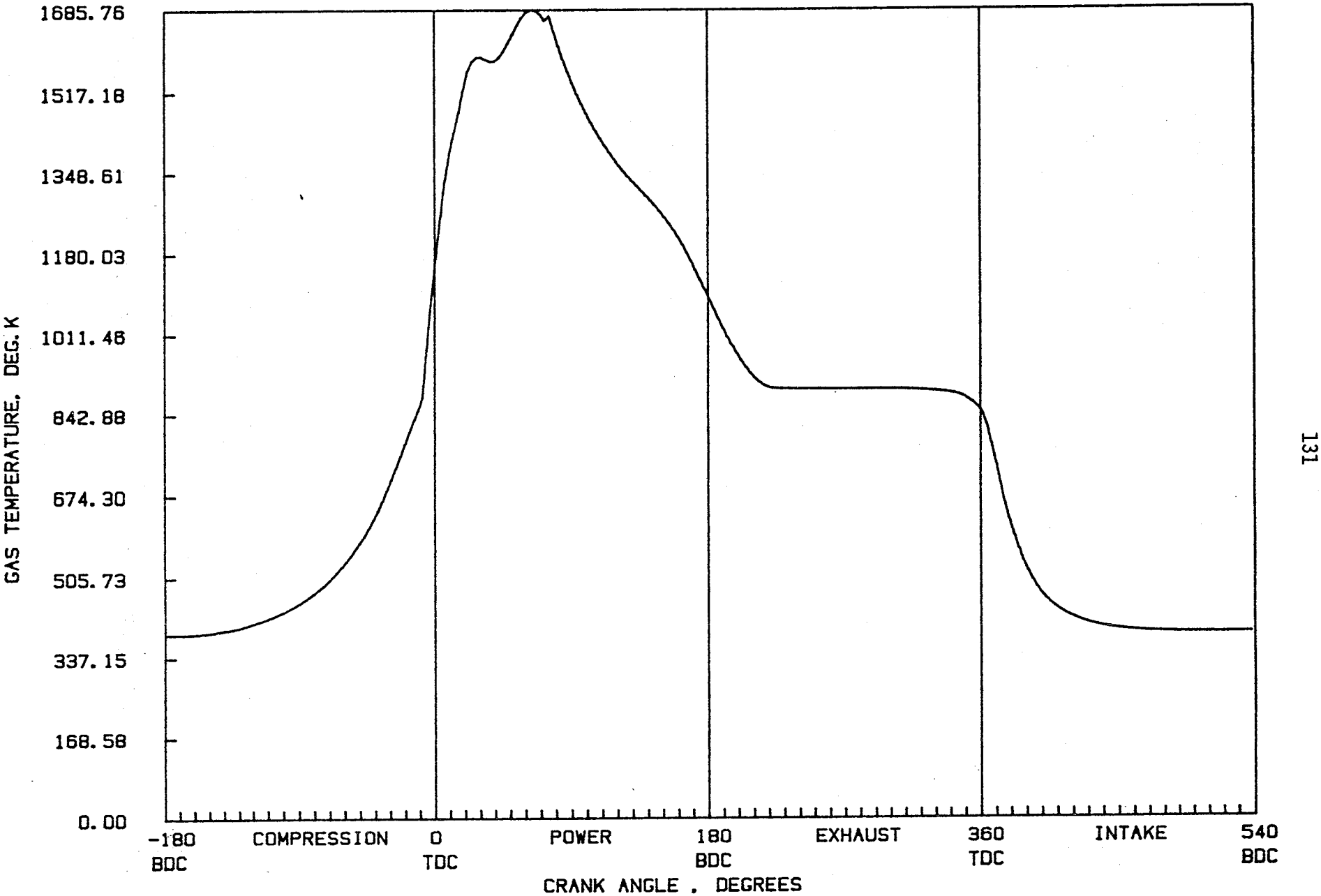

Figure 3-8. Convective gas temperature applied to the bottom of the cup.

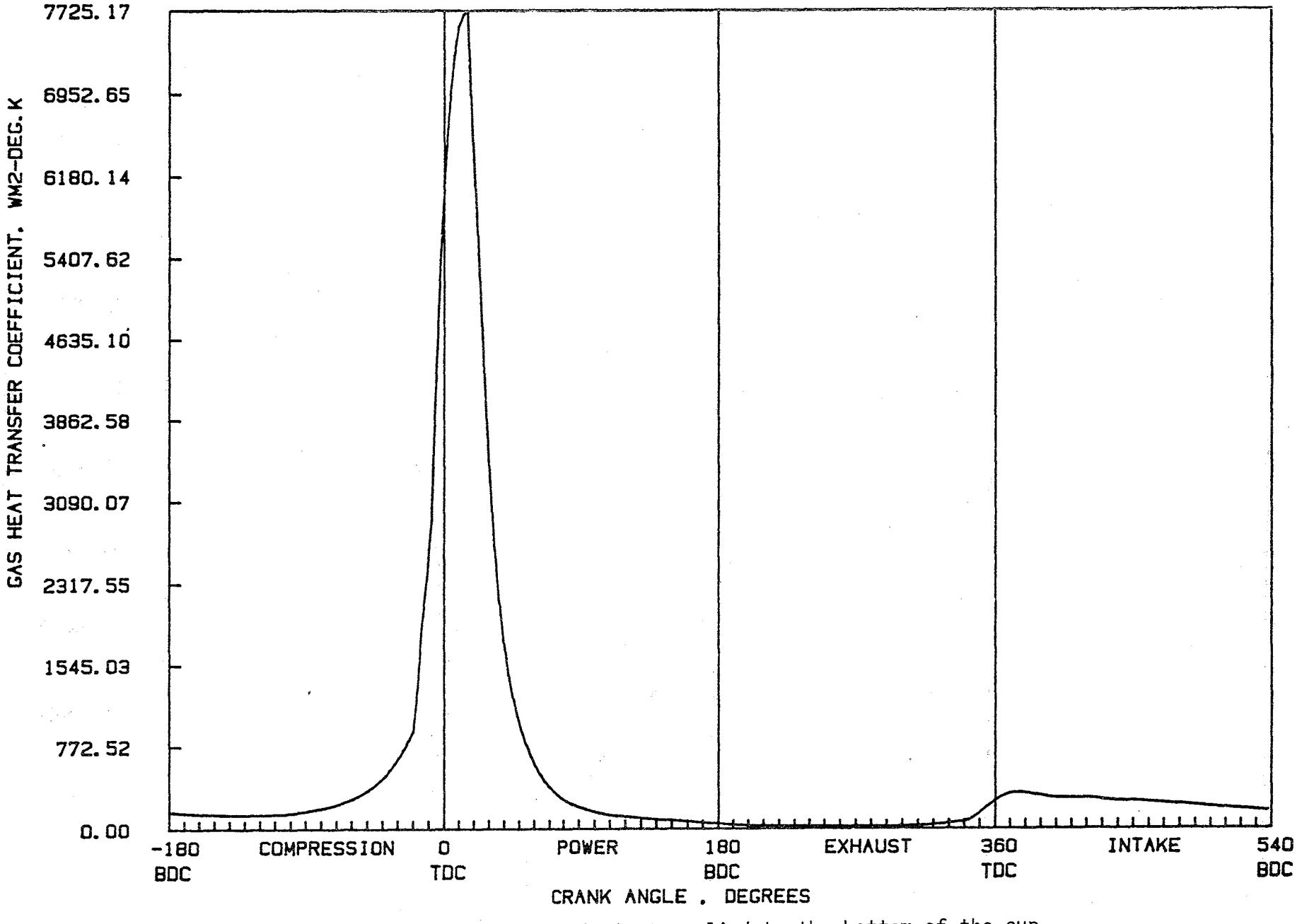

Figure 3-9. Convective heat transfer coefficient applied to the bottom of the cup.

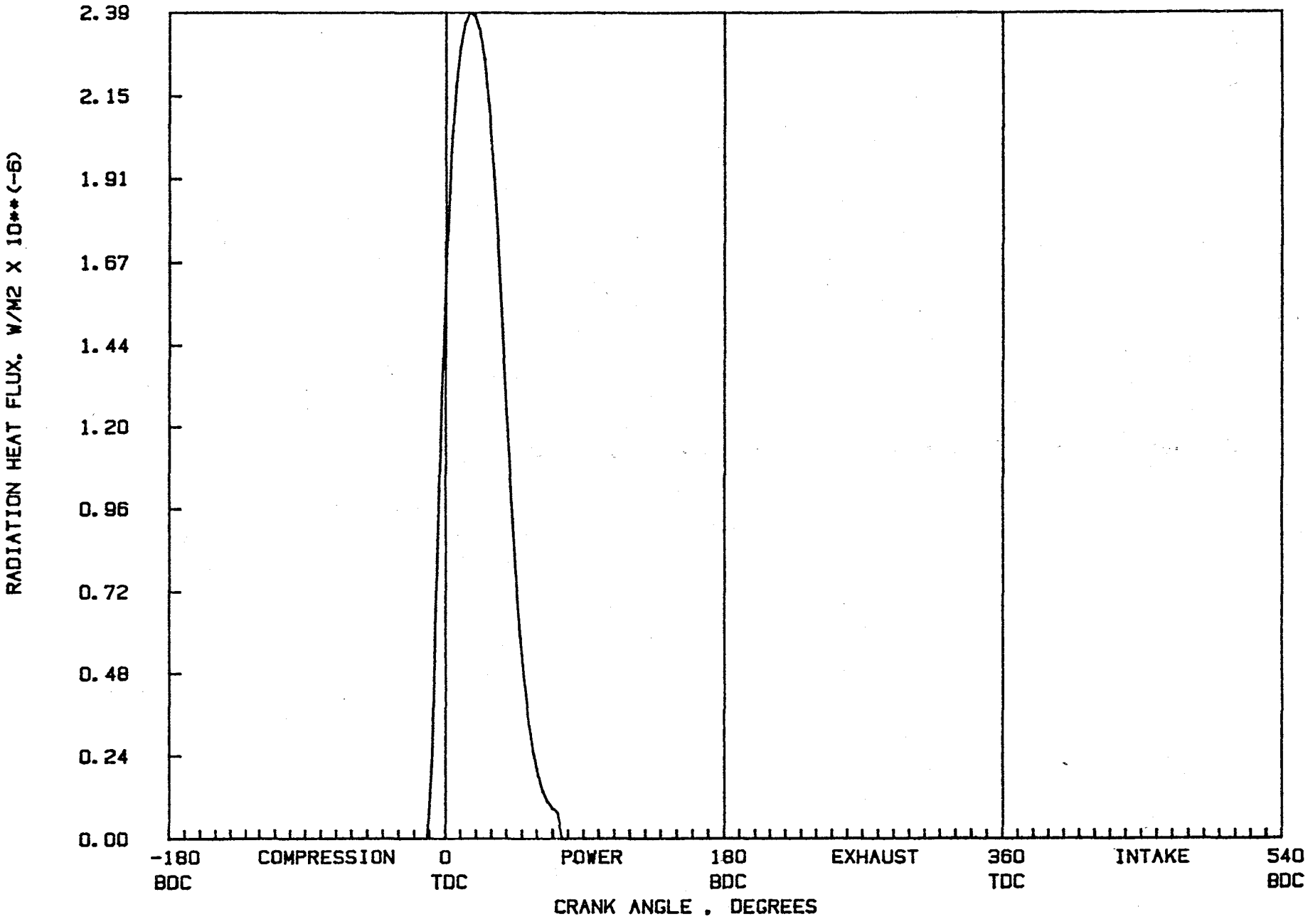

Figure 3-10. Radiation heat flux applied to the bottom of the cup.

Applying these time-dependent boundary conditions to the surface, produces transient temperature waves in the coating which require a number of engine cycles to reach stationary values. At that point one may calculate the time-history of the heat flux from

$$q = h_g (T_g - T_w) + q_{rad}$$

including the effects of time dependent wall temperature. This flux is shown in Fig. (3-11), displaying a very sharp positive peak near TDC of the compression stroke and relatively small negative heat flux during much of the rest of the cycle due to high surface temperatures. It may be seen that substantial part of the heat flux into the wall is due to radiation, as could be expected for a well insulated surface under high engine load. The time-mean surface temperature was 1037°K, i.e., 462°K above the metal temperature, and the maximum value of the surface temperature was 1280°K, or 243°K higher than the mean (Fig. 3-12). The total wall temperature swing was 331°K, and the penetration distance to the point where to swings decayed to 1% of the surface value was less than 0.4 mm.

The coating was found to reduce the cycle-averaged heat flux into that particular surface by over 60 percent compared to all-aluminum construction. This is a respectable reduction, considering that the heat radiation, which accounted for about 30 percent of the cycle-averaged heat transfer, was essentially unaffected by the insulation. As a result of suppressed convection heat transfer, the radiation is predicted to be responsible for 78 percent of the net heat flux to the wall in the insulated case. Another interesting finding is that under typical engine conditions, and with realistic material properties, one can expect very large surface temperature swings of several hundred degrees Kelvin in magnitude, increasing substantially the maximum temperatures the surfaces achieve.

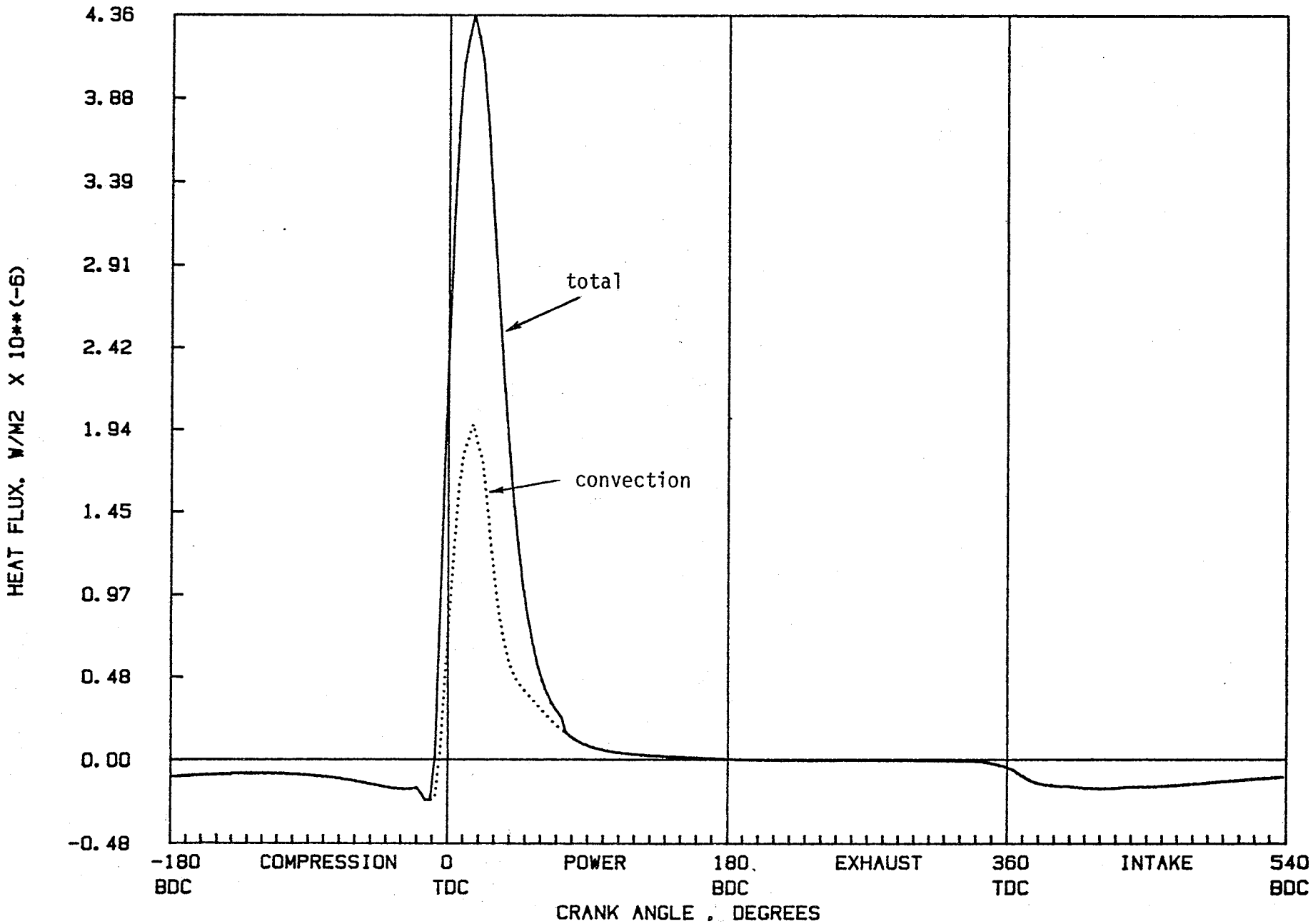

Figure 3-11. Calculated heat flux into bottom of the cup, zirconia coating 1.5 mm thick

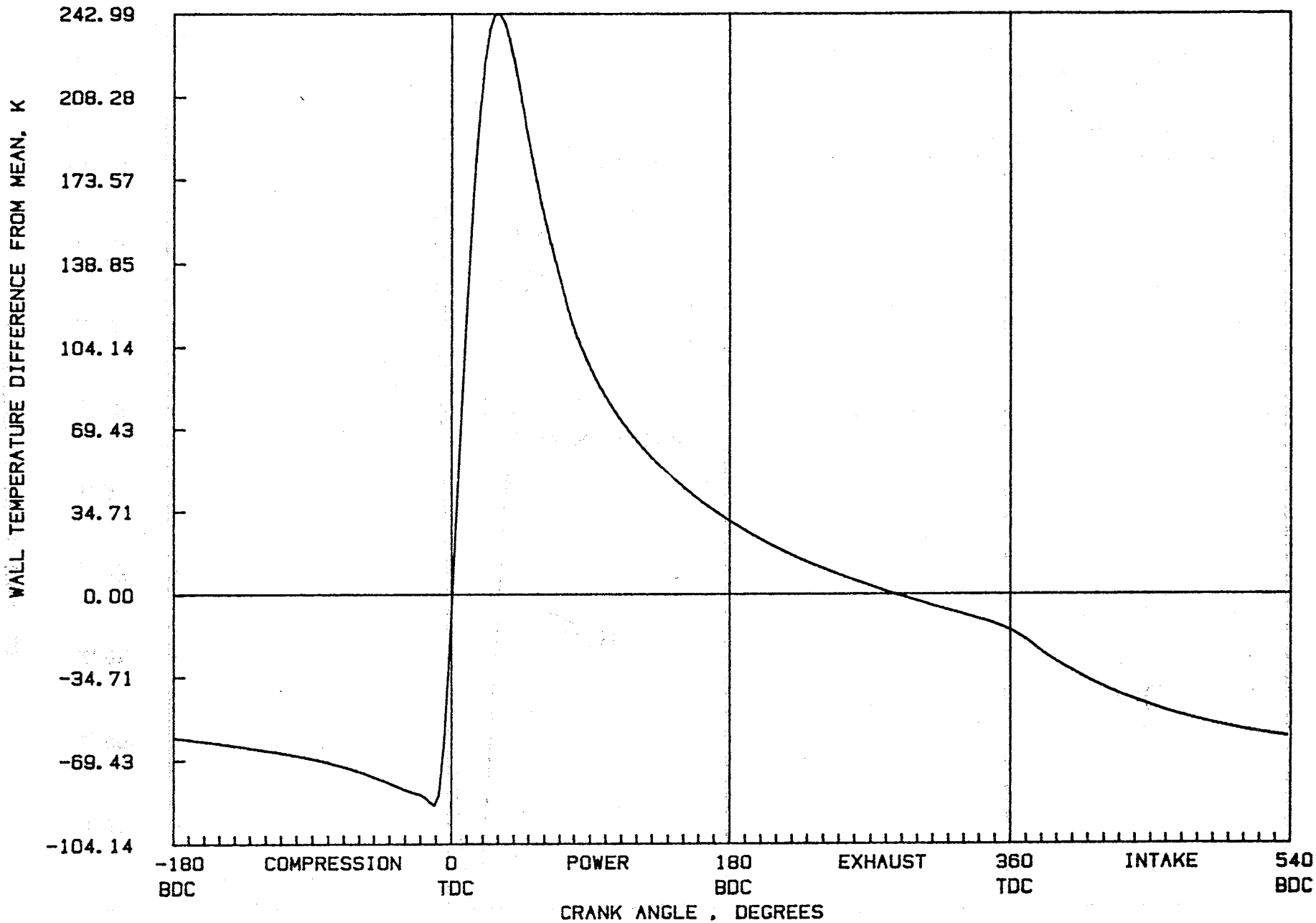

Figure 3-12. Surface temperature dynamics, zirconia coating 1.5 mm thick.

By contrast to the insulated case, iron or aluminum pistons exposed to the same conditions experienced much lower temperature swings, as may be seen in Figs. (3-13) and (3-14). For the aluminum piston, the time mean surface temperature was only 598°K, and as a result the heat flux had a much higher peak than for the insulated case due to a much larger convection heat transfer (Figure 3-15). As already noted above, heat radiation accounted for 30 percent of the total heat transfer in this particular case.

Parametric Study of the Effects of Material Properties

Using the same general test case as in the previous example, the calculations were extended to cover a wide range of material properties. The objective was to explore the general trends of various parameters with changes in material properties, specifically

1. magnitude of surface temperature swings;
2. correlation term ΔT_{wh} which reduces the effective gas temperature;
3. heat flux per unit area, convective and total (including heat radiation);
4. "pumped heat" per unit area, representing the heat that is transferred to the wall during one phase, only to be returned to the gases later (when gases are cool);
5. penetration depth of the temperature waves, defined as the distance at which the temperature amplitude decays to one percent of the surface amplitude.

In all of these calculations the thickness of the insulating layer was taken to be 10 mm, and the temperature at the interface between the insulation and the substrate was fixed at 575°K. This simulates the situation where one reduces the effectiveness or size of the cooling system to compensate for the decreasing heat transfer, in order to maintain metal temperatures at the maximum permissible values. In other words, this represents a situation where the designer takes the full

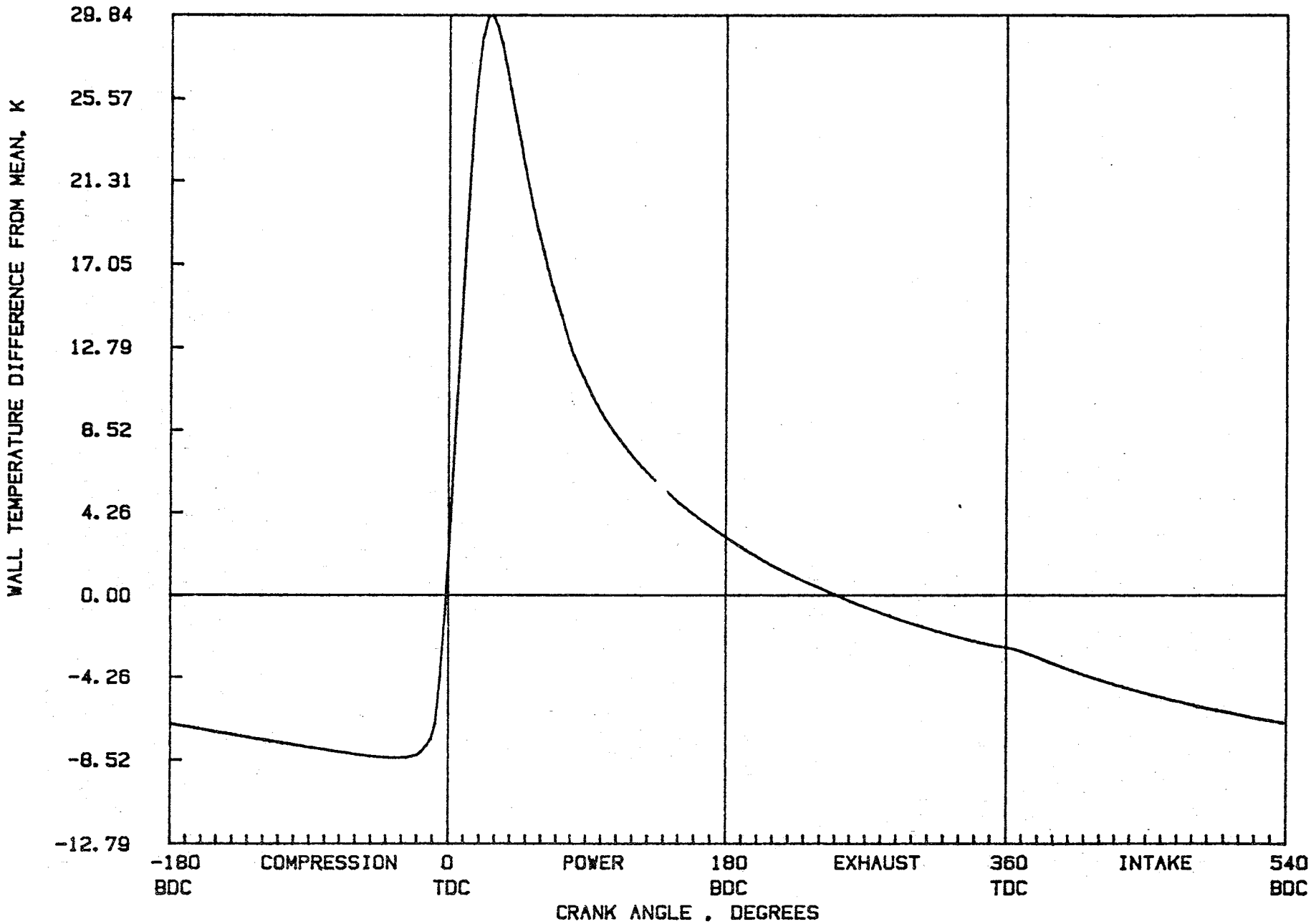

Figure 3-13. Surface temperature dynamics, iron piston.

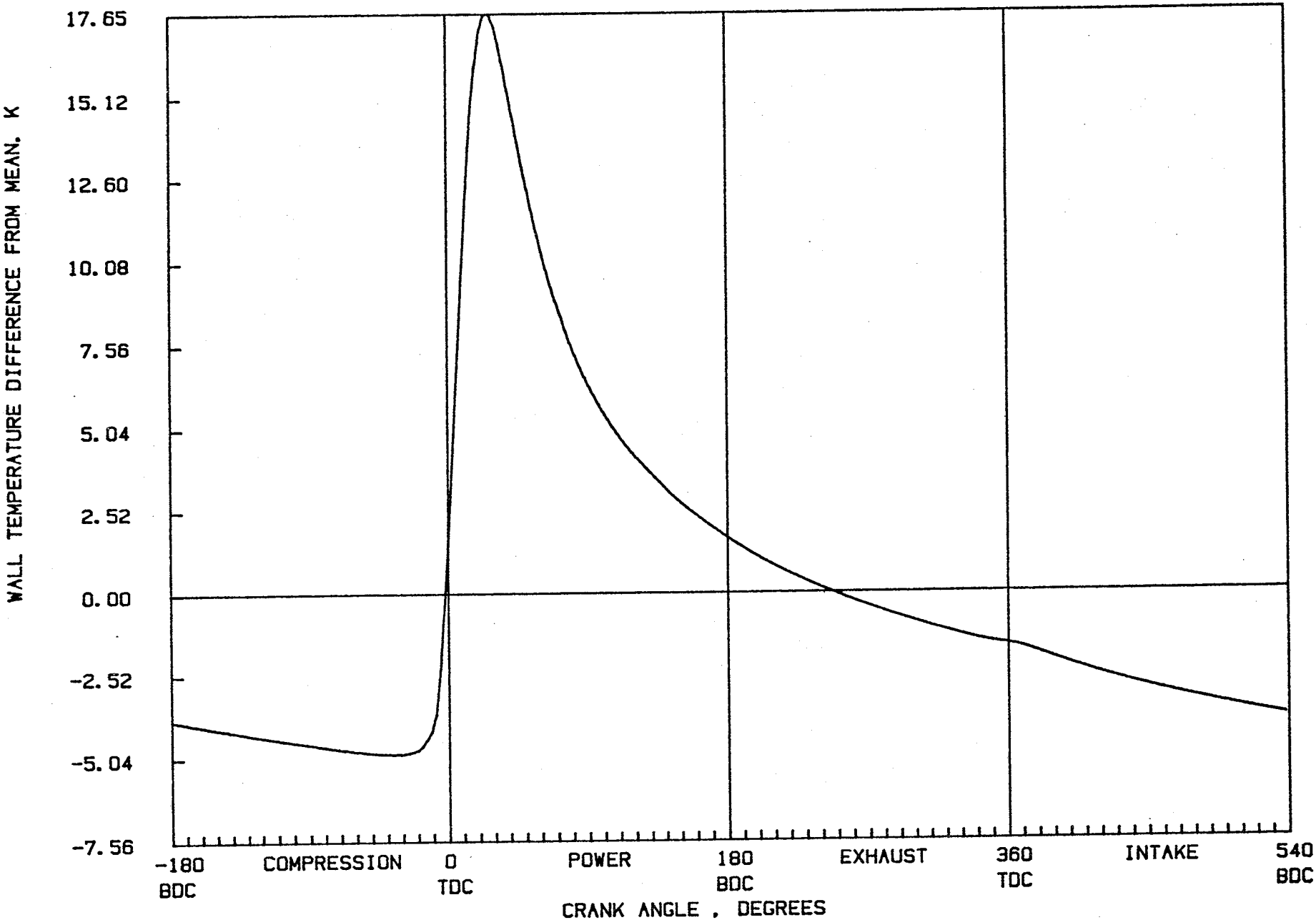

Figure 3-14. Surface temperature dynamics, aluminum piston.

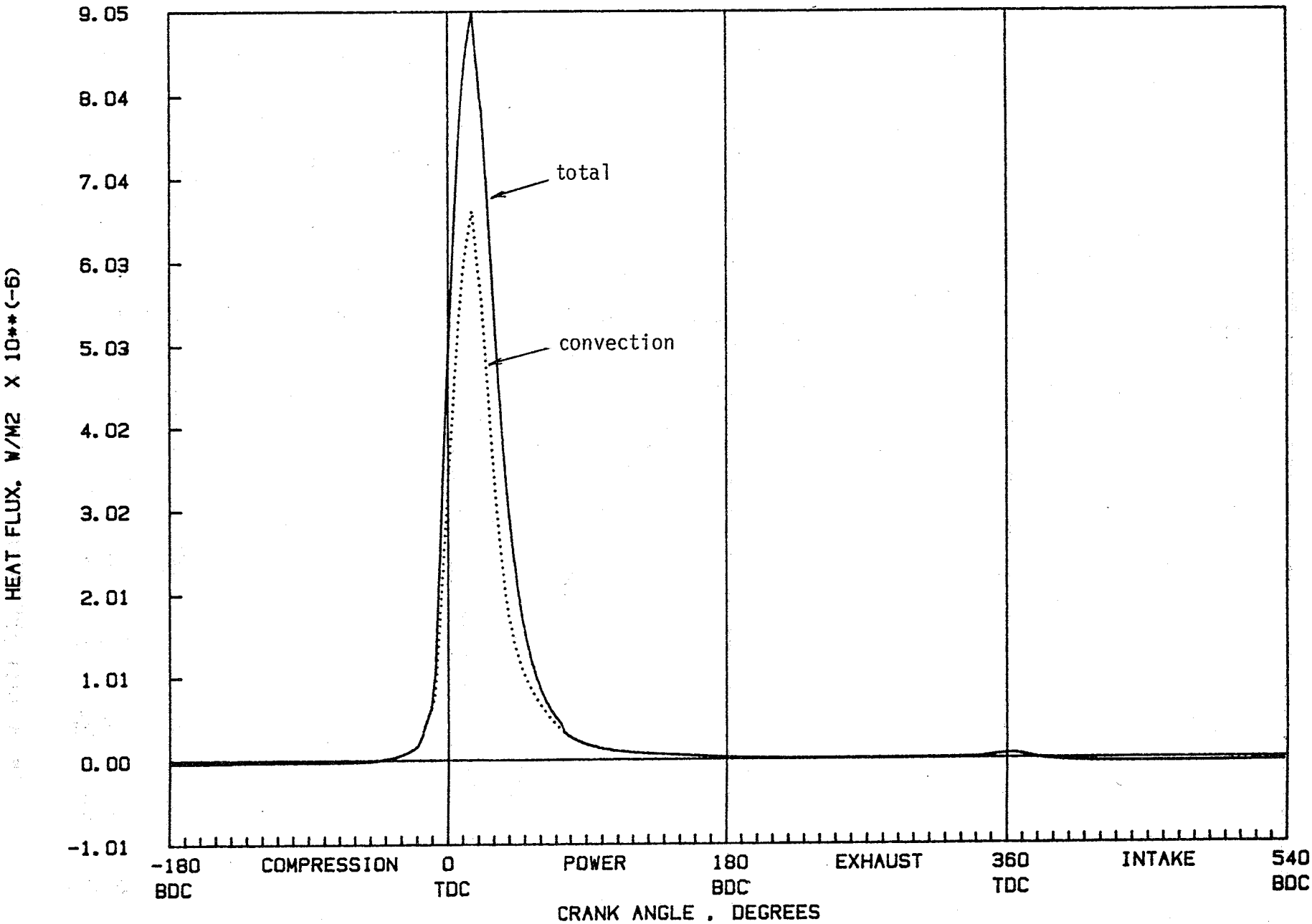

Figure 3-15. Calculated heat flux into bottom of the cup, aluminum piston.

advantage of the benefits provided by the insulation. The ranges of material properties were k = 0.02-210 W/mK and ρc = 0.1-3.1 x 10^6 J/m^3K, plus a case with $\rho c = \infty$ which produced only a steady-state solution with no swings.

The magnitude of surface temperature swings, under the specified engine conditions, is shown in Fig. (3-16). Over the range of material conditions it is found to vary from 20°K to over 1200°K, increasing with decreasing k and ρc, respectively.

The correlation term ΔT_{wh} has a behavior roughly similar to that of the swing amplitude (Figure 3-17). It may be recalled that this term represents an apparent reduction in the time-mean effective gas temperature seen by the surface due to the presence of the swings. When expressed in a dimensionless form, as a ratio to the swing amplitude, it tends to a constant value of about 0.28 for conductivities typical of metals (Figure 3-18). At lower conductivities the ratio tends to be lower, especially for high thermal capacities.

The heat flux into the walls is found to decrease with decreasing k only very slowly at first (Fig. 3-19). This is because for conventional metallic materials the heat flux is dominated by the gas-wall convection and radiation heat transfer, while the wall itself offers only a small resistance to the heat flow. Only below k of about 20 W/mK does the wall begin to exert a significant influence and the heat flux gradually becomes conduction dominated. For the specific examples chosen here, the net convective heat transfer becomes negative when k drops below 2W/mK, and begins to offset the always-positive contribution due to heat radiation. In the limit of k=0 the two components of the heat transfer are equal and opposite and there is no net flux into the wall. It is interesting to note that the net heat flux is only weakly dependent on ρc and on the swing magnitude: there is only a very small difference between the curve for $\rho c = \infty$, i.e., zero swings and the bottom curve where swings are quite substantial. This is in contrast to the results for the pumped heat discussed below.

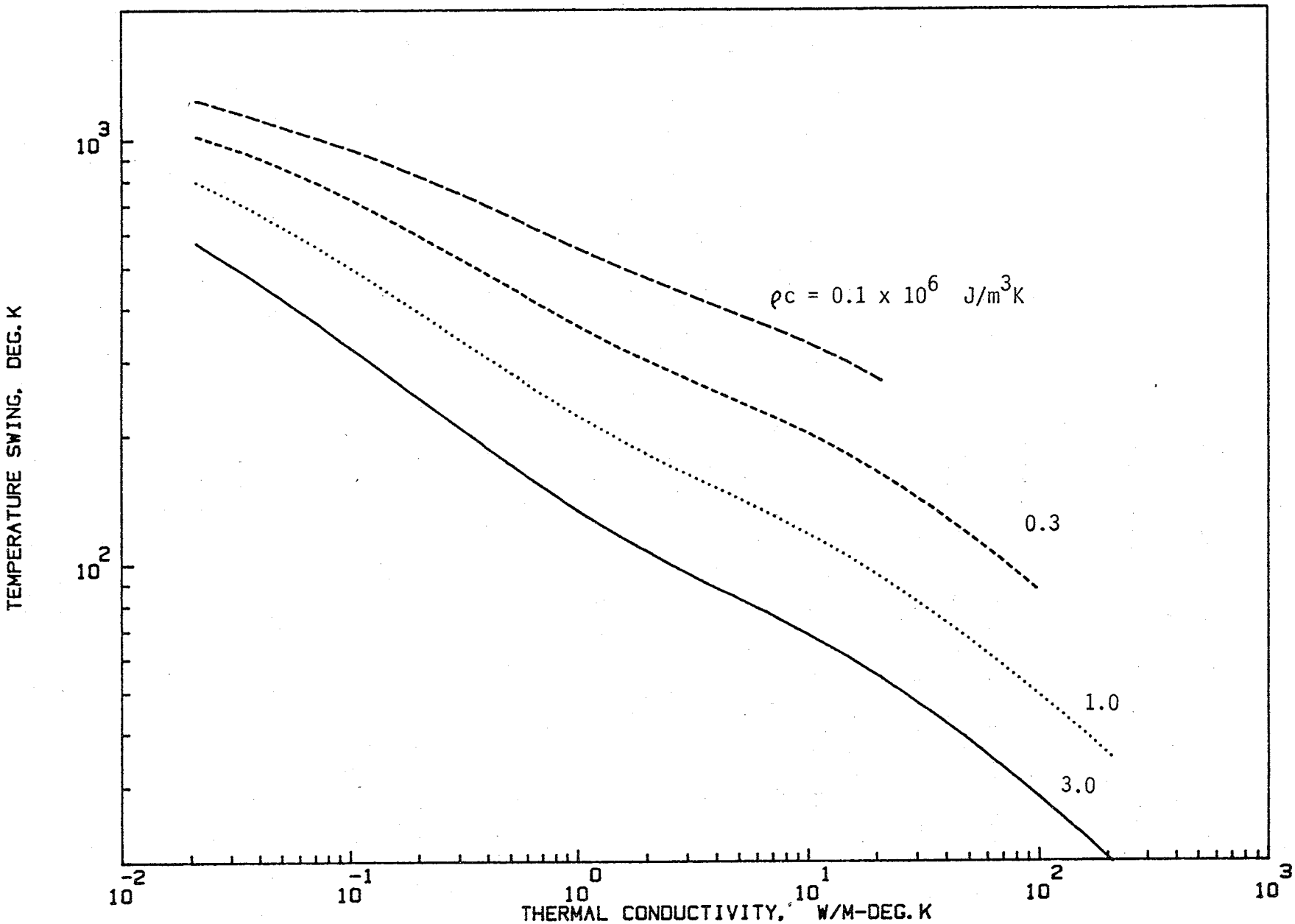

Figure 3-16. Swing magnitude on the bottom of the cup as a function of conductivity and heat capacity.

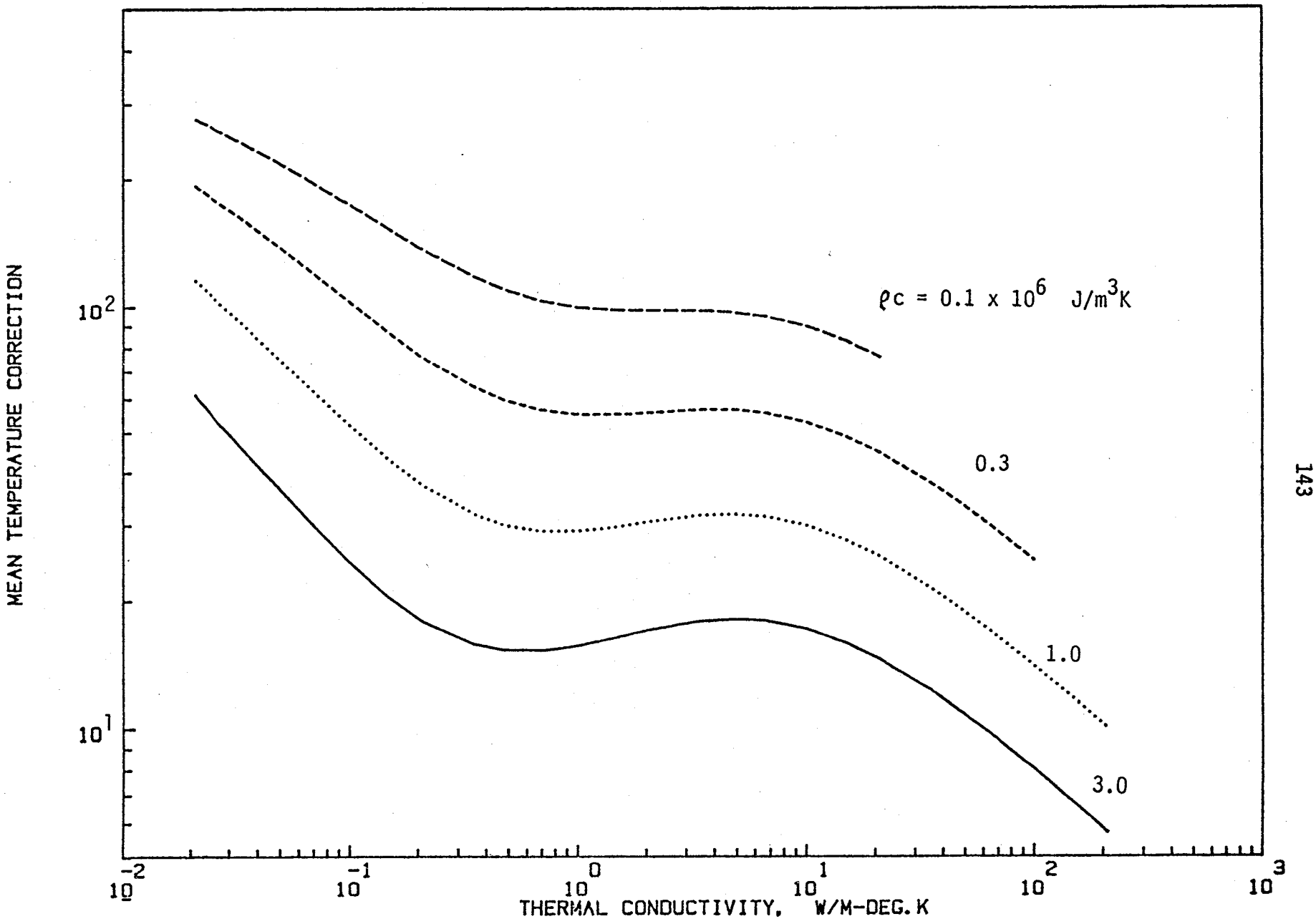

Figure 3-17. Mean temperature correction calculated from the correlation of T_W with h_g.

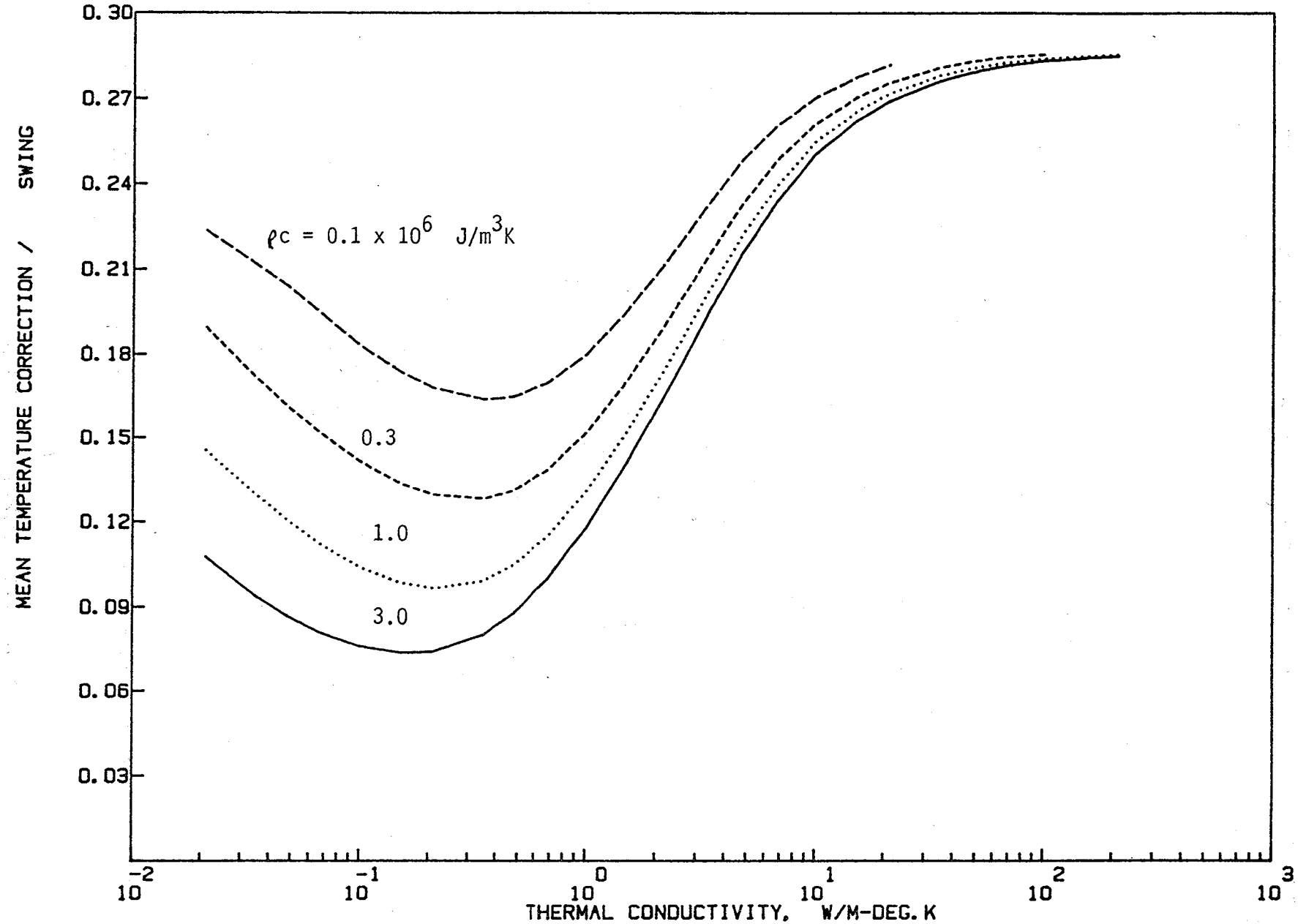

Figure 3-18. Ratio of mean temperature correction to swing amplitude

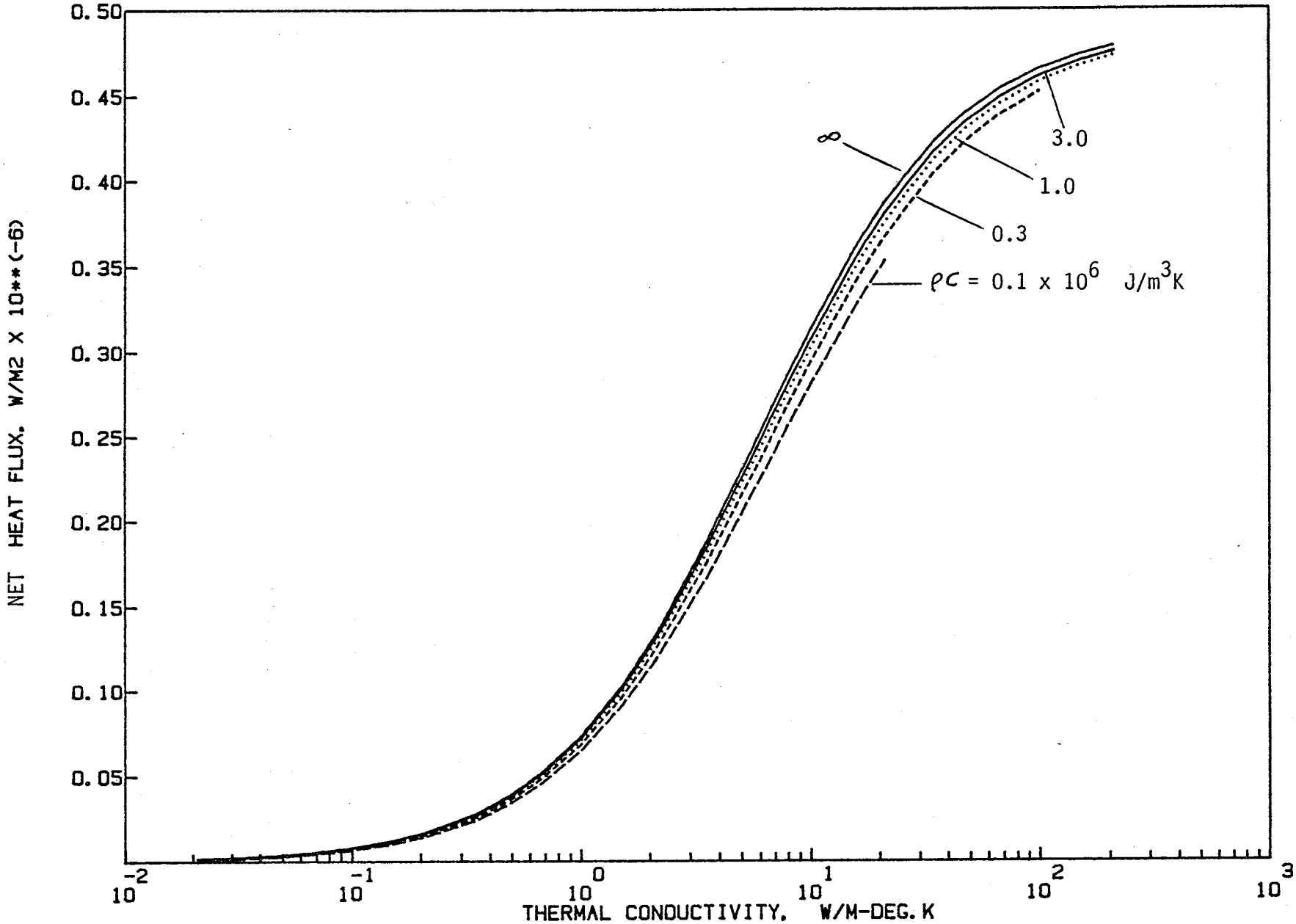

Figure 3-19. Cycle-averaged heat flux

Increasing level of insulation produces increased levels of "pumped heat", which is the heat absorbed by the wall near TDC of compression stroke and returned to gas during the rest of the engine cycle. This results from the fact that the mean wall temperatures are higher. Although this heat represents zero net flux out of the combustion chamber, its effect is detrimental. This is because heat is being extracted from the gases at the time when it is most needed (for generation of piston work) and is returned to them during the intake period when it adversely affects volumetric efficiency. The pumped heat is defined as one half of the difference between the integral of the absolute heat flux minus the net heat flux, i.e.,

$$Q_p = \frac{1}{2} \left(\overline{|q|} - \bar{q} \right) \qquad (3\text{-}22)$$

As wall heat conductivity is reduced, the wall temperatures rise and so does, initially, the pumped heat, (Figure 3-20). The pumped heat goes through a maximum and drops again (except for $\rho c=\infty$), and it tends to zero as k and ρc both go to zero. For a given k the higher the swing (the lower the ρc) the lower is the pumped heat. It may be noted that the pumped heat for a highly insulated surface can be as large as one-third of the net heat flux for a metallic un-insulated surface! The pumped heat concept is of profound importance to insulated diesels; it is an significant quantity which has to be considered together with the net heat transfer when evaluating an effectiveness of insulation layers.

Figure (3-21) shows the ratio of pumped heat to the absolute heat flux. It is seen that at high values of k, when the surface is relatively cool, there is only a small amount of pumped heat. However, as k is reduced, the net heat flux drops much more rapidly than the absolute heat flux and so the ratio of the pumped heat to the absolute heat flux increases. In the limit of very small conductivity, the net flux approaches zero, and so the ratio tends asymptotically to 0.5, as would be expected from equation (3-22) according to which Q_p tends toward $1/2|q|$.

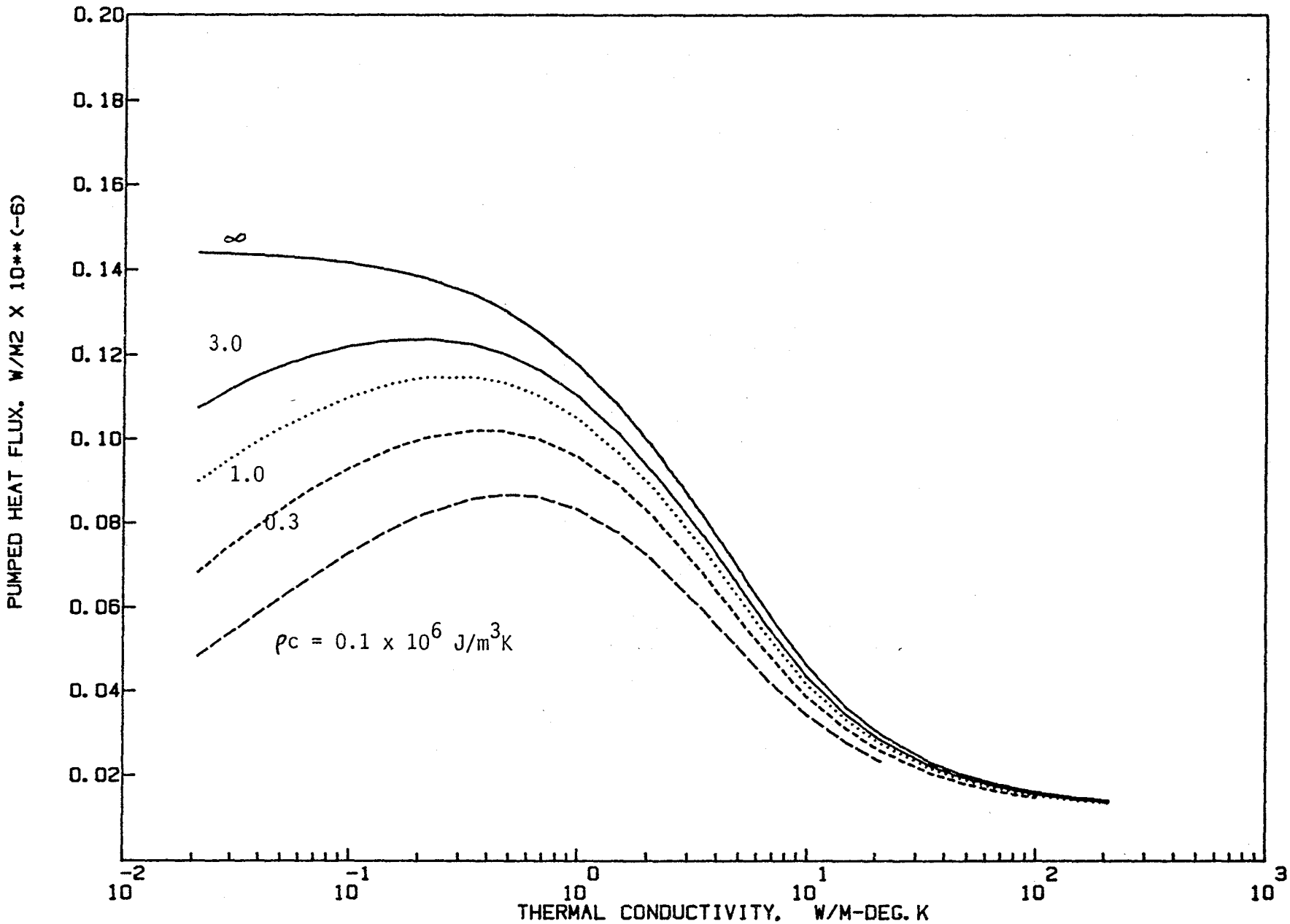

Figure 3-20. Pumped heat

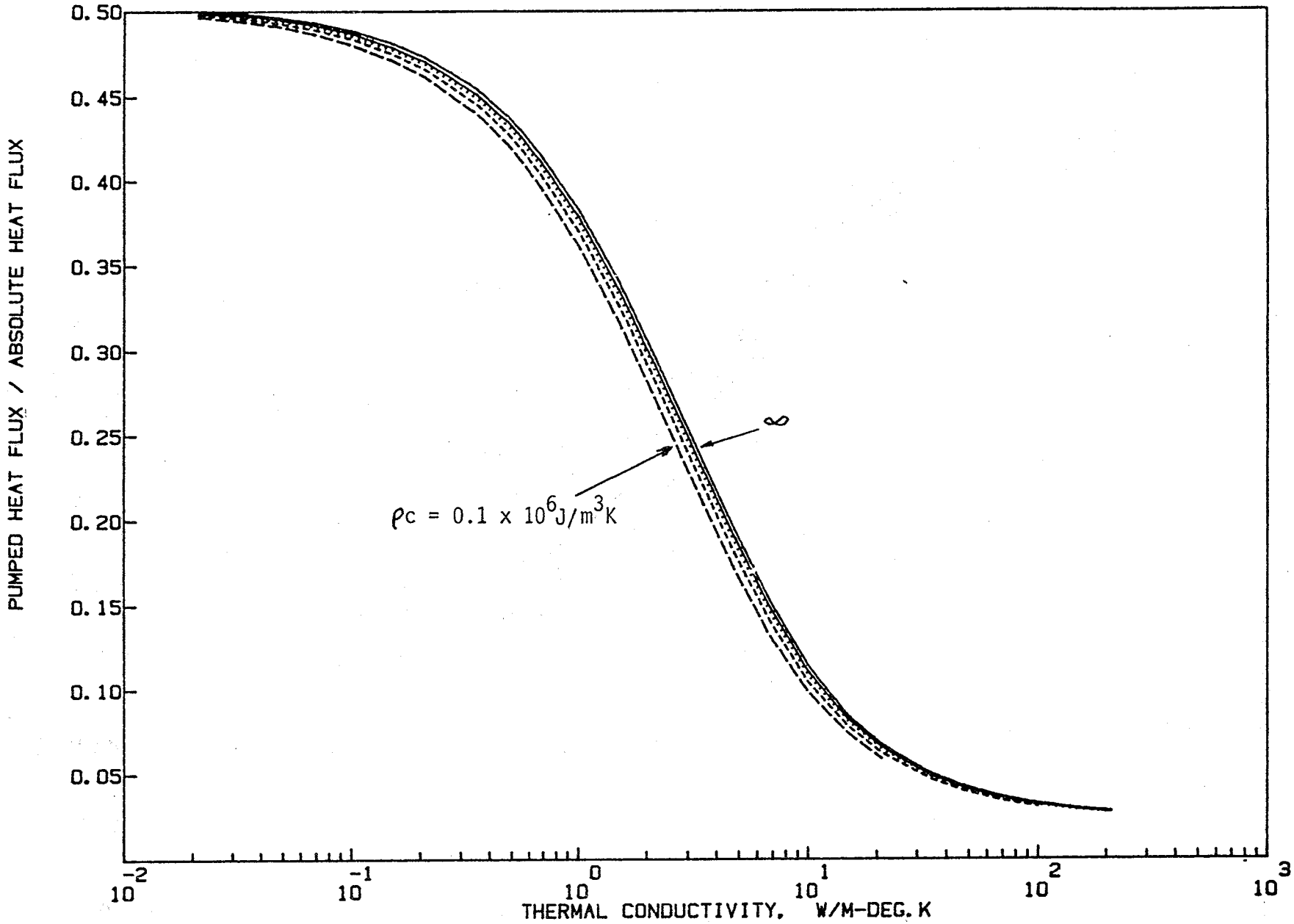

Figure 3-21. Ratio of pumped heat to cycle-averaged absolute heat flux

To complete the picture of this parametric study, one has to mention the penetration depth, which may be calculated from equation (3-16). For the given engine speed it varies over the wide range shown in Fig. (3-22). Depths as small as 0.0001 m (0.004") occur at one end of the range studied, extending to over 0.01 m at the other end. Since in this parametric study we kept the material thickness at 10 mm, the cases where the penetration distance was greater than this thickness could not be calculated with the particular boundary condition used, i.e. fixed temperature at the depth of 10 mm.

References

Bradish, J. P., Myers, P. S., and Uyehara, O. A. (1966), "Effects of Deposit Properties on Volumetric Efficiency, Heat Transfer and Preignition in Internal Combustion Engines," SAE Paper 660130.

Cawley, J. D. (1984), "Overview of Zirconia with Respect to Gas Turbine Applications," NASA Technical Paper 2286, NASA Lewis R.C.

Goldsmith, A., Waterman, T. E. and Hirschhorn, H. J., "Handbook of Thermophysical Properties of Solid Materials, Volume III: Ceramics," The MacMillan Company, New York, 1961, pp. 932-931

Shamah, E. (1967), "Unsteady Heat Transfer Simulation for a Diesel Engine," M.S. Thesis, University of Wisconsin.

Wallace, F. J., Way, R. J. B. and Vollmert, H. (1979), "Effect of Partial Suppression of Heat Loss to Coolant on the High Output Diesel Engine Cycle," SAE Paper 790823.

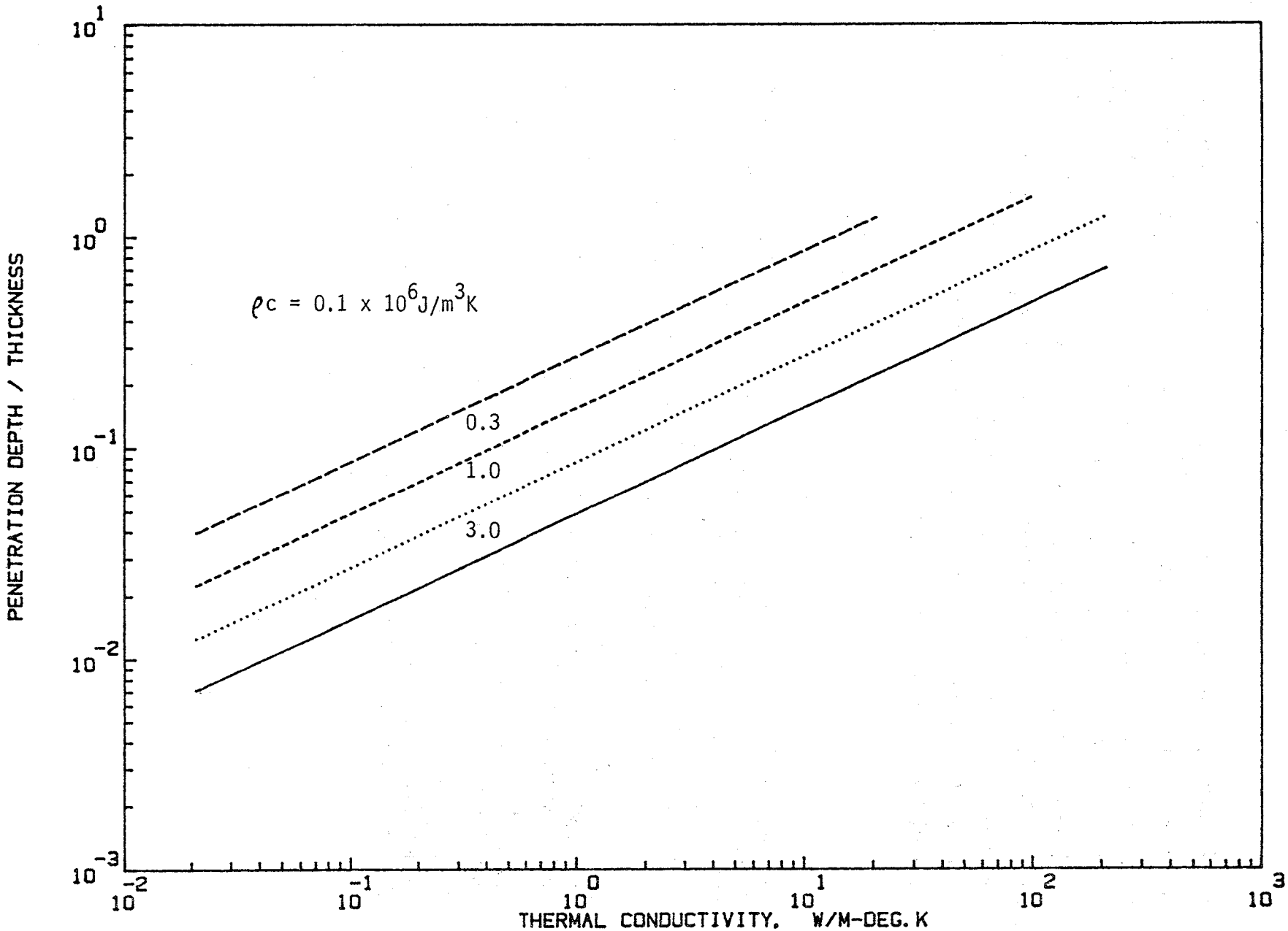

Figure 3-22. Ratio of penetration depth to layer thickness (10 mm) based on the firing frequency.

IV. STEADY-STATE HEAT CONDUCTION IN ENGINE STRUCTURES

The heat transfer from the gases to the walls is strongly coupled to the wall temperatures. These in turn depend on the net (steady-state) heat flux which establishes temperature gradients in the structure, as shown schematically in Figure 3-1. Thus, the heat transfer problem requires the simultaneous solution of all the elements of the process: convection and radiation from gases to walls, temperature transients in the thin surface layer and steady-state multidimensional heat transfer through the structure.

In the first phase of this program the steady-state heat conduction was approached via network analysis utilizing ITI network conduction model described in the Appendix. This model approximates the entire engine structure by discretization into over 150 elements. Although this level of discretization is not detailed enough to describe full three-dimensional effects, it does provide a quite realistic description of the structure in an axisymmetric form, sufficient for identification of main heat paths.

Using this model one can address a number of issues that up until now could not be addressed in the context of thermodynamic cycle simulation:

a) analysis of major heat transfer paths between the gases and the coolant or oil;
b) analysis of effects of piston geometry;
c) realistic simulation of heat deposition due to ring and piston friction;
d) meaningful breakdown of combustion chamber surface into a number of individual areas;
e) analysis of effects of different materials including effects of material layer thickness, conductivity and specific location.

The model is sufficiently detailed to permit parametric studies of the effects of various insulating strategies, such as those described in the next chapter.

During the second and third phases of the program we shall augment the present level of heat transfer analysis by going one step further to the detailed finite element methods (FEM). The objective will be to provide a more detailed description of the structure and of the temperature profiles. Using NASTRAN finite-element program we shall also address three issues that have not been up until now studied: 1) direct coupling of FEM and thermodynamic engine cycle analysis; 2) correct treatment of moving piston/liner interface; and 3) "slow" engine transients due to sudden load changes.

V. PRELIMINARY ANALYSIS OF SEVERAL INSULATED DIESEL DESIGNS

A. Introduction

One of the specific tasks of Phase I of this program was to bring together all the individual elements of the methodology available at the end of the phase, and use them in an integrated fashion to perform a preliminary parametric analysis of insulated engine operation. The objective of these studies is to exercise the integrated model, including the new flow model, convective heat transfer correlations, temperature swings on combustion chamber walls and the steady-state heat conduction network, in order to:

(1) verify correct implementation of all individual elements and of their coordination and coupling;

(2) obtain feedback on additional needed refinements and capabilities and thus guide the future work to be performed in this program; and

(3) gain preliminary insights as to insulated engine performance and thermal environment versus design strategy.

These objectives were accomplished through a matrix of preliminary insulated engine design analyses, defined jointly by ITI and Cummins.

The engine simulated in these calculations is a Cummins heavy-duty highway truck engine, the NTC-350, a turbocharged 14-liter direct injection diesel. This engine forms the basis for the Cummins single cylinder research engine on which experiments will be carried out at Purdue University in the Phases II and III of this program. For most of the calculations the engine was simulated at its rated conditions (2100 RPM and fuel flow rate of 56.4 kg/hr, producing 357 BHP in baseline configuration), although some runs were also made at other engine operating conditions -- 1300 RPM, peak torque, and 2100 RPM medium load.

In order to have a meaningful comparison with the baseline for all of the runs in which low-conductivity materials were applied or where

reduced cooling was applied, the decision was made to maintain the same air flow (fuel flow was always kept fixed for each specific engine operation condition). This necessitated a larger boost pressure to offset the effects of reduced volumetric efficiency caused by heating of the inlet air in the cylinder during the intake process. This was accomplished by running the simulation with adjusted prescribed boost and time-average back pressure levels (the pressure dynamics in the exhaust plenum were simulated by a turbine-orifice model). To minimize the effect of pumping work on the calculated brake work due to increased boost, the time-average back pressure was always raised by the same amount as the boost. It was assumed that the intercooler would be resized to maintain the same air outlet temperature for all cases.

The peak firing pressures were monitored in all simulations, and it was found that they tended to increase with increasing degree of insulation. To maintain the peak firing pressure at the baseline level (130 bar) it was necessary to retard the injection in most cases, with a maximum retard of 6 degrees for the "superinsulated" case.

Specific studies that were carried out are listed below:

- Baseline iron/aluminum cooled engine operated at peak output at engine speeds ranging from rated, 2100 rpm, down to 800 rpm. This included the peak torque operating condition at 1300 rpm.
- Superinsulated all-ceramic engine, in which all structural materials were replaced by a very low conductivity material. The engine was operated only at the rated condition.
- Effect of insulation location and material properties;
  - progressive insulation of combustion chamber
  - materials comparison
  - piston insulation details
  - liner insulation details
  - port insulation
- Baseline Iron Engine with Reduced Cooling

Among the outputs of these initial analyses were the following parameters:

BHP;
exhaust gas temperature at exhaust valve and at turbine inlet,
volumetric efficiency (and boost pressure required to adjust it to baseline levels);
component temperatures (maximum and time-averaged);
major heat paths (split between piston, liner and head);
fuel energy balance; and
detailed plots of heat transfer rates into individual combustion chamber surfaces as a function of crank angle.

B. Simulation of Cummins Engine at Full Load over a Range of Speeds

In order to evaluate the general validity of the heat transfer/cycle model at its current stage of development, a series of simulations was run for comparison with test data on a typical NT family turbocharged diesel engine, obtained during the developmental stage, whose design is common with the single cylinder engine that will be used for the experimental portion of this work, i.e., the 14 liter, NH series.

Calculations were carried out for full-load fuel rates over a speed range of 2100 rpm (rated conditions) through 800 rpm, including the effects of turbocharging, using turbocharger maps obtained from Cummins (converted to dimensionless form). The geometry of the engine was described in terms of the ITI Network Analysis using engine drawings obtained from the Cummins Engine Company. The piston top was represented by a simple cylindrical cup 102 mm in diameter and 12.2 mm deep. The clearance height between the head and the piston crown was set at 4.8 mm, producing the desired compression ratio of 14.5. The predictions of the thermodynamic engine model were then compared to a comprehensive experimental multi-cylinder data set supplied by the Cummins Engine Company.

The simulation was first run at the rated conditions, i.e., at 2100 rpm and an overall stoichiometry of ϕ=0.47 producing 357 BHP. The calculations reproduced the baseline experimental data very well. The brake power (and specific fuel consumption) was high by 3.3 percent, the air flow rate (and volumetric efficiency) was low by 2.1 percent, and turbine inlet temperatures agreed within 1°K. The turbocharger and aftercooler simulation essentially reproduced plenum pressures and temperatures, and the turbocharger speed was 0.8 percent too high. These results are within the range of agreement that can be expected between engine data and model predictions, and this provided a degree of confidence in the parametric studies that followed.

This initial test case was followed by a full set of calculations simulating the engine test conditions over the range of speeds. These calculations used as input experimental data on engine rpm, fuel flow rate (injection timing was deduced from the fuel flow rate while keeping the crank angle of end of injection fixed) and atmospheric conditions. Among the output data of the simulations were a number of parameters that could be compared directly to the test data. These are shown in Figures (5-1) and (5-2). In general, the agreement is seen to be good.

The simulation also provides a number of important outputs for which comparison test data have not been or cannot be obtained. Examples are indicated power, indicated thermal efficiency, combustion chamber heat transfer, friction work, pumping work, residual fraction, peak cylinder pressure, maximum rate of cylinder pressure rise, crank angles at peak pressure and peak rate of pressure rise, ignition delay and average combustion chamber wall surface temperatures at a number of separate locations. Even though there are no test data presently available for comparison, the values of these additional data appear very reasonable in light of similar data from other engine tests.

The results of this engine simulation exercise are very acceptable in predicting the performance of a full-scale engine at full load over its usable speed range. As a consequence there is good reason to believe

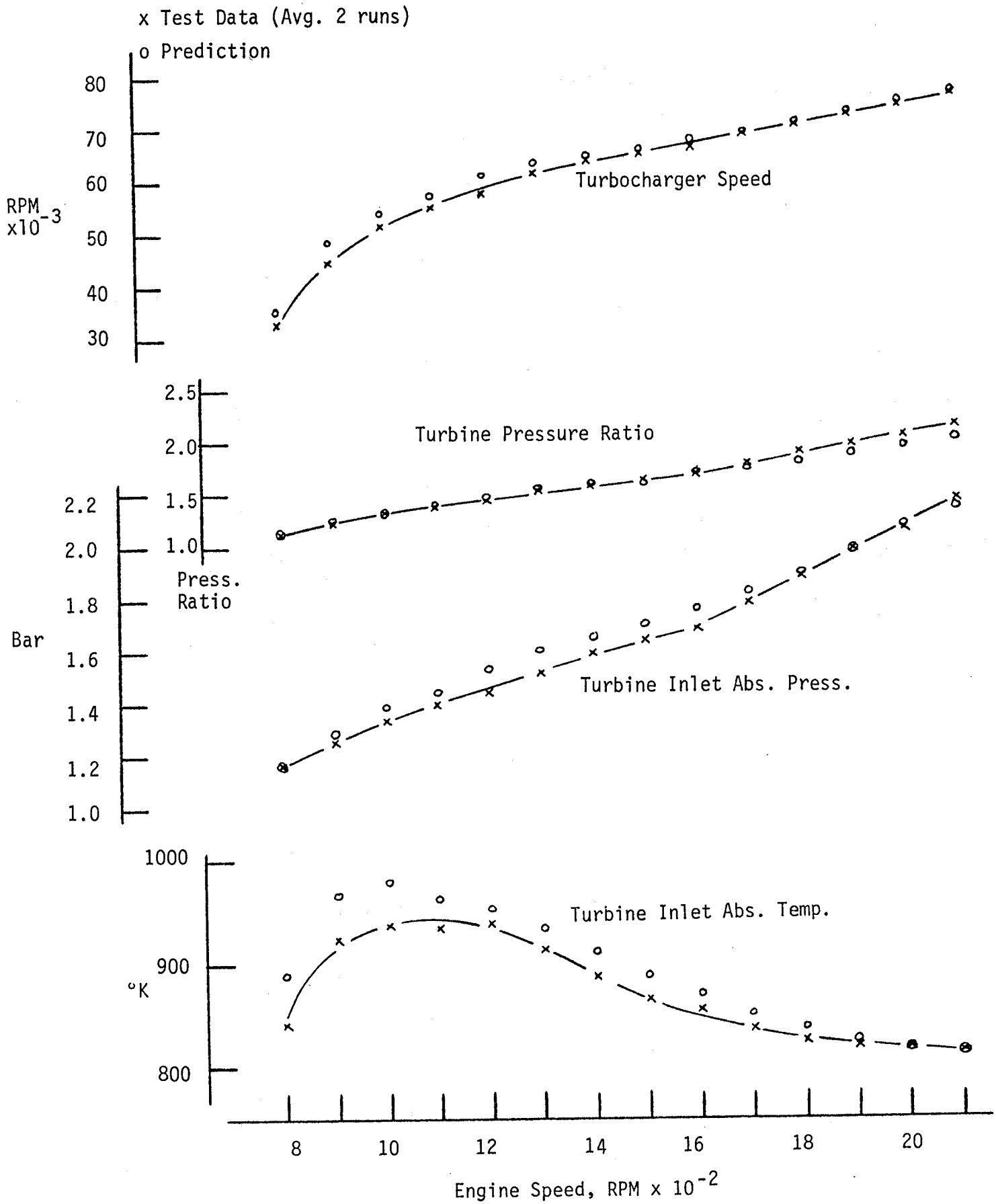

Figure 5-1. Comparison of predicted with test stand performance of a Cummins turbocharged diesel.

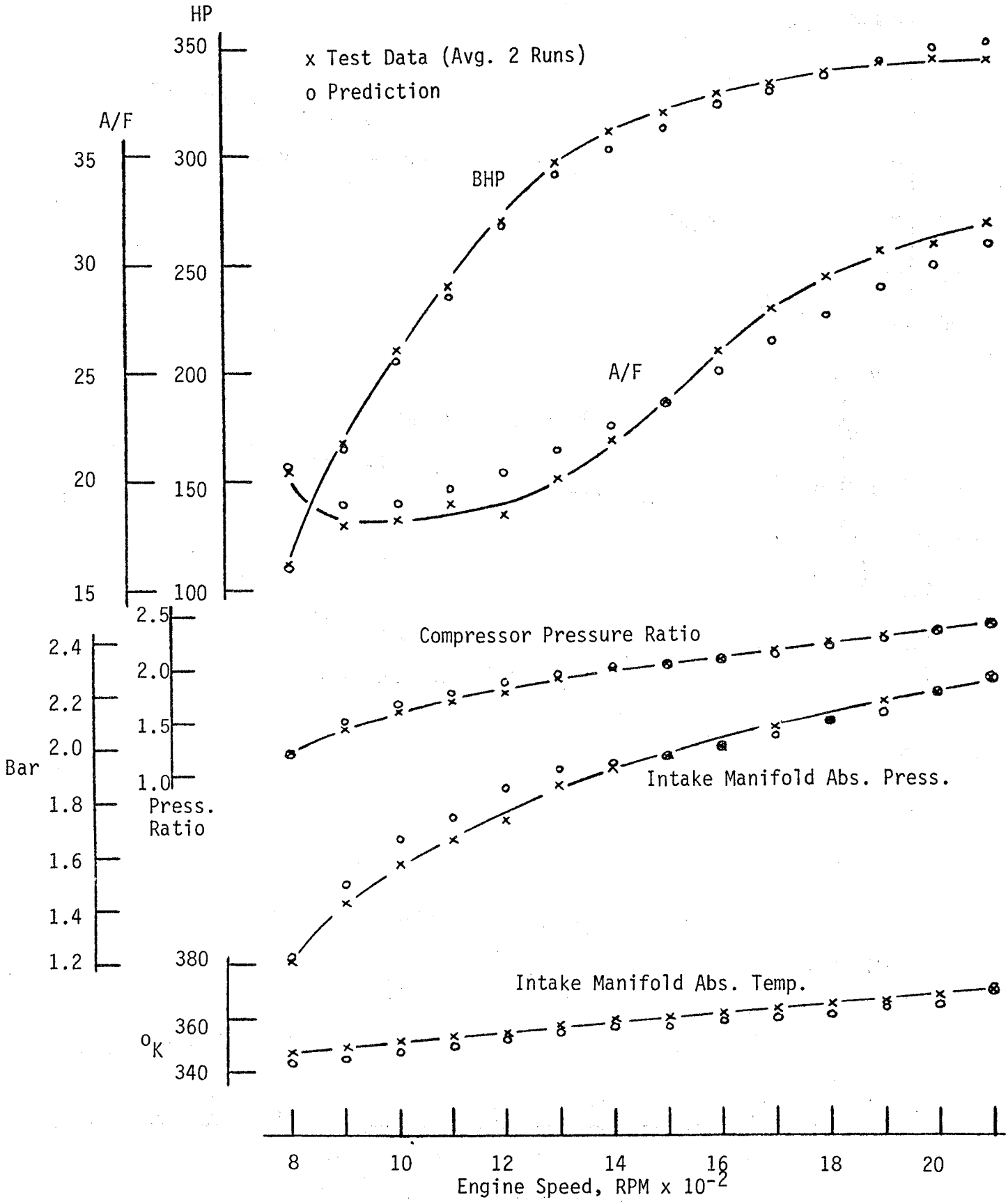

Figure 5-2. Comparison of predicted with test stand performance of a Cummins turbocharged diesel

that predictions at part load and with various insulation and cooling strategies presented later in this chapter are representative, at least with respect to general level and trends. More accuracy with respect to heat transfer and temperature profiles can be expected as the model becomes calibrated and validated with test data later in the program.

C. Standard Engine Operating at Rated Conditions

The baseline for the study of the effects of insulation on engine performance was the conventionally cooled Cummins engine operating at rated conditions.

The heat transfer and thermal analysis produced a detailed breakdown of heat fluxes into combustion chamber surfaces as a function of crank angle, and temperature distribution within the structure. The total cylinder heat transfer is shown in Figure (5-3), which displays the separate contributions of convection and radiation. The radiation heat transfer, as predicted by our present model, is seen to be brief in duration, but its maximum peak rate is about 25 percent of the total peak rate, and over the whole cycle the radiation contributes almost 18 percent to the total heat transfer. These values are within the range of values quoted in the literature. The heat transfer is spatially resolved in Figure (5-4) between the piston, liner and head (including valves). It shows that the piston receives the largest amount of heat, followed by the head and the liner. Over the whole cycle the split is as follows:

Piston	49%
Head	32%
Liner	19%

The radiation heat transfer breakdown between the three surfaces follows a similar trend as the overall heat transfer. As may be seen in Figure (5-5), the radiation deposited on the liner is the smallest of the three and is double-peaked due to the shielding effect of the piston.

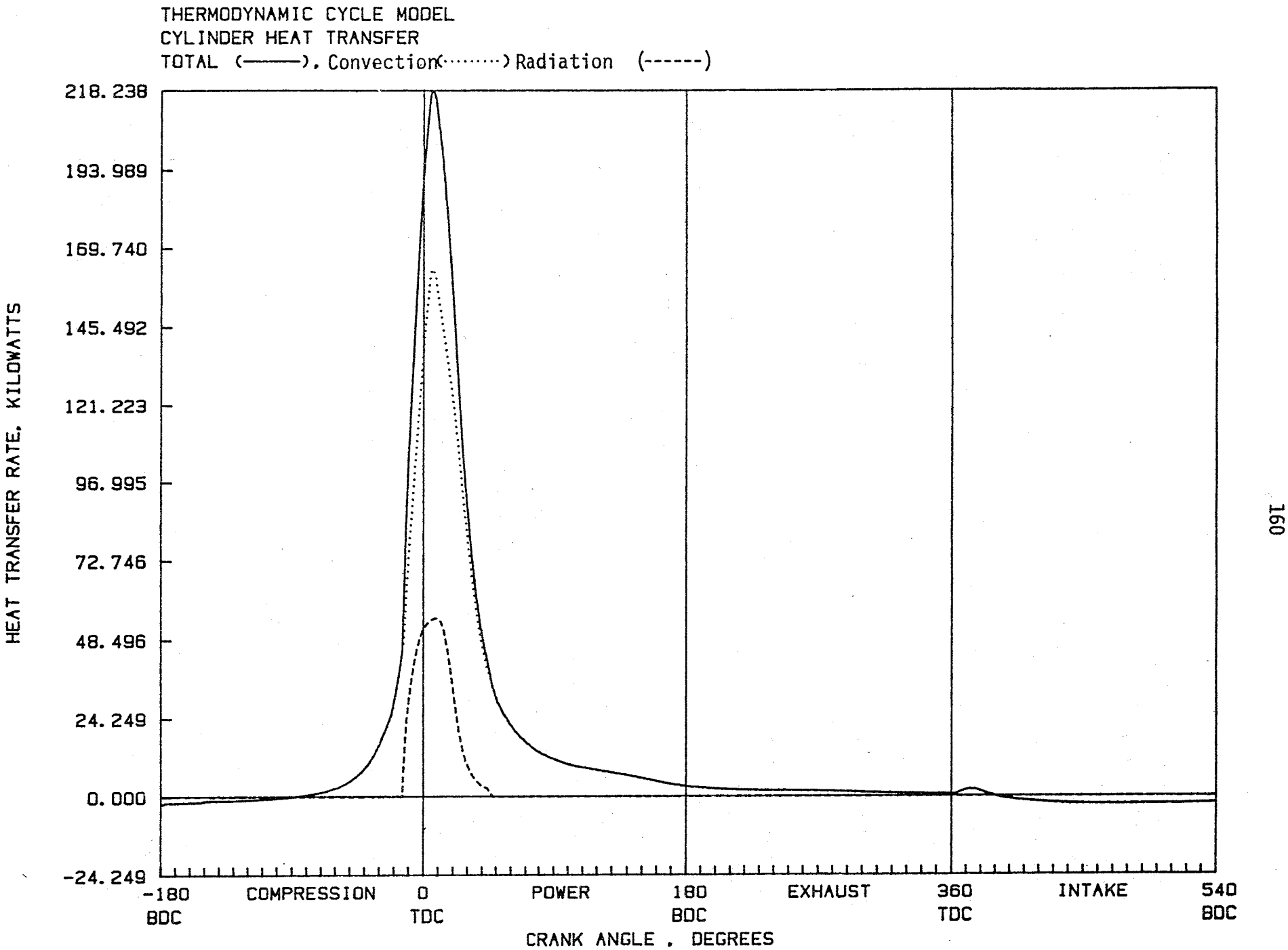

Figure 5-3. Baseline cooled engine. Total heat transfer into all 11 surfaces.

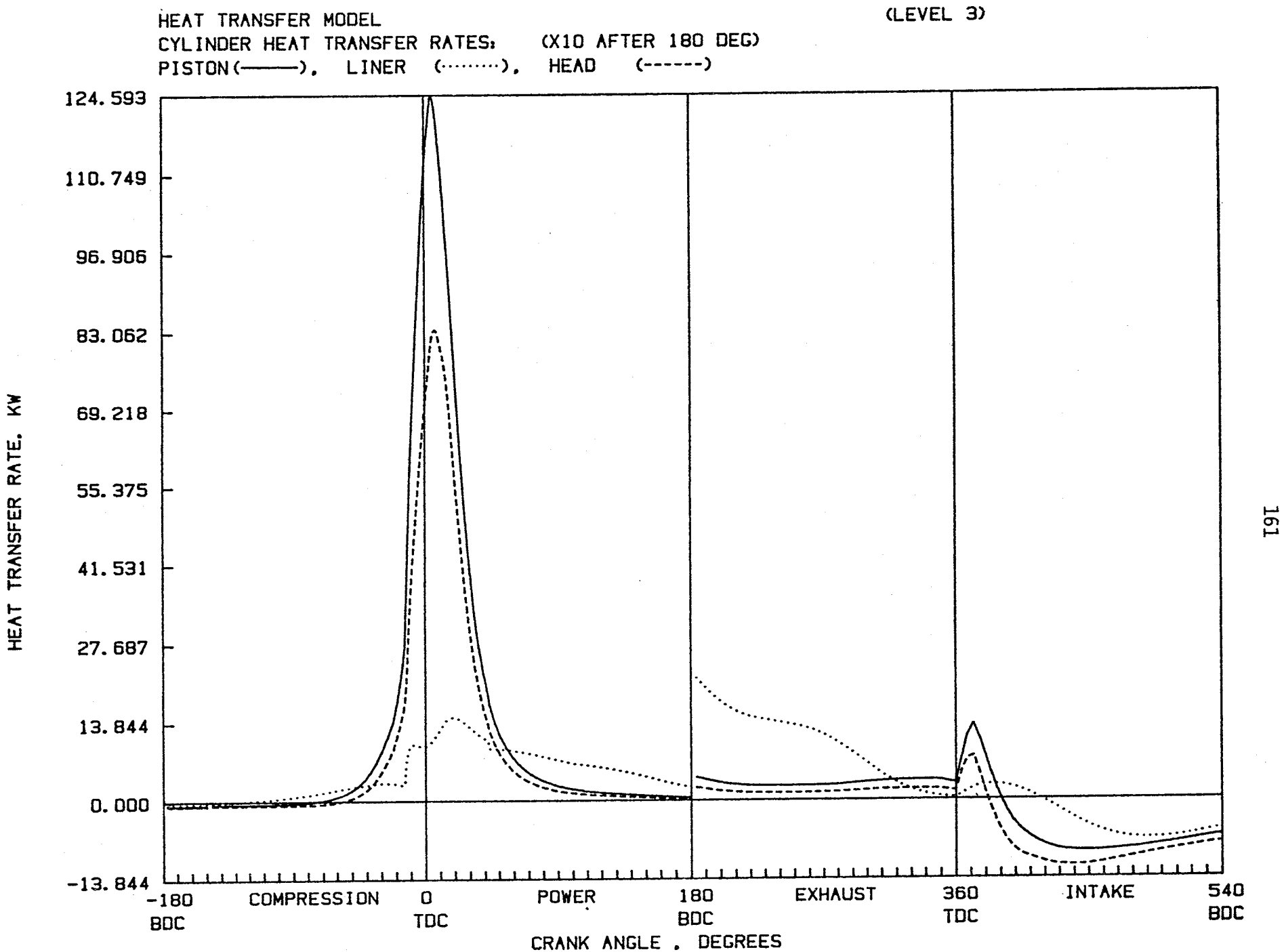

Figure 5-4. Baseline cooled engine. Breakdown of total heat transfer into piston, liner and head.

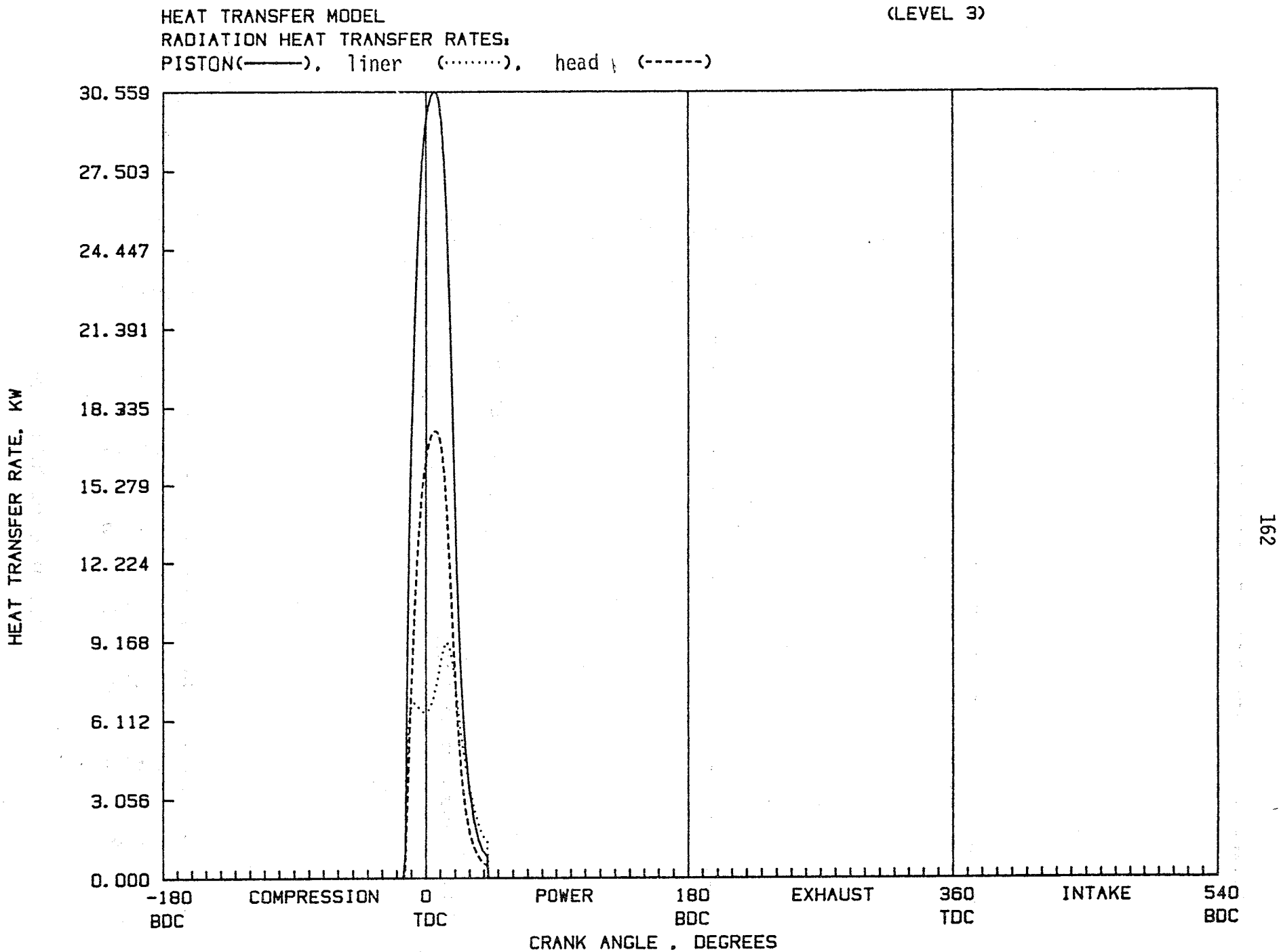

Figure 5-5. Baseline cooled engine. Breakdown of radiation heat transfer into piston, liner and head.

The total heat transfer from the gases to the three liner elements is shown in Figure (5-6). The length of top liner element is one sixth of the total (stroke + clearance), the next one is one-third of the total and the third is one-half of the total. The gas-to-surface heat transfer rate is seen to drop to zero for the two lower elements when the piston is up. During those periods the gas-liner heat transfer is replaced by piston-liner heat transfer not depicted here, but is included on a crank angle by crank angle basis in the computer model.

The resultant mean surface temperature distribution is shown in Figure (5-7), displaying the temperatures at eleven distinct surfaces.

The energy balance for the combustion chamber of the baseline cooled engine shows 47.7 percent of fuel energy going into indicated work, -1.4 percent into pumping work, 12.1 percent into heat transfer (9.9 percent for convective and 2.2 percent for radiative), and the remaining 41.6 percent represents the difference in the enthalpy flux between the exhaust and intake flows.

D. "Superinsulated" Engine Operating at Rated Conditions

The next step was the establishment of the upper limit of insulation by calculation of a case where all walls were replaced by a very low conductivity material (k=0.01 W/mK). In order to maintain the same air flow, the intake manifold pressure was raised 0.15 bar (4.4" Hg), and the exhaust back pressure was raised by the same amount.

The wall heat capacity used was $\rho c = 3 \cdot 10^6$ J/m^{3}K, and this produced, with the chosen engine operating conditions and heat conductivity, fairly large wall temperature swings on the order of 500°K. In all of the present calculations we used the swing correlation to describe the wall temperature dynamics in an approximate way. A complete solution of the temperature dynamics will be implemented during the Phase II of the program.

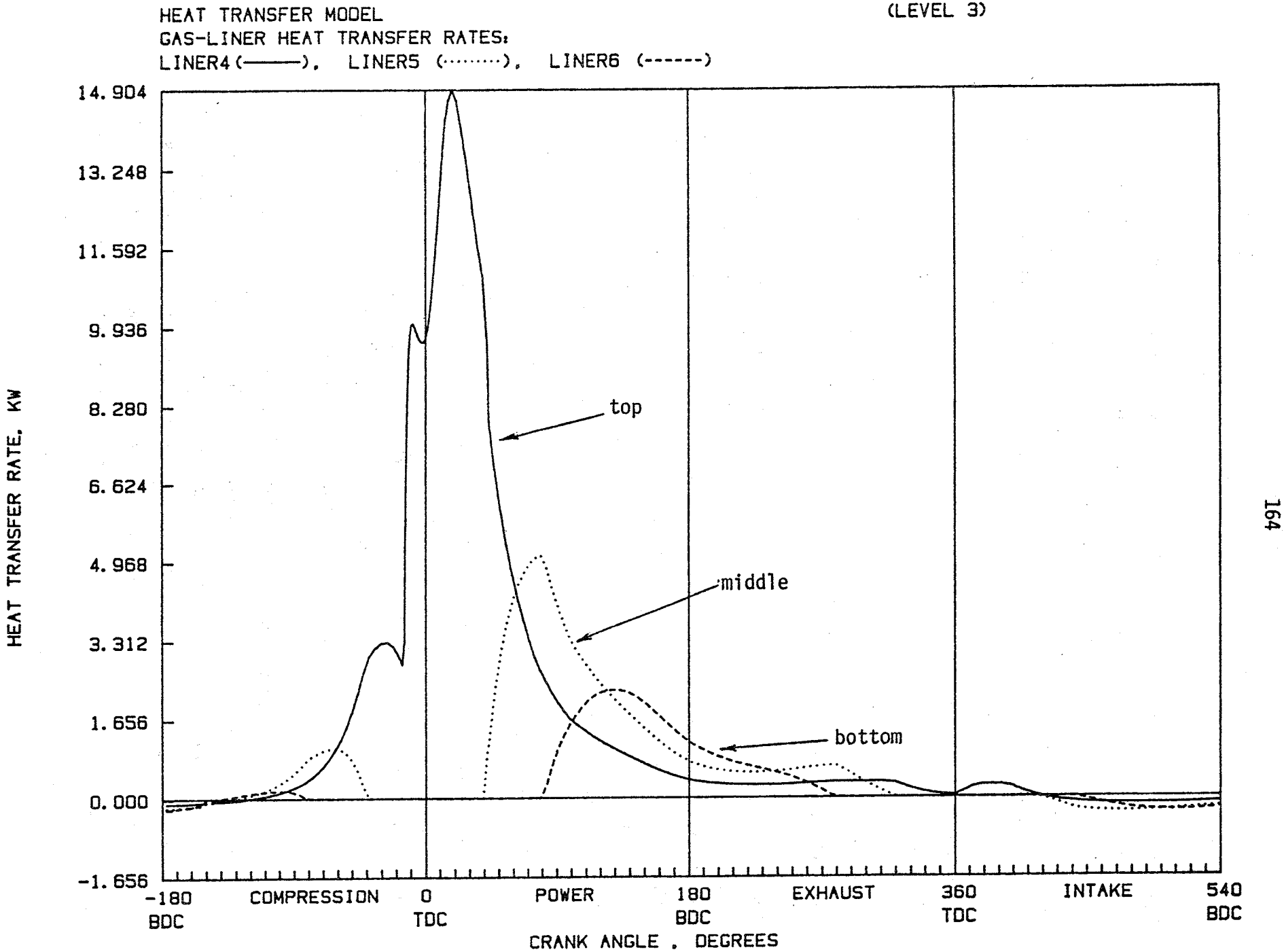

Figure 5-6. Baseline cooled engine. Total heat transfer into the three liner elements.

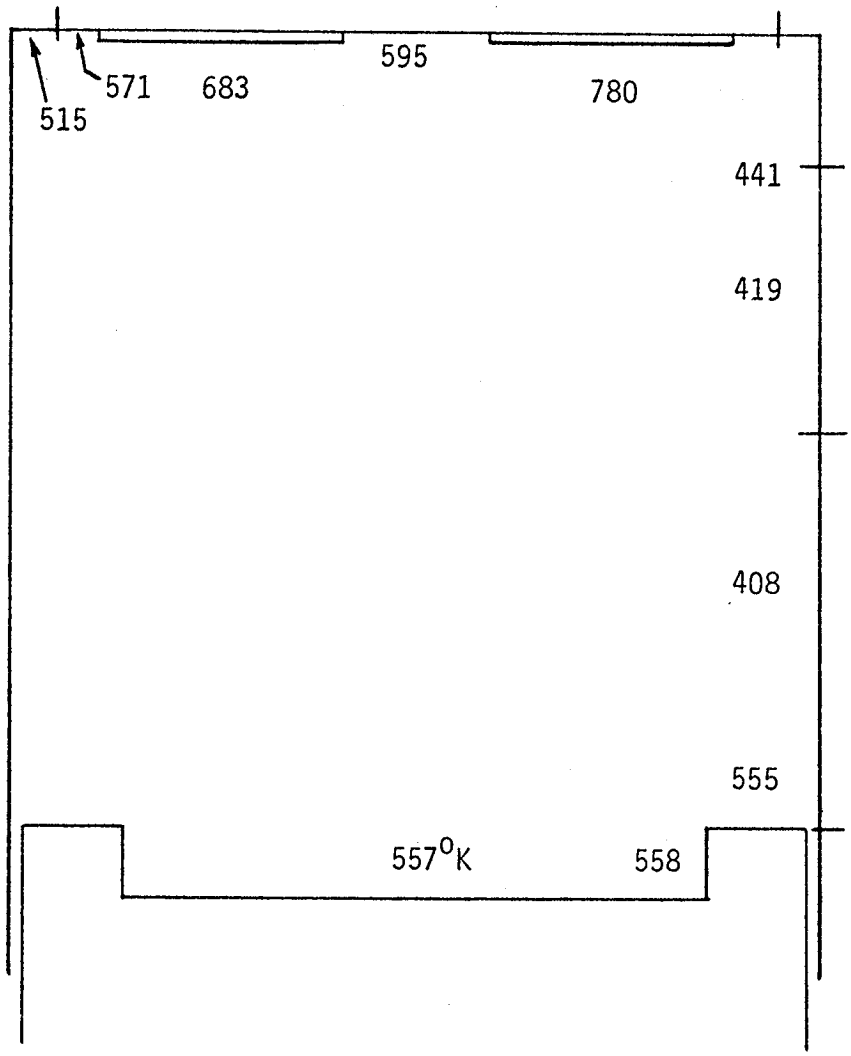

Figure 5-7. Baseline cooled engine. Temperature distribution along combustion chamber walls.

Since the conductivity was so low, there was essentially zero heat transfer through the wall for all reasonable values of coolant temperature and heat transfer coefficients. The only exception was the lower liner element exposed to oil cooling when the piston is away from BDC. The calculations proved to be sensitive to the values of T_{oil} and h_{oil} chosen there, as this boundary is the only heat path left in the super-insulated design. When the piston is near BDC it heats the surface by direct heat transfer as well as by friction heat, and when the piston is up, oil extracts the heat from the surface. The friction heat along the liner/piston interface is calculated to amount to 5% of fuel energy. In the simulation we chose T_{oil}=500°K and h_{oil}=200W/m^{2}K. With these choices the overall cycle-average heat flows are as shown in Figure (5-8).

Due to the high degree of insulation, almost no heat is transmitted through the walls. This means that the mean wall temperatures have to rise to the precise level at which the cycle averaged heat into the wall approaches zero. This has two consequences, one of which has to do with the temporal heat flux variation, and one with the relation of cycle-averaged convective and radiative components of the heat transfer. Since the total instantaneous flux into any surface has to integrate to zero, the large positive peak generated during combustion must be exactly offset by negative heat transfer during the rest of the cycle. Heat radiation is always positive (the flame temperature is always higher than the wall temperature) and this means that the convective component must be negative on the cycle-averaged basis, and that it in fact provides wall cooling.

The resulting mean wall temperatures (Figure 5-9) consequently display a wide variation along the surfaces of the piston and the head, reflecting the local balance between convection and radiation. Surfaces where radiation is high, reach a higher mean surface temperature than the rest. Similarly, surfaces with high flow velocities tend to be cooled more effectively by the convection heat transfer, and this tends to keep those surfaces cooler. The situation on the liner is quite different,

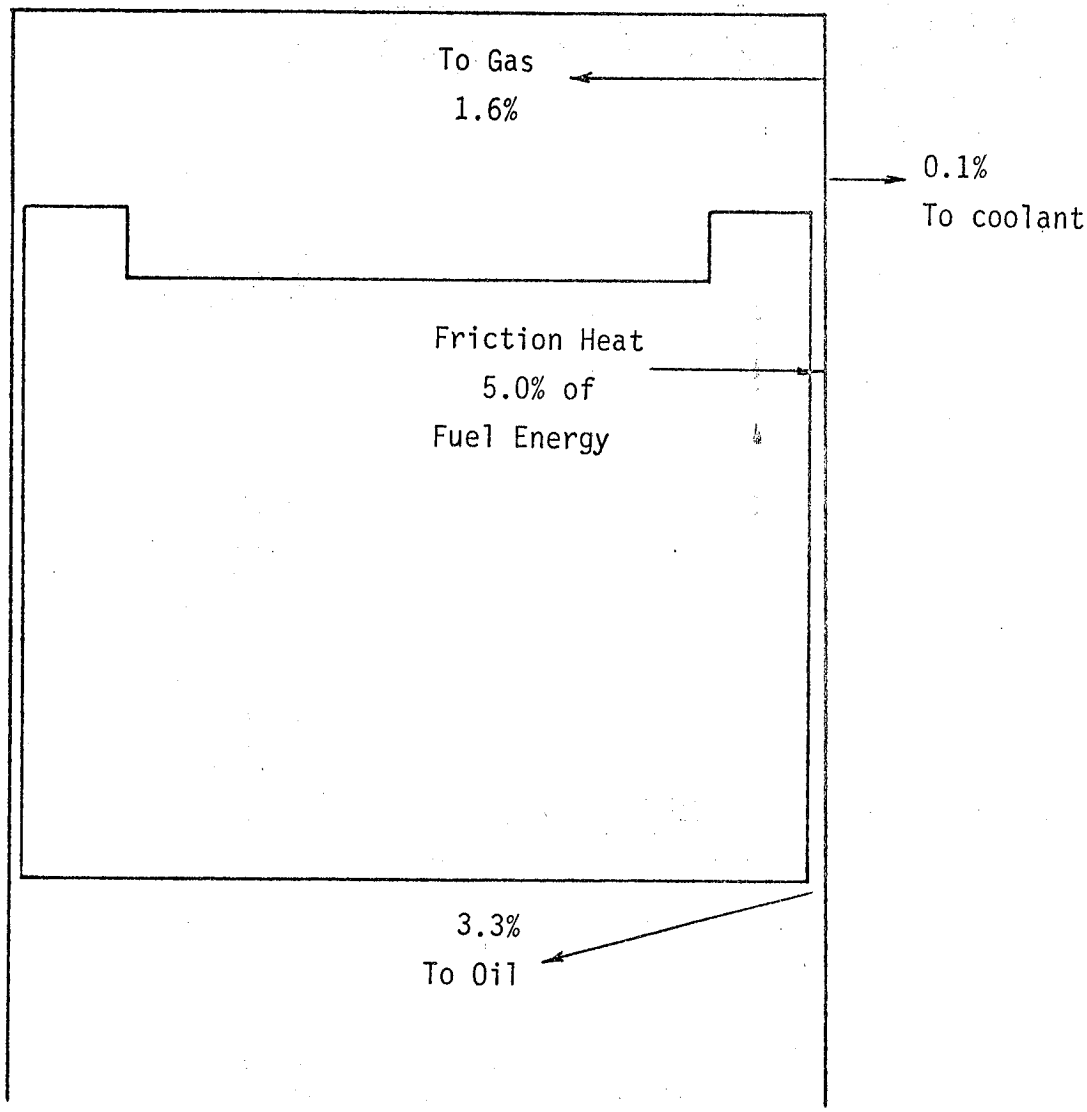

Figure 5-8. Superinsulated engine. Main heat paths.

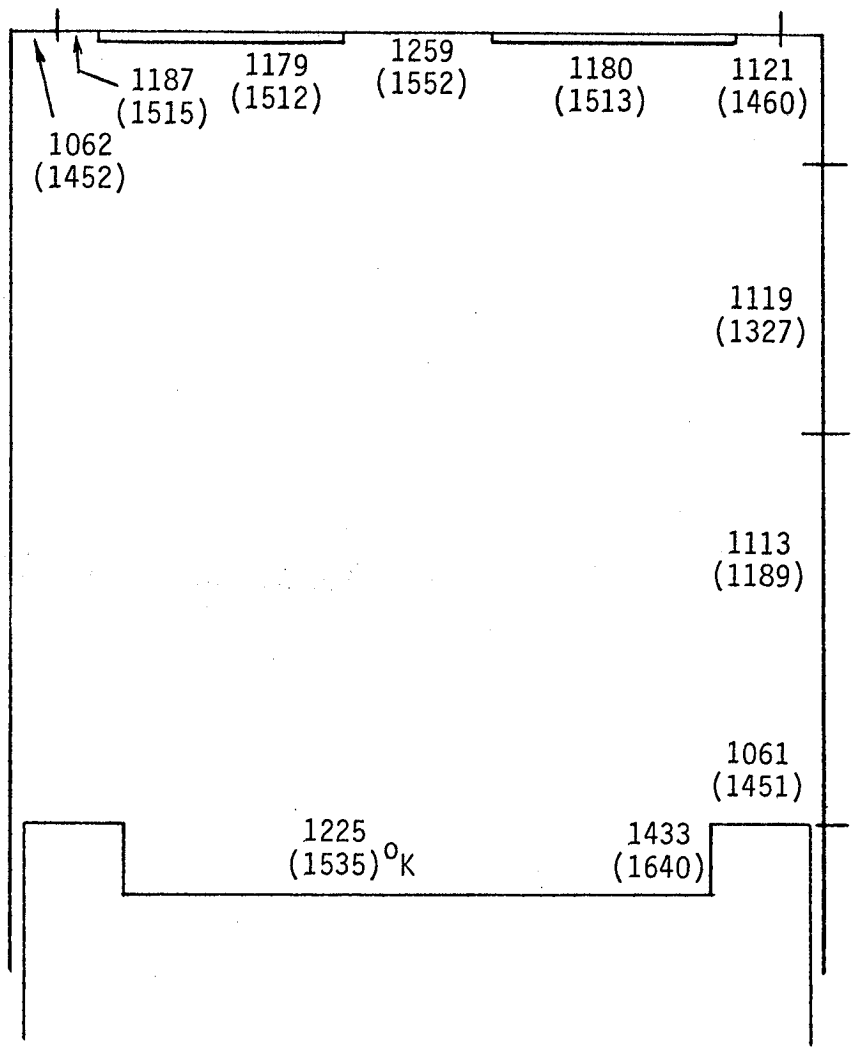

Figure 5-9. Superinsulated engine. Temperature distribution along combustion chamber walls.

as there need not be zero heat transfer even when the walls are superinsulated. The convective heat transfer dominates the total heat transfer, whose magnitude and direction depend on the wall temperatures. These in turn depend on a complex balance between friction heat deposition, gas-liner heat transfer, piston-liner heat transfer, and oil-liner heat transfer. The maximum wall temperatures, reached briefly during each cycle, are substantially higher than the mean temperatures; they are shown in Figure (5-9) in parentheses below the mean temperatures.

The time-resolved total heat transfer is shown in Figure (5-10). It demonstrates that under superinsulating conditions the heat flux is negative during most of the cycle except during parts of the compression and expansion strokes. The radiation, which emanates from the hottest portions of the gas, is always positive. The breakdown of the total heat transfer between the piston, liner and the head is shown in Figure (5-11). It may be noted that the curves for piston and head integrate to about zero net heat transfer, while that for the liner does not, integrating to a negative value equal to -1.6 percent of fuel energy. The breakdown for radiation (Figure 5-12) is very similar to that obtained in the baseline case, showing that the radiation is affected only very little by the increased wall temperatures. The overall heat radiation levels are higher, due to increased gas temperature under the insulated conditions, which more than offset the higher wall temperatures. The breakdown of the liner heat transfer rates (Figure 5-13) shows the large negative heat transfer levels during the gas-exchange period, responsible for the lower volumetric efficiency (reduced from 0.94 to 0.89) of the super-insulated design, necessitating the increased turbocharger boost.

The energy balance for the combustion chamber of the superinsulated engine shows 50.8 percent of fuel energy going into indicated work, -1.4 percent into pumping work, -1.6 percent into heat transfer, and the remaining 52.2 percent represents the difference in enthalpy flux between the exhaust and intake flows.

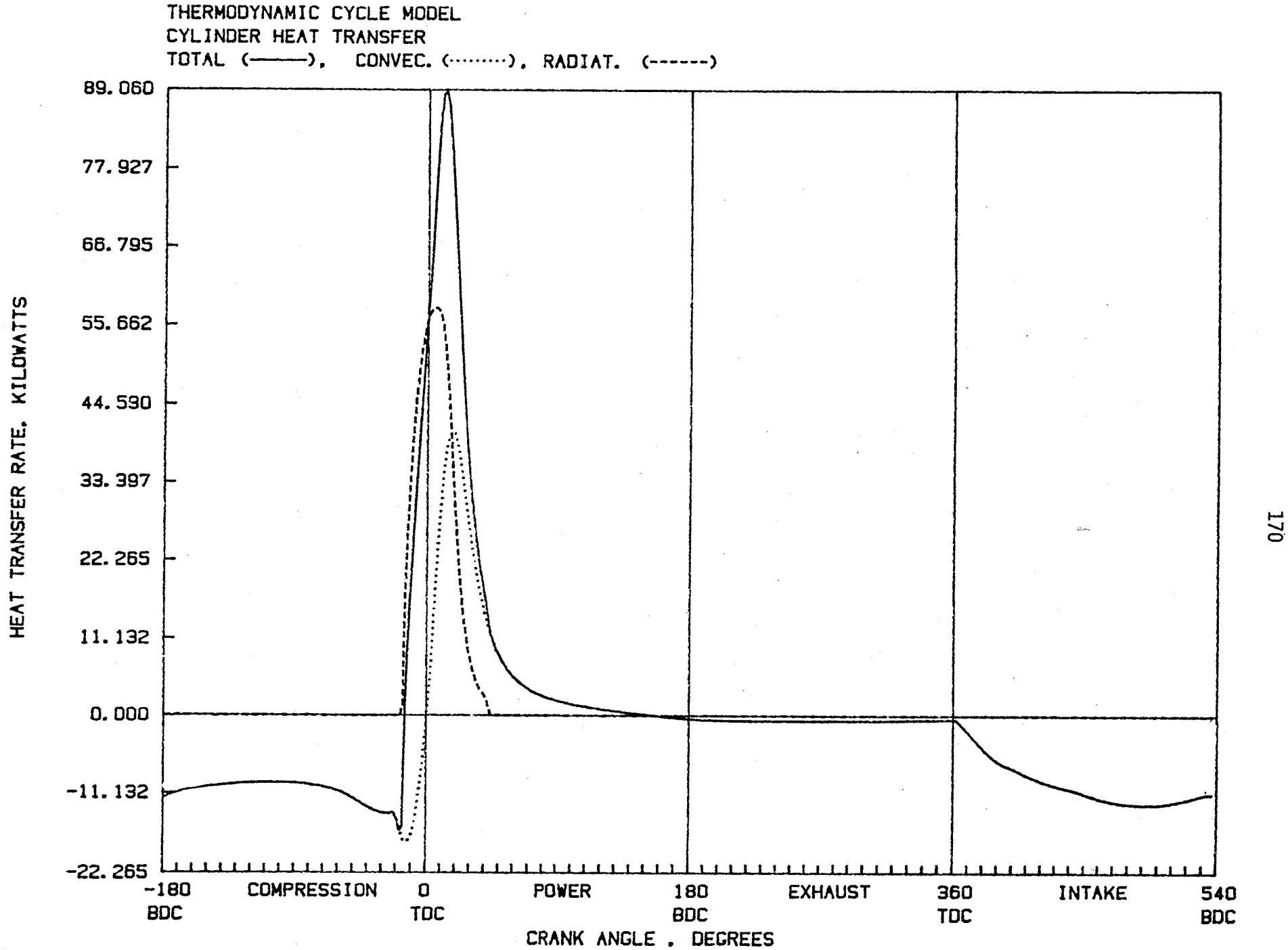

Figure 5-10. Superinsulated engine. Total heat transfer into all 11 surfaces.

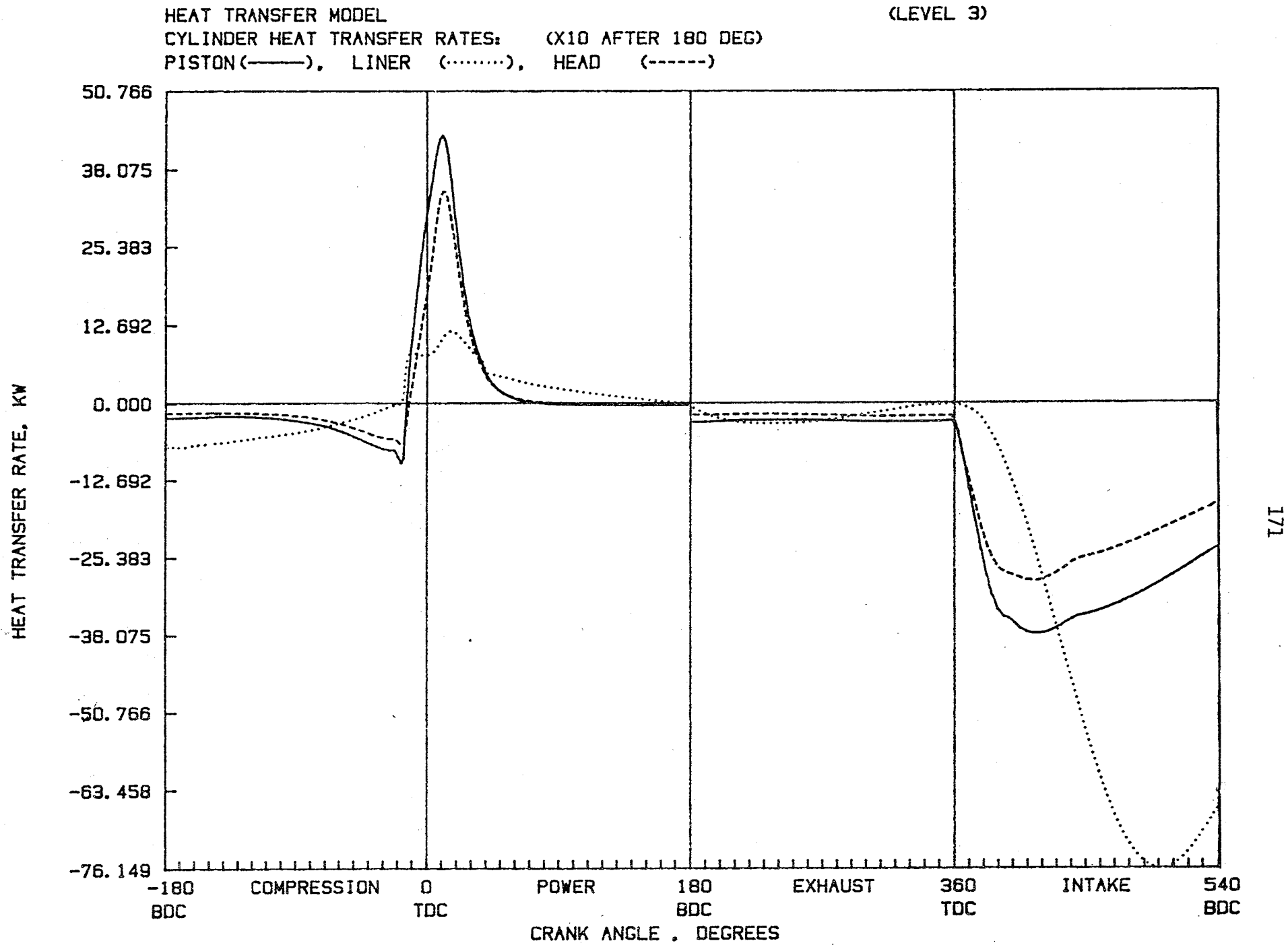

Figure 5-11. Superinsulated engine. Breakdown of total heat transfer into piston, liner and head.

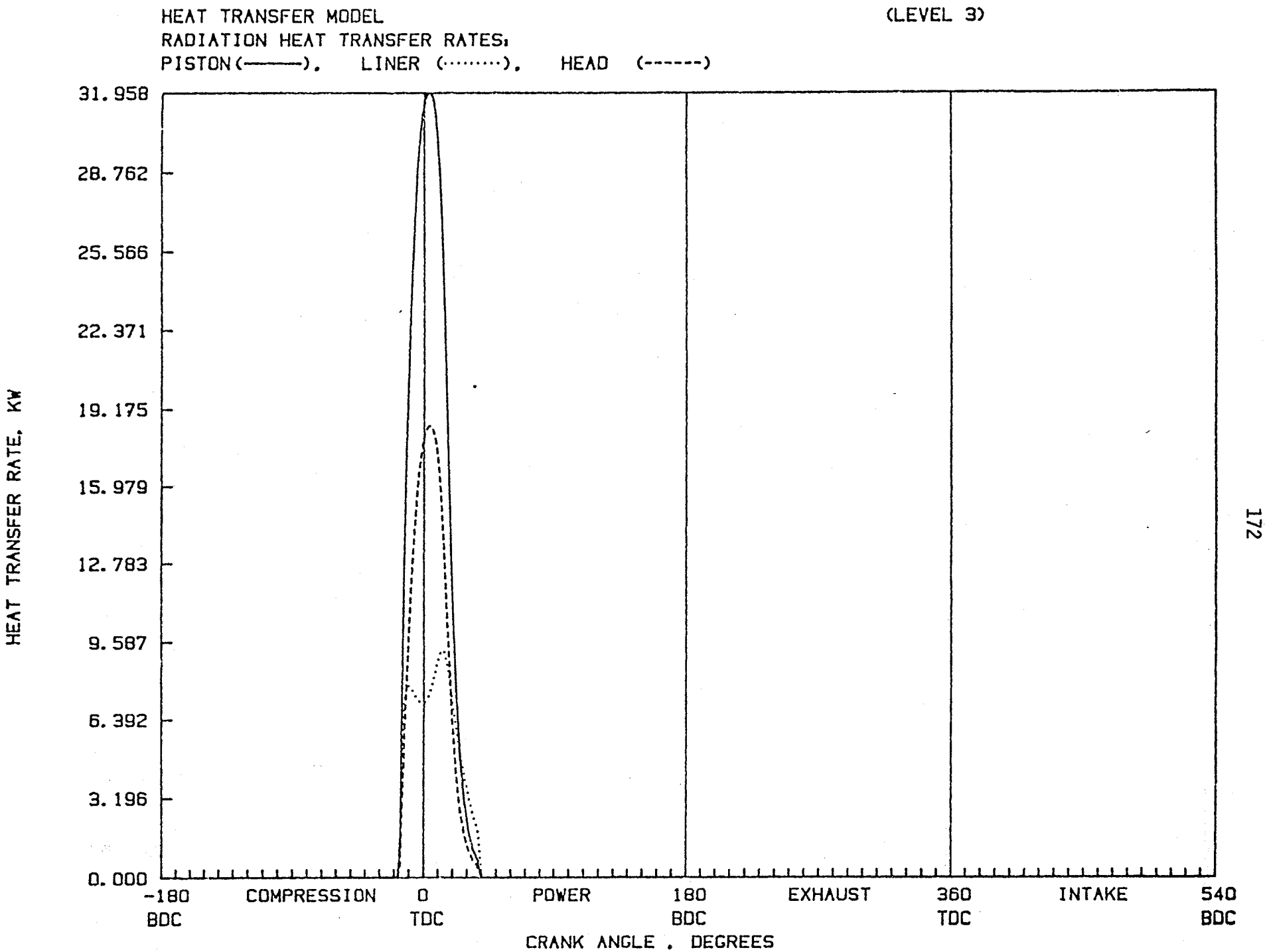

Figure 5-12. Superinsulated engine. Breakdown of radiation heat transfer into piston, liner and head.

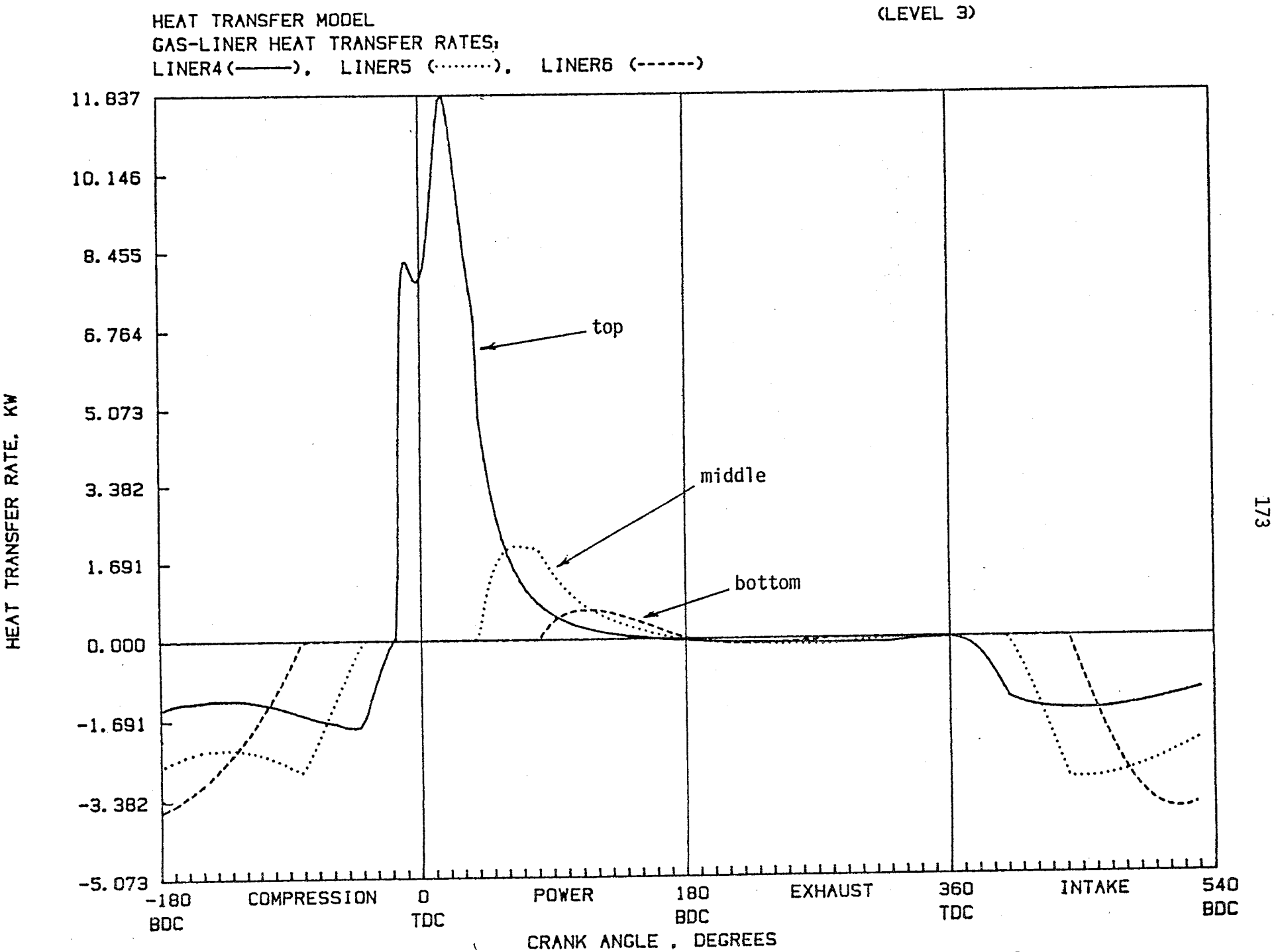

Figure 5-13. Superinsulated engine. Total heat transfer into the three liner elements.

E. Effects of Various Insulation Strategies and Insulating Materials

The previous two sections described the results of heat transfer analyses for a baseline metallic engine at rated speed and load and for the same engine "superinsulated" with a hypothetical low-conductivity material. These two cases form the boundaries for parametric studies of insulation strategies with materials of current interest. These studies should be viewed as an illustration of the trade-offs inherent in specific insulation strategies and an indication of the capabilities of the methodology under development rather than an attempt to specify an optimized insulated engine at this point in the program. The studies include the following:

1. Effect of material properties and placement
   a. progressive insulation of combustion chamber
   b. materials comparison
   c. piston insulation strategy
   d. liner insulation strategy
2. Effect of reduced coolant flow rate on insulated engine performance
3. Effect of reduced coolant flow rate on insulated engine performance
4. Effect of insulation at reduced speed and load.

1a. Progressive Insulation, 2100 RPM and Full Load

Examination of the baseline metallic engine heat transfer prediction indicates that the largest portion of combustion chamber heat loss is through the piston, followed by the head (including valves) and liner, in that order (Section C). Heat flow through the head, excluding valves, is about equal to liner flow, while valves transfer the least heat of any component section. Based on this pattern of heat flow, a typical partially stabilized zirconia (PSZ) insulating material was added progressively in the following sequence:

Case	Insulation Strategy
1	None (Baseline)
2	Piston cup, 0.01 m (0.39") thickness.
3	Piston cup and cylinder head, 0.01 m thickness.
4	Piston cup and cylinder head, 0.01 m thickness; plus upper section of liner, 0.021 m (0.83") thick.
5	Same as case 4 above, with the addition of 0.0015 m (0.060") zirconia as a plasma spray to the valve heads.

The material properties chosen for PSZ were: conductivity of 2.5 W/m°K and heat capacity of 2.3×10^6 J/m^{3}K. The plasma spray properties were taken as 0.6 W/m·°K conductivity and 1.1×10^6 J/m^{3}K heat capacity, based on the data presented by Cawley (1984).

The baseline engine uses an aluminum piston, which is substituted by iron when insulation is applied, to conform to current practice. The cylinder head and liner are iron in the base case and have an iron backing for support in insulated cases. Valves are high temperature alloy steel. Oil and jacket cooling temperatures and heat transfer coefficients are assumed to be unchanged from the base case in this series of runs, but are reduced in other cases that follow. It should be noted that this progressive-insulation series of test cases stops short of insulating the whole liner. The effect of insulation of the remainder of the liner is discussed in Section 1d below.

Major results from the progressive PSZ insulation study are shown in Figures (5-14) and (5-15). With the most effective insulation combination run, Case 4 or 5, there is a reduction in heat transfer by about 50%, leading to about 4.3% improvement in brake thermal efficiency. Over 50% of this increase is due to piston cup insulation alone, with the next largest part accounted for by insulating the head. Insulation of other surfaces offers little additional improvement. This result is attributed to the fact that combustion heat loss near top dead center affects thermal efficiency more than losses during any other part of the cycle. Thus, insulating the two principal surfaces that are exposed to combustion gases during that period offers the maximum benefit. Insula-

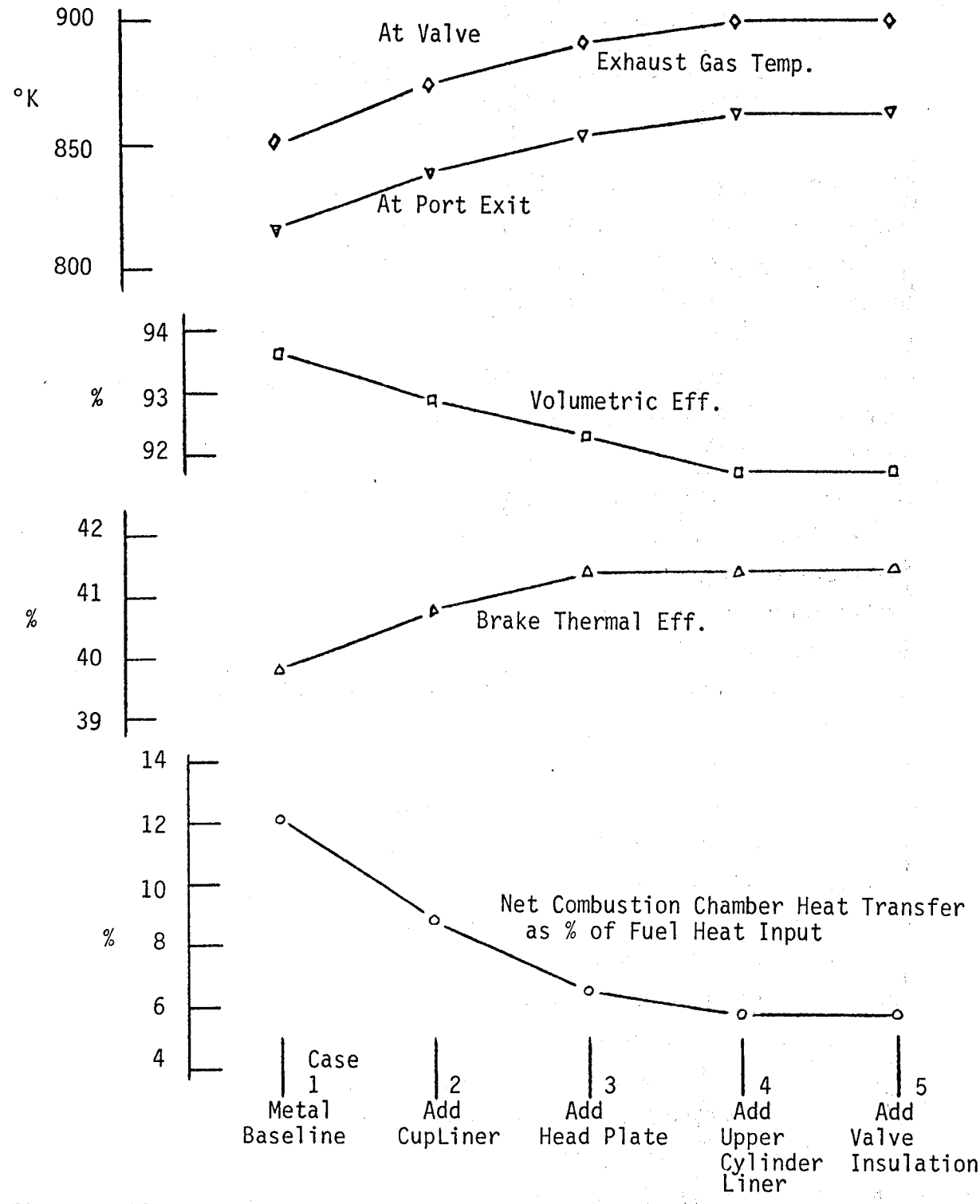

Figure 5-14. Progressive Insulation with Partially Stabilized Zirconia. 2100 RPM, Full Load Performance Characteristics.

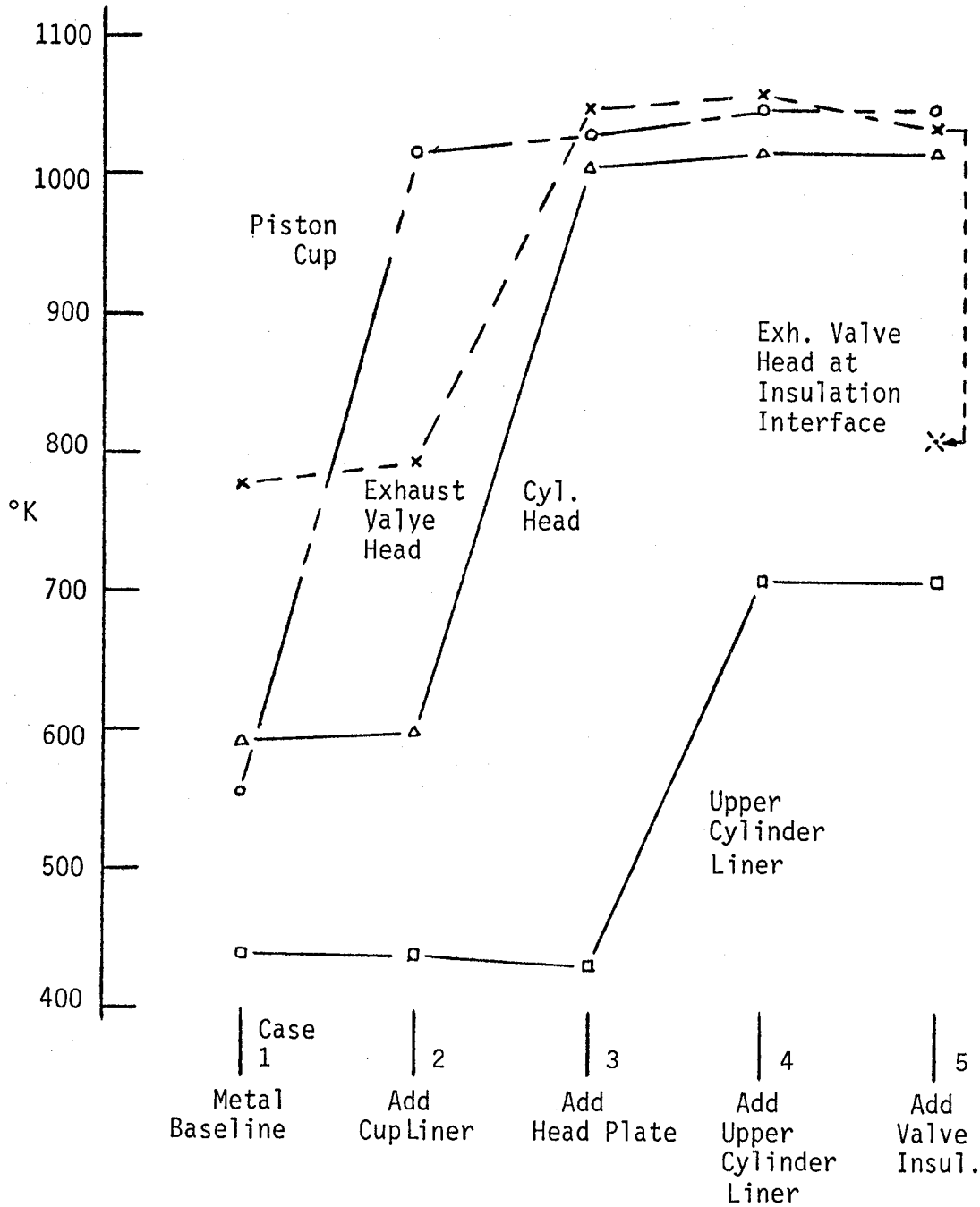

Figure 5-15. Progressive Insulation with Partially Stabilized Zirconia. 2100 RPM, Full Load, Maximum Average Surface Temperatures.

tion also increases exhaust temperature by up to 50°K, in Case 5, which provides additional energy for input to a recovery device. Approximately a 0.05 bar increase in intake manifold absolute pressure (+2%) is required to offset losses in volumetric efficiency due to additional intake charge heating. The volumetric efficiency changes from 93.6% in the base case to 91.7% for the highest degree of insulation. Also, injection timing was retarded 2° CA to maintain peak firing pressure at the baseline level (130 bar). One reason for the need to retard timing is that at the highest degree of insulation, Case 5, ignition delay was about 1.8° CA shorter than for the baseline case due to increased charge temperature.

With respect to maximum average component surface temperatures, Figure (5-15) shows the change that occurs when that specific surface is lined by the insulation material. On the other hand, the insulation of one surface has little effect on the temperature of others and, while not shown on the figure, metal temperature at the insulation interface also remains relatively constant. An exception is the exhaust valve head surface which increases by over 280°K when the head is insulated (Case 4). This effect is due to the fact that the valve heads are not directly exposed to liquid coolant. Adding 1.5 mm of zirconia plasma spray to the heads of both valves (Case 5) has almost no effect on engine performance, but reduces the exhaust valve underlying metal temperature at the metal/insulation interface back to within about 35°K of the baseline level.

1b. Material Comparison, 2100 RPM and Full Load

In order to examine the effect of materials whose properties differ from the typical partially stabilized zirconia (PSZ), additional cases were run using the same thickness (0.01 m) of a typical reaction bonded silicon nitride with a conductivity of 16 W/mK and heat capacity of 1.7×10^6 J/m^{3}K. In further cases, a zirconia plasma spray coating, typical of gas turbine experimental ceramics, used on the valve heads in Case 5, was applied over the whole the combustion chamber, using two

different uniform thicknesses. Properties of this plasma spray zirconia are 0.6 W/mK conductivity and 1.1×10^6 J/m^{3}K heat capacity. The cases analyzed are shown below:

Case	Insulation Strategy
6	Silicon nitride; piston cup, 0.01 m.
7	Silicon nitride; piston cup and cylinder head, 0.01 m.
8	Silicon nitride; piston cup and cylinder head, 0.01 m; upper section of liner, 0.021 m.
9	Zirconia plasma spray coating on all combustion chamber surfaces, including the whole liner and the valve heads, 0.0015 m.
10	Same as Case 9, but with a 0.001 m layer of zirconia.

Major results from the cases with silicon nitride insulation are shown in Figures (5-16) and (5-17), with some data on PSZ included for reference. While the trends for progressive insulation with silicon nitride are the same as for PSZ the magnitude of the effects on heat loss, thermal efficiency and increased exhaust energy are less than half as large. Component surface temperatures also did not change as much as when PSZ was used as the insulator. In contrast, the zirconia plasma spray (ZPS), Figure (5-18), at 1.5 mm (Case 9) is about as effective as the strategy in Case 5. One mm of ZPS is not as effective as 1.5 mm, but still compares favorably with Case 3 where the piston cup and head plate were insulated with 10 mm of PSZ.

1c. Piston Insulation Strategy, 2100 RPM and Full Load

From the cases presented in 1a and 1b above it is apparent that insulating just the piston cup alone is a very effective method of reducing combustion chamber heat loss and improving thermal efficiency. In order to assess the relative effectiveness of a few piston insulation strategies, three additional cases were run, for comparison to Case 2:

Case	Piston Insulation Strategy
11	Zirconia plasma spray, 0.0015 m thick, on entire iron piston top
12	Solid PSZ piston cap, 0.0132 m thick, on an iron piston
13	Solid PSZ piston

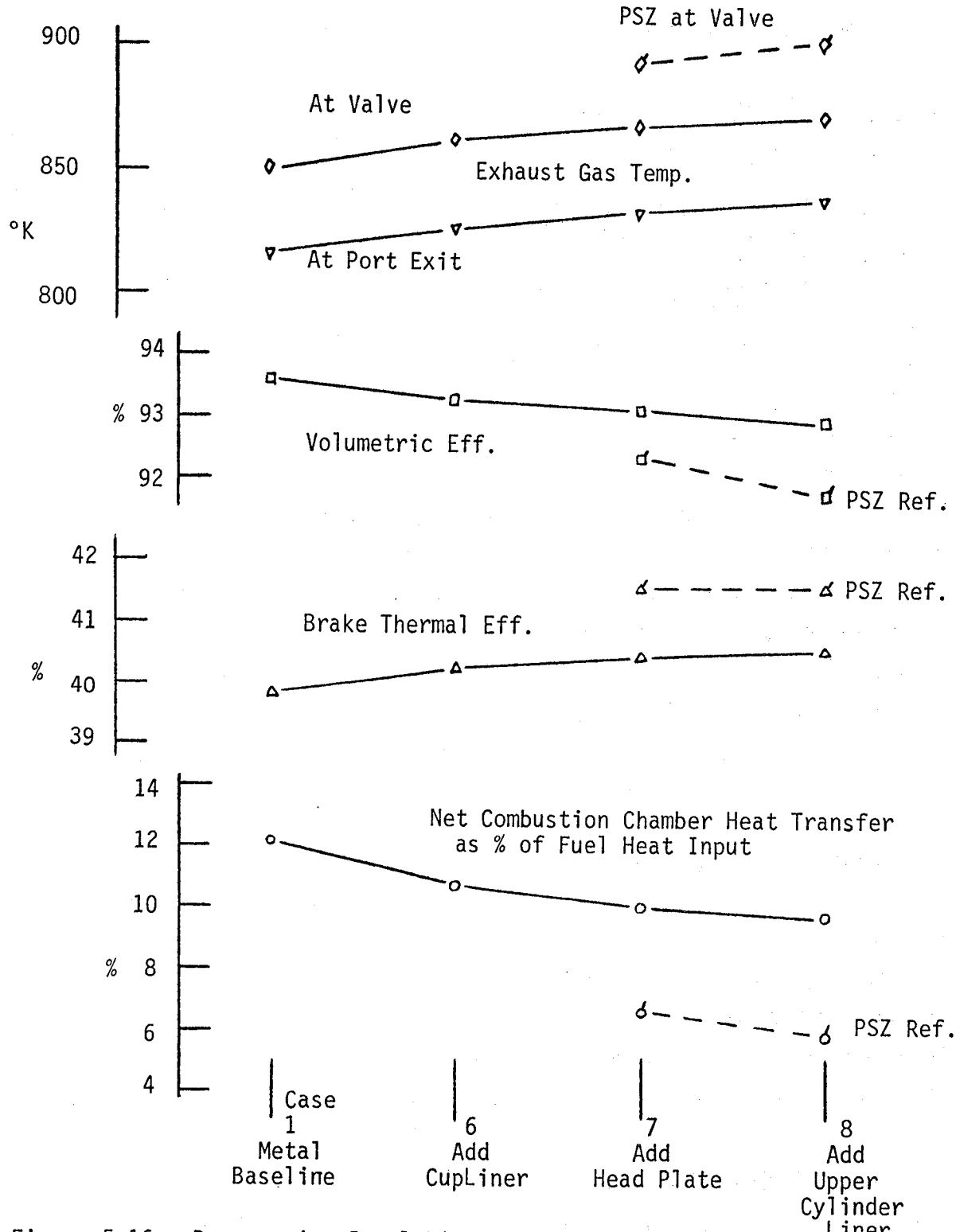

Figure 5-16. Progressive Insulation with Silicon Nitride 2100 RPM, Full Load Performance Characteristics

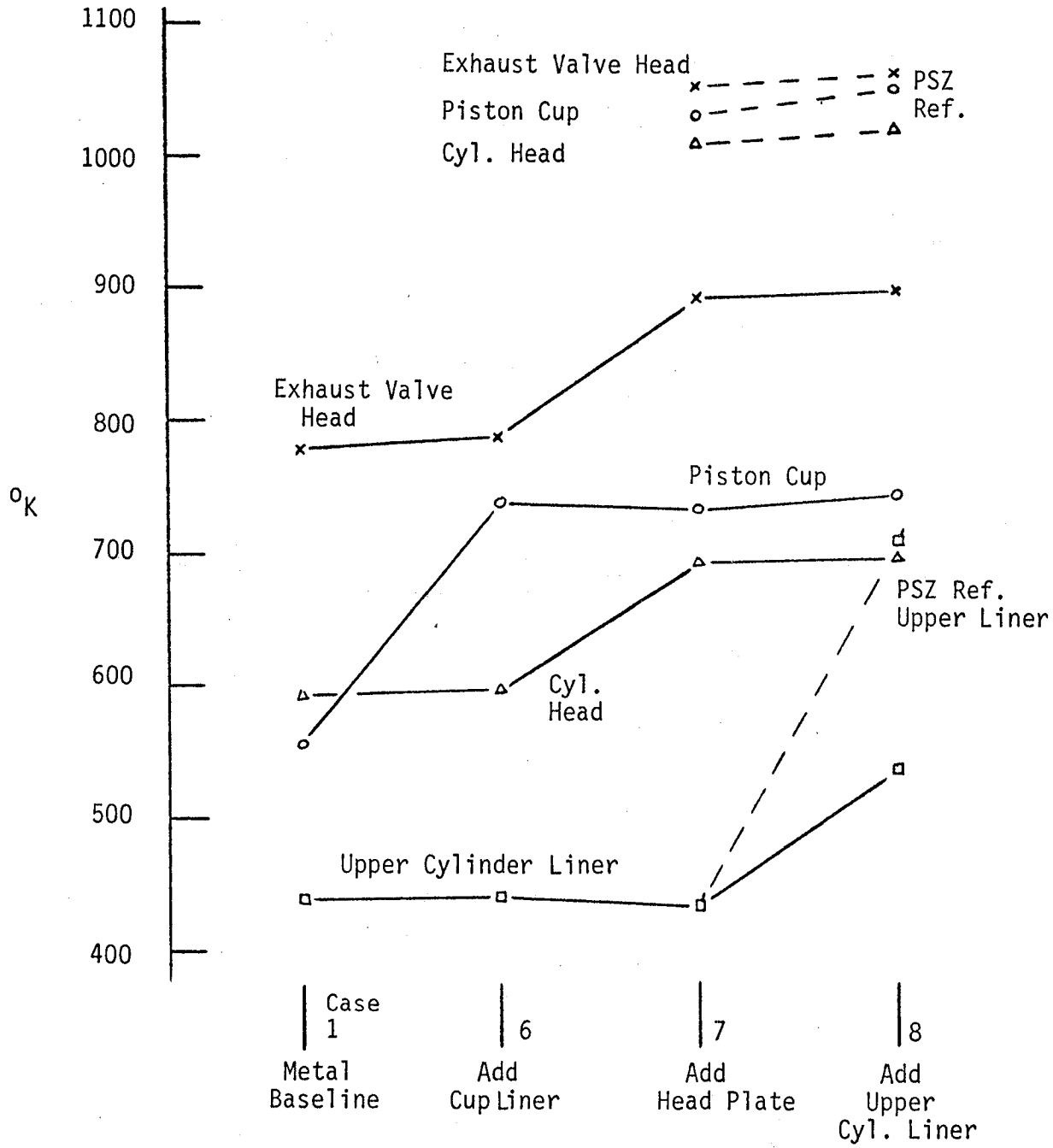

Figure 5-17. Progressive Insulation with Silicon Nitride. 2100 RPM, Full Load, Maximum Average Surface Temperatures.

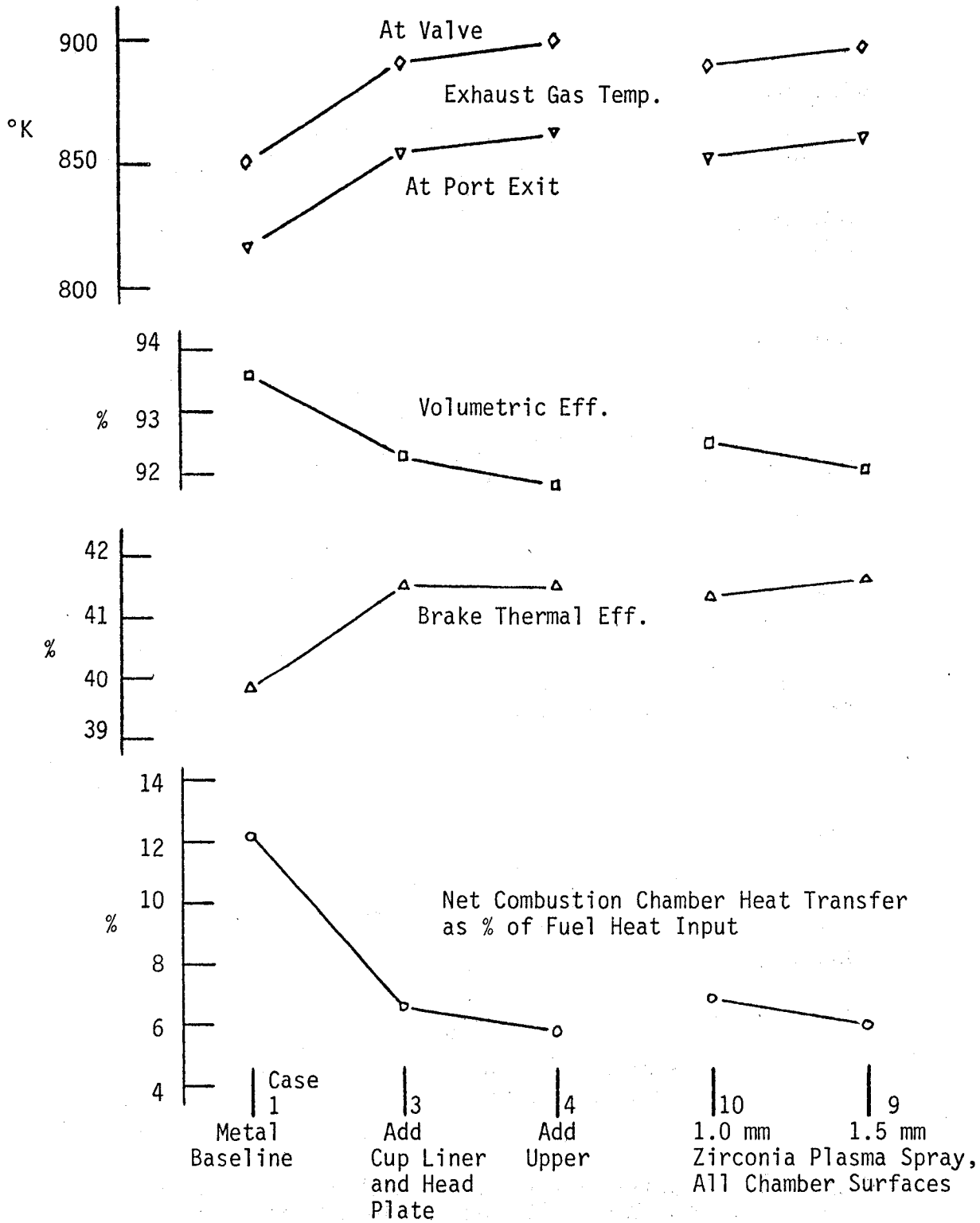

Figure 5-18. Combustion Chamber Insulation with Zirconia Plasma Spray Compared to Progressive Insulation with Partially Stabilized Zirconia. 2100 RPM, Full Load Performance Characteristics.

None of the other combustion chamber surfaces were insulated. Results are compared to those for the lined cup, Case 2, in Figure (5-19). Small benefits in reduced heat loss and increased thermal efficiency are shown for the thick piston cap or solid piston when compared to either the plasma sprayed zirconia or the PSZ lined cup. However, the maximum average piston surface temperature is elevated significantly by substituting a thick cap or solid piston for either of the other two strategies. The small increase in thermal efficiency obtained by use of the thick cap or solid piston does not appear to be worth the increase in piston surface temperature. This simple test of piston insulation strategies left open the question of coupling between piston and liner insulation. This question is examined within the context of the liner insulation strategy below.

1d. Liner Insulation Strategy, 2100 RPM and Full Load

If the liner is insulated, there are two general strategies that often are proposed. One is to insulate only the upper part of the liner, typically just above the top ring reversal point, and the other is to insulate the whole liner.

These two strategies were analyzed first by comparing Case 5 (engine insulated with a PSZ piston cup liner, head plate, upper cylinder liner section and zirconia plasma sprayed valve heads) to the same insulation package but with the addition of 0.01 m thick PSZ, backed by 0.005 m of cast iron, covering the whole length of the liner (Case 14). This liner substitution resulted in a small decrease in combustion chamber heat loss from 5.7% to 5.3% of the fuel energy. However, since the additional insulation became effective after the piston had moved relatively far down in the expansion stroke, this reduced heat transfer had no effect on thermal efficiency which was the same for both strategies. The only noticeable effect of the substitution was an increase of 25°K in average piston surface temperature and about an 100°K increase in liner temperature in the middle section. Despite this temperature increase, the volumetric efficiency was reduced only slightly, by 0.3 percentage

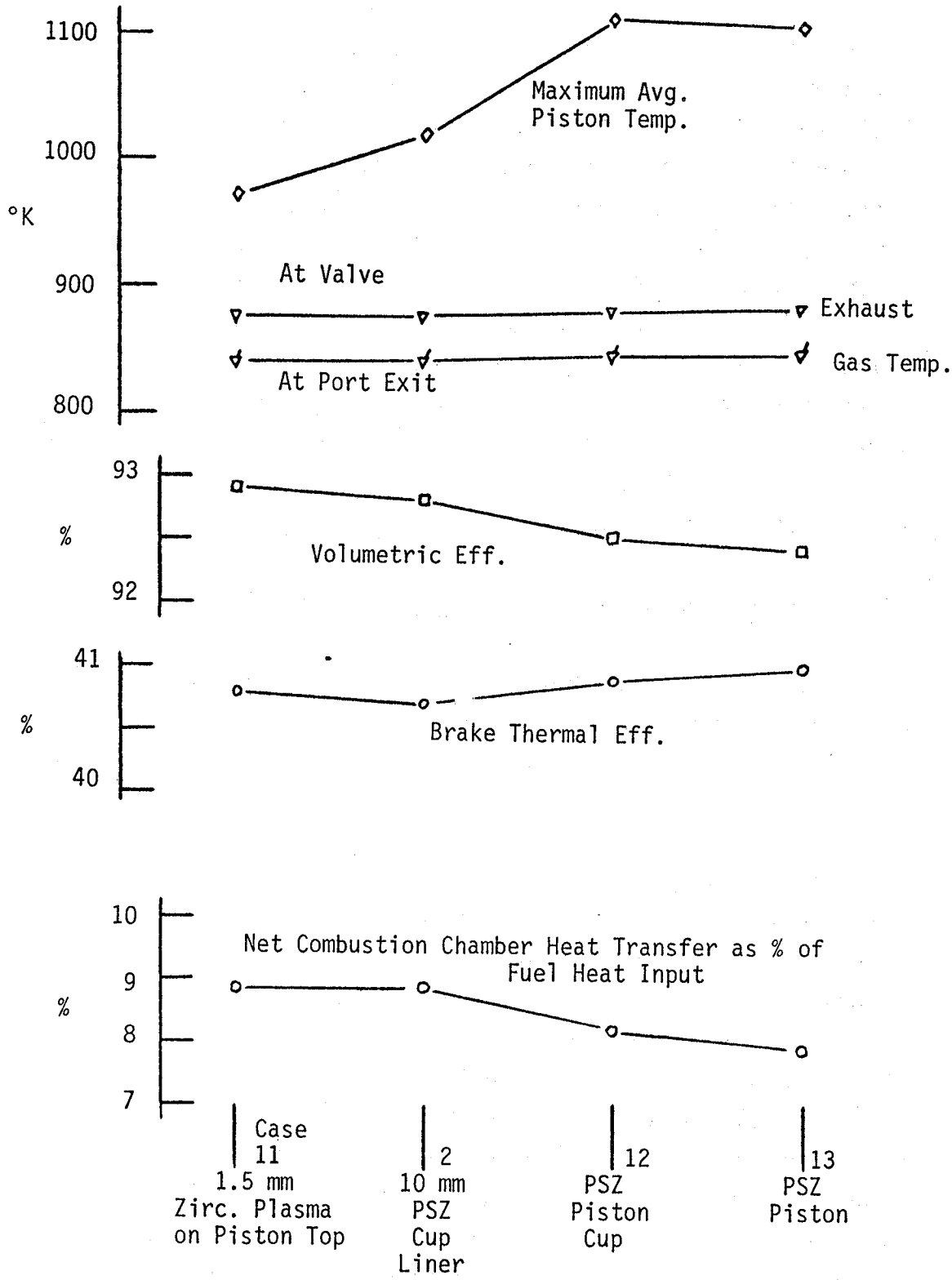

Figure 5-19. Comparison of Piston Insulation Strategies
2100 RPM, Full Load

point. The main effect of the added insulation turned out to be the change in heat paths. The presence of insulation on the full liner directed to the oil a significant amount of the rejected heat that would have gone to the liner coolant. Due to the piston cup insulation Case 5 had only 1.7 percent of fuel energy flowing into the oil, as compared to 3.2 percent for the baseline engine. Insulating the liner in Case 14 increased the amount of heat going to the oil to 5.5 percent.

As a next step we considered the effects of liner insulation for an engine which has a full ceramic (PSZ) piston. The reason for this second comparison was to analyze the degree of coupling between the piston insulation and liner insulation strategies. Thus, two additional cases were run, Case 15 which was identical to Case 5, but had a solid PSZ piston, and a Case 16 which was identical to Case 15, but had a full insulated liner. The four cases 5, 14, 15 and 16 are summarized in table below:

	Partially Insulated Liner	Fully Insulated Liner
Insulated Piston Cup	5	14
Solid PSZ Piston	15	16

Comparing Cases 14 and 16, which differ by piston insulation, one finds that the solid piston reduces the heat rejection from 5.3% down to 4.2%, which is approximately the same amount of reduction observed between Cases 2 and 13 in Section 1.c above. Again, only a small benefit in thermal efficiency was realized. The heat flux into oil was reduced from 5.5% down to 4.0% of fuel energy.

Finally, comparing Cases 15 and 16, which differ from each other in exactly the same way as Cases 5 and 14 do, we found that the liner insulation reduced the heat loss from 4.7% to 4.2%, i.e., by about the same amount as for Cases 5 and 14. Again, however, only a negligible change in thermal efficiency was produced, while wall temperatures rose

by about the same amount as before, i.e., by up to 118°K on the middle section of the liner. The amount of heat going through the piston and along the liner into the oil rose from 0.7 percent to 4.0 percent of the fuel energy.

In summary, the presence of insulation on the lower liner wall affects mainly the direction of the heat flow, diverting it from the coolant to the oil. Surprisingly, it does not have as strong an effect on engine performance, volumetric efficiency and even liner temperature, as might have been anticipated. Further, it is found that the effects of liner and piston insulation are superposable to some degree, although the details of the temperature distribution in the structure and of the heat flux distribution are closely coupled and depend on the specifics of the liner and piston insulation packages.

2. Effect of Reduced Coolant Flow Rate at 2100 RPM and Full Load (Rated Conditions).

For this part of the parametric study we made a limited comparison of an insulated engine with reduced coolant flow to the same engine with baseline coolant flow. Since one of the goals of engine insulation is minimizing jacket coolant heat rejection, this comparison illustrates the impact of such a strategy on performance and surface temperatures. Reduced coolant flow was simulated by reducing the coolant and oil heat transfer coefficients by a factor of two. The engine was insulated with 1.5 mm of zirconia plasma spray as in Case 9. The modest increase in shaft power due to reduced coolant pump work is not included in efficiency projections since the primary object is to study thermodynamic effects alone.

When coolant flow rate was reduced, only three significant effects were noted: 1) maximum average surface temperatures in the combustion chamber increased by 6 to 12°K; 2) metal-insulation interface temperatures in the piston went up by as much as 36°K (at the bottom of the cup); and 3) the heat loss from combustion decreased from 6.0% of the fuel energy

to 5.7%. Otherwise, differences in thermal efficiency, exhaust temperature, etc. were negligible.

3. Effect of Exhaust Port Insulation, 2100 RPM and Full Load (Rated Conditions).

One option in improving engine efficiency through insulation is to recover the extra energy in the exhaust with a power turbine. If this option is exercised, the exhaust gases should be kept as hot as possible by minimizing the heat transfer between the exhaust valve and the entry to the power turbine. Since the engine exhaust port usually passes through the cooling jacket, exhaust port insulation is desirable to minimize heat losses as the gases pass to the exhaust manifold.

The effect of adding a 5.0 mm layer of a typical titania-alumina exhaust-liner ceramic to the inside of the iron exhaust port was studied in conjunction with the in-cylinder insulation strategy of Case 5. A comparison of exhaust gas temperatures is shown below, where the first column refers to Case 5, and the second column shows the effect of the port insulation:

	Temperature, °K	
	No Port Insulation	With Port Insulation
Valve Plane	901	901
Port Exit	862	887

In this example, port insulation was able to reduce the port temperature drop by over 60% and thus add 25°K to the turbine inlet temperature.

4. Effect of Reduced Speed and Load from 2100 RPM and Full Load

Two operating points were analyzed for conditions other than rated: 1) 2100 rpm, medium load; and 2) 1300 rpm, full load (peak torque). The insulation strategy employed was zirconia plasma spray, 1.5 mm thick, on all combustion chamber surfaces as in Case 9 for comparison with the

iron/aluminum baseline engine at the same speed and equal mixture ratio. At 1300 rpm, full load, it was necessary to retard injection timing of the insulated engine by 5° CA to keep peak firing pressures near baseline levels, but at 2100 rpm, medium load, the timing was not changed from the metallic baseline value since the peak pressures were well under those that can be tolerated.

Results are shown in Figure (5-20). In both comparisons the insulation package substantially reduces the heat loss--about 40% at 2100 rpm, medium load and about 46% at 1300 rpm, full load--resulting in an improvement in thermal efficiency by about 4.6 and 6.0% respectively. These changes are very similar to those noted at 2100 rpm, full load, and indicate that effective insulation can produce significant cycle efficiency improvements even at conditions other than rated. There was also a gain of 30 to 70°K in exhaust temperature for potential energy recovery downstream.

Approximately 0.03 and 0.05 bar increase in intake manifold pressure, respectively, is required to offset the loss in volumetric efficiency from heat added to the air on the induction and compression strokes. This is similar to the additional boost required at 2100 rpm, full load.

F. Iron/Aluminum Metal Engine with Reduced Cooling

As an outgrowth of efforts to develop low heat rejection diesels through insulation of the combustion chamber walls, a significant attention has been focused on the potential to reduce coolant system capacity and improve engine thermal efficiency by reducing the degree of cooling in conventional metal engines. The heat transfer model developed in Phase I of this program is also useful for studying the effects of this kind of low heat rejection strategy and as an illustration of this capability, three representative cases, described below, have been studied and compared to the baseline, Case 1:

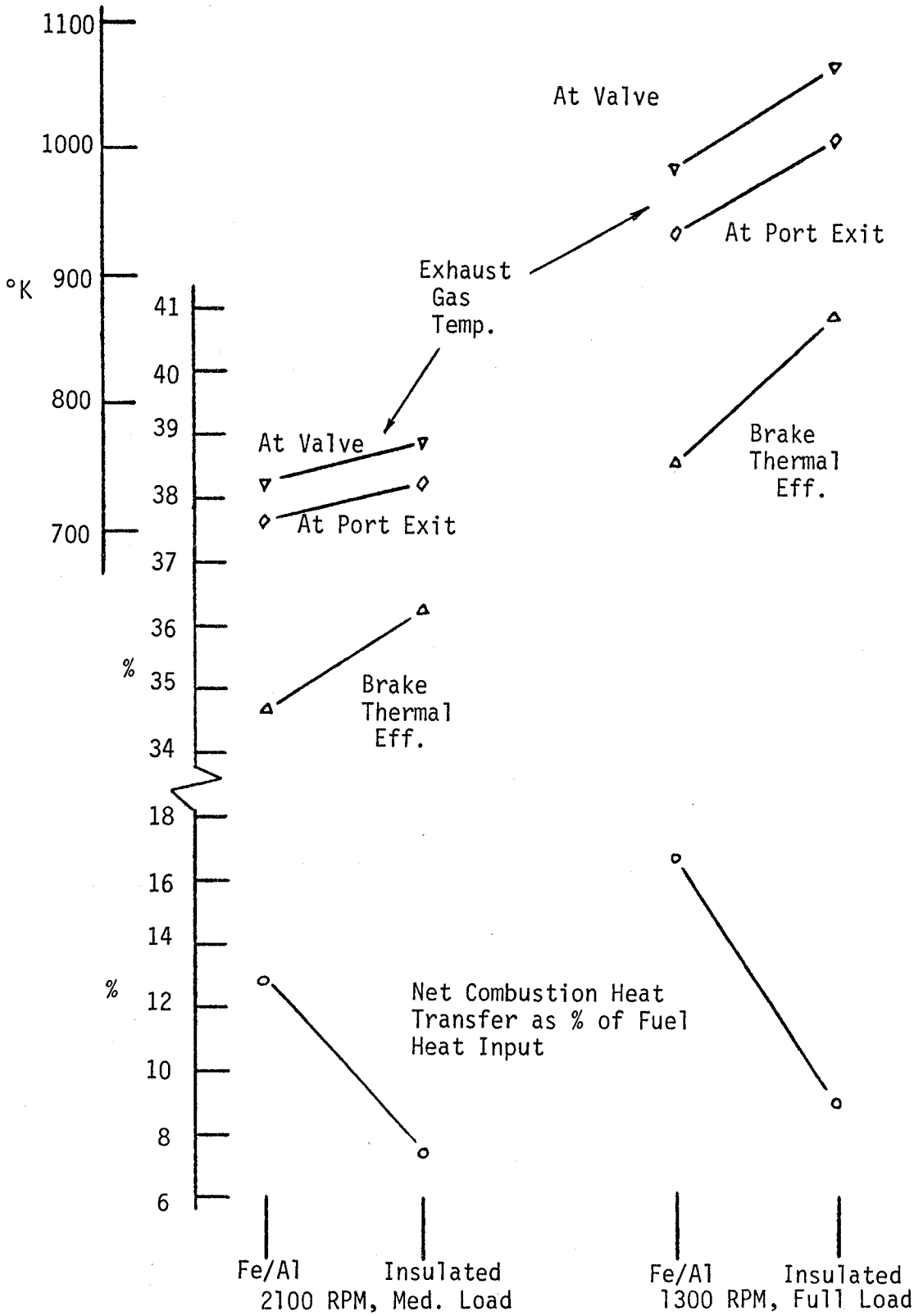

Figure 5-20. Effect of Insulating the Complete Combustion Chamber with 1.5mm of Zirconia Plasma Spray at Conditions Other Than Rated.

Case	Description
17	Basic iron engine with aluminum piston, but with cylinder liner coolant heat transfer coefficient reduced by 90% to simulate a reduced coolant flow rate.
18	Above case but with an iron piston.
19	Iron engine with iron piston, in which coolant and oil heat transfer coefficients were reduced by factor of 30 to match the net combustion chamber heat transfer obtained with Case 4.

When an aluminum piston is used with reduced liner cooling there is a small decrease in combustion chamber heat loss but no improvement in cycle thermal efficiency (Figure 5-21). For the reasons stated in Sub-Section E.2, reduced coolant pump work is not considered. Also there is only a small increase in exhaust temperature at the valve plane. This is another case in which the reduction in heat loss takes place too late in the cycle to improve thermal efficiency. A significant effect, as might be expected, is in surface temperatures, which increase about 40°K on the piston and over 110°K at the upper end of the cylinder liner. From these characteristics it is apparent that the only significant merit in this reduced cooling strategy is a reduction in required radiator capacity and the coolant pumping power. These benefits must be balanced against the undesirable increase in liner and piston temperatures. In this instance, the liner temperature would have a negative impact on lubrication and wear at the top ring reversal point, and probably would not be worth the minor benefits realized.

Substitution of an iron piston for aluminum one (Case 18 compared to Case 17) adds, in effect, a small amount of insulation to the piston area, since the conductivity of iron is lower. This modification, in conjunction with reduced liner cooling, reduces combustion chamber heat loss by about 8 percent, but only results in a 0.2 percentage points increase in cycle thermal efficiency. As with the aluminum piston, wall surface temperatures rise significantly, especially on the piston, where the area-averaged temperature rises to about 690°K, probably too hot for reliable service.

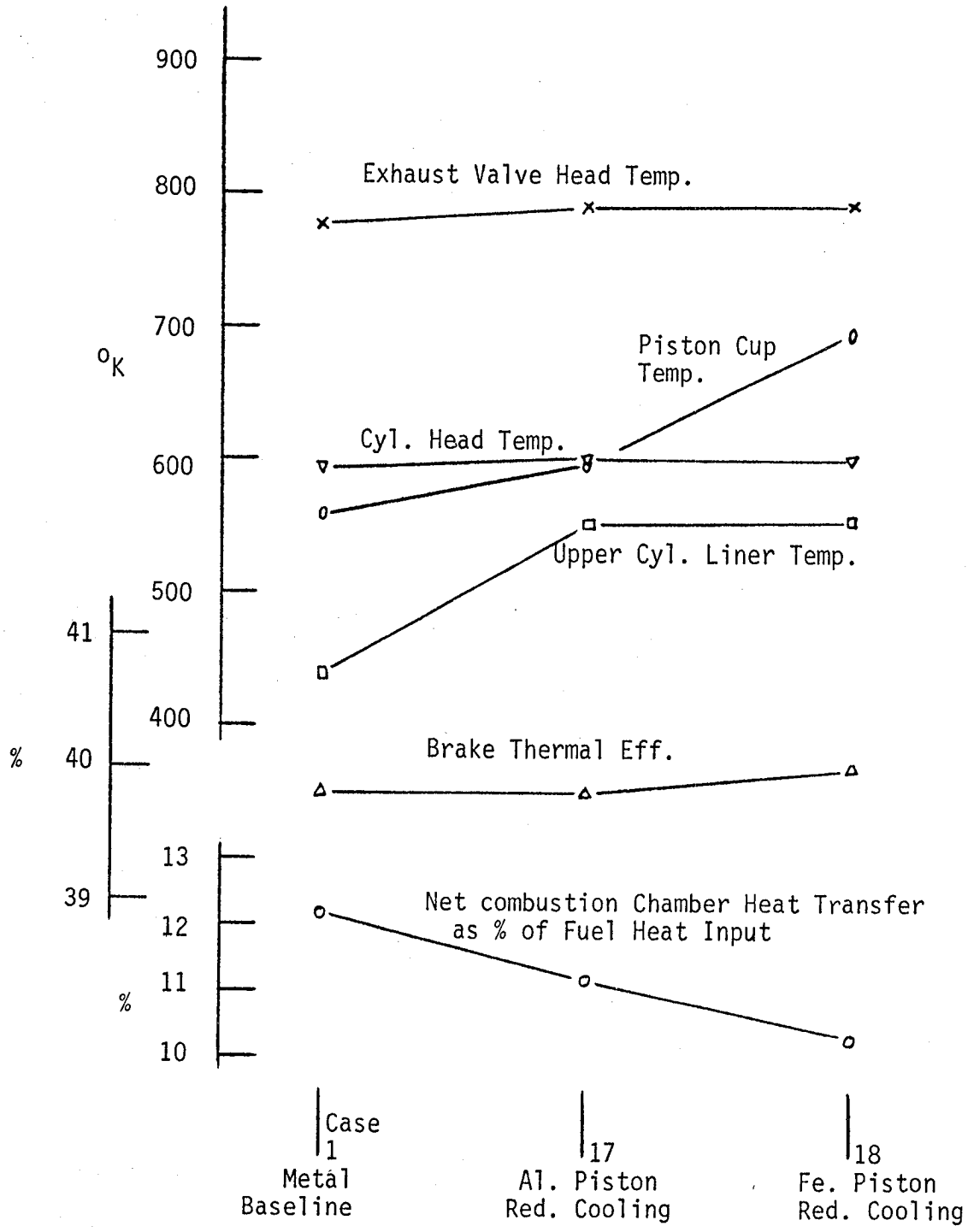

Figure 5-21. Effect of Reduced Cylinder Liner Cooling on Conventional Metal Engine Configurations. 2100 RPM, Full Load

To achieve any meaningful heat transfer reductions in the metal engine by reduced cooling, one would have to let the combustion chamber surface temperatures rise to over 1000°K, to the levels reached for example in Cases 4, 5 and 9. This would be well above the temperature at which cast iron begins to glow red (810°K) and above the lower transformation temperature (about 940°K) which means an unacceptably low creep strength. Such a situation was approached when the heat transfer coefficients on the coolant and oil sides were reduced in the simulation by a factor of 30 (Case 19). This reduced the net heat transfer to about the level found in Case 4 (heat transfer equals 5.8 percent of fuel energy), but the configuration was obviously not practical since surface temperatures ranged from 840 to 990°K.

From the results of these three cases of iron/aluminum diesels with reduced cooling, it is concluded that the most significant benefit of this concept is the reduced radiator capacity and coolant pump work, which is relatively small. These benefits must be weighed against the effects of increased surface temperatures on engine reliability and durability.

G. Heat Balance Comparisons for The Baseline and Three Insulation Strategies

The different insulation strategies may be analyzed and compared from the point of view of the overall engine energy balance. For the purposes of such a comparison we consider the following energy split for a complete engine including a turbocharger and basic accessories (which are lumped here into engine friction):

$$\begin{aligned} \text{fuel energy} = {} & \text{brake work} + \text{heat rejection to coolant and oil} \\ & + \text{heat rejection to aftercooler} \\ & + \text{available exhaust energy in exhaust stack} \end{aligned}$$

This energy balance is shown schematically in Figure (5-22). It may be noted that this definition of energy balance does not account for the

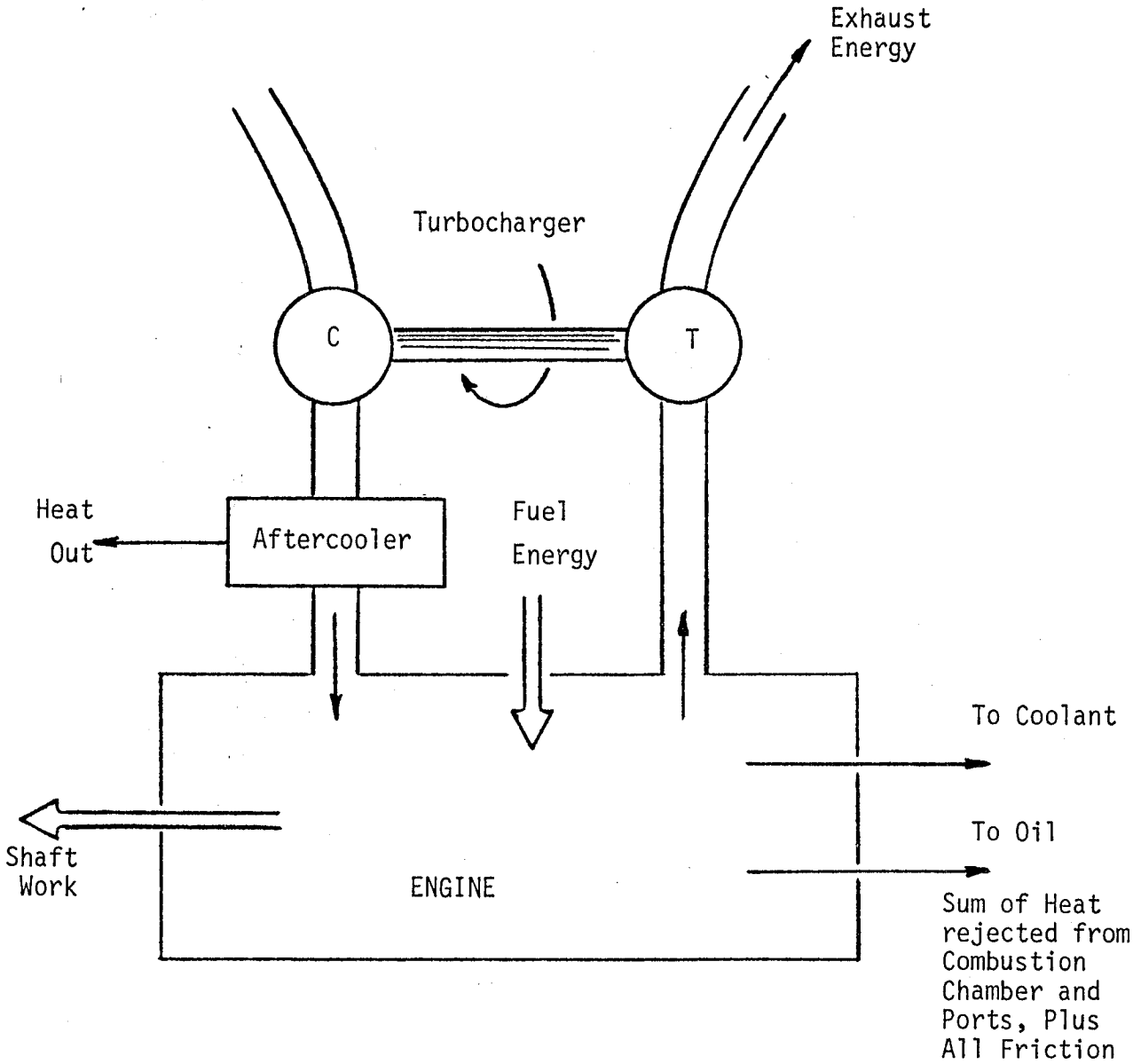

Figure 5-22. Engine Energy Balance Schematic, Neglecting Losses to Ambient Atmosphere

heat rejected to the engine surroundings, which in reality subtracts modest amounts from the values attributed to the last three terms on the right hand side of the energy balance.

The first item, brake work, is defined in a conventional way as the indicated work minus pumping work and friction (which includes basic accessories such as pumps, camshaft, drives, etc.). The heat rejection to coolant consists of three terms. The first two of these terms are obtained from the heat conduction network coupled to the thermodynamic cycle simulation as the heat received by directly by the coolant and by oil by conduction, and this includes the heat deposited at the liner/piston interface by piston friction. The third term, which relates to the remainder of the engine friction -- journal bearings, pumps, etc., is assumed to provide additional heat to the structure, which has to be carried away by the coolant. It should be noted that in these simulations the water flow rate was kept constant, and so the expected benefit due to lower water pump work for a reduced cooling design is not factored in. However, this effect is small: at the rated conditions in the baseline engine the water pump work is estimated to be less than 1/2 percent of the fuel energy.

Heat rejection to an aftercooler is calculated from the compressor exit temperature, based on the compressor pressure ratio and compressor efficiency which is assumed to be the same as for the baseline engine at rated conditions, i.e., η_c=0.76. The last term is calculated by difference. It agrees with the exhaust stack energy based on the turbine exit temperature, calculated in the same way as the compressor exit temperature; it is based on the baseline engine turbine efficiency of η_t=0.75.

Four engine configurations were compared:

- baseline engine
- reduced-cooling version of baseline engine
- engine with PSZ insulation package as in Case 5 plus Tialit exhaust port liners
- superinsulated engine

The results are presented in Table 5-1. Comparing first the two limiting cases, superinsulated and baseline, one finds the superinsulation reduced very substantially the heat rejected to the coolant, and the heat rejection from the combustion chamber is actually negative (part of the friction heat is transferred to the gas). The engine had a higher thermal efficiency, producing 6.5 percent higher brake output. At the same time the exhaust stack temperature rose by 124°K, providing an additional potential for the operation of an exhaust heat recovery device. The PSZ insulated engine had 53 percent lower heat rejection from the combustion chamber than the baseline. The brake work increased by 4.3 percent and exhaust stack temperature increased by 58°K. By contrast the reduced-cooling engine provided only minor benefits.

An important concept in evaluation of insulated engine designs is the "pumped heat" discussed in Chapter 3 and defined by equation (3-22). It refers to the heat absorbed by the combustion chamber walls during the intensive heat transfer period near TDC of compression stroke, which is returned to the gases later in the cycle, mainly during the intake period and at the start of compression. It has two important negative effects. First, the heat transfer is being extracted from the gases at the time when it is needed for generation of piston work, and second, it is returned during the intake period when it adversely affects volumetric efficiency.

The effect of pumped heat is observable when comparing the benefits gained in the PSZ and the superinsulated designs. The reduction in combustion chamber heat rejection for the PSZ engine, compared to the baseline, is 42.8kW, while for the superinsulated engine the reduction is 92.5 kW, or more than twice as large. Yet the improvement in brake power for the superinsulated engine is 6.5 percent versus 4.3 percent for the PSZ engine, i.e., only one and a half times as large. This means that the latter design is more efficient in converting the conserved heat directly into brake power. The main reason for the difference is the increase in the pumped heat, which favors an increase in exhaust temperature over increased piston work. All three lower-heat-rejection designs have pumped heat levels higher than the baseline,

Table 5-1

Heat Balance for Three Insulation Strategies Expressed in Percent of Fuel Energy

	Baseline	Reduced Cooling	PSZ Design	Super Insulated
Brake work	39.8	39.8	41.5	42.4
indicated work	47.7	47.8	49.6	50.8
pumping	-1.4	-1.4	-1.4	-1.4
friction	-6.5	-6.6	-6.7	-7.0
Heat rejection to coolant	21.4	20.6	13.6	5.4
coolant (direct)	16.2	11.9	9.9	0.1
oil	3.2	6.7	1.7	3.3
friction other than piston	2.0	2.0	2.0	2.0
Heat rejection in aftercooler	2.8	2.9	3.0	3.3
Exhaust energy	36.0	36.7	41.9	48.9
Exhaust stack temperature(K)	719	728	777	843
Volumetric efficiency	0.936	0.929	0.917	0.892
Boost pressure (bar)	2.273	2.290	2.320	2.380
Injection timing (°CA	-21	-20	-18	-15
Combustion chamber heat rejection (kW)	81.6	75.0	38.8	10.9
Piston	49%	51%	42%	0%
Head	32%	34%	25%	0%
Liner	19%	15%	33%	100%
Pumped heat (kW)	3.8	6.9	13.8	24.1

including the reduced-cooling case; the driving element behind this increase is the rise in the combustion chamber wall temperatures.

In summary, the preliminary analysis indicates that PSZ-insulated engine (with liner insulated only above the top ring reversal point) can provide very meaningful benefits when compared to the upper limit of superinsulation.

VI. SINGLE CYLINDER ENGINE INSTALLATION

At the beginning of this contract an AVL engine was installed on the test dynamometer in a fully operational condition. The engine was originally planned to be used for the experimental portion of this contract, and in fact some data was acquired on it in the early stages of the work on the polytropic exponent technique. When Cummins Engine Company joined the program, it offered to provide one of their single cylinder engines for the experimental program. The offer was accepted, since working with that engine and having their experience available will greatly facilitate the installation of ceramic parts in the later stages of the program.

The engine test laboratory is equipped with two dynamometers, and in order to accommodate the Cummins engine it was necessary to move the AVL to the smaller of the two, transferring with it the requisite subsystems.

The Cummins engine was then installed on the larger (Westinghouse) dynamometer. The dynamometer is cradled in ring-lubricated ball bearings and rated for absorption at 56 kw, 2000/5000 rpm and motoring at 45 kw, 1800/5000 rpm. The motor generator set, made by General Electric, is rated at 100 kw. The control system was designed and built by Pohl Associates.

The torque is measured using a load cell whose signal is fed into a microprocessor producing a digital readout of torque. This system was inoperative at the time the AVL engine was installed, as a different transducer was used. Since that transducer was too small to accommodate the Cummins engine, the load beam system had to be restored to service. To polish the cradle bearing surfaces, and thereby to reduce friction in the bearings and eliminate an existing occasional static hang up, electric motors were used to spin the cradle bearings relative to the dynamometer shaft over prolonged periods of time. Also, some gears in the system were pulled and polished by hand.

To connect the engine to the dynamometer it was decided to employ a flexible steel coupling. The dynamometer was raised from the floor by about 4 mm and a floor mount plate was fabricated to which the engine attaches. The plate was designed to allow x-y-z translation of the engine with respect to the dynamometer in order to precisely align their shafts. An adaptor was also fabricated to provide a means of attaching the coupling to the engine flywheel.

The Cummins engine requires external oil, water and fuel systems, having no auxiliary pumps of its own. Therefore, suitable systems had to be designed, fabricated and installed. To conserve laboratory space, a central rack was built to mount the heaters, coolers, motors, pumps, and filters comprising these various systems. Figure (6-1) is a photograph of this rack with most of those elements in place. The rack is also used to mount components used to pump hot oil into the optical access port and coolant into the pressure transducer.

A schematic of the oil system is shown in Figure (6-2). A scavenge pump sized slightly larger than the supply pump pulls oil through braided hose out of the engine at the balance box. That oil is delivered to a reservoir and recirculated to the engine through a filter by the supply pump. An electric heater is used to facilitate engine warmup, and a heat exchanger is used for cooling the oil. The total capacity of the system is approximately 50 liters. Oil temperature into and out of the engine will be measured, as will be the oil flowrate, in order to determine the heat rejected by the engine to the oil. Oil pressure is measured at the engine inlet as well as in the main gallery.

The cooling system is shown in Figure (6-3). A cooling tower was built by copying the POHL Model 600 that is being used with the AVL engine. Coolant water is supplied through the tower to fill the engine cooling system. To assist warm-up, the heater is turned on and hot water circulated through the engine until the operating temperature is reached.

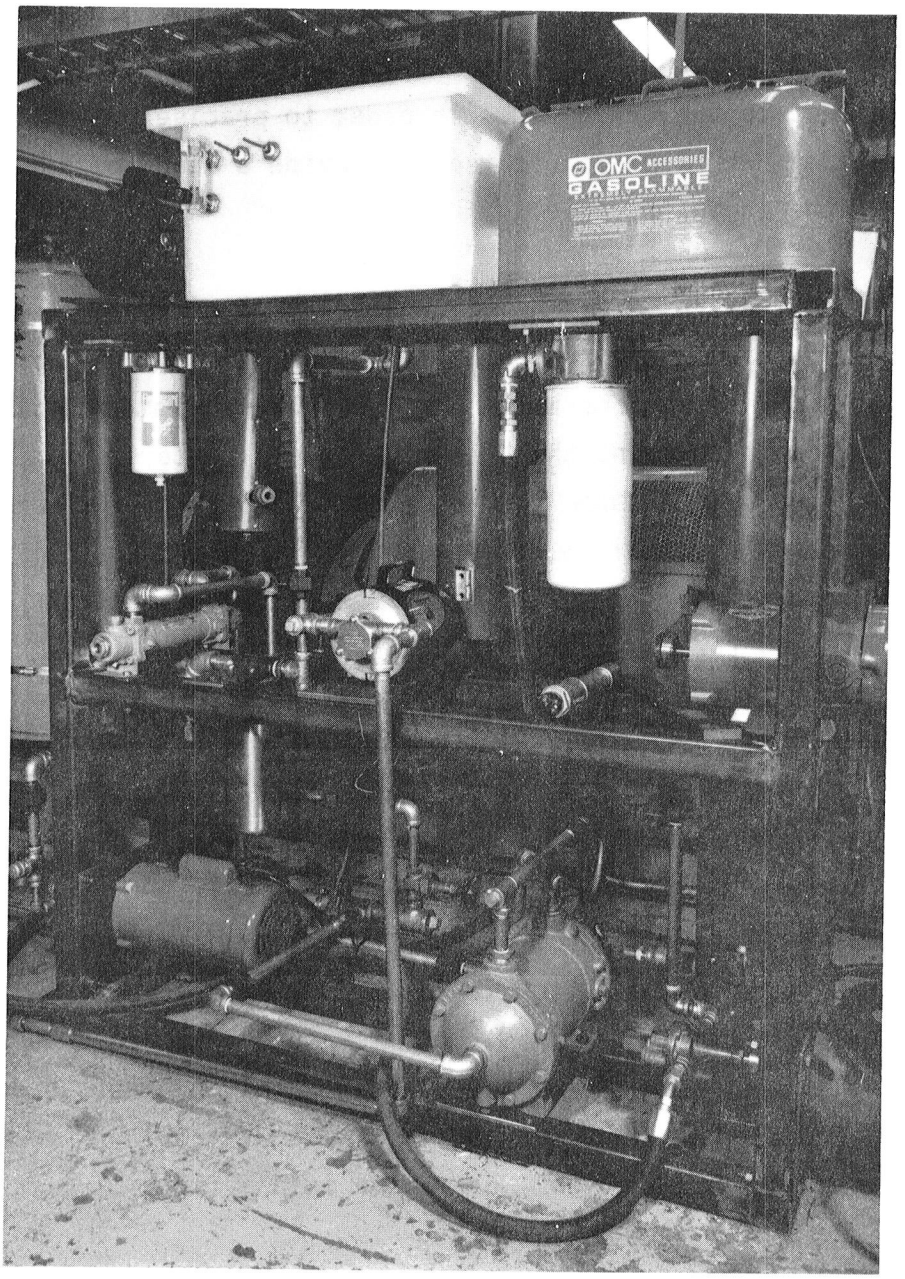

Figure 6-1. Installation of supporting sub-systems for Cummins single cylinder test engine.

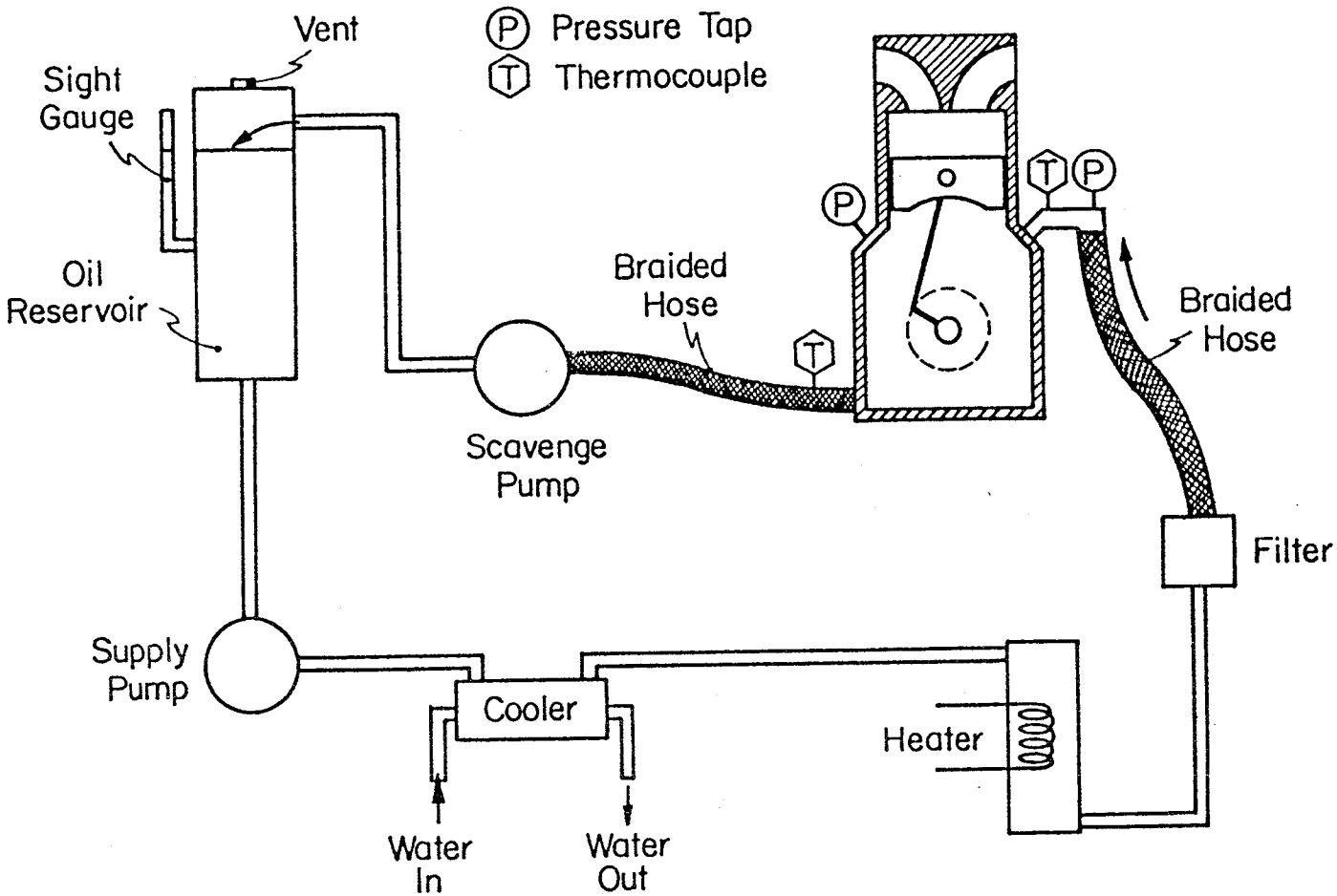

Figure 6-2. Schematic of external oil supply system.

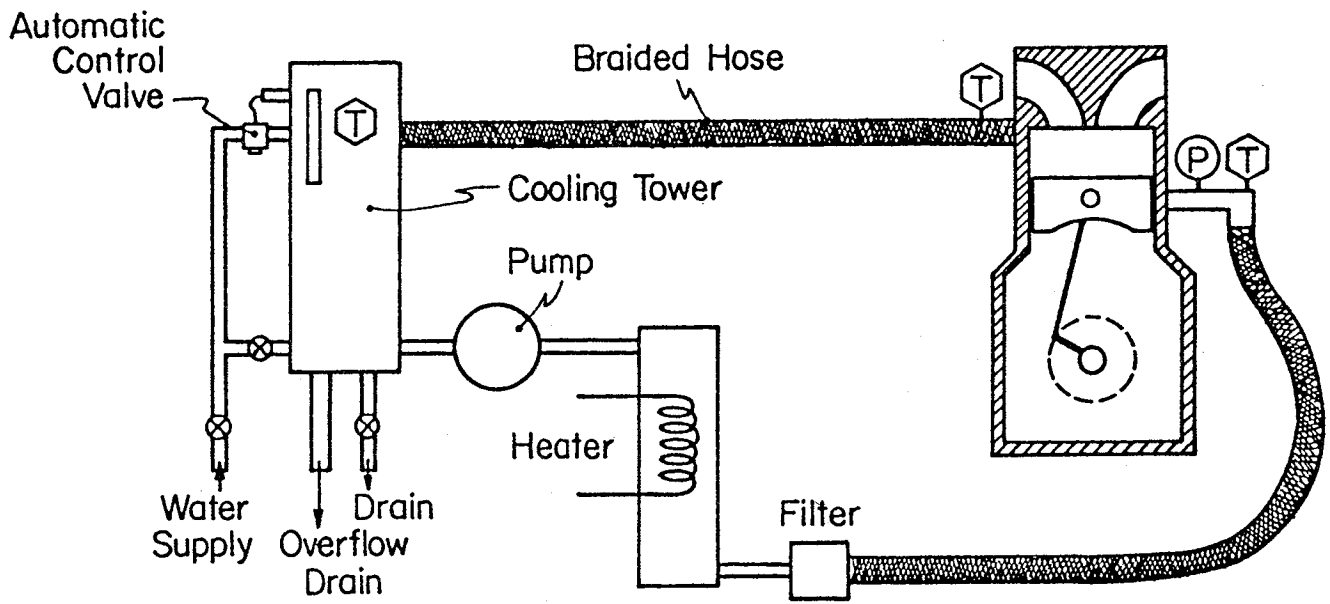

Figure 6-3. Schematic of external cooling system.

As the engine operates, the external water pump circulates water from the lower section of the tower to the engine and returns water heated by the engine to the upper section. The temperature sensing element of the control valve meters cold water into the tower to maintain a constant engine temperature. If the temperature of the returned water is below the control valve set point, the valve remains closed and no cooling water is added to the system. Excess water is removed from the system through a discharge tube to the laboratory drain. Both the engine and the tower can be drained by opening a discharge valve at the bottom of the tower.

Thermocouples monitor the water temperature in and out of the engine and a pressure gauge is installed at the inlet. As with lubricating oil, a transducer will be installed to measure the water flow rate in combination with temperature change and thus calculate the heat rejected by the engine to the coolant.

The intake and exhaust systems are shown in Figure (6-4). The volumes of the plenums each equal fifty times the engine displacement volume. Each was tested hydrostatically to a pressure of 7 bars. The pipes connecting the engine to the plenum may be considered short. Judging from curves of volumetric efficiency plotted for different-sized inlet pipes, Taylor (1977), pipes of diameter equal to about half the bore may be considered short if their length is less than about three times the stroke. In our case, we have

$$\frac{d_{ex}}{b} = 0.55 \qquad \frac{L_{ex}}{S} = 3.25$$

$$\frac{d_{in}}{b} = 0.45 \qquad \frac{L_{in}}{S} = 2.89$$

The diameters are nominal values. Both plenums are connected to the engine using stainless stell flexible hose to isolate them from engine vibration.

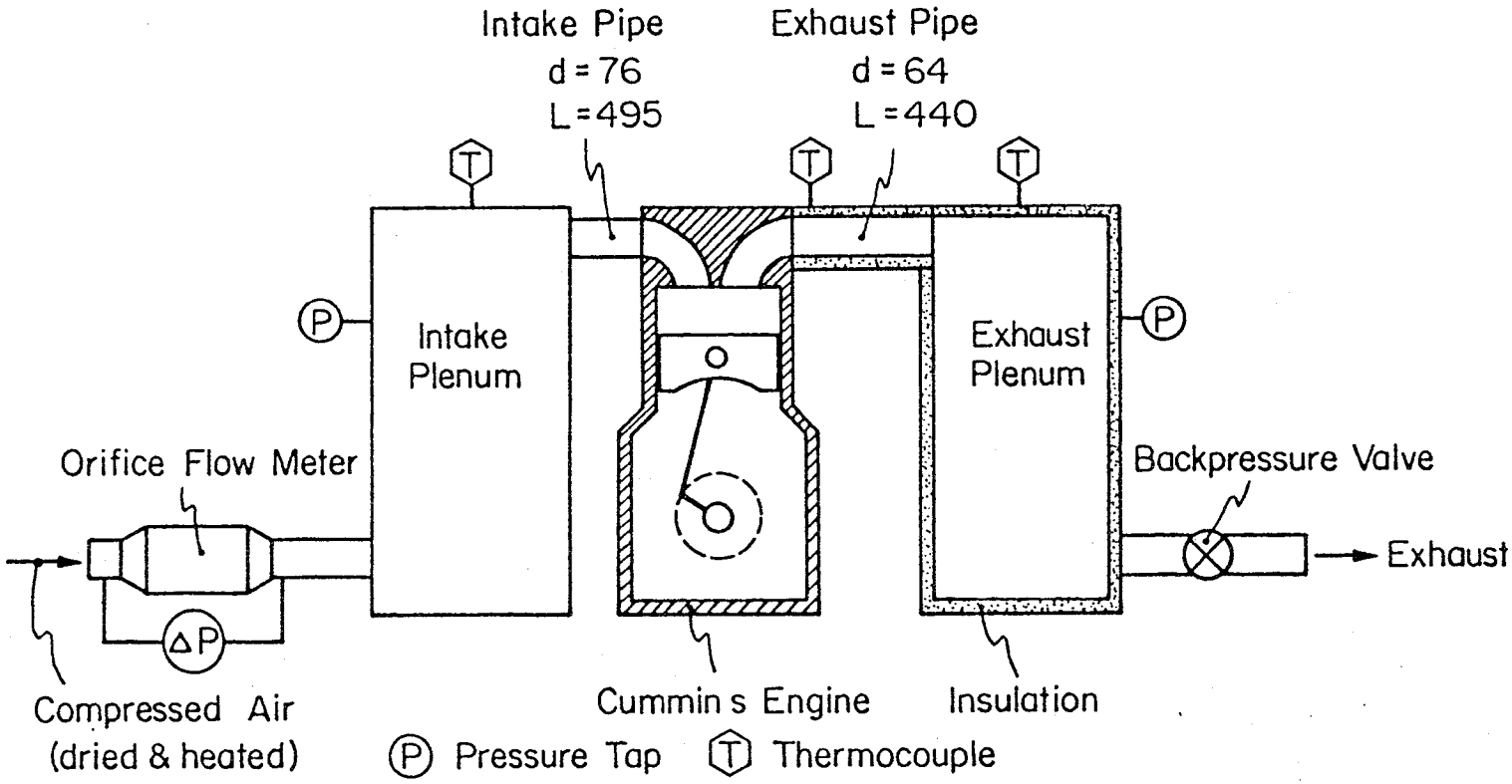

Figure 6-4. Schematic of intake and exhaust systems. Plenum volumes are fifty times cylinder displacement. Dimensions are in mm.

The exhaust tank is wrapped with insulation to minimize heat loss from the gas so that its temperature can be used to indicate the energy rejected by the engine in the exhaust. A chromel alumel thermocouple is used to record the exhaust gas temperature in the plenum and at the exhaust port. A valve is installed downstream of the plenum to compensate for changes in barometric pressure and simulate the turbocharger back pressure. Plenum pressure is measured using a manometer.

Air flow rate will be measured using an ASME orifice meter. A chromel alumel thermocouple is used to measure the air temperature at the meter and at the engine inlet. Plenum pressure is measured using a Heise Model H3915 absolute pressure gauge.

Compressed, dried and heated air is supplied to the engine. An existing air handling system will be modified for this purpose. At this writing the system components have been ordered, and they are expected to be delivered in the beginning of August.

The fuel system is shown in Figure (6-5). A variable speed motor drives a gear pump to deliver fuel to the injector. Approximately 80% of this fuel is used to cool the injector and is recirculated back to the reservoir. The quantity of fuel injected depends on the delivery pressure and the engine speed, and a 200:1 turn down ratio is required for the delivery pressure to cover the entire speed and load range. This is the primary reason for using a variable speed pump drive. Fuel pressure is also regulated in part by the throttle and by the bypass valve.

The fuel flow is measured by recording the time to consume a known mass of fuel. The supply reservoir is thus atop one pan of a laboratory balance. This reservoir is small enough so that the mass of fuel consumed during a measurement is significant compared to the mass of all the fuel in the reservoir (and the reservoir itself) for an accurate measurement. A separate, automated supply system is used to maintain the reservoir fuel level within fixed limits when measurements are not being performed.

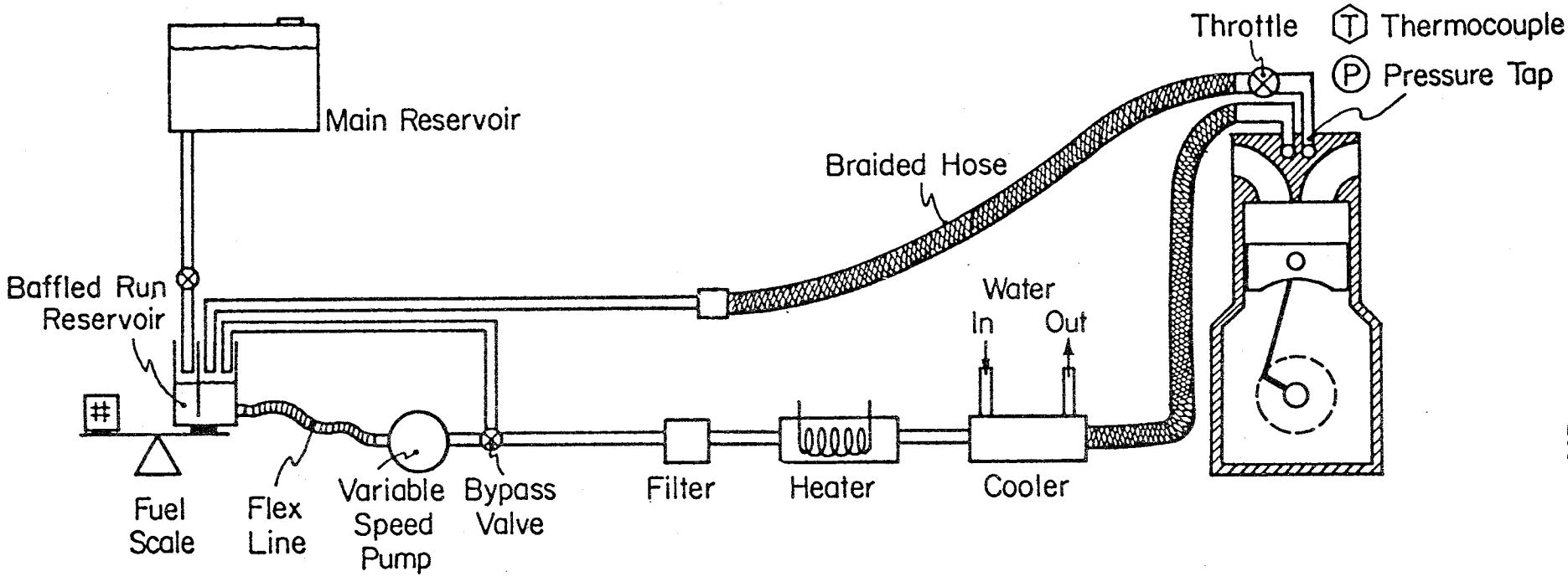

Figure 6-5. Schematic of variable pressure fuel supply system.

VII. DEVELOPMENT OF EXPERIMENTAL TECHNIQUES

As a part of this work, Purdue University is developing instrumentation and measurement techniques needed for acquisition of accurate data in the forthcoming baseline engine and insulated engine experiments. These techniques and instruments will be essential for measurements of pressure, temperatures, heat flux and heat radiation, all of which are needed for calibration and validation of the analytical models employed in the overall heat transfer and thermal analysis methodology.

A. TDC DETERMINATION

In order to use engine pressure data as a means to deduce engine heat transfer one must pay close attention to the proper phasing of the data with respect to crank angle. It may be shown that even small errors in phasing can have a significant effect on the calculations, and therefore it is one of the objectives of the experimental program to develop a method ensuring high degree of phasing accuracy on the order of 0.1°. The standard approach to crank angle phasing is to determine the TDC location by a static calibration technique using a spring-loaded detector inserted through injector port, or by a similar means. Such a calibration is not adequate as its accuracy is considered to be at best on the order of 0.3-0.5°. Also, it does not take into account the changes in phasing arising from dynamic effects at higher engine speeds.

In this work we have investigated two techniques, both dynamic, which gave a promise of attaining the desired accuracy: the polytropic exponent method and an optical proximeter.

Polytropic Exponent Method

The polytropic exponent method, described below, is a dynamic technique in which the location of the TDC is determined by analysis of the pressure signal obtained during a motoring operation. The fact that it is

dynamic offers a direct advantage over standard TDC calibration methods which are static, and in addition it is believed to be more sensitive and accurate as well.

A polytropic process is one for which the values of pressure and volume for a closed system undergoing a change in equilibrium states are governed by the equation pV^n = constant. The value of n, the polytropic exponent, depends upon the nature of the process. If the process is adiabatic, then $n = \gamma$, the specific heat ratio. If the process is isothermal, then n = 1, and if it is isobaric, n = 0. If the process is such that heat is added to the system or rejected to the surroundings while the volume is constant, then n becomes negative or positive infinity, respectively.

To a reasonable approximation, the compression-expansion processes in a motored internal combustion engine can be regarded as polytropic. Douaud and Eyzat (1977) suggested that the plot of the polytropic exponent over the compression and expansion processes of a motored engine could be used to detect phase errors in the pressure-crank angle data, and the method was used e.g. by By et al. (1981). They gave no indication of the accuracy of this method, but stated that it could be used to locate the top dead center to within 0.1 degrees of crank angle rotation. Because of its low cost, and easy implementation into a data reduction program of a digital acquisition system, we made an attempt to implement the polytropic exponent method. In the course of this investigation we studied the concept and analyzed it in a greater detail than Douaud and Eyzat had done. The goals of the investigation were to quantify the behavior of the exponent for different phase errors and determine what value the method has for locating top dead center to the desired degree of accuracy.

In the course of this study, significant errors were uncovered in the Douaud and Eyzat methodology which, when corrected, led to the conclusion that their assignment of the crank angle for top dead center was incorrect by at least one crank angle degree. Although the original

technique was found to be inadequate, we felt there was a merit in it and pursued the idea in a different form. Modeling the engine cylinder as a control volume with heat and mass transfer, the First Law of Thermodynamics states that

$$\dot{E} = -\dot{q}_{\ell} - p\dot{V} + \dot{m}_{out}h \qquad (7\text{-}1)$$

where subscript out refers to loss of mass due to blowby. Introduction of the specific heats yields

$$mc_v\dot{T} + c_vT\dot{m} = -\dot{q}_{\ell} - p\dot{V} - \dot{m}_{out}\,c_pT \qquad (7\text{-}2)$$

Using the equation of state $pV = mRT$ and the continuity equation, $\dot{m}_{out} = -\dot{m}$, one can manipulate eq. (7-2) to obtain

$$\frac{d\ell np}{d\ell nV} + \gamma = -\left[(\gamma-1)\,\dot{q}_{\ell}/(pV) + \gamma\dot{m}/m\right] V/\dot{V} \qquad (7\text{-}3)$$

By definition of the polytropic process the exponent n may be written as $n = -d(\ell np)/d(\ell nV)$. From equation (7-3) then,

$$n = \gamma + \left[(\gamma-1)\,\dot{q}_{\ell}/(pV) + \gamma\,\dot{m}/m\right] V/\dot{V} \qquad (7\text{-}4)$$

This equation applies throughout the compression-expansion process of a motored engine when the valves are closed. It does not assume constant specific heats. It indicates that heat loss and blowby cause the exponent to be less than and greater than the specific heat ratio near top dead center, respectively, and that at top dead center, where $\dot{V}$ becomes zero, the exponent becomes infinitely large.

Equation (7-4) may be approximated by expansion of the terms on the right-hand side in terms of power series in crank angle θ. Since $V/\dot{V}$ is

an even function, one can show that to the lowest order one can write

$$n \simeq (1 + \theta_p/\theta) \tag{7-5}$$

where θ_p is the crank angle at peak pressure (its value is negative for a motored engine), and a is close to the specific heat ratio. Note that $\theta_p < 0$ and TDC corresponds to $\theta = 0$. Letting n_a refer to the average value of the exponent after top dead center, and n_b refer to its average value before top dead center, then one can write

$$\bar{n}_a = \int_{\theta_1}^{\theta_2} n \, d\theta/(\theta_2 - \theta_1) \tag{7-6}$$

$$\bar{n}_b = \int_{-\theta_2}^{-\theta_1} n \, d\theta/(\theta_2 - \theta_1) \tag{7-7}$$

where θ_1 and θ_2 are selected values of crank angle over which the integral is performed ($\theta_2 > \theta_1$). Substituting equations (7-5) into (7-6) and (7-7) and performing the integration one obtains expressions for n_a and n_b which may be combined into a single equation elminating the constant a

$$(\bar{n}_a - \bar{n}_b) = (\bar{n}_a + \bar{n}_b) \; \theta_p \; \ell n \, (\theta_2/\theta_1)/(\theta_2/\theta_1) \tag{7-8}$$

This equation can be used as a rational means for detecting a phase error for the equality will be true only for a properly phased data. Letting ε denote the phase shift, one can define a "residual" δ as

$$\delta(\varepsilon) = (\bar{n}_a - \bar{n}_b) - \frac{(\bar{n}_a + \bar{n}_b) \; \theta_p \; \ell n \, (\theta_2/\theta_1)}{\theta_2/\theta_1} \tag{7-9}$$

For a motored set of pressure-angle data, the task then is to find the value of ε such that $\delta = 0$, and assign this as the phase shift in the data. The calculation of δ depends on specification of θ_1 and θ_2. The

difference between them should be large enough to make the calculation of the average values of the exponent n accurate, keeping in mind that the validity of the asymtotic expansion for n about top dead center decreases as the integration is performed farther away from top dead center.

To summarize the technique, it evaluates the polytropic exponent n (implied by the pressure data) at symmetric crank angle locations before and after TDC and fits them to a postulated equation expressing n as a function of crank angle. Adjusting the crank angle phasing of the pressure data until an imbalance in the polytropic exponent equation is zero, leads to the correct phasing.

Procedure for Evaluation of the Polytropic Exponent Method

A cycle simulation program was used to produce a realistic pressure-crank angle data, which could be treated as an exact data set, free of any measurement or phasing errors. The program accounted for effects of variable specific heats, blowby, and heat transfer from the gas to the cylinder walls. The heat transfer was evaluated on the basis of a Reynolds analogy as

$$Nu = KRe^{C_1} \tag{7-10}$$

and the blowby rate was assumed to be proportional to the mass of air in the cylinder at any given instant, that is

$$\dot{m}_{out} = Cm$$

where $\dot{m}_{out}$ is the blowby and m is the cylinder mass. As a part of this study we also used actual engine data from a motored AVL research single cylinder engine. An approximate match between the simulation and the engine data was obtained by using the following set of constants: K = 4.6, C_1 = 0.6 and C = 0.8.

A separate program was then written to evaluate the polytropic exponent method. The input to this program is the pressure-crank angle array calculated by the engine simulation program, or experimental data measured from an actual motored engine. The program calculates the polytropic exponent at each crank angle from

$$n = -d(\ell np)/d(\ell nV) \qquad (7\text{-}11)$$

To evaluate the scope of the pressure curve needed in equation (7-11) a least square technique was used. This technique fitted a cubic polynomial through the pressure value of interest and the five values of pressure before and after it. Once the polynomial was obtained, it could be differentiated to evaluate $dp/d\theta$.

The exponent evaluation program was set up to allow the introduction of an arbitrary phase shift, ε, for the input pressure-angle array, where the phase shift is defined as the angle between the actual and apparent top dead center. For each value of the input shift one can then calculate the corresponding error δ from equation (7-9), and the results can be analyzed in a graph form.

Results for Simulated Data

Initial studies of the technique indicated that a good choice for the integration limits in equations (7-6) and (7-7) are $\theta_1 = 10$ degrees and $\theta_2 = 40$ degrees. A plot of the behavior of δ for the pressure-angle array calculated by the engine simulation program for an engine operating at 1000 rpm is shown in Figure 7-1. The curve is linear, with $\delta = 0.023$ for $\varepsilon = 0°$, and $\varepsilon = 0.26°$ where $\delta = 0$. The fact that δ is not zero when ε is zero is due to the fact that the expression for n (equation 7-5) is only approximate.

This creates a problem, as the error 0.26° is too large to neglect, and so $\delta = 0$ cannot be used as the criterion indicating correctly aligned

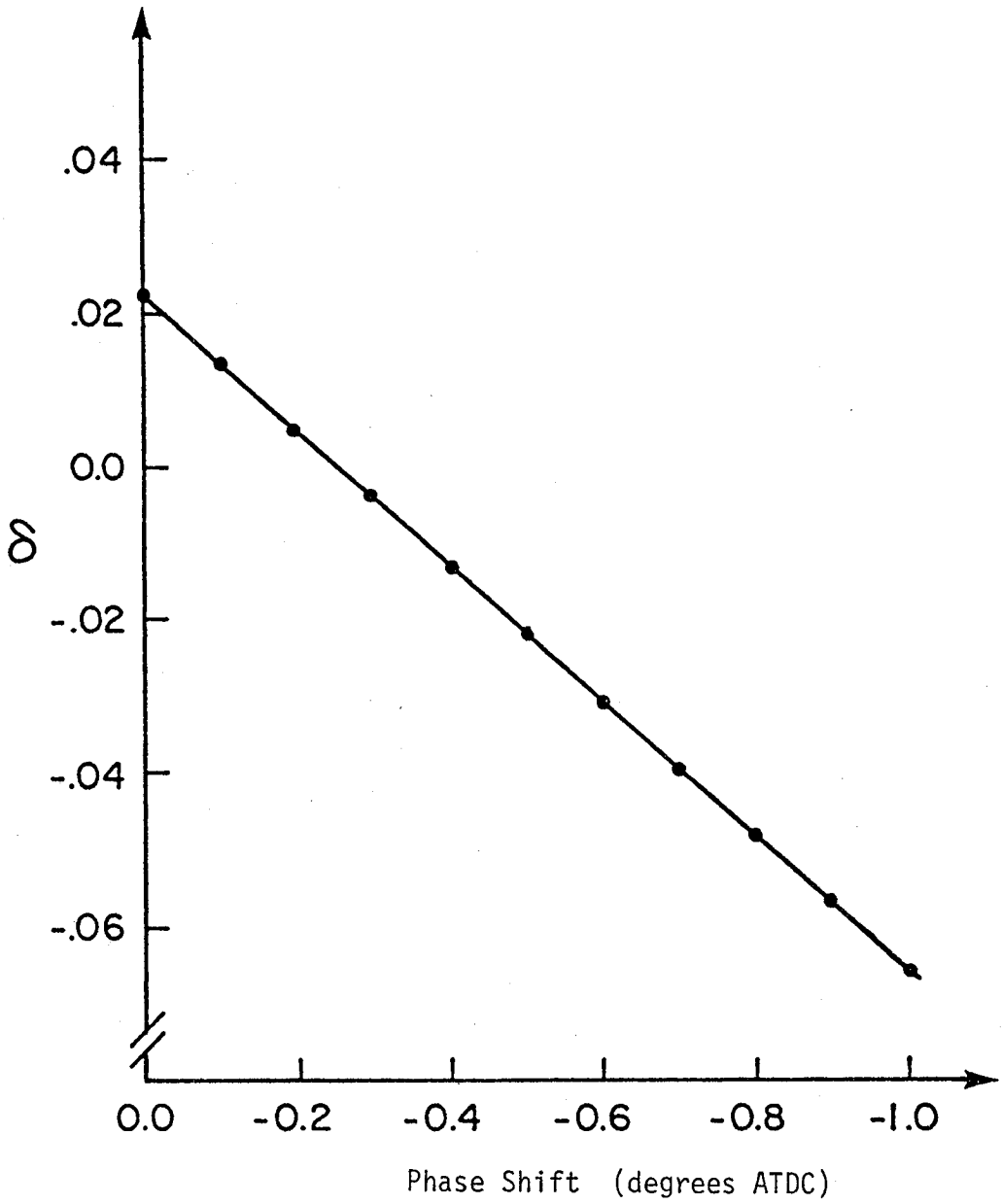

Figure 7-1. Plot of imbalance versus phase angle shift for the polytropic exponent method of TDC determination. Data generated analytically.

TDC. The only way this problem could be overcome would be if the shift at zero δ were found to be independent of engine speed and load and could thus be simply subtracted out.

To quantify the behavior of the residual, the engine simulation program was operated at a wider range of engine speeds, and the blowby coefficient, C, and the Nusselt number coefficient, K, were varied to model different engine configurations. The operating conditions at which the engine simulation program was exercised are shown below:

engine speed, N: 500, 750, 1000, 1100,
1250, 1500, 2000, 2500 rpm
blowby coefficient, C: 0.6, 0.8
Nusselt number coefficient, K: 3.0, 4.6, 5.0

The results are shown in Figure 7-2 which shows that over the range studied the values of δ lie between 0.019 and 0.027. From examination of Figure 7-1, this range of δ corresponds to a range of phase shift of about 0.10 crank angle degrees, which is just within the desired range. This indicates the method works, albeit marginally, for an analytical pressure-angle data set. However, in any experimental data set there will be some errors in pressure measurement, which may be expected to degrade the method results. Therefore, based on these results it appears the polytropic exponent method is not useful as an unequivocal means for locating top dead center.

Results for Experimental Data

The experimental pressure data was obtained on the AVL single cylinder research engine operated in a motoring mode of 1000 rpm. An optical crank angle encoder was used to trigger an analog to digital converter to sample the pressure signal every two crank angle degrees. The data was smoothed by a least squares technique and the polytropic exponent was evaluated from equation (7-11). The result is presented in Figure (7-3), which shows some inaccuracy in the exponent far from the TDC,

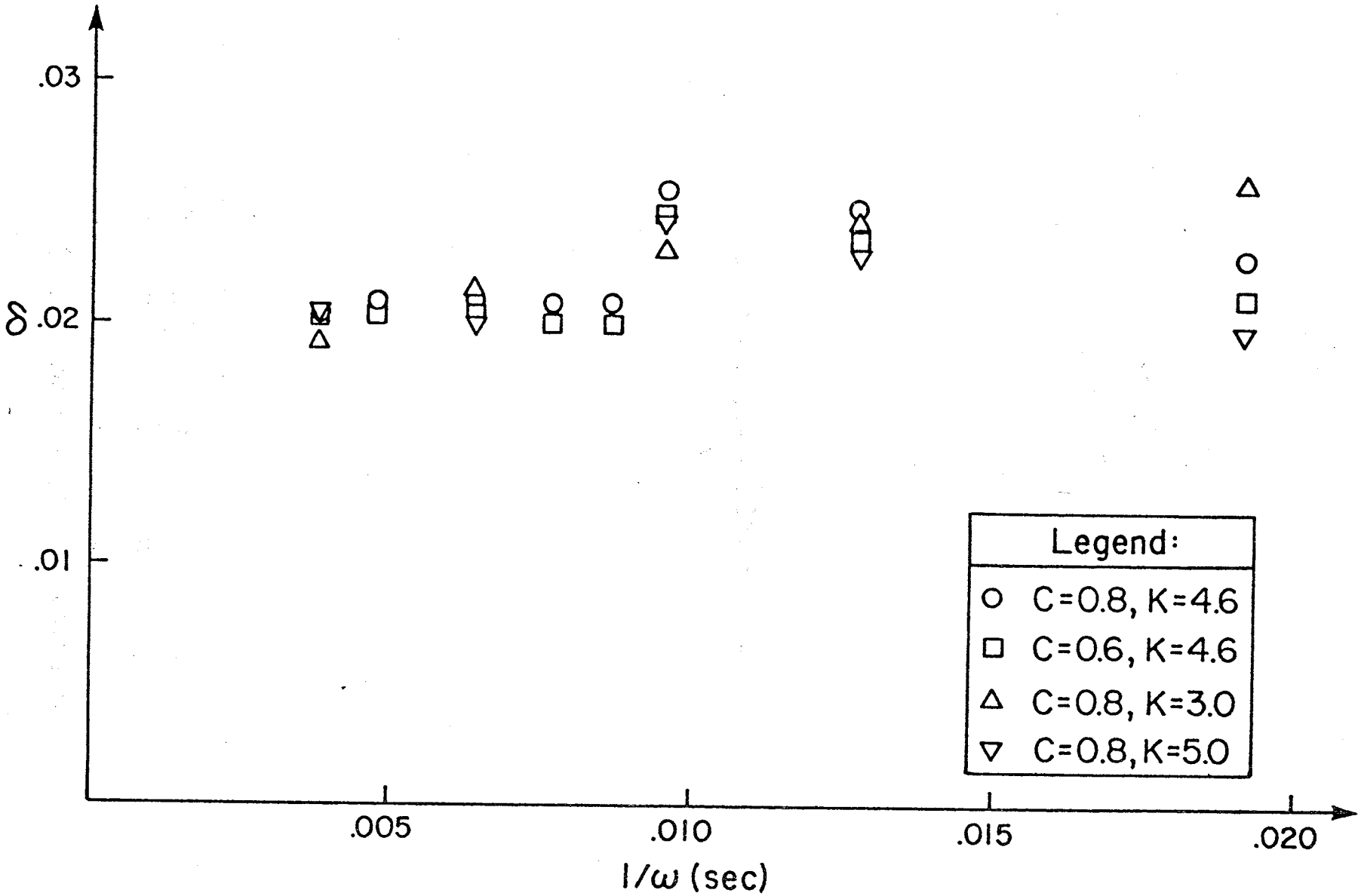

Figure 7-2. Imbalance as a function of inverse engine speed. Data generated analytically with different constants in the heat transfer and blowby models.

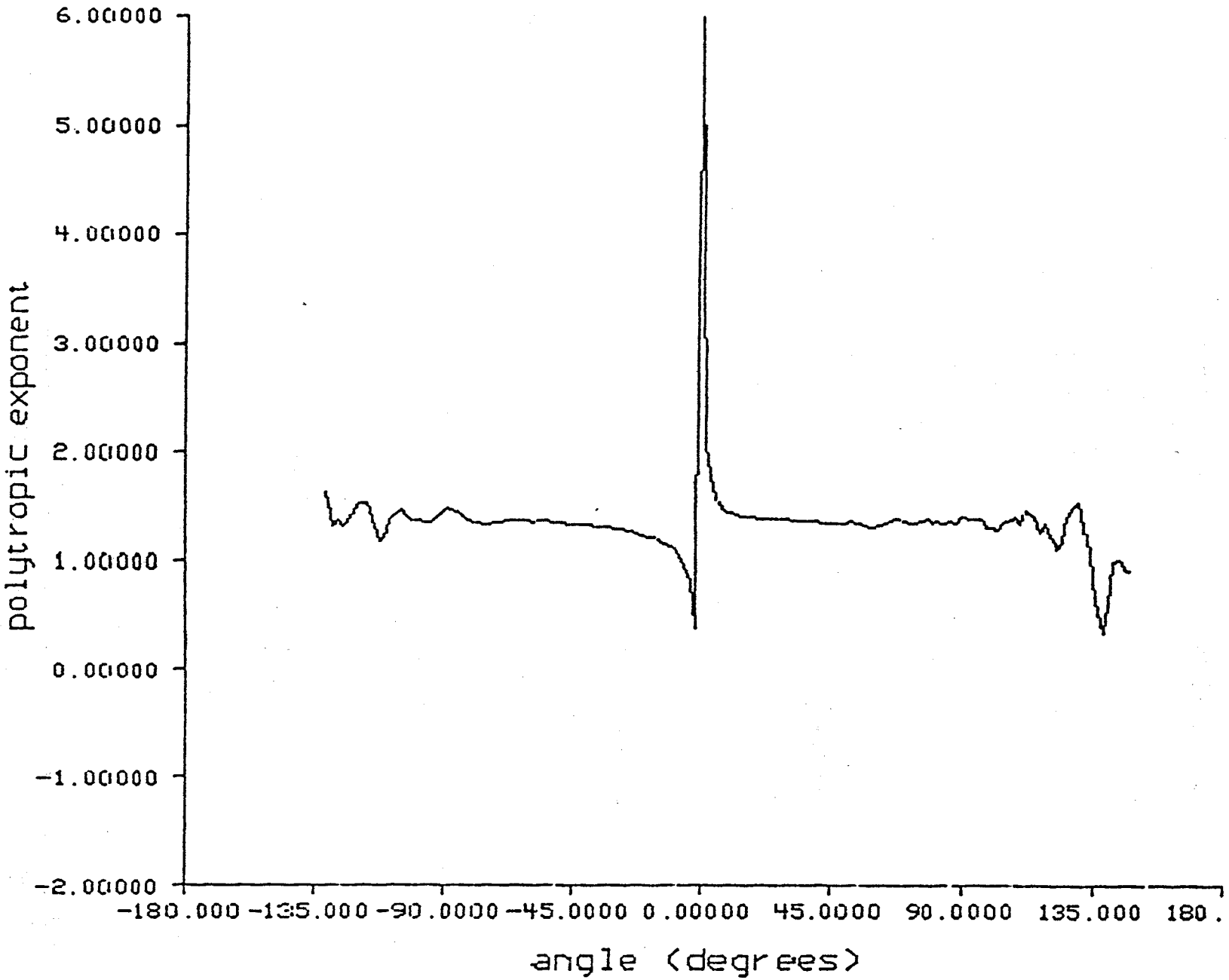

Figure 7-3. Polytropic exponent calculated from motored engine pressure data.

which disappears as the pressure level rises during the compression. Near TDC the exponent displays the characteristic behavior approximated by equation (7-5).

Using this data, phase shift was calculated between the optical crank angle encoder and the signal from a magnetic pickup pulse (once-per-revolution). The location of the magnetic pickup pulse was adjusted so as to indicate the location of the top dead center determined statically with a dial gage indicator. Four different runs were made on separate days, all at 1000 rpm, to obtain an indication of the repeatability of the results. Table 7-1 shows the calculated average exponent, crank angle at maximum pressure, phase shift deduced by the data reduction program (defined as that phase shift which produces $\delta = 0.023$), and the corrected value of crank angle at peak pressure.

An encouraging indication is that the average value of the exponent varies by only 0.005. The phase shift is positive for all four cases, indicating that the actual top dead center location as indicated by the encoder occurs after the real top dead center location. Its value ranged over a fairly wide range 0.30°-0.96°. However, the corrected values of crank angle at peak pressure, obtained by adding the phase error to the uncorrected value, vary by less than ± 0.1 degrees from a mean of about 0.80 degrees before top dead center. This indicates a respectable repeatability of the method. As for the absolute error, which in the analytical studies in which the TDC location was known was found to be a shift of 0.2 degrees, its value cannot be determined in the application to experimental data because one does not know the correct TDC location from the encoder data.

Of some concern, however, was the variation of the phase error from run to run. It is now believed that this was due to a problem with the encoder mounting. The solution to this problem was to improve the rigidity of the mounting, accomplished by replacing the encoder by a rigid toothed-wheel (made by AVL) attached directly to the flywheel.

Summary

The polytropic exponent technique falls short of the objectives of this work. However, this does not mean that the technique has no merits. The method has its advantages in simplicity, as well as in accuracy compared to standard static calibration techniques. One application of the method is to use it directly to get indication of TDC location within several tenths of degree. Another possibility is to use it as an auxiliary technique. If top dead center can be located initially to the desired accuracy by some other means, then a daily check of the residual can be used to confirm the top dead center location. From the analytical studies done using the simulated engine program, the δ vs. ε curve can be used to estimate how the phase error might grow as the residual changes, and warn when a recalibration method of the top dead center position is needed.

Table 7.1 Results of Polytropic Exponent Method Applied to TDC Determination for Four Different Motoring Runs at Nominally Identical Conditions

Run	n_{avg}	θ_{peak} uncorrected	Phase shift	θ_{peak} corrected
1	1.3261	-1.1620	.3015	-.8605
2	1.3267	-1.5027	.7797	-.7230
3	1.3241	-1.6653	.9581	-.7072
4	1.3292	-1.4166	.5223	-.8943

Fiber-optic Proximity Probe

Fiber-optic proximeters are widely used in making small displacement measurements, and as such might be considered well suited for detecting the engine piston motion near top dead center.

An illustration of the use of the fiber optic probe is shown in Figure (7-4). The probe consists of a transmitting bundle and a receiving bundle, which respectively have a light source and a photodetector on one of their ends. At their opposite ends, the two bundles meet at the probe face. The intensity of the radiation reflected off the work surface and captured by the reflecting bundle varies with the distance of the work surface from the probe face. In our application, a probe inserted into the engine head will produce a reflection from the piston from which one can deduce the location of TDC.

The variation of the photodetector output signal as a function of the distance of the work surface from the probe face is qualitatively shown in Figure (7-5). Three distinct regions are of interest; the front slope region, the optical peak, and the back slope region. The reason for this signal behavior can be explained by referring to Figure (7-6). When the work surface is closest to the probe face, as in Figure (7-6), the fraction of radiation reflected from area A and sent to the reflecting bundle is very small. This fraction is referred to as area B2. As the distance x increases, areas B1 and B2 increase, while area C decreases. Thus, there is a linear increase in the output of the photodetector in the segment defined as the front slope region. At the condition shown in Figure (7-6), the reflected radiation just illuminates exposed area of the detector bundle, producing the optical peak depicted in Figure (7-5). As the work surface continues to move from the probe face, the signal strength decreases as $1/x^2$ in the segment defined as the back slope region.

The exact shape of the curve shown in Figure (7-5) depends upon the diameter of the bundles and the arrangement of their fibers. Three

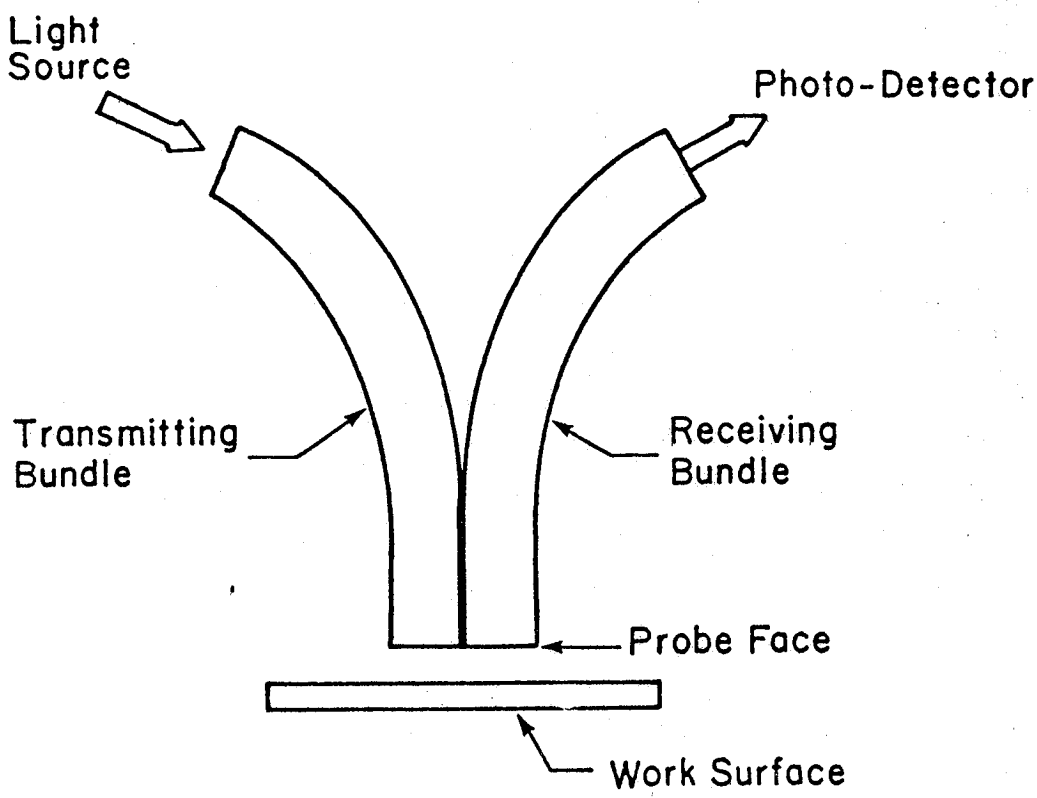

Figure 7-4. Schematic of fiber optic proximity probe sensing the distance to a surface.

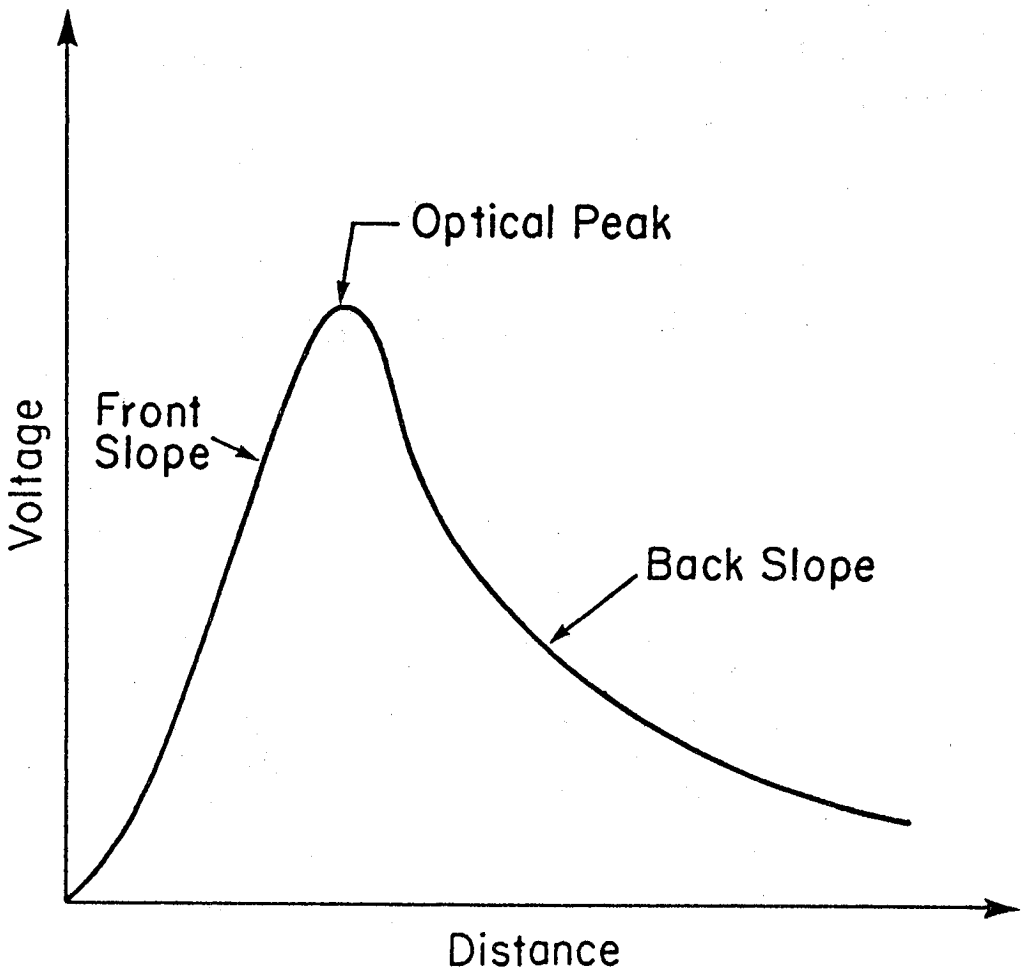

Figure 7-5. Characteristic signal output produced by a fiber optic proximity probe as a function of distance.

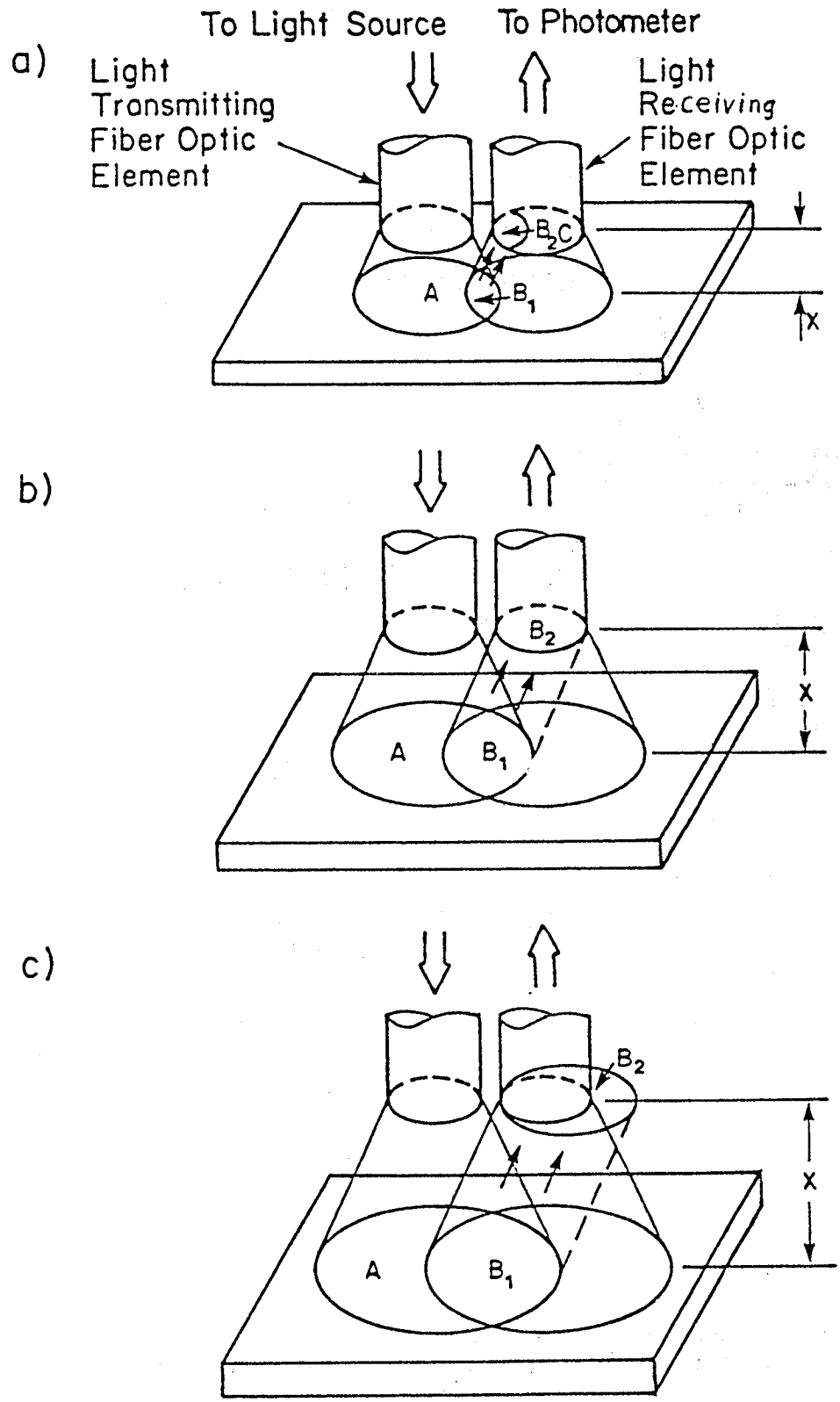

Figure 7-6. Schematic of different patterns of light reflection and collection by the receiving fiber optic element.

arrangements are shown in Figure (7-7), along with the outputs they produce. The random arrangement yields the greatest sensitivity, while the hemispheric arrangement provides the largest range; the configuration selected depends on the application.

The proximeter was designed and built at Purdue. A fiber optic bundle was purchased from Dolan Jenner, Inc. A hemispherical fiber arrangement was selected, because this gave the largest range and the greatest separation of the peaks. The bundles were enclosed in a threaded housing, which enables the fiber optics to be inserted into an adaptor. The adaptor can then be inserted into a pressure transducer or similar port. A photograph of the probe is shown in Figure (7-8).

Bench Testing of the Fiber Optic Proximity Probe

Before the proximity probe was tested in the engine, its characteristic curve was verified. This was done using the experimental setup shown in Figure (7-9). A helium-neon laser was used as a light source, and a photomultiplier tube was used to measure the intensity of the reflected light. The work surface, which was a polished aluminum plate, was attached to a special fixture which allowed accurate setting of the horizontal distance from the probe face to the work surface. The relative signal strength is shown in Figure (7-10) as a function of the distance separating the work surface and the probe face. The dots represent values obtained in four separate days, and the solid line represents the best approximation through them. The front slope region, optical peak, and back slope region are clearly identifiable. The probe is seen to be suitable for measurements of distances up to about 0.75", which is sufficient for the present purpose. The scatter is believed to originate from the photomultiplier that was used as a detector, and it is not present in the present version of the instrument. The slope of the curve is the greatest on the "front" slope, where the probe is the most sensitive. Due to the smaller distances involved, the front slope can be used in situations where the proximeter views the squish region which is closest to the proximeter at engine top dead center. The back

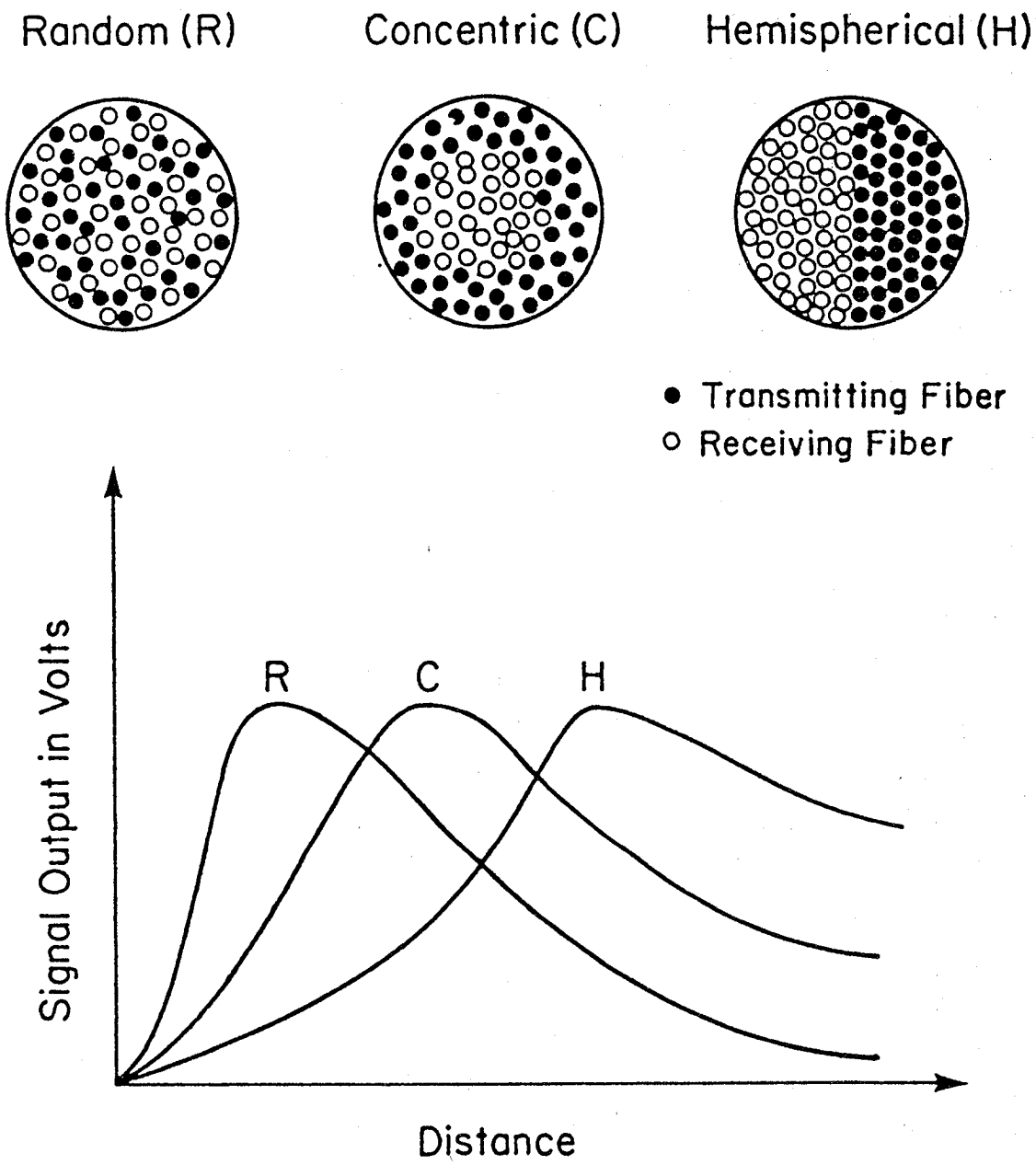

Figure 7-7. Arrangements of transmitting and receiving fibers used in construction of fiber optic bundles.

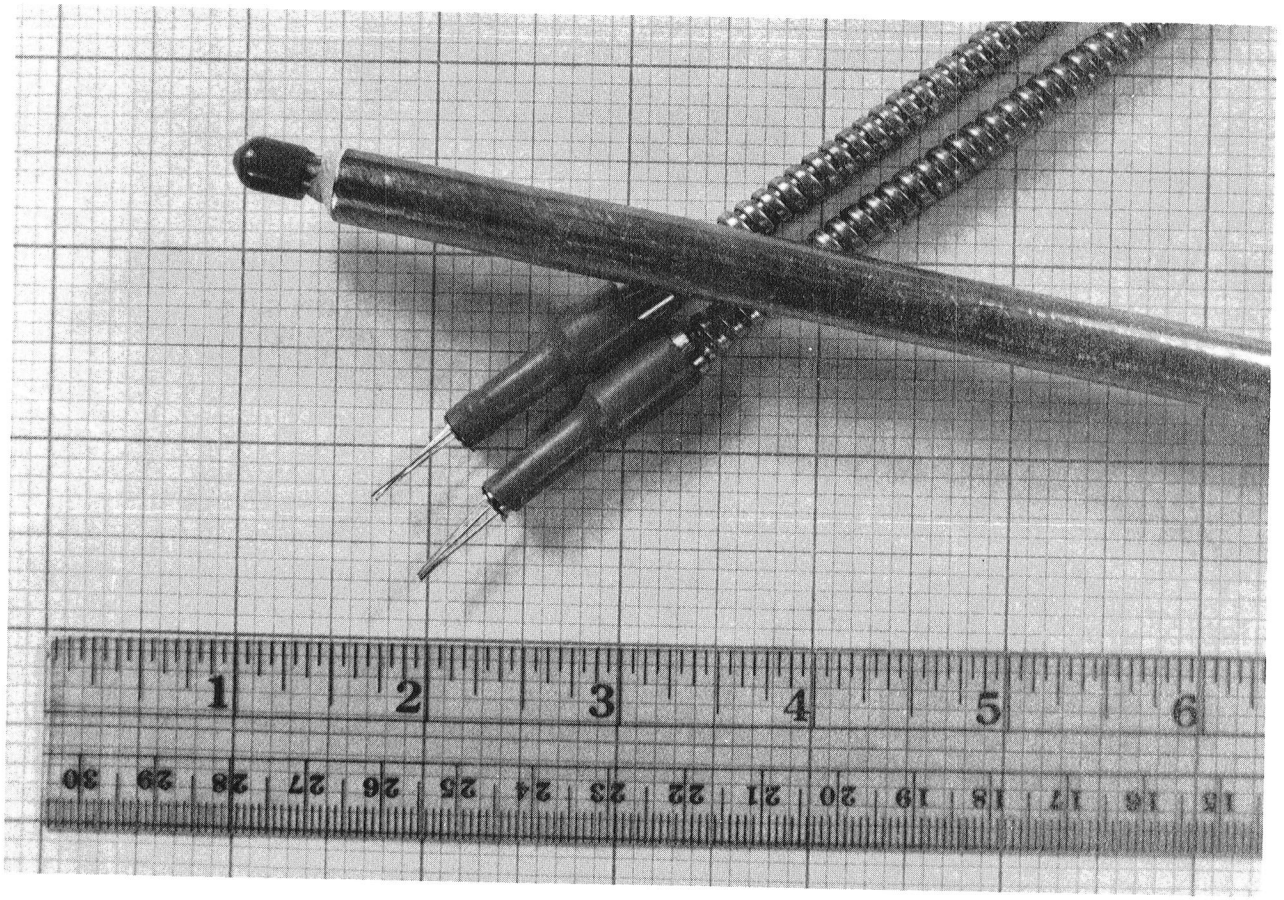

Figure 7-8. Photograph of the fiber optic proximity probe indicating its physical size

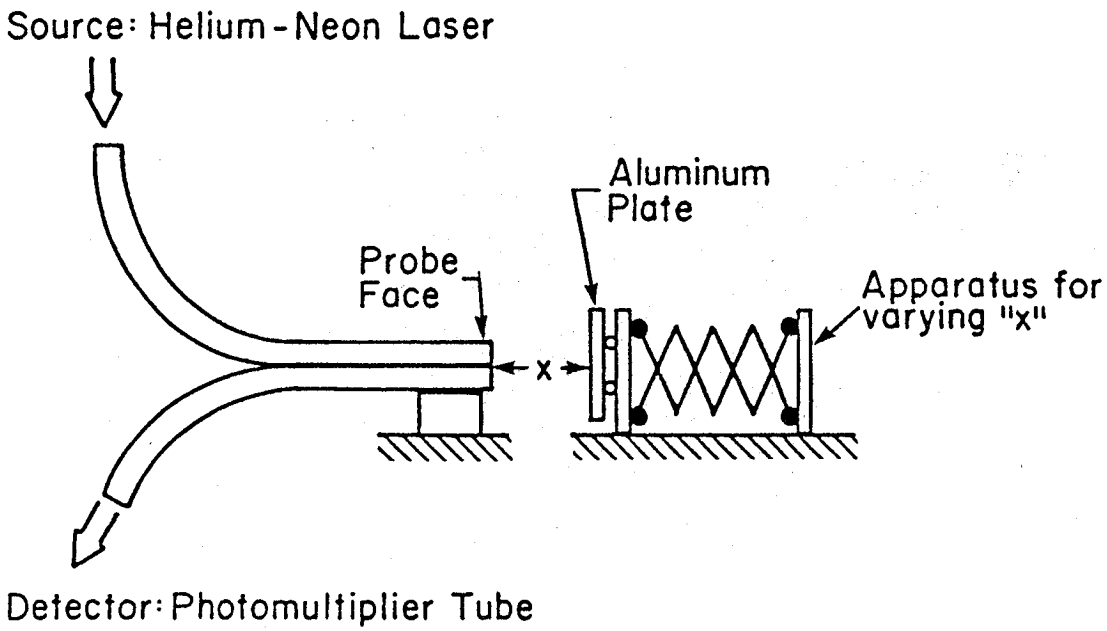

Figure 7-9. Schematic of experimental set up for bench testing the fiber optic probe.

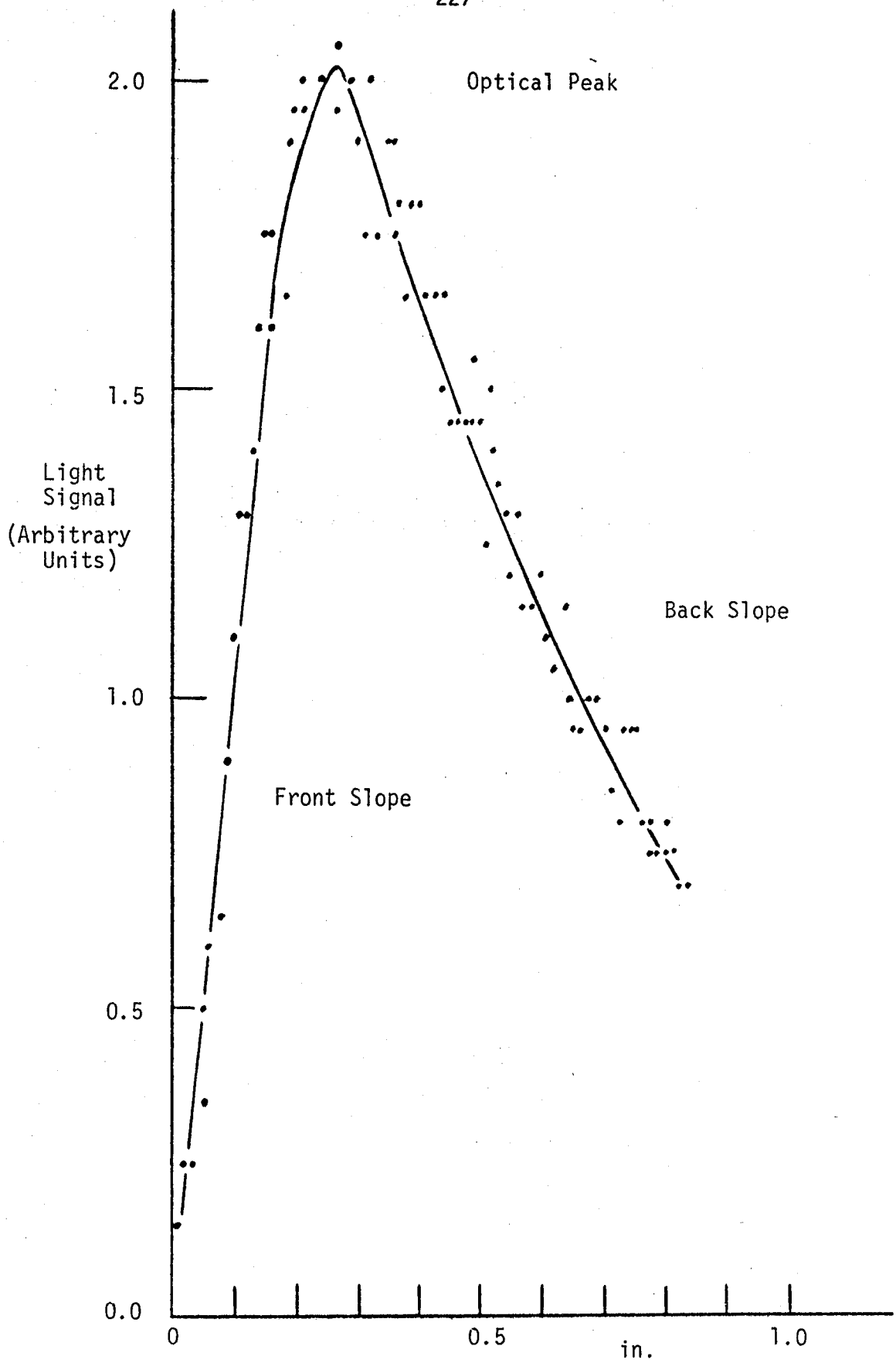

Figure 7-10. Reflected light signal vs. distance obtained in initial bench tests of the proximity probe.

slope would be used if the proximeter views the piston cup, in which case the reflecting surface would be farther away.

As delivered, the Cummins engine has a standard research head; i.e., only one access port which views the piston cup. This way the engine can be installed and operated without delay. A second head is being prepared by Cummins as a part of their contribution to the program and it will be delivered later. This head will have two access ports, the second of which is to permit access to the squish region of the piston top.

The data on Figure (7-10) can be converted into a plot of signal vs. crank angle that can be anticipated for the Cummins single cylinder engine. Taking into account the 6" stroke and squish clearance of 0.050" at TDC, one can calculate the instantaneous distance from the head to the piston top as a function of crank angle. The resulting replot of the mean line through the data is shown in Figure (7-11). The signal is symmetric about TDC, producing a double-humped curve with hump maxima near ± 21° crank angle. The location of TDC can be obtained from such a signal by curve-fitting to the middle portion a parabolic or a similar symmetric curve and splitting the analytical fit in half, which can be done with great accuracy.

Engine Testing of the Probe

The next step was to statically calibrate the probe in a research engine. First, however, a more convenient source-detector system was needed. By consulting the catalogues of various optoelectronics manufacturers, a light emitting diode and phototransistor pair was selected. The diode emits radiation in the infrared region (approximately 907 nm). A schematic of the circuit used to bias the diode and detect the output of the phototransistor is shown in Figure (7-12).

The results of the static calibration (engine slowly hand-cranked) are shown in Figure (7-13). The maxima and minimum are evident. The

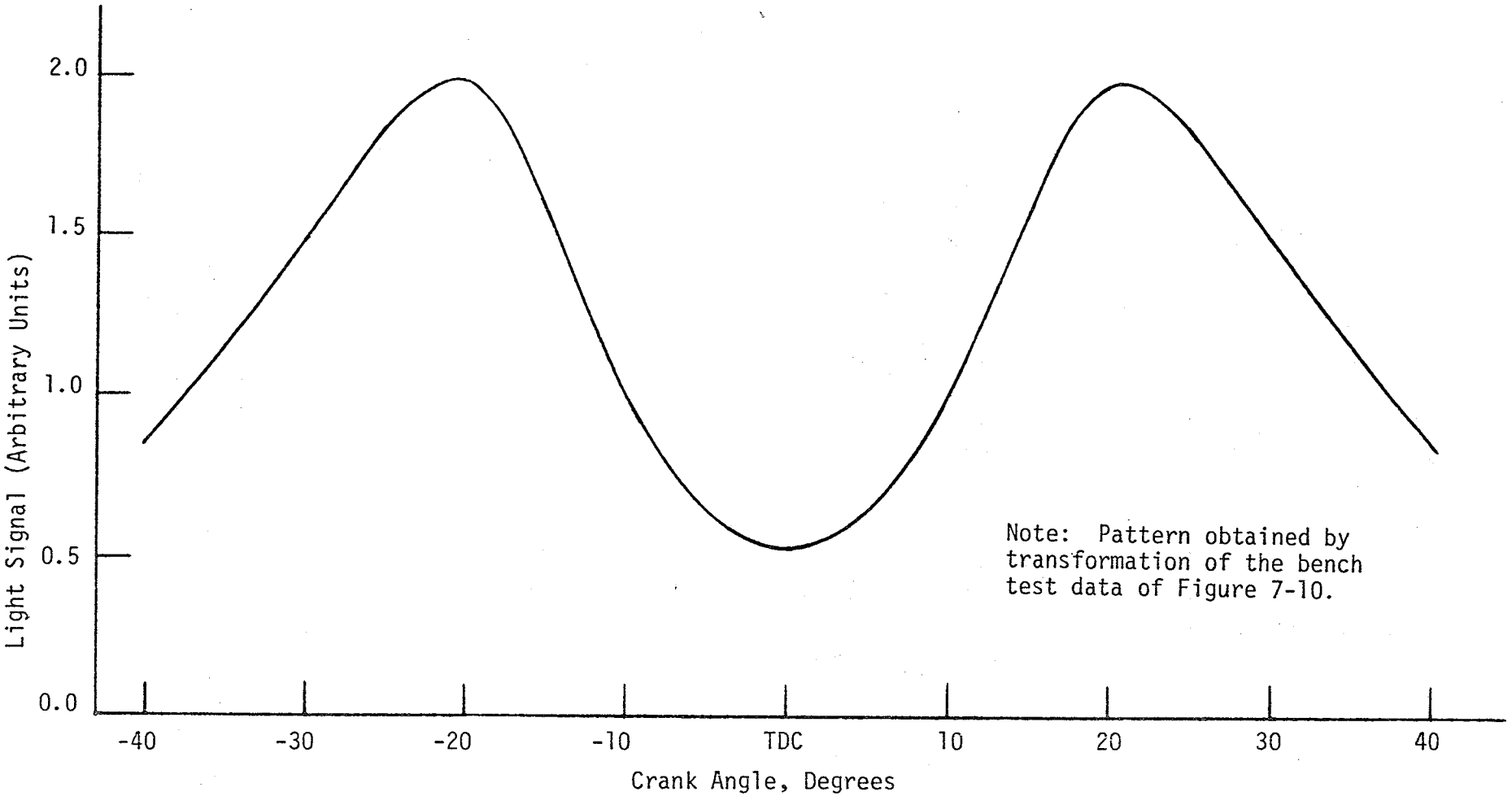

Figure 7-11. Simulated optical proximity signal expected for the Cummins single cylinder engine.

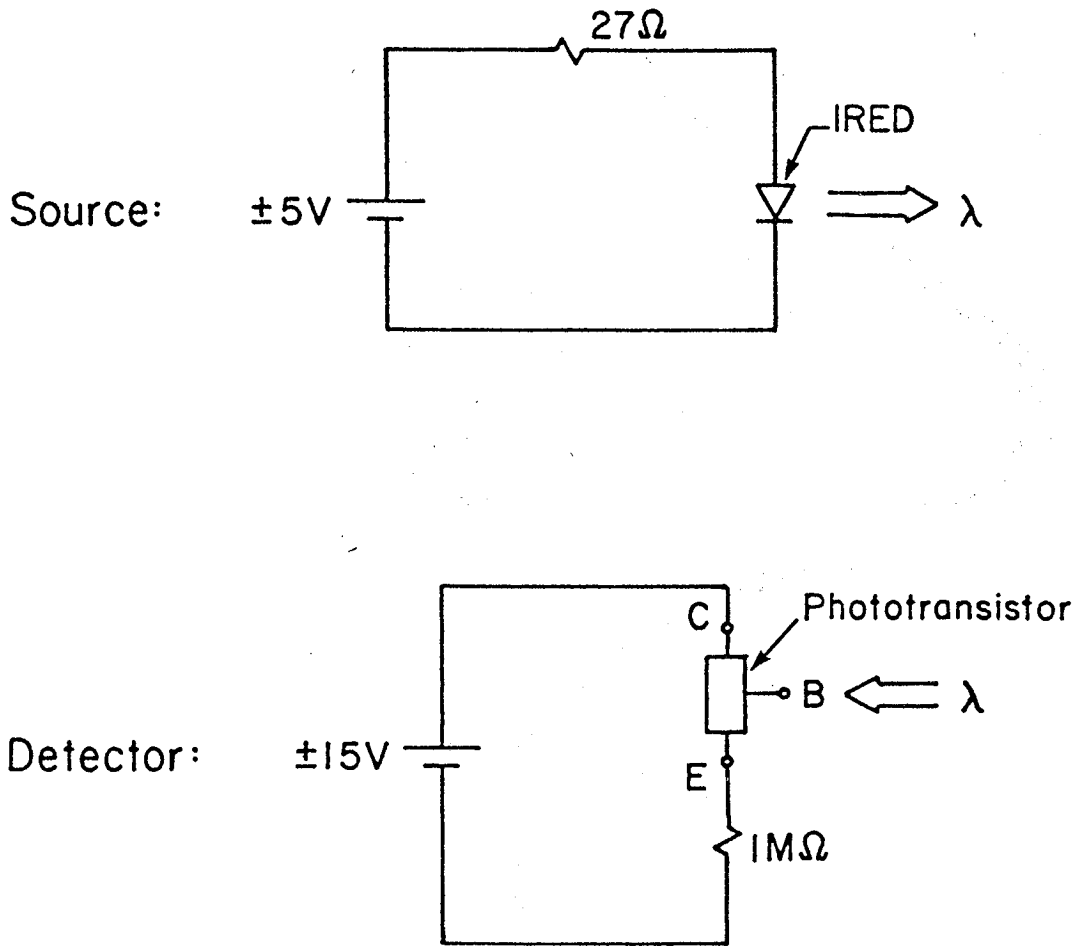

Figure 7-12. Schematic of the circuits used in the source and detector parts of the optical proximity probe.

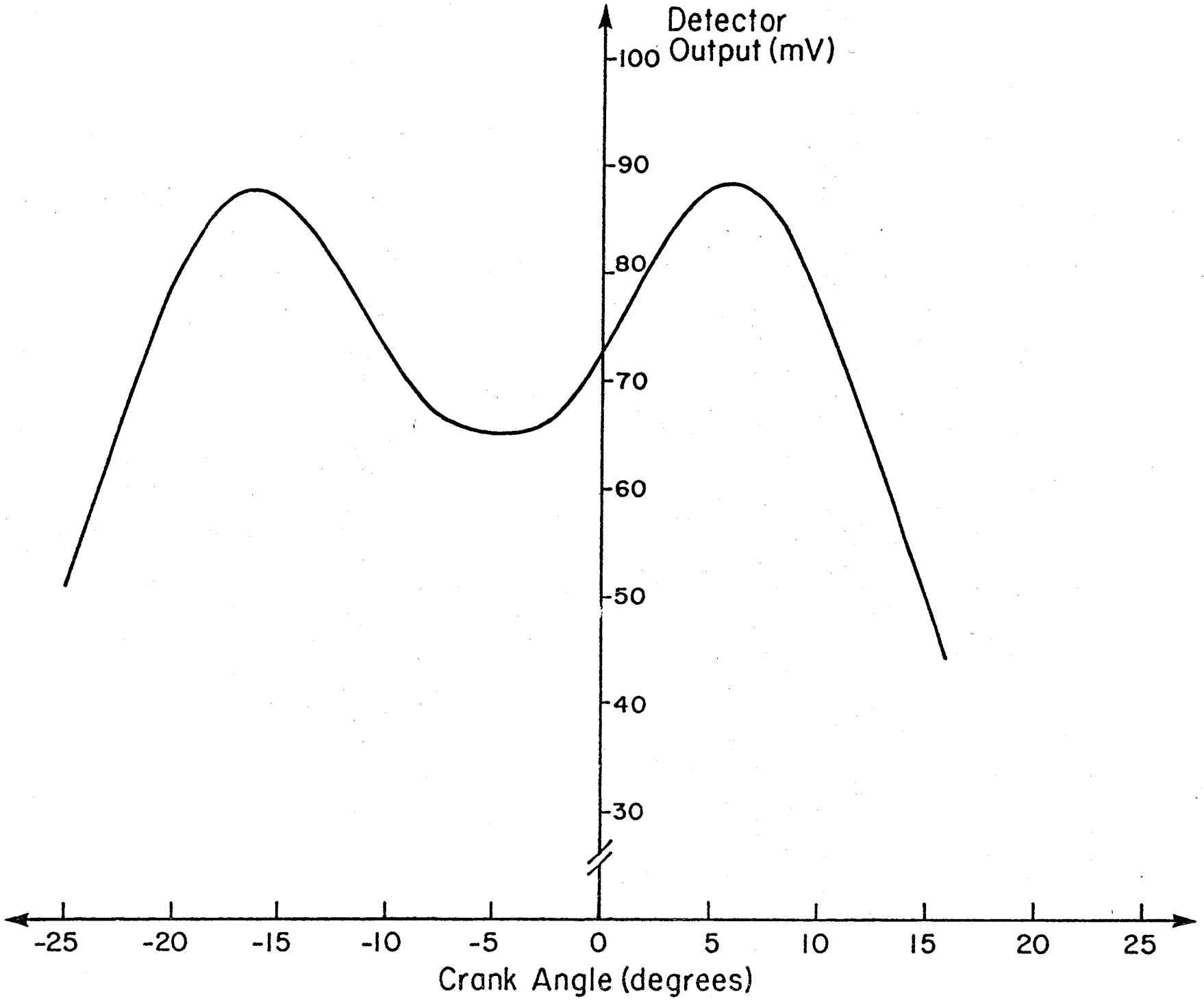

Figure 7-13. "Static" signal produced by the proximity probe (engine hand turned).

abscissa shows degrees crank angle measured with respect to a marker attached to engine flywheel.

At this point, the proximity probe was ready to be tested in a motored engine. First, a photograph of an oscilloscope trace of the probe output signal was taken to verify its shape and study how it could be analyzed (Figure 7-14). The lower trace in the photograph is the output produced by a magnetic pickup sensing the location of a marker attached to the flywheel, near top dead center position. In this figure a sudden discontinuity occurs in the signal as the TDC marker passes the pickup between the compression and expansion strokes. One item of concern is the difference in magnitudes of the two optical peaks. This may be due to the piston rocking during its travel about top dead center, thus changing the relative distance between the probe face and the piston surface, or causing the surface reflectivity of the piston to change. Work is in progress to answer this question.

The locations of the maxima and minima and the repeatability of these locations were determined next. To analyze the probe output signal, a Norland 3001 digital oscilliscope was used. This oscilloscope has the capability to sample at equal time increments as low as two microseconds and store the data in 4096 memory locations. The oscilloscope can analyze two data channels simultaneously, devoting 2048 memory locations to each, in which digitized data can be stored at time intervals as small as four microseconds (or about 250 kHz). This corresponds to 40 data samples per single crank angle at 1000 rpm engine speed. This allows the storage of finely resolved probe data and magnetic shaft encoder data from individual cycles and their subsequent analysis. Among the functions of the analyzer is an automatic maximum and minimum search routine which can be used to locate in the time domain the peaks in the probe signal. This function was used to determine the locations of the two peaks and of the minimum in between, and to check the variations of these locations with respect to the zero crossing of a conventional magnetic encoder signal commonly used to determine the TDC locations.

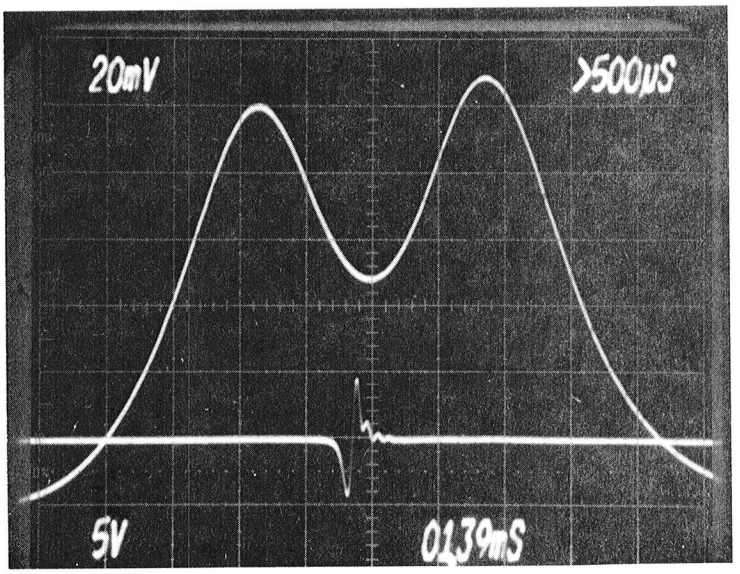

Figure 7-14. Dynamic output of the proximity probe installed in the AVL engine operating at 1000 RPM.

The repeatability of the locations of the maxima and minimum at one engine speed were checked first. The results are presented in Table (7-2) for an engine speed of 1000 rpm. The first two columns are the angular locations of the left and right maxima, and the third column is the average of these two locations as determined by the magnetic shaft encoder. The angular location of the minimum is recorded in the last column. The first ten samples are for results recorded in the gas-exchange region. It may be observed that for the gas exchange region the largest angular difference between the peak averages is 0.25 degrees, and 0.32 degrees for the signal minimum. The same values in the compression-expansion region are 0.28 degrees and 0.52 degrees respectively. The results are larger than the 0.1 degree accuracy desired. However, it should be noted that these results were obtained with no signal enhancement. For example, the function used to locate the signal maxima and minimum does not curve-fit the digital data - it only finds the memory location of the largest digital value. We expect that a significant improvement will result by application of:

1) signal averaging over the same number of cycles as the pressure data we shall be acquiring, i.e., 10-20 consecutive cycles;
2) smoothing of the signal to eliminate spurious high frequency noise;
3) fitting of the smoothed signal by an osculating polynomial in the vicinity of the signal minimum.

A brief check was made of the effects of engine load and speed on the probe results. Three engine speeds were selected: 600, 1000, and 1500 rpm. The load effects were simulated by throttling the intake air during motored operation. A substantial throttling was applied, reducing the air flow to less than 50% of the unthrottled operation. At a fixed engine speed this resulted in no change in the observed differential between the magnetic encoder signal and the optical probe signal. The reason for this test was that gas pressure forces acting on the piston affect the piston dynamics and instantaneous piston location and attitude. Changes in gas pressure could have been expected to produce

Table 7-2

Angular Locations of Maxima, Minimum, and Average Optical Proximeter Signal for Engine Speed of 1000 RPM
(data sampled every 0.03 crank angle degrees)

o: top dead center in gas exchange region
●: top dead center in compression-expansion region

	Left Maximum	Right Maximum	Average of Left and Right Max.	Minimum
o	-11.17	15.53	2.18	2.57
o	-11.29	15.44	2.08	2.60
o	-11.65	15.89	2.12	2.39
o	-11.99	16.33	2.17	2.71
o	-11.44	15.53	2.05	2.42
o	-11.39	15.55	2.08	2.53
o	-11.29	15.44	2.08	2.48
o	-10.87	15.38	2.26	2.48
o	-10.70	15.31	2.30	2.44
o	-10.76	15.31	2.27	2.62
●	-10.45	15.14	2.35	2.21
●	-10.27	14.93	2.32	2.24
●	-9.40	14.30	2.45	2.24
●	-9.44	14.29	2.42	2.11
●	-9.84	14.49	2.33	2.10
●	-9.32	14.14	2.41	2.17
●	-9.11	14.11	2.50	2.17
●	-9.61	14.48	2.44	2.21
●	-9.85	14.42	2.29	2.21
●	-9.14	14.29	2.57	2.62

Gas Exchange Region: $\Delta\theta_{avg} = 0.25°$, $\Delta\theta_{min} = 0.32°$

Compression-Expansion Region: $\Delta\theta_{avg} = 0.28°$, $\Delta\theta_{min} = 0.52°$

changes in piston motion near TDC and affect the signal. Since no measurable effects were observed, it now appears that load change will not cause problem with probe calibration.

The engine speed, on the other hand, was found to affect the observed shift, which went from 1.5° at 600 rpm to 3.3° at 1500 rpm. The reason for this shift was found to be a fixed time delay of 166 microseconds between the two signals, and this problem will be eliminated shortly.

Future Plans

A computer program will be written to construct the least squares fit curve through each portion of the signal so that a more accurate evaluation of the maxima and minimum can be found. The tests described above will be repeated for the probe used in this study and a new probe which is inserted into the bowl region of the piston. Also, the head will be removed and the target area on the piston polished to evaluate the effects of reflectivity in the target area. An attempt will also be made to compare the proximity probe to the microwave probe made by Jodon Corporation. General Motors Research Laboratories lent us their Jodon probe. The probe is in need of a new oscillator, and every effort will be made to find the right one and carry out the comparison test.

B. HEAT FLUX PROBE

The total heat flux from combustion gases to the wall, including both convection and radiation, will be measured using a heat flux probe. In principle, it is a fast response thermocouple designed to measure surface temperature as a function of time. The basic features of the sensor was adapted from Oguri and Inaba (1972). The thermocouple materials are iron and nickel. The description of the sensor is detailed in Figure (7-15). A 50 μm nickel wire is flattened into a tape of about 12 μm thickness, which is then sandwiched between the two parts of a split tapered pin. The nickel wire is insulated from the split sections by two mica sheets (20 μm). The tapered pin is assembled and then

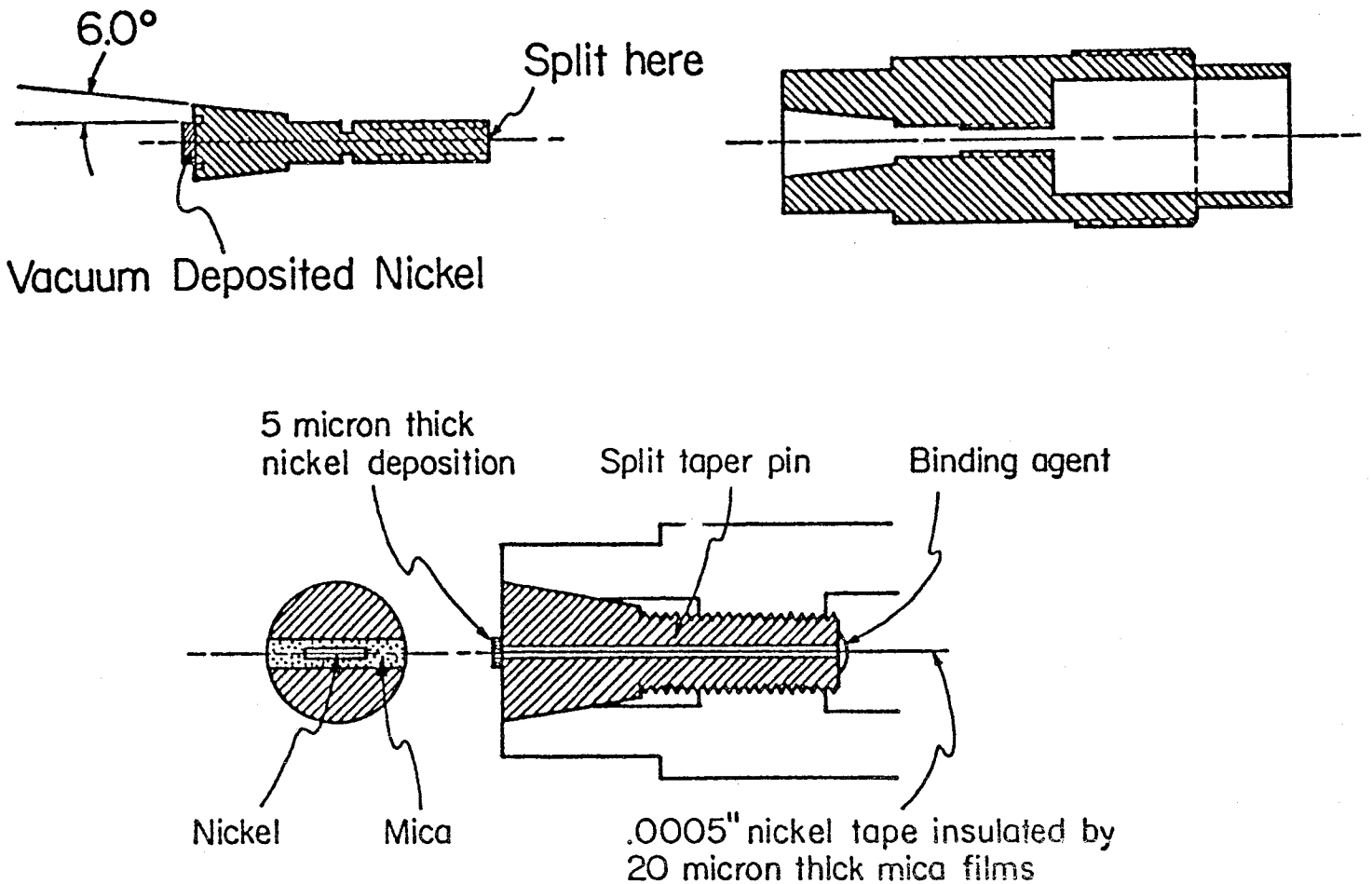

Figure 7-15. Schematic of the surface thermocouple design.

carefully inserted into an iron holder. The front section of the entire assembly is then ground, cleaned and degreased. The nickel tape and the iron body is checked to verify that there is a high electrical resistance between them. A thin film of nickel is then deposited on the front face of the pin to make a Ni-Fe junction. The active area is only about 0.3 mm in diameter. The thermocouple signal is amplified by a high-gain differential Tektronix amplifier (Model AM 503). The total resistance of the probe and leads (2 x 1 m) is about 4.9 Ω, of which less than 2 Ω is due to junction resistance.

During the course of fabrication of the probe some difficulties were encountered while machining the split tapered pin. Due to its diminutive size and the precision taper which is needed to match with that of the holder for proper self-sealing, fabrication of this part was very demanding. This necessitated the development of a special fixture which eventually made the fabrication feasible. The major problem faced then turned out to be the vacuum deposition of the thin nickel layer. Initial attempts were made with nickel wire wrapped around a tungsten heater. Though the melting point of tungsten (3382°C) is a good deal higher than that of nickel (1455°C), the two interact. As the nickel wire melted, the physical integrity of the tungsten material was lost and failure occurred, possibly due to eutectoid reaction caused by nickel going into solution with tungsten. An indirect heating of nickel was tried next. The first attempt utilized an alumina crucible heated by a tungsten coil. The result was no more successful than previous effort, as the alumina crucible appeared to be attacked by liquid nickel and was destroyed. A carbon crucible was also tried without much success. Finally, a tungsten boat was used with a few pieces of tungsten wire and small amount of nickel powder, not exceeding 9% by mass of tungsten. The boat was heated by passing current through it. The current was very carefully controlled to deposit nickel at a very slow rate, to produce a coating thickness of several microns.

Initial Probe Tests

The probe will be tested in a combustion bomb providing a controlled test environment. The experimental apparatus is a constant volume cylinder. Briefly this is composed of two cylinders, Figure (7-16), connected through a rapid acting intake valve. The working fluid is introduced into the mixing reservoir where it can be heated or cooled. The combustion chamber is initially evacuated. When the intake valve is opened, gas flows into the combustion chamber through the tangential port, and a swirling flow is established, which decays with time. The initial temperature of the combustion chamber gas tends to attain a temperature which is equal to the specific heat ratio times the initial mixing reservoir temperature. How close it approaches the ideal value depends on the heat loss during induction process, the mixing chamber volume and the kinetic energy of the flow.

In the first test, the combustion chamber was evacuated to a very low pressure, and then a valve was rapidly opened to allow an influx of argon gas into the chamber. Figure (7-17) shows the output of the surface thermocouple obtained after common mode rejection of noise and amplification by 20,000. The surface temperature is seen to rise by 2.7°C. The noise seen on the temperature signal trace is due to a slight mismatch of the impedance of the differential inputs to the amplifier. The signal to noise ratio is about 33:1 at the peak, wich is excellent, considering the small amplitude of the signal. The heat flux into the thin film can be readily deduced by making the assumptions that the heat transfer through the substrate structure below the thin film thermocouple may be approximated as a one-dimensional conduction into a semi-infinite solid. In that case one obtains

$$q_w = (k\rho c/\pi)^{\frac{1}{2}} \left[(T_w(t)-T_i)/t^{\frac{1}{2}} + \frac{1}{2}\int_0^t (T_w(t)-T_w(\lambda))/(t-\lambda)^{3/2} d\lambda\right] \quad (7\text{-}12)$$

where ρ is density, c specific heat and k conductivity of the substrate, Tw is wall temperature, t and λ are time, and Ti is initial temperature. Equation (7-12) is a representation of the exact solution to the tran-

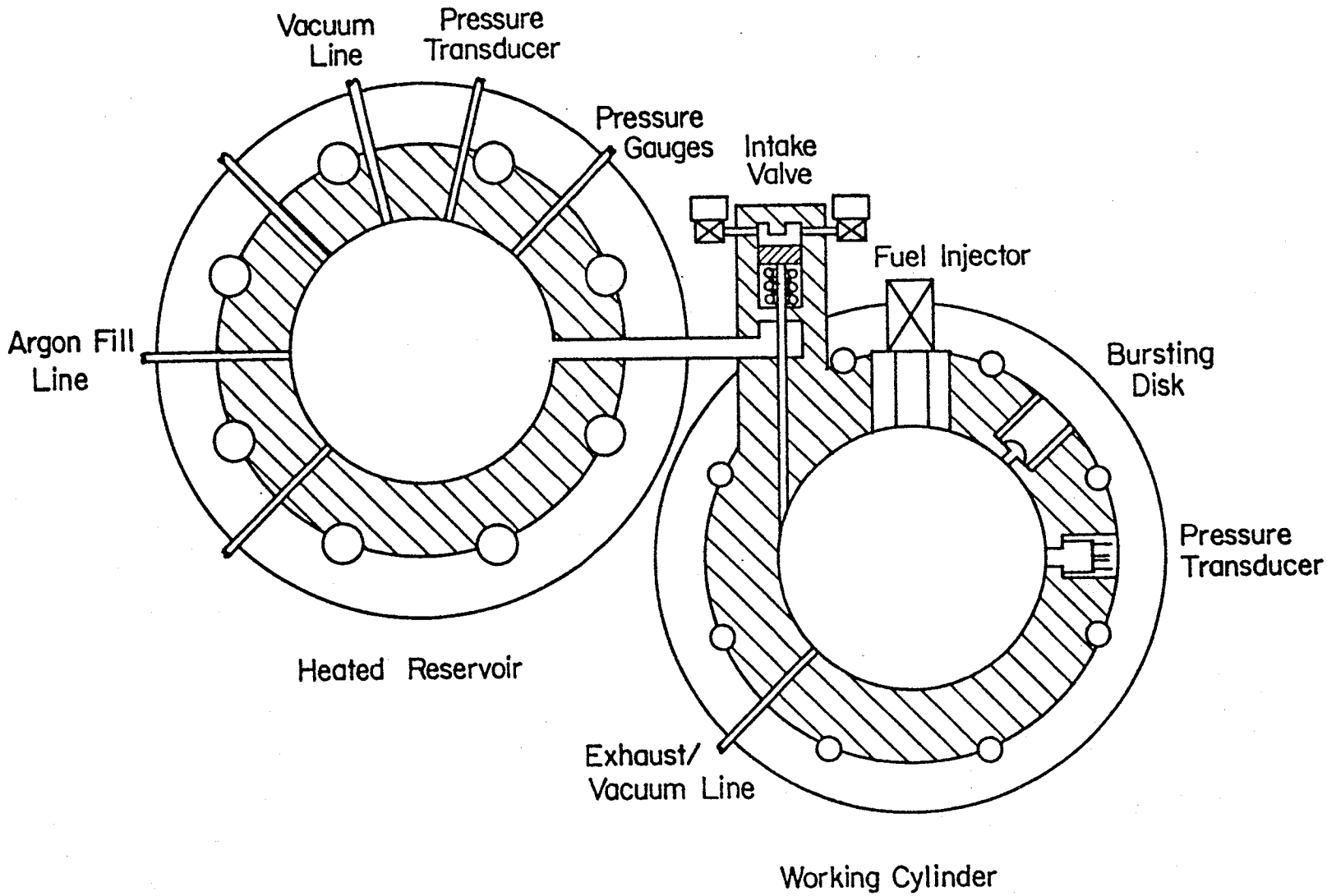

Figure 7-16. Schematic of the diesel combustion bomb.

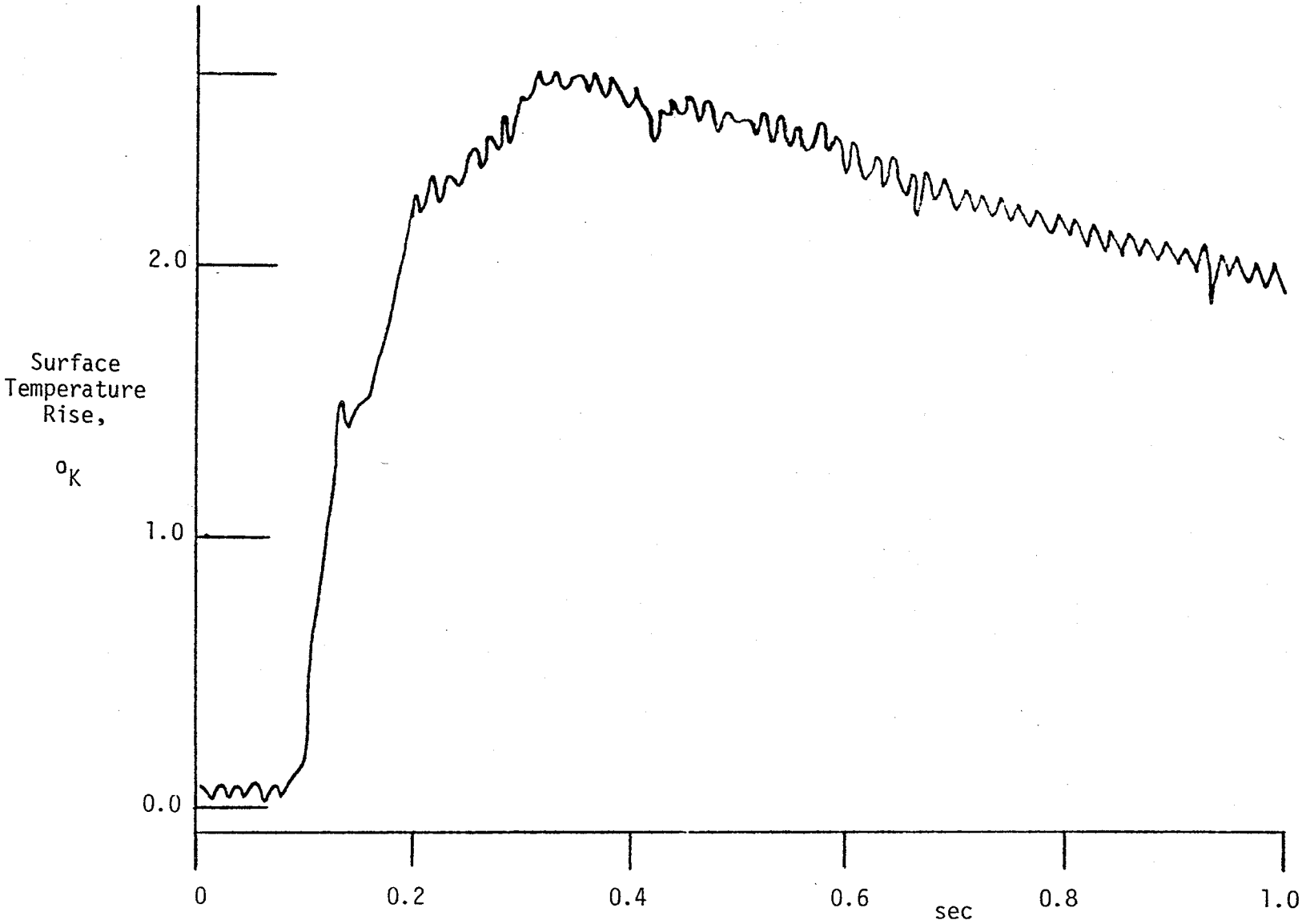

Figure 7-17. Fe-Ni surface thermocouple temperature response. Probe installed in the combustion bomb and subjected to sudden influx of gas into the bomb.

sient heat conduction equation. It has the advantage over the more commonly used alternative form that it does not require the differentiation of the signal obtained from the thin film thermocouple. Equation (7-12) in its original form assumes that the thickness of the film is small and characteristic time ℓ^2/α is small (where ℓ is the thickness of the film and α is the thermal diffusivity of the base metal) in comparison with the physical time scale of interest (Vidal 1956). Application of equation (7-12) to the signal shown in Figure (7-17) yielded the heat flux data reported in Figure (7-18). The scatter visible in Figure (7-18) is partly real and due to flow unsteadiness, and partly due to the fact that the oscilloscope data was hand digitized from a single realization and could be improved by averaging data from multiple realizations. Further tests and calibration procedures will be carried out on the heat flux probe in the near future.

Analysis of Temperature Field Around a Heat Flux Probe

The heat flux probe will be built as a plug fitting flush with the combustion chamber surface. One of the concerns in interpretation of the data obtined from the probe is that its presence will alter the measured temperatures. To support the experimental effort at Purdue, an analysis was made of the steady state heat transfer through the probe and of the resulting temperature field. The objective was to determine the magnitude of the error in the reading due to the (artificial) interference of the implanted probe and the 'plug' that houses it, which may cause a 'hot' or 'cold' spot on the wall.

This involved the solution of the steady-state heat conduction equation for a given geometry, thermal properties and boundary conditions. For a single probe and plug implanted in an infinite flat wall, the problem is formulated in cylindrical polar coordinates and two dimensions with boundary conditions as shown in Figure (7-19a). Note that a heat transfer coefficient, h_i has been prescribed to represent thermal resistance across a threaded and non-threaded interface between probe and plug and plug and wall. The problem is characterized by variation in the following non-dimensional groups:

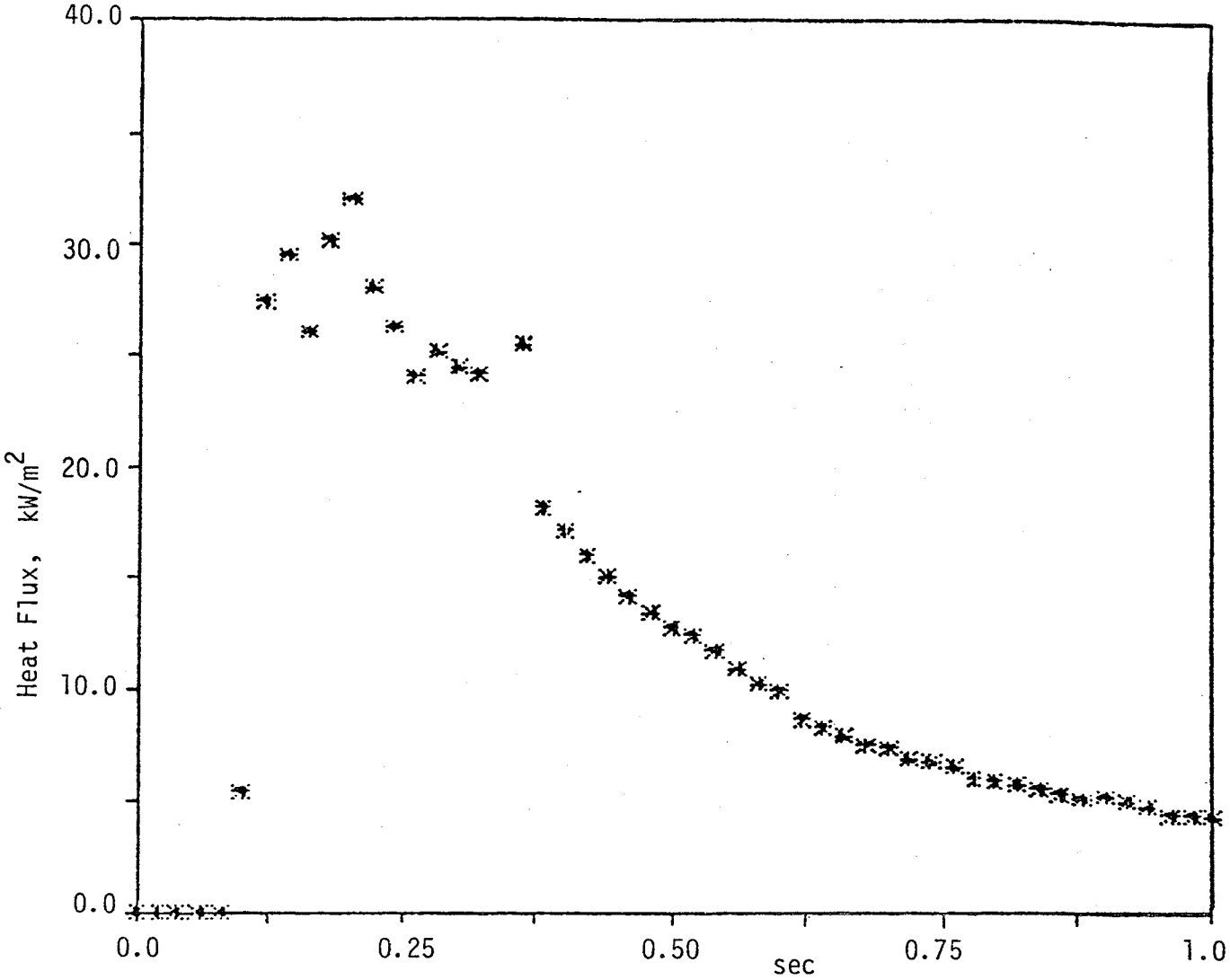

Figure 7-18. Heat flow corresponding to the data in Figure 7-17 and interpreted via eq. 7-12, which assumes one-dimensional heat flow.

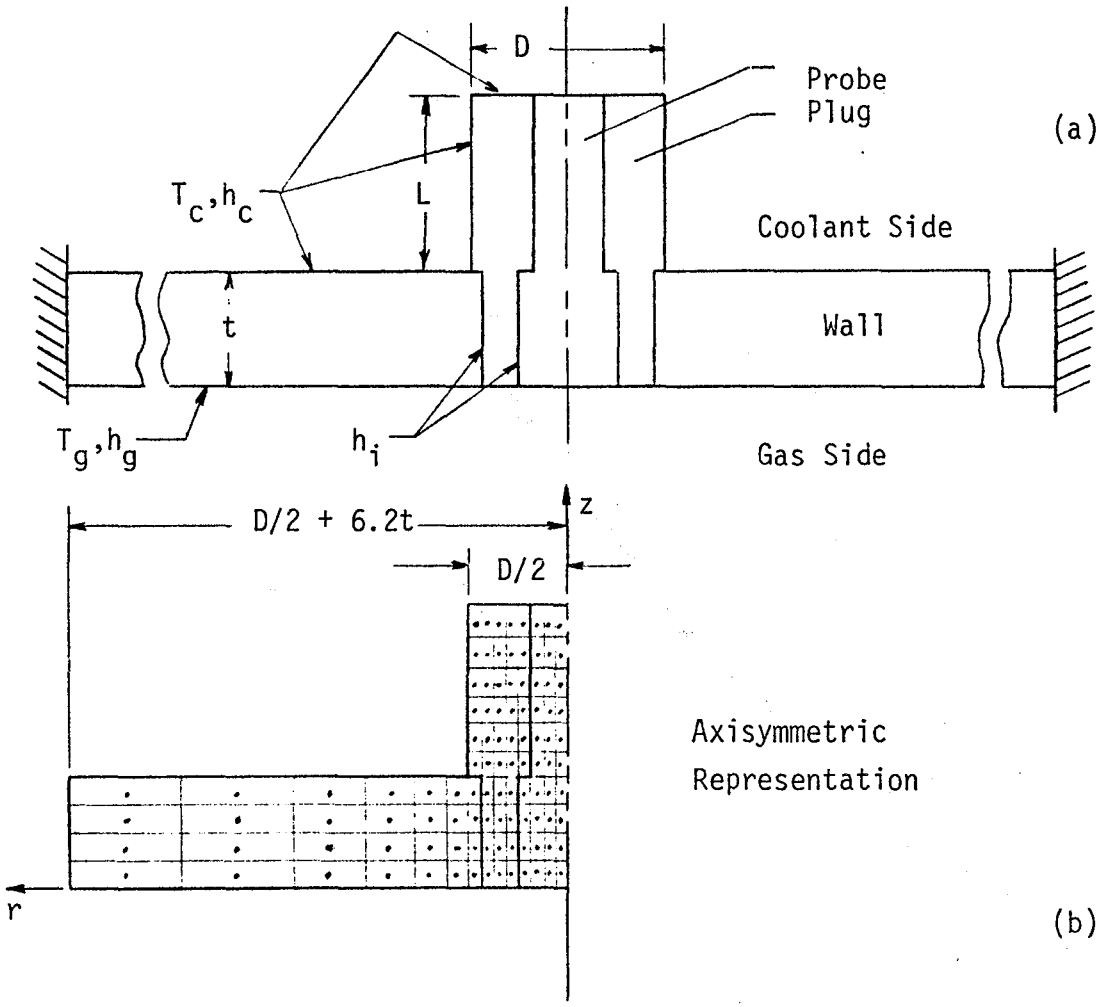

Figure 7-19. Schematic representation of the heat flux probe implanted in a wall, and a corresponding mathematical model.

D/t, L/t, $h_g t/k$, $h_c t/k$, $h_i t/k$

and, if plug and wall materials and different, k_p/k. The first two groups characterize geometry, while the next three are Biot moduli describing interface and boundary conditions. The governing equation was solved by finite differences, using the mesh shown in Figure (7-19b). For simplicity, the taper in the probe shape was idealized and taken as a cylinder.

Preliminary results were obtained for varying geometry, that is L/t and D/t, dimensionless length and diameter of plug housing probe. Probe diameter was taken to be 25% of plug diameter and the three Biot moduli have been fixed at 0.1, 0.4 and 1.0, corresponding to $t = 0.01m$, $k = 50 W/m^{\circ}c$, $h_g = 500$, $h_c = 2000$ and $h_i = 5000$ $W/m^{2\circ}K$.

The plot of typical radial surface temperature distributions presented in Figure (7-20) is a sample of the capabilities of the analytical model. It shows the effect of the length of the probe exposed to the coolant as it protrudes into the cooling passage, expressed in terms of dimensionless temperature error (departure of surface temperature from unperturbed conditions as a fraction of the difference between the gas temperature and the wall temperature). For the values of the dimensionless parameters chosen, which should be fairly representative, it is seen that the presence of the probe introduces a distortion in the surface temperature which grows with increasing L. The error is the largest at the center of the probe, i.e., at the thermocouple location, reaching values on the order of several percent. The discontinuous changes in the temperature profile are due to the contact resistances in the probe assembly. The contact resistances are seen to amplify the cooling effect on the probe surface, as they reduce the heat flux in the radial direction which would otherwise act more effectively to diffuse the local cooling. This can be seen when comparing Figure (7-20) to Figure (7-21). The latter figure shows the surface temperature profiles in the absence of contact resistances, displaying much smaller temperature distortions.

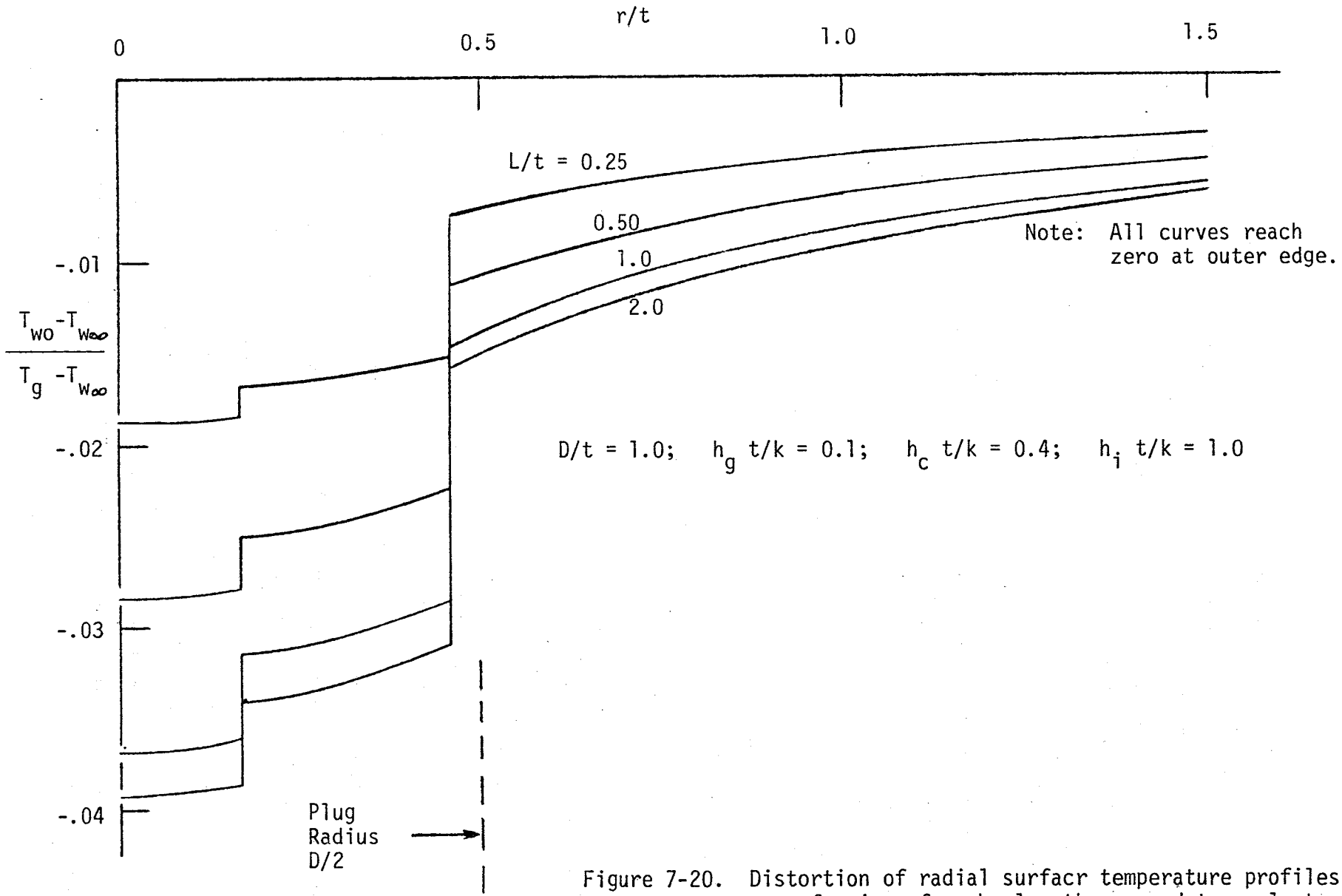

Figure 7-20. Distortion of radial surfacr temperature profiles as a funcion of probe length exposed to coolant. Distortions amplified by contact resistance.

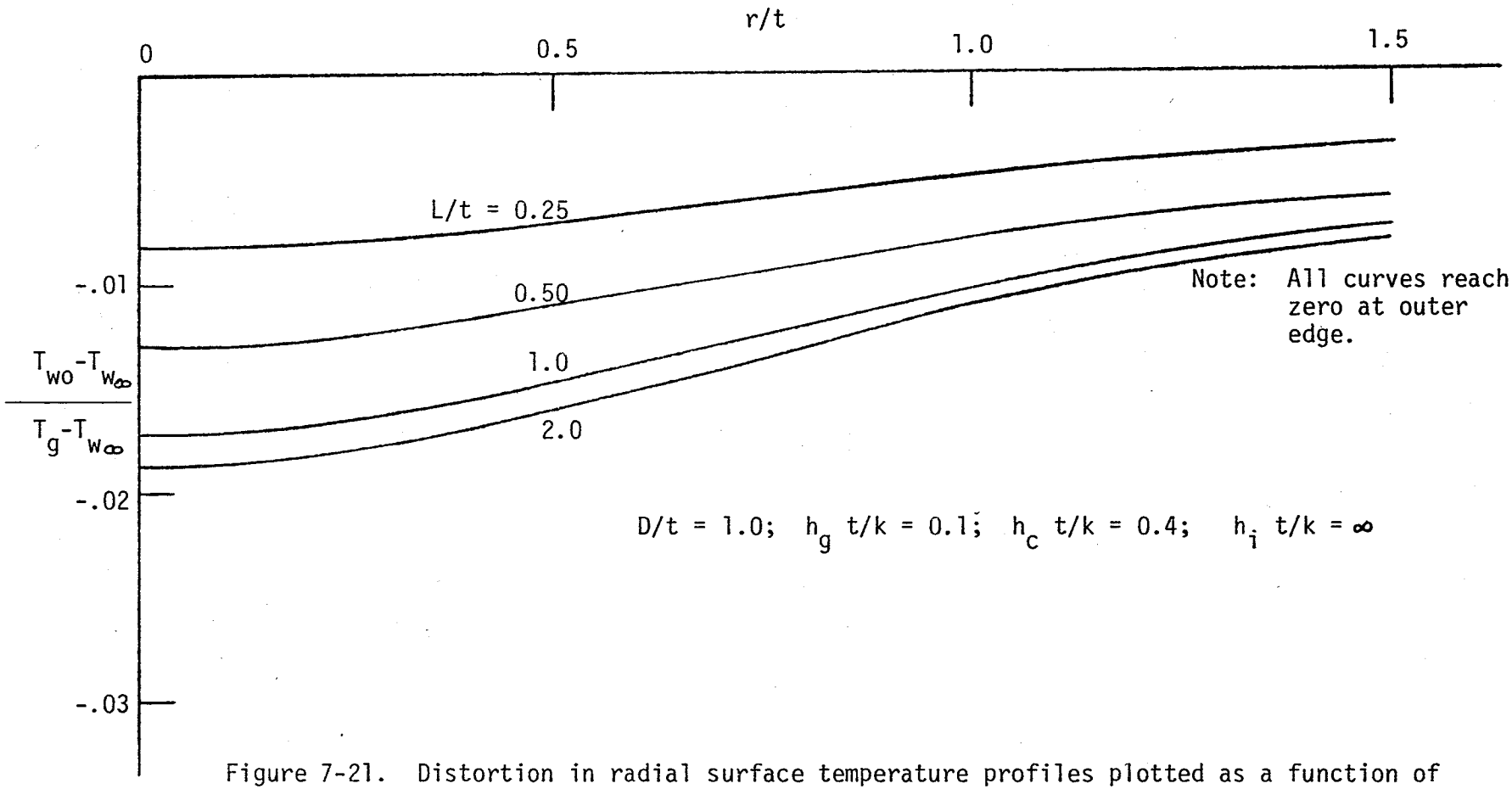

Figure 7-21. Distortion in radial surface temperature profiles plotted as a function of probe length exposed to coolant. Contact resistance set to zero.

The observed probe-induced error should become more important when probe and wall conductivities differ greatly, such as for a ceramic wall and a metal probe. The results also depend on interface resistances and Biot moduli for gas and coolant heat transfer coefficients. Some sample calculations have been made, extending the work to the case of a ceramic wall with an implanted steel heat flux plug. The calculations showed that in this case the presence of the plug produces very large local surface temperature distortion. The magnitude of this distortion is very sensitive to the geometrical details, such as ceramic thermal conductivity, thickness of the ceramic and of its metal backing (if any), interface contact resistance between the plug and the wall and the extent to which the plug is exposed to the cooling environment outside of the wall.

In summary, a framework of study for this problem is now in place and the developed computer code can now be exercised to obtain additional results pertaining to heat flux probe geometries and engine conditions. The developed analytical capability will permit us to make estimates of the probe-induced error and to correct the measurements for the effects of probe interference.

C. HEAT RADIATION MEASUREMENTS

The heat radiation will be measured using a multichannel infrared detector. This instrument will allow spectral resolution of the radiation on an instantaneous basis, from which one can deduce the radiation heat flux and radiation temperature.

Optical Access

One of the greatest difficulties in radiation heat transfer measurements in diesel engines is securing a good optical access. For cup-in-piston geometries the access can be gained only through the head. Due to the very complex geometry of a typical engine head there are only limited possibilities for optical access. The Cummins single cylinder engine

will have two access ports that can be used for radiation measurements. However, one of the ports is located towards the cylinder sidewall and would not permit a good view of the radiating gas. The other has another problem, as there is an obstruction of the head structure which precludes direct viewing through a window inserted into this port. This means that the light coming through this latter window would have to be brought, by some means, to the collection optics located outside of the engine, for example, by using optical fibers capable of transmitting infrared radiation. Surveying the availability of such fibers, it was found that most fiber optics manufacturers are set up to serve the communications industry, and they are not working with infrared radiation. The only company which has a fiber that could be useful is the Spec Tran Corporation in Sturbridge, Massachusetts. They manufacture a fiber using zirconium fluoride cladding which is claimed to be useful over the wavelength range of 1 to 4 microns. However, the cost of such fibers is very high. In the course of the search for a suitable fiber optics another possiblity was identified. Advanced Kinetics, Inc. manufactures metallic light guides, which basically are tubes that are internally polished and gold plated. They are useful for frequencies spanning visible light all the way out to the microwave radiation. Although their standard components are not small enough for our application, the concept may be useful in handling the radiation once it has been brought out of the engine through a short fiber optics bundle. In this way the detector can be remotely positioned with respect to the engine and thus be more thermally stable.

An alternative solution could be the design of a new viewing port. One idea is to remove one of the intake valves to provide a more flexible means of optical or probe access. Any resultant loss in engine volumetric efficiency would be compensated for by use of a higher intake pressure. It appears, at this time, that the removal of one of the intake valves is a viable option. We have discussed this option with Cummins Engine Company, and are now working on the design of such a viewing port and of the hardware that would be needed to replace the regular valve-and-spring assembly.

Another difficulty in optical access is associated with soot deposition on the window during engine operation, which can rapidly build up and obstruct the measurements. A survey of the literature revealed that workers in this field have used basically three techniques to keep windows clean: (1) purging, (2) flush windows with injection tripping and (3) recessed heated windows.

In the purging technique, as used e.g., Oguri and Inaba (1972), a continuous stream of gas is directed at the window to keep it clean. Unfortunately, the purging perturbs the flow field, and to some unknown degree also the radiation process. We have used a similar purging technique to keep windows clean in another application measurements of particulates in an exhaust pipe (Ferguson et. al., 1983). By suddenly shutting the purge off at the time a measurement is to be made, we were able to eliminate the flow perturbations in that particular case. Based on our experience from that work we estimate that Oguri and Inaba used a purge flow rate equivalent to about 25% of the engine air flow. Even so they found that the purge was not effective enough to allow running the engine long enough to reach steady running before the window became sooty. They therefore were forced to develop a different system, which uses injection tripping.

In systems employing injection tripping, Ahn et al (1981), Greeves and Meehan (1976) and probably Dent and Suliaman (1977), the instrumented cylinder is brought up to speed in a motoring mode, being driven by either the dynamometer or by firing the other cylinders in a multi-cylinder engine. The engine is brought up to temperature by circulating the water and oil through external heaters. When a measurement is to be made, a solenoid or some other rapid actuating mechanism, trips and injection commences. Measurements are then made during the first few cycles after tripping, while the window is still clean. We chose not to use this method, because in the case of an insulated engine this technique will not allow the walls to come up to a steady-state operating temperature. One possible solution would be to fire the cylinder during warm-up using spark ignition and a homogeneous propane charge. When a

measurement is desired, the propane system is then shut off and the diesel fuel injection is initiated.

The approach we are adopting involves recessing the window and heating it. This has been used with varying degrees of success by Flynn et al (1972), Matsui et al (1972, 1982) and Kajiyama et al (1982), who used hot water to heat up the windows. It's not clear why heating the window works. Some people claim that if the window is hotter than the gas in front of it, thermophoresis pushes soot particles away from the windows. Others claim that if the window is hot enough, the depositing soot burns up. We are of the opinion that both processes are involved. To enhance the effectiveness of the system, we decided to generate higher window temperature than used by Matsui et al (1982), achieving this by use of hot oil instead of hot water. Figures (7-22) and (7-23) show a window housing that was designed and constructed for use in our experiments. This housing is interchangeable with an AVL pressure transducer.

In order to size the oil pump and heater, some bench experiments were performed using a spare AVL head. The apparatus is shown in Figure (7-24). Hot ethylene glycol was circulated through the window housing installed in the AVL head. Measurements were made of the pressure and temperature drop of the ethylene glycol as it flowed through the head. These results, coupled to simple global analysis, led us to conclude the window temperature will stabilize at roughly the average of the engine wall temperature and the inlet oil temperature.

The maximum achievable window temperature is limited by material problems, including those of high temperature oils and seals. Reviewing all available options and costs associated with them, we concluded that the optimum sytem will be limited to maximum oil temperature of 530°K. This is well above (by 150°K) the temperatures used in any of the previous experimental studies using hot water window heating, and it is hoped to be sufficient for successful soot free operation.

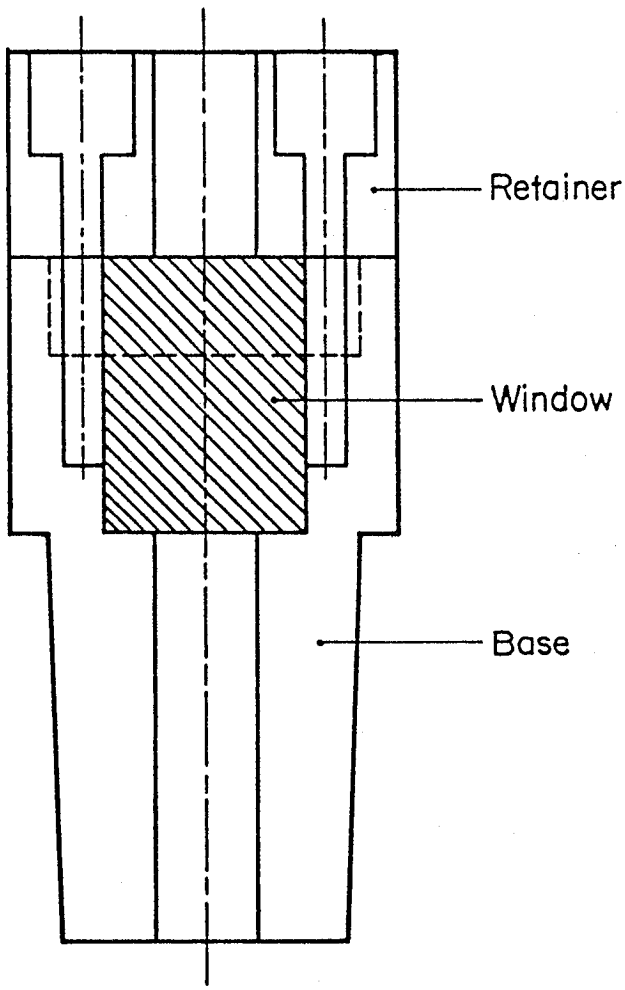

Figure 7-22. Drawing of heat radiation probe window and housing assembly

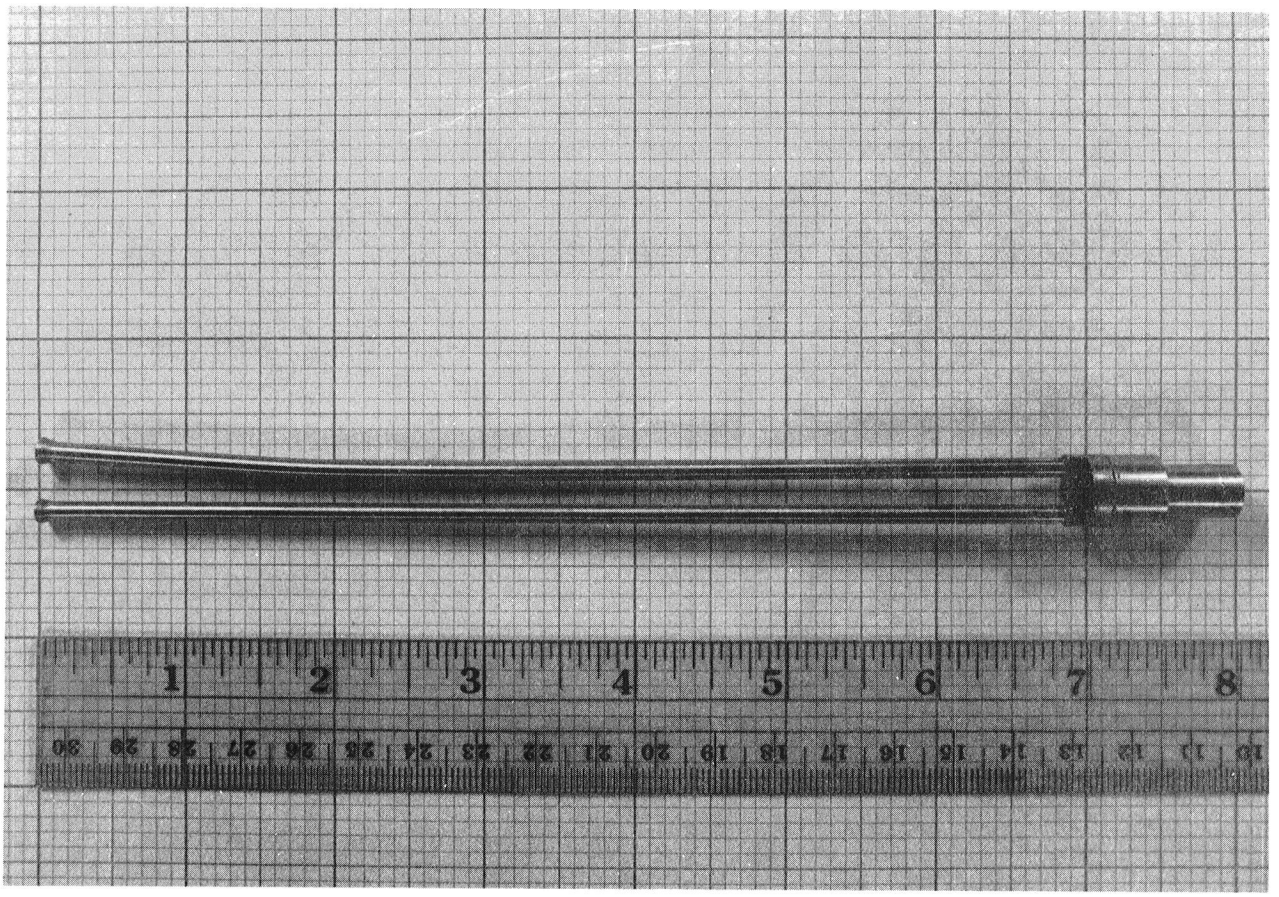

Figure 7- 23. Photograph of the window and housing assembly indicating its physical size.

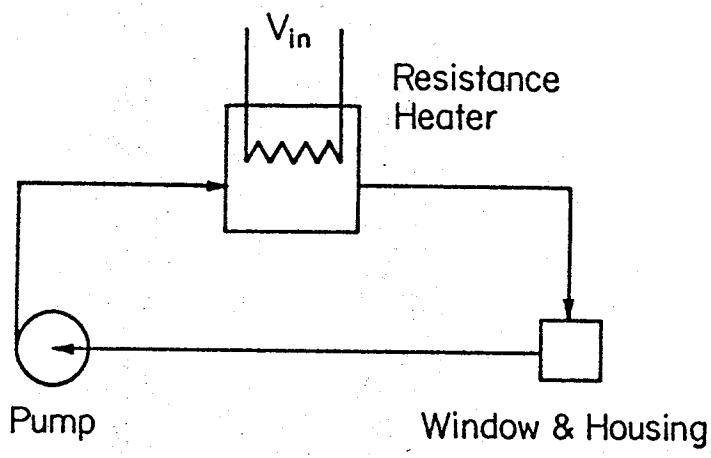

Figure 7-24. Schematic of window temperature control system

The work yet to be done includes minor modifications to the window housing, the purchase of some additional hardware, calibration of the device, and actual testing of the device in a diesel engine. Modifications to the window housing include changes to obtain a tight seal and enhance the heating of the window at the surface exposed to combustion. With the maximum temperature of 530°K, silicon rubber can be used to seal the window. This requires a change in the housing to include grooves for o-ring placement. To enhance the heating of the window surface, the inlet tube will be extended to bring the high temperature incoming fluid flow close to the surface. This also could be accomplished by placing an obstruction in the flow path to force the fluid nearer the surface. Both the addition of the o-rings and flow path changes will tend to restrict the size of the inlet and outlet passages. This size restriction should not present a problem since the pressure drop through the device is currently low, and any increase should still be within the limits of the equipment to be used. A change to a sapphire window will be made to utilize its higher strength and thermal conductivity than that of fused silica, Brady and Clausen (1977). Also the sapphire material has a better transmissivity in the range of the wavelengths associated with diesel combustion.

To date, a pump, a heater, and some of the stainless steel tubing required for the project have been purchased. Additional stainless steel tubing and the insulation for this tubing still need to be purchased. The heater oil also needs to be purchased. Testing and adjustments of the window-heating system will involve recording the transmission through the window at various degrees of sooting. The quantity of soot may not be measurable, but a qualitative idea of the level of soot build up that begins to impair measurements has to be known prior to use in the engine. The actual test of the system will involve varying the temperature of the window and, if needed, increasing the buffering volume in front of the window.

D. DATA ACQUISITION

An improved high speed data acquisition system is under development for use in the engine laboratory, as well as the adjacent diesel bomb laboratory. This system is based around a Digital Equipment Corporation (DEC) LSI-11/23+ microcomputer connected to a DEC VAX 11/780 computer system, the larger system being used for program development and for uploading of experimental data for permanent storage. Use of the Mechanical Engineering Department VAX computer system for program and data storage eliminates the considerable expense of providing local mass storage capabilities for the 11/23+. The two systems will be interconnected via a high speed serial data link.

The VAX computer uses the UNIX operating system and has a cross-assembler and C language cross-compiler available that will generate PDP-11 (same as LSI-11) machine code. These facilities are being used for program development. Most of the software for the data acquisition system is being written in C, a systems programming language very appropriate for this application.

The hardware contained in the system consists of the DEC LSI-11/23 processor card (which includes two serial ports and a bootstrap ROM), a 1 million byte memory card manufactured by Clearpoint, and an ADAC Corporation high-speed 8 channel 12-bit analog to digital converter (A/D) and direct memory access (DMA) interface. By using the DMA interface, the A/D converter will be capable of a maximum total throughput of 100,000 conversions per second. A DEC VT100 computer terminal will be used to communicate with the system, and in the future we hope to add a graphics feature to this terminal to allow immediate display of experimental results. This will allow results to be evaluated before transfer to the VAX system, thus poor data may be identified before transfer to permanent storage. This system is being developed as an improvement over an existing LSI-11/03 system that has been in use in the lab. The principal performance improvements will be much higher A/D conversion speed (100 KHz vs. 20 KHz), and much greater local data storage capability (1 Mbyte, expandable to 32 MBytes, vs. 64 Kbytes).

When applied to the engine experiments, the system will accept and digitize upon command from a crank angle marking device which outputs a symmetrical square wave, the signals from up to eight transducers connected to the engine. The zero crossings of the square wave correspond to a crank angle increment of 0.1 or 0.4 degrees (selectable). These zero crossings will be used to trigger the A/D converter when performing an experiment. Upon being triggered, the A/D converter will sweep through the 1 to 8 channels to which transducers are connected, digitize the voltages, and store the values in memory for later transfer to the VAX computer for analysis.

E. CRANK ANGLE ENCODER

Upon application of the polytropic exponent method to different sets of motored pressure-angle arrays obtained from the AVL research engine, it was discovered that the mounting shaft angle encoder used to trigger the analog to digital convertor was inadequate. This conclusion was reached because the angle of peak pressure fluctuated from day to day, even though the encoder mounting was never touched. A photograph of the encoder and its mounting arrangement is shown in Figure (7-25). The encoder is manufactured by Sequential Information Systems, Incorporated, in Dobbs Ferry, New York. It produces 360 pulses and one triggering pulse during one revolution of its shaft. The plate on the left was used to couple the encoder to the engine camshaft. The coupling is manufactured by Renbrandt, Incorporated in Boston. This coupling is specially designed to accommodate small amounts of misalignment between the encoder shaft and plate shaft. Because it is held to the shafts by only two small allen-head screws, the possibility exists for relative motion between the shafts and the coupling. Also, it is uncertain if the coupling can transmit the variations in rotational speed of the camshaft, thus causing the frequency of the encoder signal to vary.

The problem was solved by purchasing a crank angle degree marking device manufactured by AVL. The components of the device are shown in Figure (7-26). The signal generator wheel is firmly connected to the engine

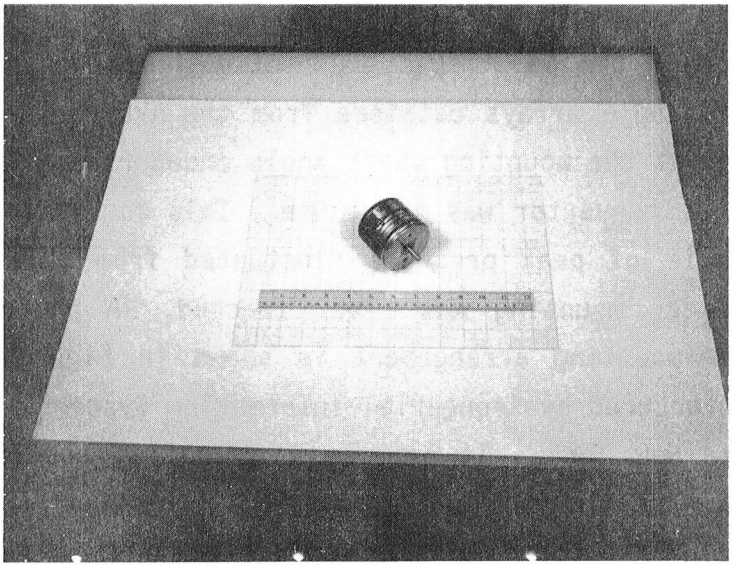

Figure 7-25. Typical shaft angle encoder

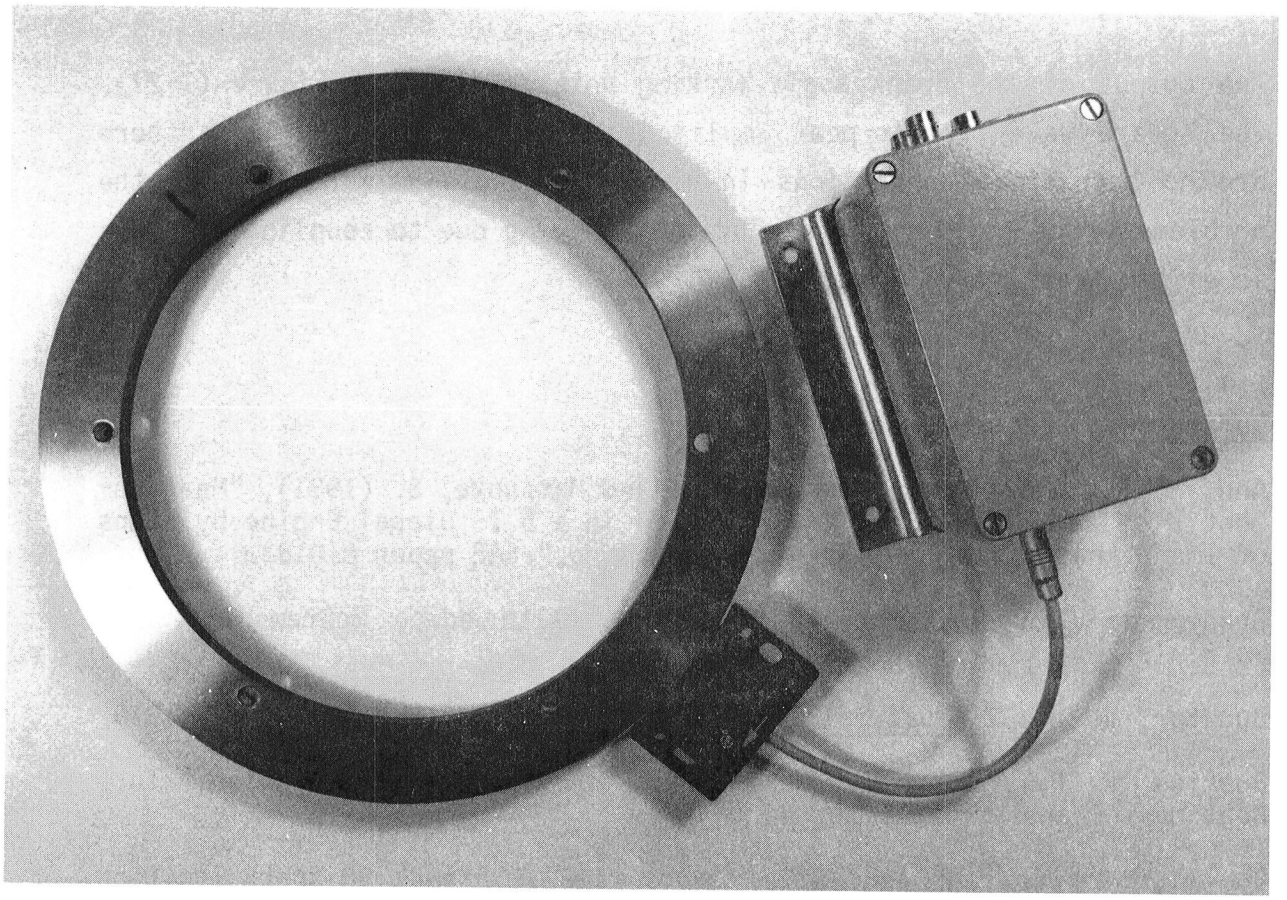

Figure 7-26. AVL crank angle degree marking device

camshaft. It has one track of 450 teeth for crank angle marking and another track with a slit for triggering. The inductive pickups are used to sense the field variations produced by the slots. The pick-up electronics unit converts the inductive pick-up signals to square waves and quadruples the crank angle marks. With the signal generator wheel attached to the camshaft then a crank angle signal can be obtained for every 0.4 degrees of crank rotation.

The output of the crank angle marking unit is shown in Figure (7-27). The square wave peak-to-peak amplitude is about 5 volts. Since there are no mechanical connections in the crank angle marking device, the problem of the trigger signal location varying due to coupling slippage is eliminated.

References

Ahn, S. K., Matsui, Y., Kamimoto, T. and Matsuoka, S. (1981), "Measurement of Flame Temperature Distribution in a D.I. Diesel Engine by Means of Image Analysis of Nega-Color Photographs," SAE paper 810183.

Brady and Clausen, "Materials Handbook (11th ed.), McGraw-Hill, New York, 1977.

Buchter, H. H., Industrial Sealing Technology, Wiley, New York, 1978.

Buckius, R. O. and Tien, C. L. (1977), "Infrared Flame Radiation," Int. Heat Mass Transfer, Vol. 20, pp. 93-106.

By, A., Kempinski, B. and Rife, J. M. (1981), "Knock in Spark Ignition Engines," SAE Paper 810147.

Dent, J. C. and Suliaman, S. J., (1977), "Convective and Radiative Heat Transfer in a High Swirl Direct Injection Diesel Engine," SAE paper 770407.

Douaud, A., and Eyzat, P., (1977), "Digitap - An On-Line Acquisition and Processing System for Instantaneous Engine Data Applications," SAE Paper 770218.

Ferguson, C. R., Chapman, M., Kizawa, H. and Nash, R. F. (1983), "Diesel Exhaust Opacity: At the Port and a Meter Downstream," SAE paper 831724.

Flynn, P. Mizusawa, M., Uyehara, O. A., and Myers, P. S. (1972), "An Experimental Determination of the Instantaneous Potential Radiant Heat Transfer Within an Operating Diesel Engine," SAE paper 720022.

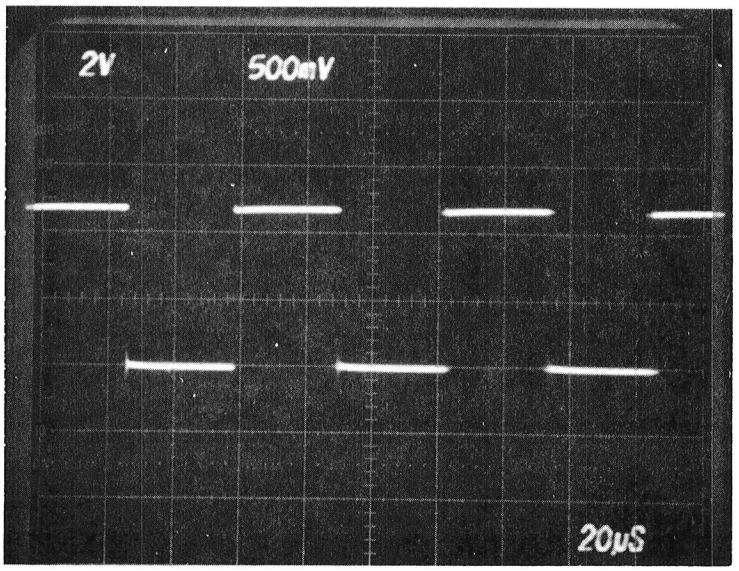

Figure 7-27. Typical signal output from AVL crank angle degree marking device

Greeves, G. and Meehan, J. O., (1976), "Measurement of Instantaneous Soot Concentration in a Diesel Combustion Chamber," Paper C88/75 in Combustion in Engines, The Institution of Mechanical Engineers, London.

Kajiyama, K., Sajiki, K., Kataoka, H., Maeda, S., and Hirose, C. (1982), "N_2/CARS Thermometry in Diesel Engines" SAE Trans., vol. 91, paper 821036.

Kunugi, M. and Jinno H. (1966), "Determination of Size and Concentration of Soot Particles in Diffusion Flames by a Light-Scattering Technique," Eleventh Symp. Int. Combustion, pp. 257-266.

Lagace, L. J., and Kissinger, C. D., "Non Contact Displacement and Vibration Measurement Systems Employing Fiber Optic and Variable Capacitance Transducers," proceedings of the 23rd International Instrumentation Symposium, Las Vegas, Nevada, May, 1977.

Matsui, Y., Kamimoto, T. and Matsuoka, S. (1979), "A Study on the Time and Space Resolved Measurement of Flame Temperature and Soot Concentration in a D.I. Diesel Engine by the Two-Color Method," SAE paper 790491.

Matsui, Y., Kamimoto, T. and Matsuoka, S., (1982), "Formation and Oxidation Processes of Soot Particulates in a D.I. Diesel Engine--An Experimental Study via the Two-Color Method."

Menadier, D., Kissinger, C., and Adkins, H., "The Fotonic Sensor," Instruments and Control Systems, Volume 40, June 1967.

Oguri, T. and Inaba, S. (1972), "Radiant Heat Transfer in Diesel Engines," SAE paper 720023.

Powell, J.A., "A Simple Two Fiber Optical Displacement Sensor," Review of Scientific Instruments, Volume 45, No. 2, February, 1974.

Vidal, R. J., "Model Instrumentation Technique for Heat Transfer and Force Measurement in a Hypersonic Shock Tunnel," Report No. AD-917-A-1, Cornell Aeronautical Laboratory, Inc., Buffalo, New York, 1956.

APPENDIX

ITI Thermodynamic Cycle Model and Heat Conduction Network Analysis

The thermodynamic cycle model developed by ITI is an advanced 4-stroke engine simulation. It builds on the extensive base of technical literature, which has demonstrated the utility of such cycle simulations for predictions of wide variety of engine processes and parameters. The code incorporates highly detailed and rigorous global descriptions of key engine processes. It addresses in an integrated manner many of the engine processes others have looked at in separate studies and brings into a single computer program the capability of solving them simultaneously. In addition, the ITI cycle code has other features and elements not found in other codes.

Among the unique features of the code is an accurate solution of the energy equation using an implicit solution technique that is stable and cost-effective. Much of the flexibility of the code derives from the details of the combustion fluids that are being tracked. These are composed of a mixture of air, water vapor, liquid fuel, gaseous fuel, and products of combustion. The thermodynamic properties for the individual components of the mixture are calculated at every time step from very efficient polynomial fits as a function of temperature and pressure, and for the products of combustion also as a function of the equivalence ratio (including dissociation). The fits are based on thermodynamic equilibrium calculations which describe the properties of products of combustion of a general fuel $C_xH_yO_z$ with air. Eleven species are considered - H, H_2, H_2O, CO, CO_2, O_2, O, OH, N_2, N, and NO. Using supporting ITI thermochemical software, new fits are generated for each fuel under consideration and these are linked with the cycle program at execution time. This approach to combustion chamber fluids allows studies of details such as pure air bypass in diesel engines, intake of unevaporated fuel in S.I. engines, gas blowby, etc., all within the same computer program.

During combustion the solution tracks two separate zones, one unburned and one burned, solving the energy equation for each. A submodel for diesel combustion has been implemented which accounts for premixed combustion, diffusion burning and a slow mixing "tail" burning region. The extent of premixed combustion is calculated from the extent of fuel vaporization in the ignition delay period which is based on the injection schedule, injection pressure and mean droplet size . The ignition delay itself is calculated from an empirical expression as a function of cylinder gas temperature, pressure and fuel cetane number. Heat transfer from the unburned zone is calculated from a convective heat transfer correlation and is based on the unburned zone temperature. The heat transfer from the burned zone is calculated as a sum of convective heat transfer based on burned zone temperature, and radiation, which is based on the temperature of the actively burning zone. The heat transfer correlations include the effects of fluid motions, turbulence and zoned combustion, and the resulting heat transfer rates are resolved in a uniquely detailed spatial manner.

Among the features of the code is its internal coupling to a built-in geometrical model describing heat conduction through the engine structure. This model is based on a thermal resistance network approach, and it represents the structure by an axisymmetric approximation consisting of over 150 distinct temperature nodes. Most of these nodes are internal points, although 40 of them are surface nodes. Of these, 19 are exposed to the gas in the combustion chamber and in the ports, and 21 are exposed to engine coolant and to oil. A typical network is shown schematically in Figure 1-22. By matrix operations, the full 150 node system may be reduced to an equivalent system involving only the 40 surface nodes, resulting in a highly efficient solution of the heat conduction problem at each engine cycle iteration. The full system may then be solved, if desired, only once after the convergence of the calculations, to produce temperatures at the interior points as well. Another special feature is the calculation of the piston/liner inter-

action, which is represented by time-averaged resistances and boundary thermal loads based on "time-sharing" of the following events: gas-to-liner, oil-to-liner, piston-to-liner and ring-to-liner heat transfer and heat deposition due to friction at the piston-liner interface. This time-sharing is represented correctly by consistent integration of all of these processes as they occur during the engine cycle.

Cyclic transients in thin layers adjoining the combustion chamber are handled by a fully validated one-dimensional, time-dependent calculation which has been automated and optimized with respect to grid size. It can resolve temperature swings even in extremely thin layers of material (as small as 0.00001 inch). The resulting temperature swings are a function of engine speed, heat transfer coefficient, gas temperature history, mean wall temperature, and material properties of thermal conductivity, k, and thermal capacity, ρc.

The code is structured to permit analysis of the complete multicylinder engine as a system, including turbocharger, intercooler and power turbine. The turbocharger model is of the quasi-steady type in which finite exhaust plenums are simulated, producing a pulsating flow into the turbine. The turbine and compressor models use dimensionless performance maps allowing component sizing studies. The overall system model is schematically shown in Figure A-1.

The mechanical friction model simulates the piston-connecting rod dynamics, which together with gas forces provides the total piston-liner contact force as a function of crank angle. Then, solving for ring hydrodynamic lubrication, one calculates instantaneous friction at the ring-liner interface for hydrodynamic, boundary and mixed conditions. A similar solution is carried out for the piston/liner interface. The remaining elements of engine friction, i.e. bearings, cams, and pumps (water, oil, fuel), are also simulated.

☆USGPO: 1985 — 559-109/10421

1. Report No.	2. Government Accession No.	3. Recipient's Catalog No.
NASA CR-174783		

4. Title and Subtitle	5. Report Date
Methods for Heat Transfer and Temperature Field Analysis of the Insulated Diesel - Phase I Progress Report	August 1984
	6. Performing Organization Code

7. Author(s)	8. Performing Organization Report No.
Thomas Morel, Paul N. Blumberg, Edward F. Fort, and Rifat Keribar	
	10. Work Unit No.

9. Performing Organization Name and Address	11. Contract or Grant No.
Integral Technologies Inc. 415 East Plaza Drive Westmont, Illinois 60559	DEN 3-342
	13. Type of Report and Period Covered
12. Sponsoring Agency Name and Address	Contractor Report
U.S. Department of Energy Office of Vehicle and Engine R&D Washington, D.C. 20585	14. Sponsoring Agency ~~Code~~ Report No. DOE/NASA/0342-1

15. Supplementary Notes

Interim Report. Prepared under Interagency Agreement DE-AI01-80CS50194. Project Manager, James C. Wood, Propulsion Systems Division, NASA Lewis Research Center, Cleveland, Ohio 44135.

16. Abstract

This report describes work done during Phase I of a 3-year program aimed at developing a comprehensive heat transfer and thermal analysis methodology oriented specifically to the design requirements of insulated diesel engines. The technology developed in this program will make possible a quantitative analysis of the low heat rejection concept, including the determination of the degree of heat transfer reduction and performance improvement that may be realistically achieved, the identification of design strategies that may be adopted toward that end, and a detailed characterization of the thermal environment in which new materials, lubricants and lubricant concepts will have to exist.

The program is comprehensive in that it addresses all the heat transfer issues that are critical to the successful development of the low heat rejection diesel engine:

(1) In-cylinder convective and radiative heat transfer
(2) Cyclic transient heat transfer in thin solid layers at component surfaces adjacent to the combustion chamber
(3) Steady-state heat conduction in the overall engine structure

Key heat transfer data for development and validation of the methodology are being acquired at Purdue University under subcontract. In order that practical considerations are adequately taken into account in the development of the analytical methods, the program is structured around a commercial, state-of-the-art, heavy-duty diesel engine.

The ITI program is comprised of a set of integrated analytical and experimental tasks. This Phase I report provides a detailed review of the ITI program approach, including the technical issues which underlie it, a summary of the methods that have been developed, and the results which have been obtained in the first year of the contract effort.

17. Key Words (Suggested by Author(s))		18. Distribution Statement
Diesel engine	Fuel consumption	Unclassified - unlimited
Transportation	Heat transfer	STAR Category 85
Computer model	Insulated engine	DOE Category UC-96
Energy		

19. Security Classif. (of this report)	20. Security Classif. (of this page)	21. No. of pages	22. Price*
Unclassified	Unclassified	275	A12

*For sale by the National Technical Information Service, Springfield, Virginia 22161

528 FS- 1
NATIONAL AERONAUTICS AND SPACE ADM
ATTN LIBRARY
LANGLEY RESEARCH CENTER
HAMPTON, VA 23665